Development of architectured micro-composite duplex stainless steels : manufacturing, microstructure and mecganical behavior

Hasan Naser

To cite this version:

Hasan Naser. Development of architectured micro-composite duplex stainless steels : manufacturing, microstructure and mecganical behavior. Mechanics of materials [physics.class-ph]. Université Grenoble Alpes, 2016. English. NNT : 2016GREAI024 . tel-01446717

HAL Id: tel-01446717
https://theses.hal.science/tel-01446717

Submitted on 26 Jan 2017

Communauté
UNIVERSITÉ Grenoble Alpes

THÈSE

Pour obtenir le grade de

DOCTEUR DE LA COMMUNAUTE UNIVERSITE GRENOBLE ALPES

Spécialité : **Matériaux, Mécanique, Génie Civil, Electrochimie**

Arrêté ministériel : 7 août 2006

Présentée par

Hasan NASER

Thèse dirigée par **Alexis DESCHAMPS**
et codirigée par **Marc MANTEL**

préparée au sein du **Laboratoire de Science et Ingénierie des Matériaux et des Procédés (SIMaP)**
dans **l'École Doctorale d'Ingénierie – Matériaux Mécanique Energétique Environnement Procédé Production (I-MEP2)**

Development of architectured micro-composite duplex stainless steels: Manufacturing, Microstructure and Mechanical behavior

Thèse soutenue publiquement le **26 mai 2016**,
devant le jury composé de :

M. Ludovic THILLY
Professeur, Université de Poitiers, Rapporteur
M. Eric MAIRE
Directeur de Recherche, CNRS, Rapporteur
M. Sébastien ALLAIN
Professeur, Université de Lorraine, Président
M. Alexis DESCHAMPS
Professeur, Grenoble-INP, Directeur de thèse
M. Marc MANTEL
Professeur PAST, Grenoble-INP, Co-directeur de thèse
Mme. Muriel VERON
Professeur, Grenoble-INP, Co-encadrant de thèse
M. Guillaume PARRY
Maître de Conférence HDR, Grenoble-INP, Invité

“…Knowledge calls out for action: if it responds to the call then it lives on . . . otherwise it perishes.”

Ali ibn Abi-Talib
(600 – 661 A.D.)

Remerciement

Ce travail a été effectué au Laboratoire de Sciences et Ingénierie des Matériaux et des Procédés (SIMaP) ainsi qu'au Centre de Recherche Ugitech (CRU). Cette thèse est le fruit d'une collaboration entre le Centre d'Excellence des Matériaux Architecturés Multifonctionnels (CEMAM) et l'entreprise UGITECH.

J'exprime ma gratitude au labex CEMAM ainsi qu'à UGITECH d'avoir assuré le financement de ce projet.

Je voudrais, tout d'abord, exprimer ma gratitude à Monsieur Sébastien Allain, Professeur à l'Université de Lorraine, qui m'a fait l'honneur de présider le jury.

Je remercie vivement Monsieur Ludovic Thilly, Professeur à l'Université de Poitier, et Monsieur Eric Maire, Directeur de Recherche CNRS à l'INSA-Lyon, d'avoir accepté d'être les rapporteurs de ce travail et aussi pour le temps qu'ils ont consacré à la lecture de ce manuscrit. Vos remarques constructives ont contribué à l'amélioration de la qualité de ce travail et nourri les réflexions sur les différentes problématiques de cette thèse.

Je suis tout spécialement reconnaissant à mon directeur de thèse Alexis Deschamps, à Marc Mantel qui a codirigé cette thèse, ainsi qu'à Muriel Véron qui a participé à l'encadrement de ce projet. Alexis, je te remercie sincèrement pour ta disponibilité, ton écoute, tes conseils et ton appui scientifique. Ton leadership bien *« architecturé »*, qui est doté de franchise et de pragmatisme avec un bon dosage entre rigueur et gentillesse, a fait le travail avec toi très enrichissant tant au niveau scientifique qu'au niveau humain. Je suis très heureux d'avoir travaillé avec toi tout au long de ces trois années de thèse. Marc, Je t'adresse un grand merci pour ta disponibilité, ta bonne humeur, tes conseils mais aussi pour tes idées toujours innovantes pour améliorer nos fils composites (qui valent de l'or !). Merci également pour ton soutien au quotidien lors des moments difficiles. Muriel, je tiens à te remercier pour ton expertise dans les méthodes de caractérisations microstructurales en particulier le MET, et aussi pour tes remarques pertinentes lors des réunions d'avancement. Un grand merci également pour ton aide à la préparation de la soutenance.

Lors de cette thèse, j'ai eu l'opportunité de réaliser la grande partie expérimentale de ce travail, en particulier le tréfilage, au Centre de Recherche Ugitech (CRU) à l'entreprise Ugitech. Cela m'a permis de rencontrer et de travailler avec différentes personnes. Je pense particulièrement à Nicolas Meyer à qui j'adresse mes vifs remerciements pour l'aide qu'il a apporté pour m'initier aux logiciels DICTRA et ThermoCalc et aussi pour le temps qu'il m'a consacré. Bien sûr, je ne peux citer le tréfilage sans parler de Frédéric Moser avec qui j'ai passé des milliers d'heures devant la tréfileuse Marshall. Je te remercie chaleureusement pour ton génie pratique qui était toujours décisif pour surmonter toutes les complexités rencontrées lors du tréfilage. Merci également pour ton bon sens de l'humour ; tu as toujours réussit à me faire rire même lors des moments difficiles (je n'oublierai pas tes réflexions sur l'homme préhistorique !).

Je tien à remercier aussi Didier Labrosse, Pierre Chemelle, Didier Molliet-Ribet et Sylvain Thevenet qui m'ont aidé pour les caractérisations mécaniques et microstrcturales.

Je suis très reconnaissant à toutes les personnes qui ont contribué aux résultats de ces travaux. Je remercie vivement Florence Robaut pour les cartographies EBSD. J'adresse également mes remerciements à Frédéric Charlot pour l'analyse chimique par EDS-MEB et aussi tous les personnels du CMTC. Je remercie vivement Frédéric De Gauser pour les traitements des essais effectués à l'ESRF. Je tiens aussi à remercier Thomas Buslaps responsable de la ligne ID15 à l'ESRF. Je remercie enfin Shujun et Chris qui ont contribué à plusieurs résultats de cette thèse.

Je souhaite aussi remercier tous les permanents, les ingénieurs et les techniciens du groupe Physique du Métal. Merci à Frédéric Livet pour les discussions sur des différentes thématiques autour d'un café et parfois d'une tarte aux pommes. Merci également à Guillaume Parry, Fabien Volpi, Marc Verdier et Hugo Van Landeghem.

Je tiens à remercier tous les doctorants du bâtiment Thermo. Merci à Kitti, Olivier, Mahmoud, Rosen, Audrey, Bassem, Ayman, Solène, Zélie, Martin, Nadia, Elham.

Je remercie tous mes amis pour les bons moments partagés autour d'une tasse de thé ou d'un repas. Je tiens à remercier particulièrement Sayed pour les bons moments passés à discuter de nos thèses et sur les différents sujets d'actualité, politiques…etc.

Enfin, aucun mot ne peut exprimer ma profonde gratitude à ma famille. Sans votre soutien, je ne serais jamais allé jusqu'à là. Votre soutien m'a permis de surmonter les moments les plus difficiles durant cette thèse en particulier lors du décès de mon père.

Je dédie naturellement ce manuscrit à la mémoire de mon père et à ma famille.

Abstract

The use of duplex stainless steel (DSS) grades for structural applications is considered as one of the most significant advances impacting the construction sector. This is because of their high mechanical properties coupled with interesting functional properties such as corrosion resistance or their low thermal conductivity compared to carbon steels. A better understanding of the relationship between their microstructure and properties is needed to obtain breakthrough properties and to provide the possibility to design tailor-made, architectured DSS for specific applications. In this work we propose a *top-down* strategy in which at least two bulk metals with well-known properties are mechanically alloyed by Severe Plastic Deformation (SPD). This proposed strategy serves two main objectives: i) enhancing the properties by microstructure refinement down to sub-micron scale ii) elaborating a model material for understanding the behavior of DSS obtained by the conventional metallurgical methods. The first objective of this work was the implementation of a manufacturing methodology using co-drawing, aiming at obtaining an ultra-fine microstructure of 316L/430LNb composites. One of the challenges met during our study was the significant inter-diffusion during the heat-treatment step necessary during processing preventing by consequence refining below the µm scale. An optimization investigation was carried out to account for this inter-diffusion for 316L/430LNb couple. Multi-scale micro-composites have then been obtained. The limitation of this process in terms of microstructure refinement has been rationalized by a systematic study of recrystallization and diffusion kinetics. In parallel with the microstructural evaluation, the mechanical behavior of these new micro-composites was examined. In situ tensile tests using high energy X-ray synchrotron enabled an in-depth understanding of the plastic interaction of the two phases.

Résumé

L'utilisation de l'acier inoxydable duplex (DSS) pour des applications structurales est considérée comme présentant l'un des plus grands impacts potentiels sur le secteur de la construction. Ceci est grâce à ses propriétés mécaniques élevées couplées avec des propriétés fonctionnelles intéressantes telles que la résistance à la corrosion, ou la faible conductivité thermique par rapport aux aciers au carbone. Une meilleure compréhension des relations entre microstructure et propriétés de ces aciers est nécessaire pour obtenir des propriétés exceptionnelles et concevoir des DSS sur mesure et architecturés pour des applications spécifiques. Dans ce travail, nous avons proposé une approche dite *top-down* dans laquelle au moins deux métaux ayant des propriétés bien connues sont mécaniquement assemblés par déformation plastique sévère (SPD). Cette stratégie proposée a pour objectifs: i) améliorer les propriétés par raffinement de microstructure jusqu'à une échelle sub-micrométrique ii) l'élaboration d'un matériau modèle permettant de comprendre le comportement des DSS obtenus par des méthodes conventionnelles. Le premier objectif de ce travail était, par conséquent, la mise en œuvre d'une méthodologie de fabrication en utilisant le co-tréfilage, en vue d'obtenir une microstructure ultrafine de composites 316L / 430LNb. L'un des défis rencontrés au cours de notre étude a été l'inter-diffusion significative lors du traitement thermique indispensable, limitant le raffinement de la microstructure en-deçà du µm. Une étude d'optimisation a été effectuée pour tenir compte du rôle de cette inter-diffusion pour un couple 316L / 430LNb. Ainsi, des micro-composites multi-échelles ont été obtenus. La limitation du raffinement de la microstructure par diffusion a été rationnalisée par une étude systématique des cinétiques de recristallisation et de l'inter-diffusion. Parallèlement à l'évaluation de la microstructure, le comportement mécanique de ces nouveaux micro-composites a été examiné. Des essais de traction in situ par rayonnement X synchrotron à haute énergie ont permis d'appréhender les interactions plastiques entre les deux phases.

Contents

I Introduction & context of the study

I.I Stainless steels in construction

Stainless steels have become a ubiquitous material in the construction market not only as reinforcement for concrete but also as an architectural design tool. Large construction projects nowadays use stainless steel as their main construction material (Figure I-1 and Figure I-2). This increased use of stainless steels is due, besides their interesting mechanical properties in terms of strength and ductility, to their functional properties such as corrosion resistance and comparatively lower thermal conductivity compared to carbon steels. The corrosion resistance, in particular, is related to the chromium content (minimum 10.5%), which gives remarkable resistance to wet corrosion by forming a thin passive layer on the surface of the metal [Baroux 1990].

Besides, significant development over the last 20 years in finishing technology makes stainless steels more and more attractive for architectural designers. In fact, excellent surface finishes ranging from matt to very shiny, smooth to rough, can be obtained. Moreover thanks to new developments in metallic, organic coating and PVD (Physical Vapor Deposition), finishing with colors are possible. The Capital Gate in Abu-Dhabi is one of the examples of such projects in which a distinctive stainless steel "splash" (that descends from the 19th floor) is used as a shadow device to protect the building from over than 30% of sun heat, see Figure I-1. The ability of stainless steels to respond simultaneously to creative architectural design requirements and to material specifications in terms of mechanical resistance and properties makes it a better candidate for many construction projects than the classical carbon steels.

Figure I-1: Capital Gate tower Abu-Dhabi (United Arab Emirates)

Figure I-2: Universum Science Center, Bremen (Germany)

Among the stainless steels, several types exist and are distinguished by their: chemical composition, mechanical properties and functional properties. The main families are the austenitic stainless steels, ferritic stainless steels and duplex stainless steels.

The solute additions contained in stainless steels play an important influence on their crystallographic structure. They are classified into two main categories:

- alphagenous elements : such as chromium, molybdenum, titanium, silicon and niobium, they promote the formation and the stabilization of a body centered cubic (b.c.c) crystallographic structure (ferrite)
- gammagenous elements: such as nickel, manganese, carbon and nitrogen, they promote the formation and stabilization of a face centered cubic (f.c.c) crystallographic structure (austenite)

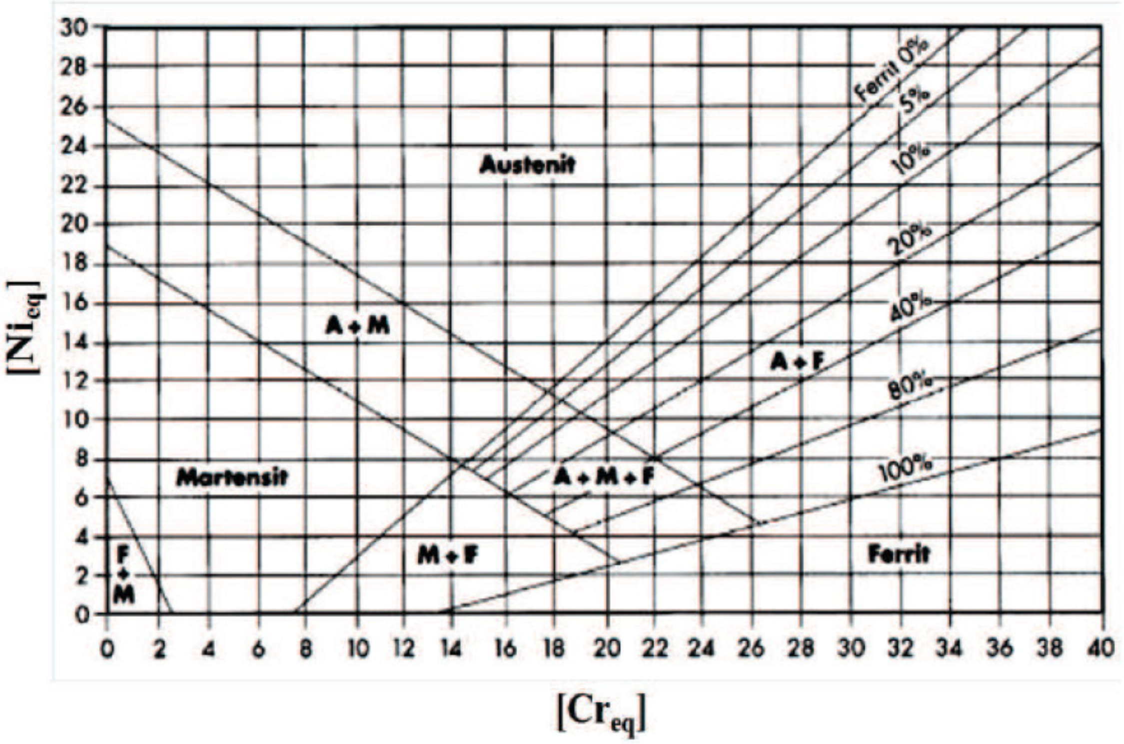

Figure I-3: Shaeffler diagram for stainless steels [Shaeffler 1949]

[Schaeffler, 1949] constructed a diagram in which the compositional limits of phase coexistence at room temperature in terms of chromium and nickel equivalents are illustrated (Figure I-3). This diagram was obtained on the basis of rapid cooling from liquid metal. It is for this reason that this diagram is frequently used in welding applications. The Cr and Ni equivalents can be estimated by the empirical formula of [Honeycombe and Bhadeshia, 1995]:

$$Cr_{eq} = w\%Cr + 2w\%Si + 1.5w\%Mo + 5w\%V + 5.5w\%Al + 1.75w\%Nb + 0.75w\%W \quad \text{Eq. I-1}$$

$$Ni_{eq} = w\%Ni + 2w\%Co + 0.5w\%Mn + 3w\%Cu + 25w\%N + 30w\%C \quad \text{Eq. I-2}$$

I.I.1 Characteristics and mechanical properties

From Figure I-3 we can distinguish four different types of the most widely used types of stainless steels in construction applications; austenite (A), ferrite (F), martensite (M) and duplex (A+F). In this section, we are interested only in austenitic, ferritic and duplex stainless steels.

- **Austenitic stainless steels**

Austenitic stainless steels are alloys that contain, in general, between 17-20% of chromium, 9-14 % of nickel [Cunat , 2000] and other elements such as copper, silicon, titanium, niobium, etc. The mechanical properties of austenitic stainless steels are relatively low, their elastic modulus is about 200 GPa ; the yield strength and tensile strength are of the order of 200 MPa and 500 MPa, respectively [Bavay , 1990; Cunat , 2000]. However, a significant increase of the mechanical properties of austenitic stainless steels can be obtained thanks to the martensitic transformation during the application of plastic strain [Angel and Cina 1954] [K.H Lo 2009]. It is well established that this transformation occurs depending on the chemical composition of the austenitic stainless steel and on the temperature at which it is (pre)strained [Spencer 2004] [K.H Lo 2009]. It is found that the elements such as nickel and nitrogen limit this martensitic transformation and therefore they are considered as stabilizer for the austenitic stainless steel. 316L and 316LN are two examples of a stabilized austenitic stainless steel by nickel and nitrogen respectively.

[Pickering 1984] schematized the influence of some alloying elements, in solid solution, on the mechanical properties. See **Error! Reference source not found.**.

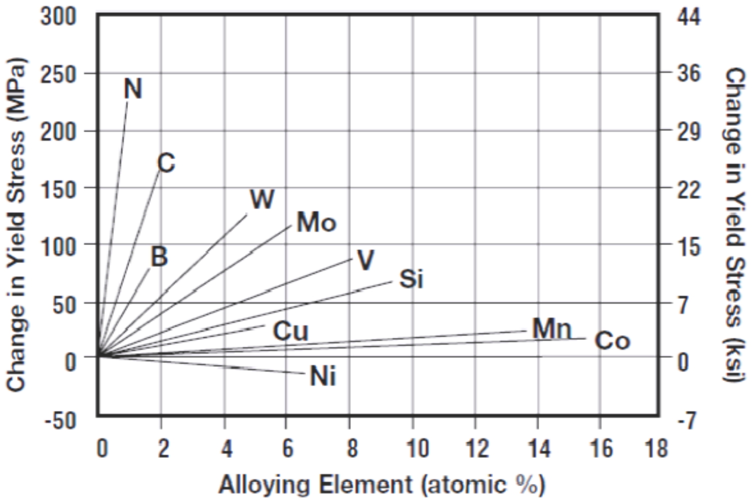

Figure I-4:Influence of different alloying elements on the yield strength [Pickering 1984]

- **Ferritic Stainless steels**

Ferritic stainless steels are alloys that contain generally 11-17% of chromium and low content (<0.03%) of carbon and nitrogen. Ferritic stainless steels are generally stronger than austenitic stainless steels. They have minimum yield strength of 250 MPa. However, they show a limited ductility (18-25% of elongation) compared to the austenitic stainless steels [Elbartali

2007]. Moreover, their corrosion resistance is lower and they are more brittle at low temperature [Davis 1994] [Lacombe 1990]. In case where medium resistance to corrosion is sufficient, ferritic stainless steels are used due to their lower cost, linked to the lower solute content. Ferritic stainless steels have also good magnetic properties. They are widely used for magnetic components in corrosive environment such as the fuel injection valve inside automotive engines.

- **Duplex stainless steel (DSS)**

Duplex stainless steels have a mixed microstructure consisting of ferrite and austenite. Indeed, shows a ternary phase diagram cut at 70% of iron. This diagram illustrates that the duplex can be obtained from a specific chemical composition by aiming a nickel content between 4-7%, a chromium content of 18-25% [Davis 1994] [Lacombe 1990]. During the solidification at this specific chemical composition, one can notice that only a ferritic phase is produced whereas the austenitic phase starts to be formed at post-solidification temperatures. The volume fraction of the ferritic phase depends in fact on both chemical composition, thermomechanical treatment and on the cooling rate. Generally, manufacturers seek to obtain an equal proportion of austenite and ferrite.

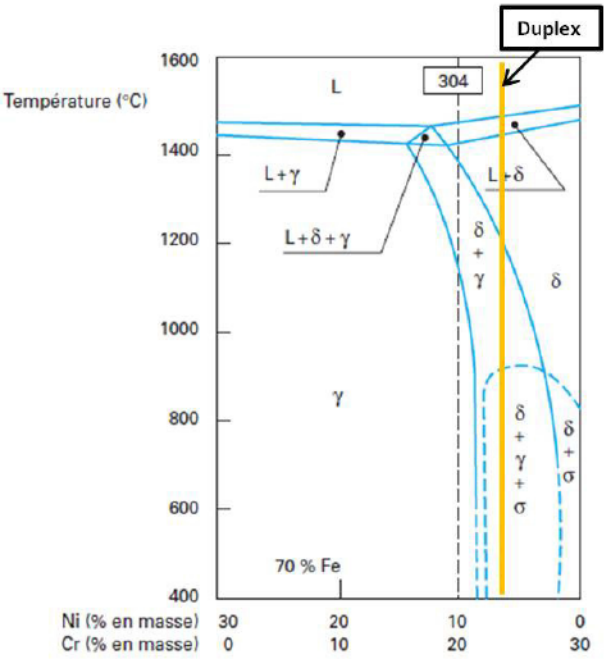

Figure I-5: Peseudo-binary Cr-Ni phase digram at equilibrium cut at 70wt% of iron. The chemical composition of the duplex steel (continuous yellow line) compared with that of austenitic steel 304 (dashed black line). [Cunat 2010]

Duplex stainless steels combine the mechanical and corrosion properties of both austenitic and ferritic stainless steels. They have high yield strength (450-650MPa), which is characteristic of ferrite and high ductility (25-30%), which is characteristic of austenite [Desestret 1990] [Moussavi 1997]. The yield strength can be increased by increasing nitrogen and carbon content in the solid solution such as shown in Figure I-6 [Desestret 1990]. This good compromise between strength/ductility makes DSS one of the most interesting stainless steels in the last four decades.

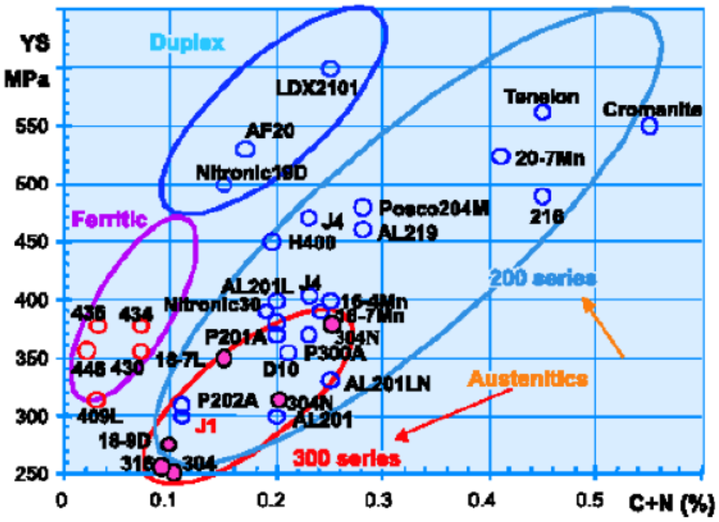

Figure I-6: Yield strength of different alloys as a function of carbon and nitrogen content% [Desestret 1990]

Figure I-7 and Table I-1 sum up the mechanical properties of the different families of stainless steels mentioned above:

Table I-1: Mechanical characteristics of different stainless steels type [Gympel 1990] [Leffler 2005] [Nirosta 2002]

Stainless steel	Yield strength (MPa)	Tensile strength (MPa)	Ductility (%)	Young's Modulus (GPa)	Hardness (HV)
Austenite	200-250	570-900	50-60	200	210
Ferrite	250-400	300-650	18-25	220	190-220
Duplex	450-650	730-900	25-30	200	260-290

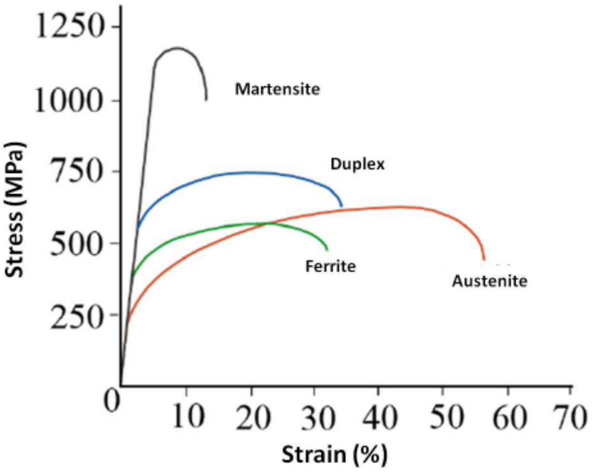

Figure I-7: Stress-strain curves of different types of stainless steel [Leffler 2005]

I.I.2 Functional properties

One of the most important functional properties, in addition to the corrosion resistance, is the thermal resistance; i.e. the capacity of insulation for a metal. In constructions such as those shown in Figure I-1 and Figure I-2, the thermal properties of the used metal become an important factor to be taken into consideration. In addition, the stainless steels, used as reinforcement for building balconies, are considered as one of the responsible element for thermal bridging Figure I-8. The latter occurs when heat flow bypasses the insulated elements of the building enclosure. Heat flow through thermal bridges can be very significant. Thermal properties are usually referred to the three important physical properties: thermal conductivity, thermal diffusivity and thermal expansion.

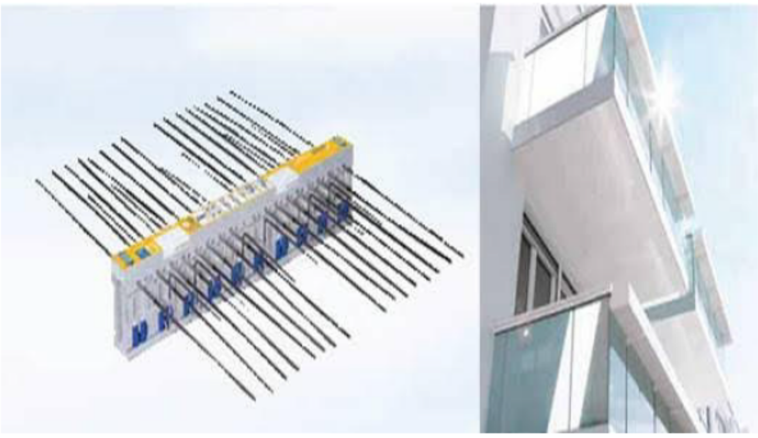

Figure I-8: Example of balcony structure slab reinforced with stainless steel bars

In general, thermal conductivity in stainless steel is much lower than that of carbon steels. The thermal conductivity for carbon steel at room temperature is about 53W/mK whereas for austenitic stainless steels it decreases to reach about 15W/mK [Gardner 2006].

The value of the thermal conductivity in stainless steels varies also as a function of their type. For example, the thermal conductivity of ferritic stainless steel is about 30W/mK whereas for austenitic stainless steels it decreases by half (15W/mK). In DSS, a low thermal conductivity can also be achieved (to almost 12W/mK). Table I-2 sums up the physical properties of the different types of stainless steels.

Table I-2: Physical properties of different stainless steels type*

	Austenite SS	Ferrite SS	Duplex SS	Martensite SS
Density(g/cm^3)	7.9-8.1	7.7	7.8	7.7
Thermal expansion (*10^{-6}/K) 200-400°C	16-18	11	15	12
Thermal conductivity (W/mK) 20°C	15	30	12-15	30
Resistivity (μΩm)20°C	0.8	0.6	0.5	0.6

**Handbook of stainless steel, Outokumpu Oyj, 2013*

I.I.3 Duplex stainless steels (DSS): industrial context

The use of DSS grades for structural applications is considered as one of the most significant advances impacting the construction sector. As presented above, they have very interesting properties which make them a very competing material not only compared to carbon steels but also to austenitic stainless steels. The mechanical and functional properties of the DSS can be summarized in the following points:

- Very good strength/ductility compromise
- Interesting functional properties in particular a low thermal conductivity coefficient (<15W/mK)
- Capacity of weight saving due to their high strength compared to the austenitic stainless steel. Almost 40% of weight reduction of cylindrical shell can be achieved by changing 316L to Duplex 2205.
- Their low Ni content (0-4%) makes the price of DSS lower and more stable.

It is for these reasons that a lot of steel companies and steel institutes are working on these grades. UGITECH, for example, is one of the steel manufacturers in France which invests in the development of new stainless steels duplex grades with several patents on lean duplex stainless steel.

It has been proposed that the mechanical properties of DSS result from a complex interaction between ferrite and austenite leading to a mechanical behavior that cannot be predicted from the properties of the constituents alone [Nelsson and Chai 2010]. Several authors [Nyström 1994] [Cho 1988] [Byun 1991] have attempted to model the plastic deformation of duplex stainless steels starting from the mechanical properties of single phase tie-line alloys.

The high strength and the deviation from the law of mixture of DSS are usually attributed, in the literature, to the difference in plastic behavior of both phases. [Nyström 1994] found for example that the linear law of mixture cannot predict the variation in monotonic yield stress due to a possible influence of the residual stresses if the texture effects are neglected. In addition to the plasticity interaction between ferrite and austenite, [Noyan and Cohen 1986] showed that the distribution of austenite in a ferritic matrix in a hot rolled duplex stainless steel sheet led to a variation in stress within one phase causing an inhomogeneous deformation within the phases. This is thought to be the origin of the deviation from the rule of mixture.

The effect of the microstructure morphology on the mechanical properties has been observed not only in DSS but also in other two-phase alloys. For example, [Winholts and Cohen 1992] studied the behavior of 1080 steel with pearlitic and spheroidal microstructure during low-cycle fatigue.

They found that the micro-stresses are higher in the pearlitic condition than in the speroidal condition. They attributed these differences to the morphology. Indeed, the pearlite lamellae transfer the load more effectively to the cementite phase.

Therefore, several authors used multi-scale modeling and in-situ experiments in order to analyze the different parameters cited above and in particular the load sharing and stress interaction between phases and consequently the micro stress-strain curves [Chai 2006] [Jia

2006] [Lin 2006]. However, this approach seems to be insufficient to explain the complex plastic interaction between the ferrite and the austenite [Nilsson 2010].

In fact the key to the unique properties of duplex stainless steel lies on its structure and the complex interaction between the phases. The work of [Herrera et al. 2011], for example, showed the possibility of enhancing the mechanical properties by playing with the structure of DSS. Indeed, they designed a new DSS alloy with 1 GPa of tensile strength and 60% of ductility by reducing the austenite stability and introducing the Transformation Induced Plasticity (TRIP). Therefore, providing a good understanding and a full description of the mechanical behavior of DSS may provide a significant potential for breakthrough mechanical properties and particularly improving the couple strength/ductility. Moreover, a better understanding will give also the possibility to design **tailor-made, architectured** DSS for specific applications, which is essential for steel producers.

Hence, the aim of the present project is to propose a different approach from that used until now to understand the behavior of DSS. It is within this framework that collaboration between Ugitech and Centre of Excellence of Multifunctional Architectured Materials (CEMAM) has been developed to launch this project. Two strategies have been proposed in this project. Each one is treated in a separate PhD project:

- *First strategy: "Bottom up"*

In this strategy, the chemical compositions of both phases in the DSS have been measured and then each phase fabricated separately by conventional metallurgical methods. This allowed examining the properties of the austenite and ferrite phases together with that of the DSS and separating the architecture effect. This work has been achieved during the PhD thesis of Audrey Lechartier.

- *Second strategy: "Top down"*

In this approach, we attempt to fabricate a DSS starting from bulk ferrite and austenite stainless steels that have a well defined and known mechanical behavior. This strategy necessitates a specific elaboration method, which allows assembling bulk materials to fabricate a micro-structured DSS. Severe Plastic Deformation (SPD) is one the most used and adapted technique for this kind of application. **The investigation carried out in the current thesis is devoted to the application of this strategy**.

The advantages of the second strategy using SPD technique is that it offers potentially more degrees of freedom in terms of controlled parameters such as: chemical compositions of the constituent phases, phase distribution, scale, volume fraction etc. Moreover, this approach may not only allow understanding DSS behavior by creating model materials with controlled parameters but also developing new properties by structure refining.

Several techniques based on SPD concept exist nowadays. These techniques differ from one to another by their manufacturing routes, sample shape and dimension, the final application etc. Indeed, some techniques are more adapted for designing two-phase materials from bulk metals such as Accumulative re-Bundling Drawing (ABD) or Accumulative (Cold) Rolling (A(C)R) than others such as High Pressure Torsion (HPT) or Equal Channel Angular Pressing (ECAP). The latter two techniques can be also used for powder metallurgy and consolidation

[Valiev et al.1996]. However, some applications necessitate a combination of SPD techniques. The Cu-Fe composite of [Quelennec 2008] is one of the examples of such cases in which both ABD and HPT technique were used to obtain a solid solution of copper and iron at atomic scale.

I.II Material design by Severe Plastic Deformation (SPD)

In the current section we will give, before presenting examples of the use of SPD techniques for materials design by structure refining, a brief description of the most used SPD techniques in the literature either at lab-scale or industrial scale. It is also important to note that the following techniques could be used at either high or low temperature.

I.II.1 SPD techniques

I.II.1.a Accumulative Rolling Bonding (ARB)

This technique is based on rolling process in which a sheet metal is passed between two rolls. The sheet undergoes therefore a reduction in thickness by compression. The ARB can be also used as assembling technique introduced originally in the 1960s by [Vaydanath 1960] as we will see in chapter III. The concept of the ARB is schematically illustrated in Figure I-9. Indeed, a stack of two sheets of equal thickness is deformed to 50% reduction thickness. The resultant rolled sheet is then cut in two halves and stack up again. The repetition of the previous steps gives a very fine multi-layer structure. Before stacking, surface preparation and heat treatment are needed to ensure a better adhesion (see chapter III).

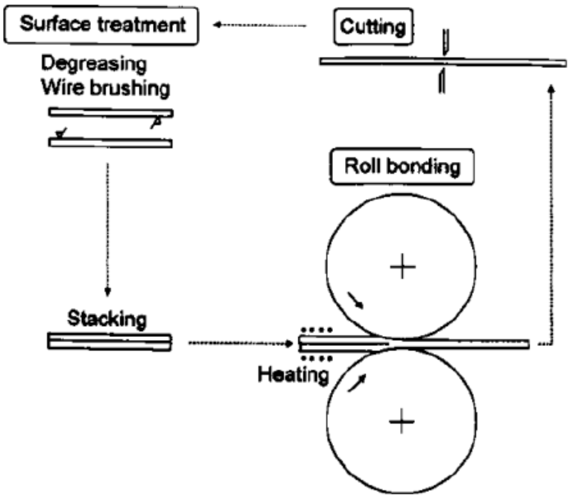

Figure I-9: Schematic illustration showing the principal of ARB process [Saito 1998]

I.II.1.b Accumulative re-Bundling and Drawing (ABD)

ABD technique is based on the drawing process which consists on section reduction of wire or rode through a die (see Chapter III). The refined structure results therefore from the reduction of the one of the samples dimension (here the wire diameter). The use of the drawing process as an alloying technique to produce two-phase composites was firstly introduced by [Levi 1960]. Indeed, [Levi 1960] attempted to elaborate a superconductor wires with high strength. His idea was based on the alloying mechanically iron tubes with copper wires by section reduction (drawing). The drawn wire is then re-bundled in another tube. The repetition of the previous two steps constitutes the core of the ABD process providing by consequence a very fine multi-filamentary structure. In some cases a heat treatment step, which aims to soften the material in question, is necessary to continue the process. A more detailed description of this technique will be given in chapter III.

I.II.1.c Equal Channel Angular Pressing/Extrusion (ECAP/E)

ECAE/P was firstly developed in the 1970s by [Segal 1977]. The issue raised by Segal was how to introduce a large plastic strain in a metal without changing its dimension. The principal of the ECAP/E is schematized in Figure I-10; a billet is pushed or extruded through two channels of equal cross-section with help of punch press. Since the dimension of the sample remains unchanged during processing, the sample can be reintroduced in the channel and pressed again inducing therefore a large accumulated strain. [Wu and Baker 1997] found experimentally that these accumulative strains are, in fact, additive. In addition, the effective strain provided by this process is expressed as a function of the outer curvature angle, Ψ and the angle between the two parts of the channels, Φ.

$$\varepsilon_n = \frac{n}{\sqrt{3}}\left[2\cot\left(\frac{\Phi}{2}+\frac{\Psi}{2}\right)+sin^{-1}\left(\frac{\Phi}{2}+\frac{\Psi}{2}\right)\right]$$

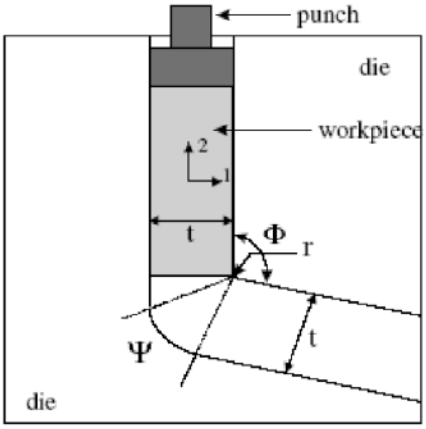

Figure I-10:Schematic illustration showing the principal of ECAP process [Valiev 2006]

Considering these two facts (i.e. the additivity of the strains and the dependence of the latter on the angles of the die), the resultant microstructure depends indeed on the routes chosen for processing. Figure I-11 illustrate the most fundamental routes of ECAP process. As we can see from Figure I-11.b the shape of the billet is also influenced by the chosen route. Though, several investigations were made to find the optimal route in which a maximum strain in all directions is introduced and the initial billet shape is recovered. The route Bc was found to be the optimum where the shape is recovered after 8 passes and both a homogeneous equiaxed microstructure and a high fraction of grain boundaries having high angles of misorientation are obtained. This technique is widely used nowadays to produce ultrafine grain structure (UFG) and nanomaterials. It is used for either single phase or two-phase materials obtained by co-melting (or in-situ composite; see next subsection). For more detailed description about this technique, interested readers are encouraged to read [Valiev and Langdon 2006] review.

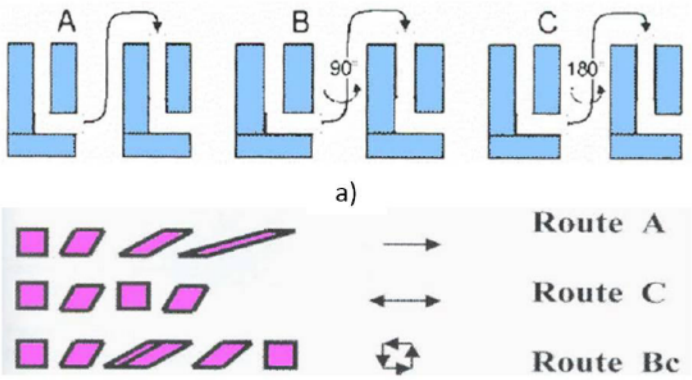

a)

b)

Figure I-11: The different routes used in ECAP process [Huot et al.2012]

I.II.1.d High Pressure Torsion (HPT)

Although the origin of the principal of this technique is traced to more than 2000 years ago in ancient China [Wang JT 2006], [Bridgman 1943] is considered as the first one who established the fundamental scientific concept of the HPT processing based on experimental investigations. The concept of HPT process is illustrated in Figure I-12. The sample in form of disk is positioned between two anvils and subjected to both compressive pressure, P and torsional strain imposed the rotation of one the anvils or both of them. The true deformation (ε_{true}) amount induced in HPT process is found to be dependent on the radius of the sample, r, and thickness of the sample, h, and the number of rotations. This can be written as following:

$$\varepsilon_{true} = \ln\left(\frac{2\pi r N}{h}\right)$$

One can deduce from the previous relation that the produced microstructure is highly inhomogeneous due to the direct dependence of the true deformation amount on the radius. Naturally, when r equals zero (center of the disk), the true deformation diverges and when r increases (outer skin) the true deformation increases as well. In the literature, the homogeneity of a structure obtained by HPT is usually evaluated by microhardness measurements. Several authors attempted to correlate microhardness measurements with microstructural TEM observations. Indeed, it has been shown by experimental investigation in different materials such as cooper [Horita and Langdon 2005] and in pure Ni [Zhilyaev et al. 2001] that albeit the microhardness is lower in the central region, reasonable microstructure homogeneity across the disk can be attained when the number of rotation is increased with a high imposed pressure.

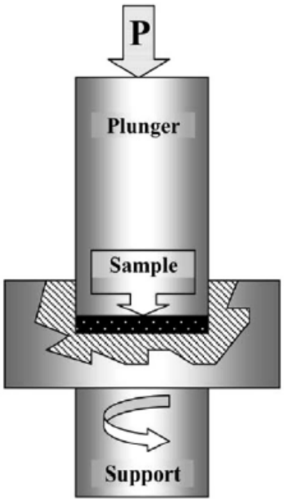

Figure I-12: Schematic illustration for HPT technique

I.II.2 Resultant microstructure and mechanical properties

I.II.2.a Examples of refined microstructure

As presented above, SPD techniques are widely used to obtain either an ultra-fine (or nano) grains structure (in case of mono-phase material) or micro/nano composites (in case of two-phase alloys). Hereafter, some applications using SPD techniques for enhancing mechanical properties will be presented:

i) Single-phase materials

- Stainless steels:

[Pakiela et al. 2006] investigated grains refinement of 316L using ECAP and HPT techniques. Ultra-fined grains are obtained, using ECAP with an angular channel set at an angle of 90°, of 316 nm whereas the initial grain size of 316L is about 21µm. However, HPT technique gives more refined grains. Indeed, Figure I-13 shows the microstructure obtained by HPT in which the grain size reaches 55nm.

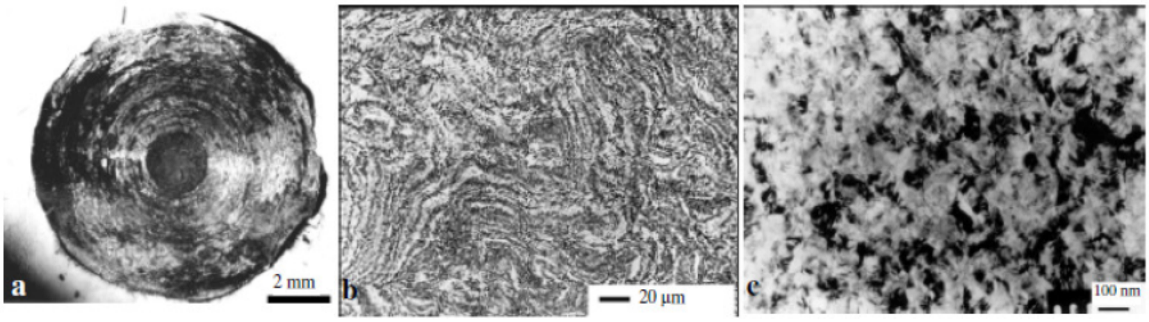

Figure I-13: 316L processed by HPT: a) macroscopic image of the specimen; b) microstructure of the specimen revealed by light microscopy; c) nanostructure of the specimen revealed by TEM [Pakiela et al. 2006]

Recently, [Rajaskhara et al.2010] examined the microstructure evolution of refined austenitic stainless steel (301LN) using cold-rolling. Sheets of 301LN have been cold-rolled to 63% of reduction by rolling (i.e. from 1.5 mm to 0.8 mm of thickness). The cold-rolled samples were then heated with a heating-rate of 200°C/s and annealed at 600°C, 700°C, 800°C, 900°C and 1000°C for 1, 10 and 100 seconds and forced-air-cooled at cooling rate 200°C/s. it is found that a nano/submicron grained structure could be obtained depending on the annealing conditions. Indeed, samples in as-cold-rolled state consist of regions of dislocation cell-types martensite. After annealing at 600°C for 100s and 700°C for 1s a reversion of martensite to austenite starts to take place giving in turn a nano/submicron austenite structure (200nm). At higher temperature 800°C, 900°C and 1000°C an almost complete martensite reversion and a formation of large grain size have been observed. For example, the microstructure obtained after 800°C of annealing showed a mixture of equiaxed large grains and nano/submicron grains. This inhomogeneity has been attributed to i) presence of different types of martensite (dislocation-cell type and lath) in the cold-rolled sample leading to different rates of austenite nucleation ii) nucleation of austenitic grains at lower annealing temperatures, which grow in size as the annealing temperature is rapidly brought to 800°C. See Figure I-14 and Figure I-15.

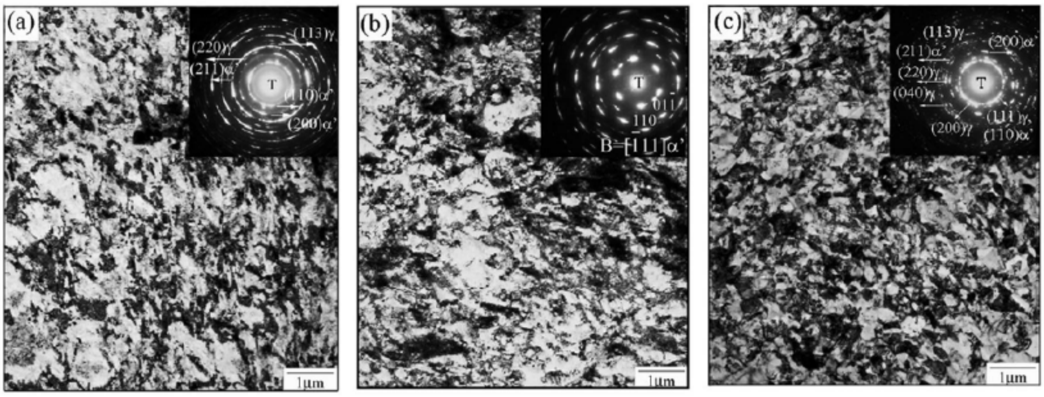

Figure I-14: TEM images and diffraction patterns corresponding of 63% cold-rolled AISI 301LN annealed at 600°C for a) 1s; b) 10s; c) 100s [Rajaskhara et al.2010]

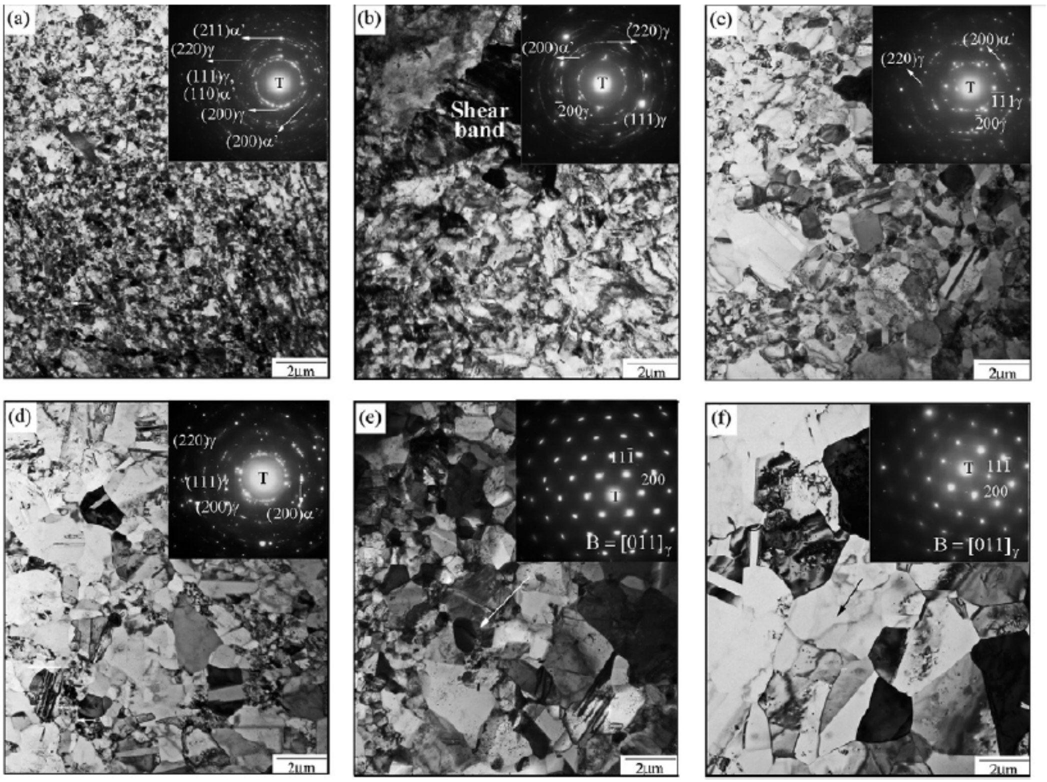

Figure I-15: TEM images and diffraction patterns corresponding of 63% cold-rolled annealed at 700°C a) 1s; b) 10s; c) 100s, and 800°C d) 1s; e) 10s; f) 100s [Rajaskhara et al.2010]

- Copper

Copper is one of the materials that have been widely investigated in structure refining by SPD techniques in particular HPT and ECAP. [Mishra et al.2007], for example, attempted in their work to provide an analytical explanation of the deformation mechanism during sever plastic deformation. This investigation was based on copper specimens processed by ECAP. The resultant microstructure of these specimens, obtained after 0, 2, 4 and 8 passes using different routes A, C and Bc, was evaluated using TEM observations. Interesting features have been obtained:

- Strong dependence of the ECAP microstructure on the deformation path. Indeed, Figure I-16 shows an elongated grain structures after processing via routes A and C (8 passes) while route Bc results homogeneous equiaxed grains.
- Using the optimum deformation path i.e. Bc, the microstructure showed also a significant dependence on the number of passes realized. In fact, Figure I-17 reports the microstructure of Cu in transverse and longitudinal section before (initial state) and after processing as a function of number of pass. In the transverse section, an equiaxed grains have been already obtained after only two passes with significant fraction of grains below 200nm while the initial grains is about 30µm. On the other hand the, in the longitudinal section, elongated grains can be still observed after 4 passes. However, a finer equiaxed grains is reached after 8 passes.

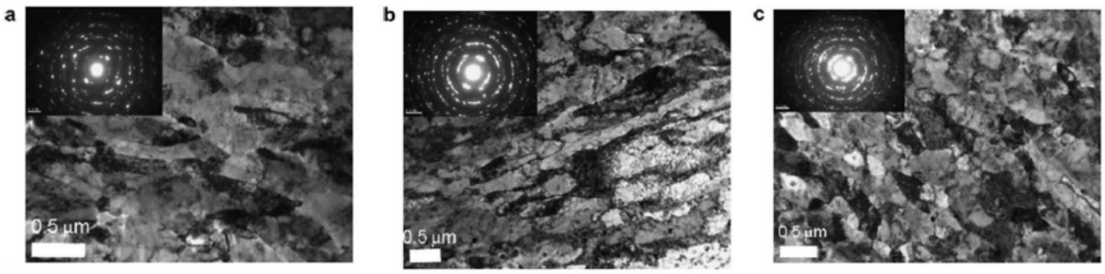

Figure I-16: Transvers TEM images of Cu processed by ECAP after 8 passes using diffrent routes a) Rout A; b) Rout C; c) Rout Bc [Mishra et al.2005]

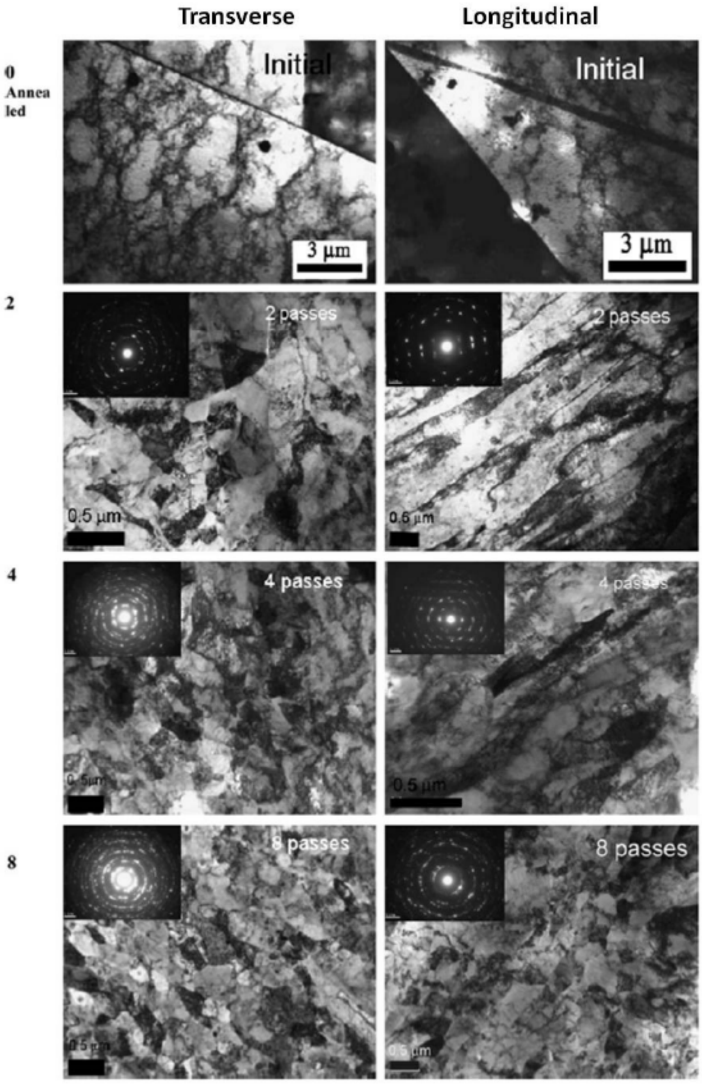

Figure I-17: TEM images of Cu processed by ECAP in transverse and longitudinal section after 0 (annealed), 2,4 and 8 passes [Mishra et al.2005]

ii) ***Two-phase materials***

Metal-metal composites have emerged with the increase interest in the development of superconductors with high mechanical strength (>800 MPa). Thus, a wide range of copper based composites have been investigated since the 1960s. Indeed, copper, with high electrical conductivity but low mechanical strength, is always combined with another metal with higher mechanical strength such as Cr, Nb, Ta, Ag etc.

In the literature, two types of metal-metal composites can be distinguished depending on their fabrication routes:

- The first type is prepared by co-melting two metals that are miscible as liquids but immiscible as solids followed by large section reduction using SPD techniques to obtain filamentary reinforcement. These composites are called *in-situ composites* [Russell 2000].
- The second type is directly obtained by SPD techniques where two bulk metals are assembled and alloyed mechanically via section reduction as presented above. These composites are called *co-deformed composites (or continuous composites).*

- In-situ composites

Many authors consider that the first in-situ composites study is the Fe-Fe_3C composites performed by [Embury and Fisher 1966] at U.S Steel Corporation Research Center. The composite was simply obtained after heavy drawing of hypereutectoid pearlite samples. They observed decreasing size and spacing of Fe_3C lamellae within the ferrite matrix as the deformation of the specimens progressed. An increase in yield and tensile strength was observed. The maximum value reached for tensile strength is 4.8 GPa.

Since then, in-situ copper-based composite such as Cu-Ag, Cu-Nb, Cu-Ta, Cu-Cr have been investigated widely for producing high strength superconducting wires.

For example, the composite Cu-Ag of [Frommeyer and Wasserman 1975] and Cu-Nb of [Bevk et al. 1978] [Spitzig and Krotz, 1987] showed a synergetic effect in mechanical properties, namely that the strength of the composites exceeds that predicted by the isostrain rule of mixture Figure I-18. Moreover, the electrical properties cannot be predicted by a law of mixture, which was mainly attributed to the geometry and the scale of the structure [Frommeyer and Wasserman 1975].

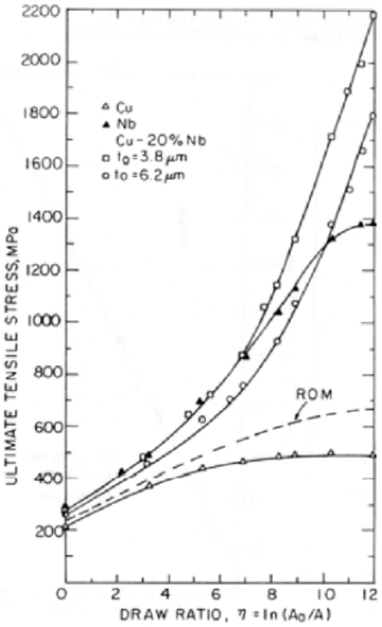

Figure I-18: Illustration of the strength of Cu-20%Nb wires, above the level predicted by isostrain rule of mixture (ROM) [Spitzig and Krotz, 1987]

The final scale structure of such composites depends in fact of the initial scale structure. Indeed, a finer initial structure will require much smaller drawing strains to refine the structure and attain the final scale. This will result a much higher strength [Schwartz and Shen 2003]. The initial structure can be refined by rapidly solidifying a near-eutectic composition, which allows a large degree of undercooling prior to solidification. This leads to a very fine dendritic structure [Schwartz and Shen 2003]. Figure I-19 shows an example of an in-situ nanocomposite Cu-Nb.

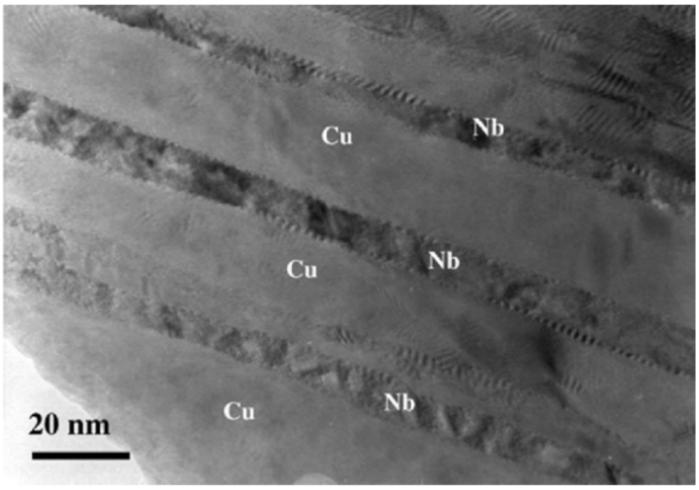

Figure I-19: TEM image of in-situe Cu-Nb composite after heavy drawing [Sauvage et al.2001]

Another very recent example of ultrafine-grained in-situ composite is duplex steels of austenite and ferrite designed by [Yen et al.2015]. Unique mechanical properties have been obtained with yield and ultimate strength above 1GPa and a ductility of almost 25%. The microstructure of this duplex steel was designed by hot rolling process at 850°C from 6mm thick plate to 2.5mm thick strip followed by cold rolling from 2.4 to 1.2 mm. The cold rolled sheets were then annealed at different conditions. The average measured grain size for the ferritic phase obtained after annealing is 679±110nm whereas the average austenite grain size was found to be below 300nm.

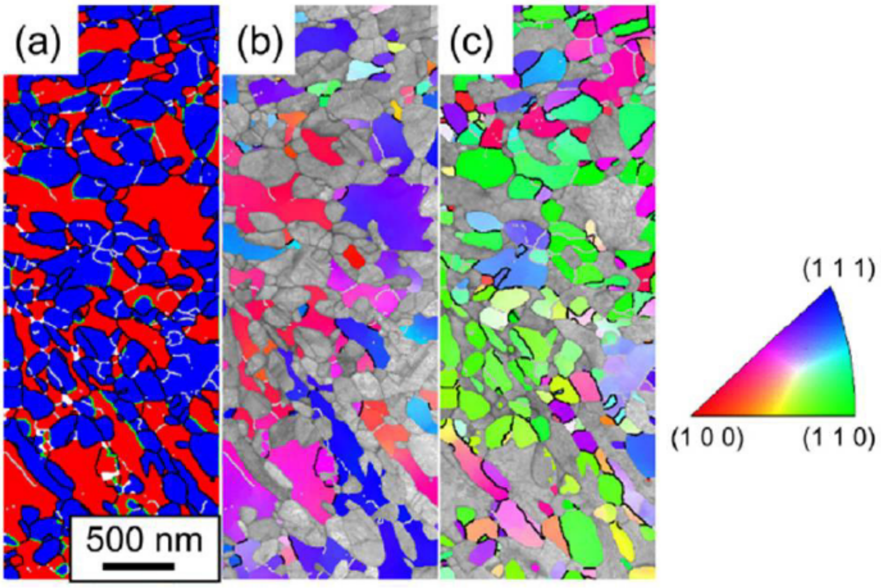

Figure I-20: SEM analyses for cold rolled duplex steel after annealing at 610°C for 8 minutes a) the phase map showing ferrite (red) and austenite (blue); b) the inverse pole figure-Z of ferrite, c) the inverse pole figure-Z of austenite [Yen et al.2015]

- Co-deformed composites

The most successful and studied example of mechanically alloyed composites using SPD techniques is Cu-Nb, in terms of the resulting properties and the comprehension of the deformation mechanisms.

The Cu-Nb composite studied by [Dupouy-Lecouturier, 1995] for high-field magnets coils shows a very good compromise between high mechanical properties and low electrical resistivity using continues fibers with controlled distribution using ADB process. This composite has been consecutively studied by [Thilly et al. 2002] and [Vidal 2006]. Figure I-21 shows an example of Cu-Nb nanocomposite obtained by ADB.

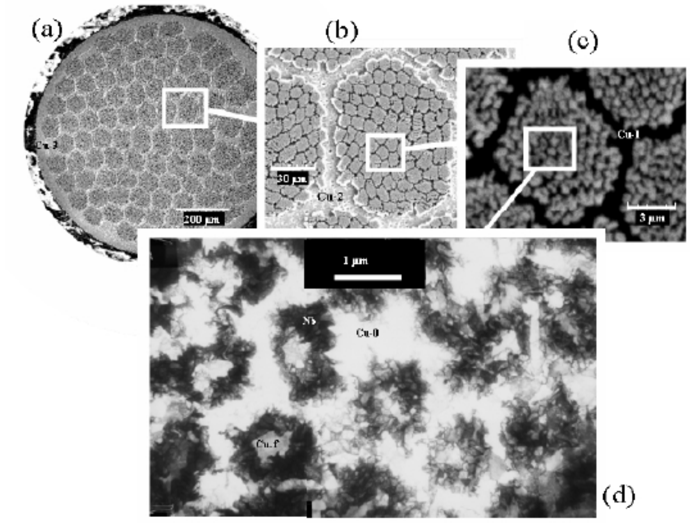

Figure I-21:Microstructure of Cu/Nb co-deformed composite obtained by ABD process: a), b) and c) SEM image of the global structure; d) TEM image of the detailed structure [Vidal 2006]

Based on in-situ TEM observations, [Thilly et al. 2002] provided a physical explanation of the synergetic effect on the macroscopic strength of the composite. Indeed, they observed that when the diameter of the Nb filaments is less than 200nm, they become single crystals with large dislocation-free regions.

I.II.2.b Mechanical properties

If so many researches and scientific papers appeared in the last three decades on the application of SPD technique for obtaining grain refinement to the submicro/nano-meter level is because of the real expectations in term of unique properties that these structures may provide. Particularly, these investigations were primarily motivated by the possible enhancement of strength/ductility couple which are two conflicting properties. The exceptional enhancement has been, indeed, reached and widely observed in several materials SPD-processed via different techniques. An overview of the resultant mechanical properties of the refined structures shown above will be primarily presented in the first paragraph. Particular attention will be given for strength and ductility of the refined structure in second paragraph.

i) Overview on the resultant mechanical properties: examples

Investigations carried out by [Valiev et al.2003], for example, on high purity Ti processed by HPT revealed very interesting properties in terms of strength and ductility. Figure I-22 shows stress-strain curves of pure Ti samples processed by HPT compared with that of coarse grain sample tested at 250°C. A dramatic increase in strength and ductility can be clearly noticed in the processed sample to 5 revolutions. This sample was examined by MET observations and revealed equiaxed grains of about 100nm. [Valiev et al.2003] observed also similar features in copper SPD-processed by different techniques as Figure I-23 shows. Recently, [Estrin and

Vinogradov 2013] found also similar behavior in nanostructured copper SPD-processed by cold rolling and ECAP via route A. See Figure I-24.

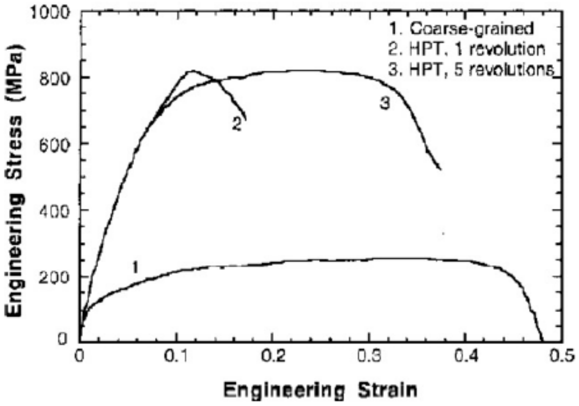

Figure I-22:Engineering stress-engineering strain curves for commercial Ti tested at 250°C [Valiev et al.2003]

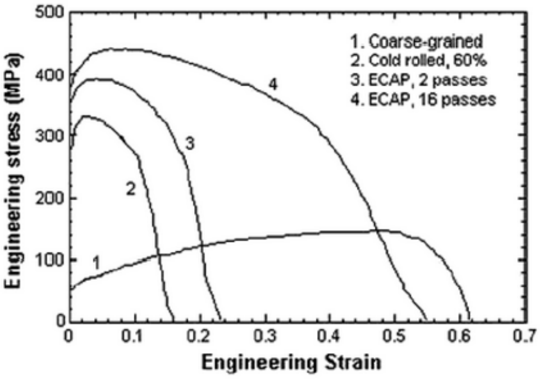

Figure I-23:Tensile engineering Stress-strain curves of copper SPD-processed by different schemes [Valiev et al.2003]

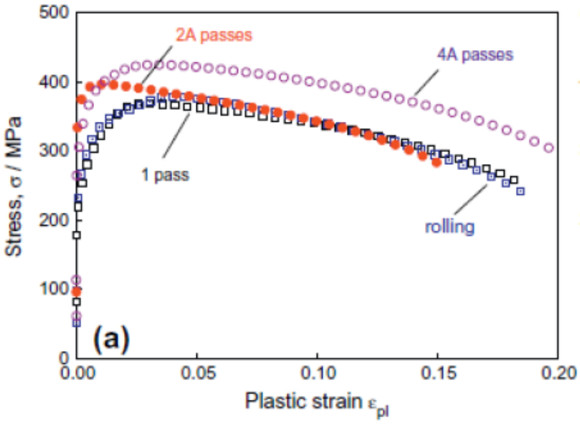

Figure I-24: Tensile curves for SPD-processed copper (rolled to 75% equivalent strain or ECAP-prodiuced by 1, 2 or 4 passes via route A) [Estrin and Vinograndov 2013]

Unique mechanical properties (yield and ultimate strength above 1GPa and a ductility of almost 25%), Figure I-25, are obtained in the ultra-fined grains duplex steels of [Yen et al.2015] by refining the austenite phase down to 300nm.

[Uneo et al.2011] developed a nanostructured 316 by ECAP process performed up to four passes via route Bc at 427K. Figure I-26 shows the increase of the strength as a function of pass number. At the fourth pass, interesting compromise in terms of ductility and strength is found.

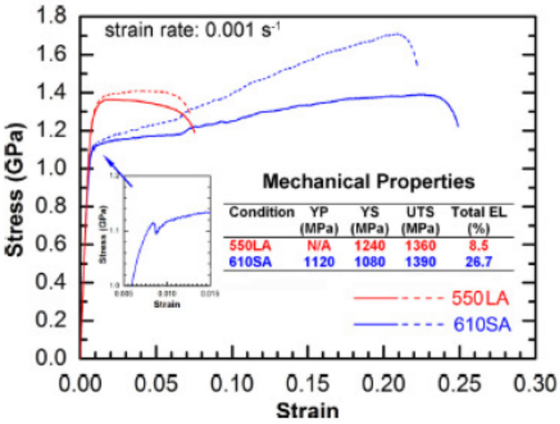

Condition	YP (MPa)	YS (MPa)	UTS (MPa)	Total EL (%)
550LA	N/A	1240	1360	8.5
610SA	1120	1080	1390	26.7

Figure I-25: Engineering stress-strain curves (solid line) and true stress-strain curves (dashed line) of SPD-processed duplex steels after annealing at 550°C for 2h (550LA) and 610°C for 8 minutes (610SA) [Yen et al.2015]

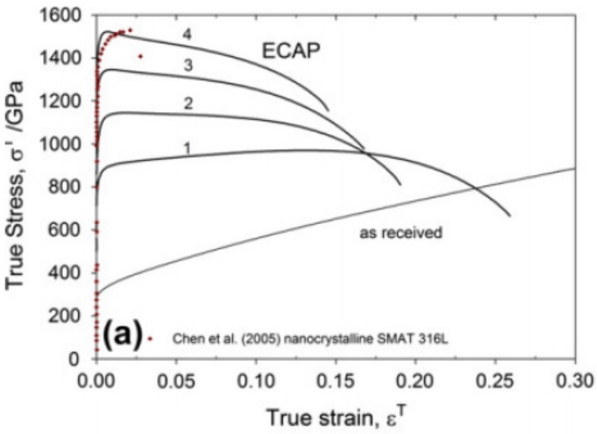

Figure I-26: True stress-strain curves of 316L stainless steel after ECAP process as a function of as number [Ueno et al.2011]

One can notice from the previous examples that the post-necking ductility is significantly improved nevertheless the uniform elongation doesn’t enhance systematically as a result of SPD process. The enhancement of the uniform elongation in some materials such as in 316L Figure I-26, duplex steel Figure I-25 and Ti Figure I-22 is usually attributed to other parameters rather than a direct association to grain sizes. Indeed, the mechanical properties of SPD processed materials have been, and still is, a subject of a lot of discussions and investigations in the literature which will be discussed in the following paragraphs.

ii) ***Strength and ductility***

- Yield strength

Enhancing the strength of a metallic material via grain structure refinement is one of the most classical strategies used to this day. This strategy was rationalized for the first time by [Hall 1951] by establishing an empirical relation linking the flow stress (or yield strength at 0.02% of plastic deformation) of a metal with its grain size (d) as follows:

$$\sigma_y = \sigma_0 + \frac{k}{\sqrt{d}}$$

Eq. I-3

Where σ_y is the yield strength for a grain of diameter d and σ_0 is the friction stress opposing motion of dislocation and k is a constant measuring the extent to which dislocations are oiled-up at barriers called also “unpinning constant”. The concept of this relation is based on the fact that the dislocations are accumulated within the grain boundaries which impede their movement. The shear stress increases with the increase of the number of dislocations until a critical value. This threshold value allows the dislocations to cross and the nucleation of a new source in the neighboring grains without applying any supplementary shear stress.
However, the ability of the Eq. I-3 to predict the yield strength is limited by the grain size d. Indeed, experimental findings in some materials recorded a significant deviation from the Hall-Petch law which is established at large grain sizes. In copper for example, it has been shown that the linear relation between the yield strength and the inverse square root of grain size ceased to apply by reaching grain sizes below 25 nm (i.e. $1/\sqrt{d}$) see Figure I-27. Two trends can be observed in this figure: i) a saturation of the yield strength as d decrease; ii) a drop of the yield strength arriving to certain grain size interpreted by a negative slope. The latter phenomenon was attributed to diffusional creep in nanocrystals according to [Chokshi 1998].

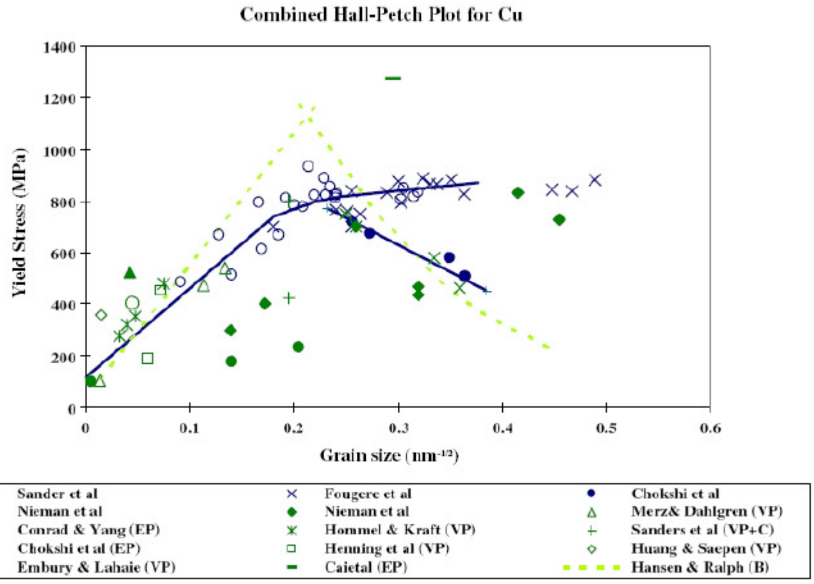

Figure I-27: Compiled yield stress versus grain size plot for Cu from various sources ranging from coarse to nanograin size. The plots show different trend as the grain size falls below a critical size [Meyers et al.2006]

Generally speaking, in both cases, the limitation of the HP relation for submicro/nano-metric grain sizes is referred to the involvement of different deformation mechanisms. In the case of bulk materials, several theories have been proposed to provide a physical explanation for the mechanism responsible of this behavior. The formation of Grain Boundary (GB) segregation is considered as the most widely referred mechanisms providing the physical nature of super strength of Ultra-Fine Grain (UFG) materials [Liddicoat et al. 2010] [Valiev et al. 2010]. Indeed, for materials of about 100nm the deformation mechanisms changes and the process of dislocation generation occur within the GBs becomes more difficult [Valiev et al. 2010]. Thus the role of the GB segregation is determinant in a sense that these GB segregations may significantly harden the dislocation emission and lead to high-strength state. For a more detailed scope about the deformation mechanisms in UFG and nanostructure materials, interested readers are encouraged to read [Meyer 2006] and [Valiev et al. 2016] reviews.
On the other side, the ultra-strength of two-phase materials has been investigated described through several investigations. In particular, the influence of the thickness (h) of the reinforcement in multilayer composites on the yield strength has been studied by [Misra et al. 2005]. A multilayer composites of Cu-Nb with copper and niobium layers of length scale ranging from one micron to less than one nanometer. They distinguished three regions in function of the thickness h:

- h>100nm: in this regim, the deformation mechanism is based on the dislocation pile-up within the interface of both phases which explains the good prediction of the Hall-Petch law and the proportionality of the flow stress with $h^{-1/2}$.

- 5nm<h<100nm: in this range of thickness, it was found that the dislocation pile-up within the interface of the both phases becomes very difficult and impossible. [Misra et al. 2005] suggested that a different deformation mechanism takes place in this range where the plasticity of a nanometric multilayer is governed by the propagation of single dislocation loops within the layer. This feature of deformation mechanism is commonly called Orwan mechanism. The latter has been observed in nanocomposite wires of Cu-Nb obtained by ADB process thanks to in-situ tensile test in TEM [Thilly 2000].

- h<5nm: at this regime the dislocation dimension becomes similar to that of the phase thickness. Moreover, the phase interface is no longer an obstacle for dislocation movement. Hence, it was found that the yield strength of the multilayer composite in this case is independent of the layer thickness.

These three regimes are schematized in Figure I-28.

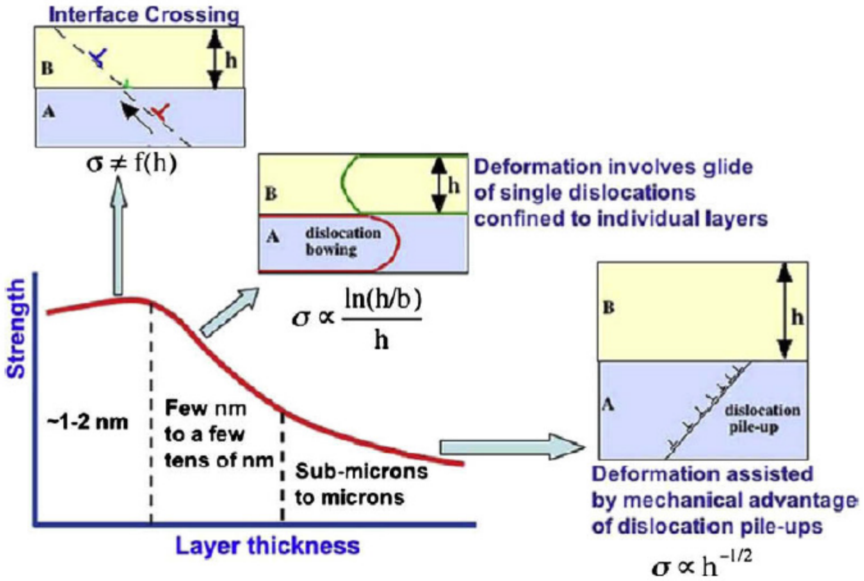

Figure I-28: Strength-controlling doslocation mechanisms in multilayers operative at diffrent length scales [Misra et al. 2005]

- Ductility

The ability to plastic deformation without failure under tensile stress is called “ductility”. The ductility of extreme refined grain structure is usually low. This low ductility is commonly attributed in the literature to the reduction in strain-hardening capability. Indeed, the distribution of dislocations during deformation of UFG material is not homogeneous; one can find dislocation-rich area such as cells or grain boundary and regions with less populated dislocations such as grain interiors or cell. [Park et al. 2000] estimated, on the other hand, the characteristic time necessary to spread the trapped lattice dislocation into grain boundary during deformation. They found that the time necessary to do so is shorter than the total deformation. This leads to non accumulation of dislocation and consequently to absence of strain hardening.

The low ductility caused by the reduction of the strain hardening can be also rationalized via a mechanistic approach based on the Considère criterion which states that failure by necking under tensile loading occurs if the following inequality is fulfilled:

$$\frac{d\sigma^T}{d\varepsilon^T} \leq \sigma^T \qquad \text{Eq. I-4}$$

Where σ^T and ε^T are the true stress and true strain respectively. Indeed, when the grain size is reduced down to sub-micro or nanometric scale, the flow stress increases significantly and the capacity of the material to strain-harden decreases systematically. Therefore, the Consière criterion can be met even at small tensile strains and hence a low uniform elongation is obtained.

In recent years, several investigations have been performed to design microstructures with high strain hardening rate by introducing different deformation mechanisms. Some of these strategies

It is now well established that the enhancement of the ductility, parallel to the high strength, in UFG and nanostructured metals is considered as a matter of exceptions rather than a rule. In fact, some authors, [Estrin and Vinogradov 2013] [Valiev et al. 2016], attributed the success of some applications (examples above) to the choice of the chemical composition and the specific processing routes. Indeed, some successful examples in terms of strength/ductility enhancement are not directly attributed to the grain size but to other related factors such as:

- Presence of second phase or phase stability: The unique mechanical properties obtained in the ultra-fined grains duplex steels of [Yen et al.2015] for example were attributed to the TRIP effect of α' martensite. In fact, they suggested that both the refined austenite (300nm) and the chemical composition lead to a significant contribution of the stress-assisted martensite in the deformation mechanism of the designed alloys. See Figure I-25.

- Presence of high density of twins: The contribution of intensive twining to the fatigue and tensile properties of austenitic stainless steel 316L, for example, was found to be very significant in the investigation carried out on the recent work of [Uneo et al.2011] in which a nanostructured 316 was obtained by ECAP process performed up to four passes via route Bc at 427K. At the fourth pass, interesting compromise in terms of ductility and strength is found. See Figure I-26. [Uneo et al.2011] attributed mainly these results to the mechanical twining in nanoscopic twins of which the inter-twin spacing is about 30-40nm. See Figure I-26.

- Mixture of coarse and fine grains: this strategy consists on designing microstructures of two grain sizes populations; micrometer-sized grains embedded in nanocrystalline and ultrafine (<300nm) grains. The first population will be responsible for enhancing ductility by promoting the strain hardening while the second will contribute to increase strength. This strategy has been suggested by [Höppel et al. 2004] and then by [Wang et al. 2002]. However the challenge of this strategy lies on the control of the distribution of the two populations from one hand, and from other hand the evaluation of the level of interaction between them. These problematic remain a subject of several investigations and discussion in the literature.

The development of new strategies to enhance simultaneously strength and ductility in nano/ultrafine structure is still a subject of large investigations and discussions. Some authors suggest a combination of more than one strategy. The very recent work of [Wu et al. 2016], for example, proposed an interesting approach of microstructure design strategy based on the benefits from bimodal grain size distribution and TRIP effects. Indeed, an austenite stainless steel 304 has been produced with two gradient structures layers, obtained by surface mechanical attrition, squeezing two coarse-grained core layers. These layers played in fact a significant role in enhancing the uniform elongation simultaneously with strength by i) causing a strain partitioning which continues to large strains; the core deforms plastically while the gradient layer is still deforming elastically; ii) prolonging the TRIP effect to large plastic strains; during tensile deformation, an early transformation γ→α' occurs inside the coarse-grained core while the compressive stress within the layers delay the TRIP effect to large strains. Interesting compromise of high strength and uniform elongation is obtained as a result of this design.

I.III Conclusion

The successful applications presented, in particular the nanocomposite Cu-Nb obtained by ABD technique, give the inspiration to utilize this technique for enhancing and understanding the mechanical properties of duplex stainless steels.

Indeed, using SPD techniques for enhancing mechanical properties in particular the strength/ductility couple showed its efficiency for either single-phase or two-phase materials. However, these breakthrough properties are obtained only for dimensions below the micrometric scale in which other deformation mechanisms are involved. As presented above, the classical Hall-Petch law, for example, is no longer valid for scale less than 25 nm.

In the present work, a first stage will be naturally to develop a process allowing the co-deformation to large strains of ferrite and austenite, and to evaluate the limits of the process in terms of microstructure refinement. This will be developed in Chapter 3. One of the challenges met by our study is that in most cases reported in the literature, the co-deformed materials were immiscible. In the case of DSS this is not the case and the optimization of the process will need to account for the possible role of inter-diffusion between the phases during the annealing steps necessary during the processing. The evaluation of the microstructure of the obtained composites and the rationalization of the limits met by our process will be given in chapter 4. Last, chapter 5 will present the resulting mechanical properties, discuss and model the deformation mechanisms.

References

[Angel 1954]
Angel T Formation of Martensite in Austenitic Stainless Steel, J. Iron and Steel Inst.: JISI, 1954,177, 165-174.

[Baroux, 1990]
Baroux, B., Mantel, M., Gex, D., Pedarre, P. The effect of niobium on the recrystallization of 17% chromium ferritic stainless steel. Proceedings of Recrystallization '90,1990, Chandra, T. (ed), pp. 345-350. The Minerals, Metals & Materials Society.

[Bavay , 1990]
Bavay, J. C., Aciers inoxydables austénitiques. Les aciers inoxydables, 1990, Les Editions de Physique, 564-610.

[Bevk et al., 1978]
Bevk, J., Harbison, J. P., & Bell, J. L., Anomalous increase in strength of insitu formed Cu-Nb multifilamentary composites. Journal of Applied Physics,1978, 49(12), 6031-6038.

[Byun 1991]
Byun, T. S., & Kim, I. S., Stress and strain partition in elastic and plastic deformation of two phase alloys. Journal of materials science,1991, 26(14), 3917-3925.

[Chai 2006]
Chai, G. C., & Lillbacka, R., Damage and crack initiation behavior of duplex stainless steel during cyclic loading. In Key Engineering Materials, 2006, (Vol. 324, pp. 1117-1122).

[Cho 1988]
Cho, K., & Gurland, J., The law of mixtures applied to the plastic deformation of two-phase alloys of coarse microstructures. Metallurgical Transactions A, 1988, 19(8), 2027-2040.

[Chokshi 1989]
Chokshi, A. H., Rosen, A., Karch, J., & Gleiter, H., On the validity of the Hall-Petch relationship in nanocrystalline materials. Scripta Metallurgica, 1989, 23(10), 1679-1683.

[Cunat , 2000]
CUNAT, P. J., Aciers inoxydables. Propriétés. Résistance à la corrosion. Techniques de l'ingénieur. Matériaux métalliques, 2000, (M4541), M4541-1.

[Davis 1994 Handbook]
Davis J., Ed., ASM Specialty Handbook : Stainless Steels, 1994.

[Desestret 1990]
Desestret, A. & Charles, J. Les aciers inoxydables austéno-ferritiques, Les aciers inoxydables, 1990, 31- 677. Les éditions de physique.

[Dupouy-Lecouturier, 1995]
Dupouy-Lecouturier F.. Contribution au développement des champs magnétiques pulsés très intenses : R&D des conducteurs renforcés. PhD thesis, INSA de Toulouse, 1995.

[Elbartali 2007]
Elbartali. A Apport des mesures de champs cinématiques à l'étude des micromécanismes d'endommagement en fatigue plastique d'un acier inoxydable duplex (Doctoral Desseration),2007.

[Embury and Fisher 1966]
Embury, J. D., & Fisher, R. M., The structure and properties of drawn pearlite. Acta Metallurgica, 1966, 14(2), 147-159.

[Estrin and Vinogadov 2013]
Estrin, Y., & Vinogradov, A. (2013). Extreme grain refinement by severe plastic deformation: a wealth of challenging science. Acta materialia, 61(3), 782-817.

[Frommeyer and Wasserman, 1975]
Frommeyer, G., & Wassermann, G., Microstructure and anomalous mechanical properties of in situ-produced silver-copper composite wires. Acta Metallurgica, 1975, 23(11), 1353-1360.

[Furukawa et al.2001]
Furukawa, M., Horita, Z., & Langdon, T. G., Developing ultrafine grain sizes using severe plastic deformation. Advanced Engineering Materials, 2001, 3(3), 121-125.

[Gardner 2006]
Gardner, L., & Ng, K. T., Temperature development in structural stainless steel sections exposed to fire. Fire Safety Journal, 2006, 41(3), 185-203.

[Gympel 90]
Gympel, P. & Norbert, A. Constitution et propriétés. Les aciers inoxydables : Propriétés, mise en oeuvre, emploi, normes, 1990, Technique et Documentation-Lavoisier.

[Hall, 1951]
Hall, E. O. Sylwestrowicz, W., The deformation and ageing of mild steel. Proceedings of the Physical Society. Section B, 1951, 64(6), 495.

[Herrera et al. 2011]
Herrera, C., Ponge, D., & Raabe, D., Design of a novel Mn-based 1GPa duplex stainless TRIP steel with 60% ductility by a reduction of austenite stability. Acta Materialia, 2011, 59(11), 4653-4664.

[Honeycombe and Bhadeshia 1995]
Honeycombe, R. W. K., & BHADESHIA, H., The bainitic reaction. Metallurgical and Materials Science Steels-Microstructure and Properties, 1995, 115-139.

[Höppel et al. 2004]
Höppel, H. W., May, J., & Göken, M. (2004). Enhanced Strength and Ductility in Ultrafine-Grained Aluminium Produced by Accumulative Roll Bonding. Advanced Engineering Materials, 6(9), 781-784.

[Horita and Langdon, 2006]
Horita, Z., & Langdon, T. G., Using torsion to produce severe strain and ultafine grains, TMS Annual Meeting, 2006, 17pp.

[Jia 2006]
Jia, N., Peng, R. L., Wang, Y. D., Chai, G. C., Johansson, S., Wang, G., & Liaw, P. K., Interactions between the phase stress and the grain-orientation-dependent stress in duplex stainless steel during deformation. Acta materialia, 2006, 54(15), 3907-3916.

[Koch 2003]
Koch, C. C., Optimization of strength and ductility in nanocrystalline and ultrafine grained metals. Scripta Materialia, 2003, 49(7), 657-662.

[Lacombe 1990]
Lacombe P., B. Baroux, G. Béranger, Eds., Les aciers inoxydables, Les éditions de physique, 1990.

[Leffler 2005]
Leffler, B., Stainless stainless steels and their properties, Les aciers inoxydables, 2005, Les Editions de Physique: 564-610.

[Levi 1960]
Levi, F. P., Permanent magnets obtained by drawing compacts of parallel iron wires. Journal of Applied Physics, 1960, 31(8), 1469-1471.

[Liddicoat et al. 2010]
Liddicoat, P. V., Liao, X. Z., Zhao, Y., Zhu, Y., Murashkin, M. Y., Lavernia, E. J., ... & Ringer, S. P. (2010). Nanostructural hierarchy increases the strength of aluminium alloys. Nature communications, 1, 63.

[Lin 2006]
Lin P R, Gibmeir J, Eulert S, Johansson S and Chai G C, Materials Science Forum, 2006,524-525, p 847.

[Lo 2009]
Lo, K. H., Shek, C. H., & Lai, J. K. L., Recent developments in stainless steels. Materials Science and Engineering, 2009, R: Reports, 65(4), 39-104.

[Lowe , 2006]
Lowe, T. C., Metals and alloys nanostructured by severe plastic deformation: Commercialization pathways. JOM, 2006, 58(4), 28-32.

[Lowe 2002]
Lowe, T. C., & Valiev, R. Z. (2002). Investigations and applications of SPD. Nato science series, 3, 2002.

[Lowe and Zhu , 2003]
Lowe, T. C., & Zhu, Y. T., Commercialization of nanostructured metals produced by severe plastic deformation processing. Advanced Engineering Materials, 2003, 5(5), 373-378.

[Lu et al. 2004]
Lu, L., Shen, Y., Chen, X., Qian, L., & Lu, K. (2004). Ultrahigh strength and high electrical conductivity in copper. Science, 2004, 304(5669), 422-426.

[Mayers et al. 2006]
Meyers, M. A., Mishra, A., & Benson, D. J., Mechanical properties of nanocrystalline materials. Progress in materials science, 2006. 51(4), 427-556.

[Mishra et al. 2005]
Mishra, A., Richard, V., Gregori, F., Asaro, R. J., & Meyers, M. A., Microstructural evolution in copper processed by severe plastic deformation. Materials Science and Engineering: A, 2005, 410, 290-298.

[Misra et al. 1998]
Misra, A., Verdier, M., Lu, Y. C., Kung, H., Mitchell, T. E., Nastasi, M., & Embury, J. D., Structure and mechanical properties of Cu-X (X= Nb, Cr, Ni) nanolayered composites. Scripta Materialia, 1998, 39(4), 555-560.

[Moussavi 1997]
Moussavi Torshizi S.E. Ecrouissage cyclique d'aciers inoxydables austénitique, ferritiques et austéno-ferritique : influence de l'histoire de chargement. Thèse de doctorat, Université de Lille1, 1997.

[Nakamura et al., 2004]
Nakamura, K., Neishi, K., Kaneko, K., Nakagaki, M., & Horita, Z., Development of severe torsion straining process for rapid continuous grain refinement. Materials transactions, 2004, 45(12), 3338-3342.

[Neishi et al., 2002]
Neishi, K., Horita, Z., & Langdon, T. G., Grain refinement of pure nickel using equal-channel angular pressing. Materials Science and Engineering: A, 2002, 325(1), 54-58.

[Nilsson and Chai 2010]
Nilsson, J. O., & Chai, G., Physical metallurgy of duplex stainless steels, 2010, In Proc. Of Conf. DSS (p. 35).

[Nirosta 2002]
Nirosta, K.T. Practical guidelines for the fabrication of duplex stainless steels. 2002. http://www.nidi.org/index.cfm/ci_id/10683.htm

[Noyan and Cohen 1986]
Noyan, I. C., & Cohen, J. B., X-ray diffraction study of changes in stress-strain distributions during the fatigue of a two-phase alloy. Materials Science and Engineering, 1986, 79(2), 149-155.

[Nyström 1994]
Nyström, M., & Karlsson, B. (1994). Duplex Stainle-ss Steels' 94. Glasgow, Scotland. TWI, Cambridge, U.K. 1994.

[Pakieła et al. 2006]
Pakieła, Z., Garbacz, H., Lewandowska, M., Drużycka-Wiencek, A., Suś-Ryszkowska, M., Zieliński, W., & Kurzydłowski, K. (2006). Structure and properties of nanomaterials produced by severe plastic deformation.Nukleonika, 51, 19-25.

[Petch, 1953]
Petch, N. J., The cleavage strength of polycrystals. J. Iron Steel Inst., 1953, 174, 25-28.

[Pickering 1984]
Pickering Physical Metallurgical Development of Stainless Steels. In Proc. Conf. Stainless Steels 84, Gothenburg, Sept 1984, pages 2-28, 1984.

[Rajasekhara et al.2010]
Rajasekhara, S., Karjalainen, L. P., Kyröläinen, A., & Ferreira, P. J., Microstructure evolution in nano/submicron grained AISI 301LN stainless steel. Materials Science and Engineering: A, 2010, 527(7), 1986-1996.

[Russell 2000]
Russell, A. M., Chumbley, L. S., & Tian, Y., Deformation processed metal–metal composites. Advanced Engineering Materials, 2000, 2(1-2), 11-22.

[Saada, 2005]
Saada, G., Hall–Petch revisited. Materials Science and Engineering: A, 2005, 400, 146-149.

[Saito et al. 1998]
Saito, Y., Tsuji, N., Utsunomiya, H., Sakai, T., & Hong, R. G., Ultra-fine grained bulk aluminum produced by accumulative roll-bonding (ARB) process.Scripta materialia, 1998, 39(9), 1221-1227.

[Saito et al. 1999]
Saito, Y., Utsunomiya, H., Tsuji, N., & Sakai, T., Novel ultra-high straining process for bulk materials—development of the accumulative roll-bonding (ARB) process. Acta materialia, 1999, 47(2), 579-583.

[Sakai et al., 2005]
Sakai, G., Horita, Z., & Langdon, T. G., Grain refinement and superplasticity in an aluminum alloy processed by high-pressure torsion.Materials Science and Engineering: A, 2005, 393(1), 344-351.

[Sauvage et al.2001]
Sauvage, X., Renaud, L., Deconihout, B., Blavette, D., Ping, D. H., & Hono, K., Solid state amorphization in cold drawn Cu/Nb wires. Acta materialia, 2001, 49(3), 389-394..

[Schaeffler, 1949]
Schaeffler, A. Constitution diagram for stainless steel weld metal. Metal progrees, 1949, 56, 680-680.

[Schwartz and Shen 2003]
Schwarz, R.B. and T.D. Shen, "High-Strength, High Conductivity Bulk Nanostructured Ag-Cu Alloys", in Proc. 2003 TMS Fall Mtg., Chicago, Il, Nov. 9-11, Processing and Properties of Nanostructured Materials, B. Pandey et al., eds., ISS and TMS, Chicago, p. 141, 2003.

[Segal, 1995]
Segal, V. M., Materials processing by simple shear. Materials Science and Engineering: A, 1995, 197(2), 157-164.

[Shen et al.2005]
Shen, Y. F., Lu, L., Lu, Q. H., Jin, Z. H., & Lu, K., Tensile properties of copper with nano-scale twins. Scripta Materialia, 2005, 52(10), 989-994.

[Spencer 2004]
Spencer K., The work hardening od austenitic stainless steel, Applied to the fabrication of high strength conductors (Doctoral Desseration),2004.

[Spitzig and Krotz, 1987]
Spitzig, W. A., & Krotz, P. D., A comparison of the strength and microstructure of heavily cold worked Cu-20% Nb composites formed by different melting procedures. Scripta metallurgica, 1987, 21(8), 1143-1146.

[Thilly et al. 2002]
Thilly, L., Lecouturier, F., & Von Stebut, J., Size-induced enhanced mechanical properties of nanocomposite copper/niobium wires: nanoindentation study. Acta Materialia, 2002, 50(20), 5049-5065.

[Uneo et al.2011]
Ueno, H., Kakihata, K., Kaneko, Y., Hashimoto, S., & Vinogradov, A. (2011). Enhanced fatigue properties of nanostructured austenitic SUS 316L stainless steel. Acta Materialia, 59(18), 7060-7069.

[Valiev et al. 1991]
Valiev, R. Z., Krasilnikov, N. A., & Tsenev, N. K. (1991). Plastic deformation of alloys with submicron grained structure. Materials Science and Engineering: A, 1991, 137, 35-40.

[Valiev et al. 1996]
Valiev, R. Z., Ivanisenko, Y. V., Rauch, E. F., & Baudelet, B., Structure and deformaton behaviour of Armco iron subjected to severe plastic deformation. Acta Materialia,1996, 44(12), 4705-4712.

[Valiev et al., 2000]
Valiev, R. Z., Islamgaliev, R. K., & Alexandrov, I. V., Bulk nanostructured materials from severe plastic deformation. Progress in materials science, 2000, 45(2), 103-189.

[Valiev et al.1996]
Valiev, R. Z., Mishral, R. S., Grozal, J., & Mukherjee, A. K. (1996). Processing of nanostructured nickel by severe plastic deformation consolidation of ball-milled powder. Scripta materialia, 1996, 34(9), 1443-1448.

[Valiev et al., 2002]
Valiev, R. Z., Alexandrov, I. V., Zhu, Y. T., & Lowe, T. C., Paradox of strength and ductility in metals processed bysevere plastic deformation. Journal of Materials Research, 2002, 17(01), 5-8.

[Valiev et al., 2010]
Valiev, R. Z., Enikeev, N. A., Murashkin, M. Y., Kazykhanov, V. U., & Sauvage, X. (2010). On the origin of the extremely high strength of ultrafine-grained Al alloys produced by severe plastic deformation. Scripta Materialia, 63(9), 949-952.

[Valiev et al., 2016]
Valiev, R. Z., Estrin, Y., Horita, Z., Langdon, T. G., Zehetbauer, M. J., & Zhu, Y. (2016). Producing bulk ultrafine-grained materials by severe plastic deformation: ten years later. JOM, 68(4), 1216-1226.

[Vidal 2006]
Vidal V., Optimisation des propriétés mécaniques des conducteurs nanofilemntaire (Doctoral dessertation), 2006.

[Wang 2002]
Wang, Y. M., Ma, E., & Chen, M. W., Enhanced tensile ductility and toughness in nanostructured Cu. Applied physics letters, 2002, 80(13), 2395-2397.

[Winholts and Cohen 1992]
Winholtz, R. A., & Cohen, J. B., Load sharing of the phases in 1080 steel during low-cycle fatigue. Metallurgical Transactions A, 1992, 23(1), 341-354.

[Wu et al. 2016]
Wu, X. L., Yang, M. X., Yuan, F. P., Chen, L., & Zhu, Y. T. (2016). Combining gradient structure and TRIP effect to produce austenite stainless steel with high strength and ductility. Acta Materialia, 112, 337-346.

[Yang and Welzel, 2005]
Yang, Z., & Welzel, U., Microstructure–microhardness relation of nanostructured Ni produced by high-pressure torsion. Materials Letters, 2005, 59(27), 3406-3409.

[Yen et al. 2015]
Yen, H. W., Ooi, S. W., Eizadjou, M., Breen, A., Huang, C. Y., Bhadeshia, H. K. D. H., & Ringer, S. P. (2015). Role of stress-assisted martensite in the design of strong ultrafine-grained duplex steels. Acta Materialia, 82, 100-114.

[Zhao et al., 2005]
Zhao, Y. H., Liao, X. Z., Zhu, Y. T., Horita, Z., & Langdon, T. G. (2005). Influence of stacking fault energy on nanostructure formation under high pressure torsion. Materials Science and Engineering: A, 2005, 410, 188-193.

[Zhilyaev et al, 2003]
Zhilyaev, A. P., Nurislamova, G. V., Kim, B. K., Baró, M. D., Szpunar, J. A., & Langdon, T. G., Experimental parameters influencing grain refinement and microstructural evolution during high-pressure torsion. Acta Materialia, 2003, 51(3), 753-765.

[Zhilyaev et al., 2001]
Zhilyaev, A. P., Lee, S., Nurislamova, G. V., Valiev, R. Z., & Langdon, T. G., Microhardness and microstructural evolution in pure nickel during high-pressure torsion. Scripta materialia, 2001, 44(12), 2753-2758.

[Zhu 2002]
Zhu, Y. T., Lowe, T. C., Valiev, R. Z., Stolyarov, V. V., Latysh, V. V., & Raab, G. J., U.S. Patent No. 6,399,215. Washington, DC: U.S. Patent and Trademark Office, 2002.

[Zhu 2004]
Zhu, Y. T., & Liao, X., Nanostructured metals: retaining ductility. Nature materials, 2004, 3(6), 351-352.

II Experimental methods

Contents

II.I Materials

Two industrial grades from UGITECH, whose compositions are reported in Table II-1 have been chosen for this thesis. The reasons behind this choice will be explained in Chapter III:

- Ferritic stainless steel of type 430LNb rich in niobium
- Austenitic stainless steel of type 316L

Table II-1: Nominal composition (wt.%) of the stainless steel alloys used initially in the present work.

Grade	C	Cr	Ni	Mo	Mn	N	Nb	Si
430 LNb	0.014	18.05	0.2	0.039	0.382	0.016	0.490	0.398
316 L	0.019	16.73	11.10	2.034	0.795	0.029	0.028	0.505

II.II Thermo-mechanical treatment

II.II.1 Cold drawing

In the current work the deformation process used to fabricate the architectured composites is cold drawing, which consists in reducing the cross-sectional area of the wire by pulling through a die whose geometry will determine the final dimensions of the wire. A more detailed description about this operation will be provided in Chapter III. The drawing machine used is the mono-pass Marshall apparatus at Centre de Recherches Ugitech (CRU-Ugine). It is composed of 4 parts; uncoiling, straigthners, die and its lubrication system, capstan. See Figure II-1. The machine engine allows drawing for a velocity up to 3.3 m/s. The drawing velocity used in our experiments was between 0.5-1.5 m/s.

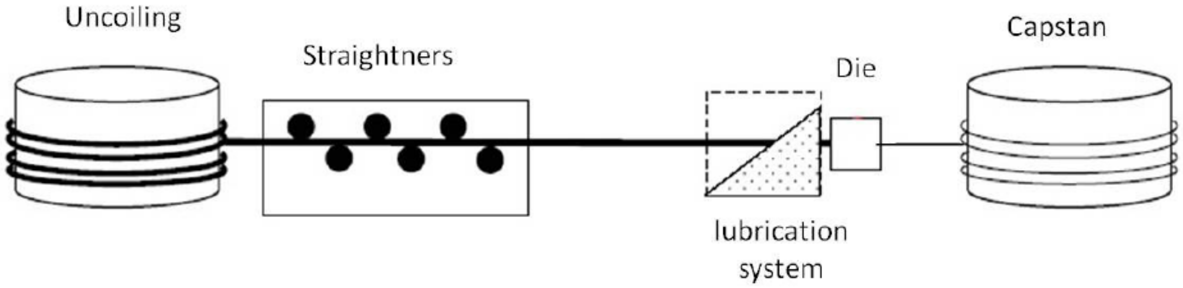

Figure II-1:Schematic illustration of the drawing machine

II.II.2 Annealing

After cold deformation, the wire is usually annealed to restore its properties and provide enough ductility. Two types of furnaces, depending on the investigation carried out, were used.

II.II.2.a Vacuum furnace

A vacuum vertical furnace Ugine-Infra® of capacity 850mm*1500mm was used during the manufacturing process (see Chapter III). The maximum heating rate of this furnace is 70°C/hour. At the end of the heating cycle, a rapid cooling down to ambient temperature under argon atmosphere is operated once the vacuum is broken.

II.II.2.b Salt bath

For recrystallization study (Chapter IV), a salt bath was used. Short duration annealing treatments were carried out in a barium chloride salt bath previously heated at the target temperature. The main advantage of salt bath is its very fast heat transfer rate. In this study, the duration of salt bath treatments was comprised between 30s and 1h, for holding temperatures ranging from 750°C to 950°C. At the end of the annealing treatment, the sample was immediately quenched in water, down to room temperature.

II.III Metallurgical characterization

II.III.1 Sample preparation

Herein, we present the experimental techniques used to prepare specimens for various characterization techniques: microscopy, orientation maps using Electron Backscattering Diffraction (EBSD) and hardness.

Naturally, for wires two particular surfaces have been observed: the transverse section and the longitudinal section. They are schematized in Figure II-2.

Figure II-2: a) Longitudinal section performed in the middle of the sample (parallel to the drawing direction); b) Transverse section performed perpendicular to wire axis

After cutting following the transverse or longitudinal section, the specimens were polished by mechanical grinding with silicon carbide until 1200 grade. Mechanical final polishing consisting in 9µm, 6µm, 3µm and 1µm diamond paste polishing followed by an Oxide Polishing Suspension (OPS) has been performed. The time spent for the final OPS polishing depends on the characterization technique. For example, for samples dedicated for EBSD analysis, at least 20 minutes are necessary to obtain a good final surface. For other characterization such as microscopy and hardness, time between 2-5 minutes is sufficient.

II.III.2 Microscopy

II.III.2.a Optical microscopy

Optical microscopy has been used mainly to characterize the grain structure and to reveal the different phases of the composites. Before observation, the specimens were polished mechanically until OPS finishing and then etched using electro-nitric method. The etching solution is a mixture of 97mL of water (H_2O) and 553mL of nitric acid (HNO_3). The etching should be realized using a current generator. For our materials, the current density necessary for good etching is about 50mA.cm^{-2}. The time necessary for a successful etching depends on the type of the metal; 10-15 seconds for 430LNb and 30 seconds for 316L.

II.III.2.b Scanning Electron Microscope (SEM)

In some cases the light microscope does not reveal clearly the grain boundaries or the phases present in the specimen (in particular composite with fine microstructure) even with a good etching quality. Therefore, SEM has been used for observations demanding higher resolution. The conventional SEM LEO 440 has been mostly used for imaging.

> *Notice: Concerning the fabricated 316/430LNb composites, we can distinguish both phases in SEM with only OPS finishing without etching by using the Backscattered Electron detectors (BSE) as Figure II-3 shows. This is due to the chemical composition of both phases; the austenite 316L is rich in Ni which is a heavy element whereas the ferrite 430LNb has a low Ni content (See chapter III).*

In addition to the use for micrography, SEM is usually used for other microanalysis investigation such as chemical composition via Energy Dispersive X-ray Spectroscopy (EDS) and 2D texture measurements via EBSD.

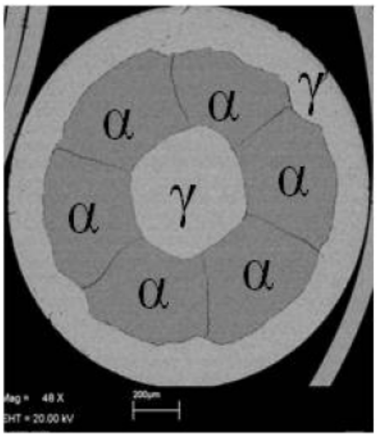

Figure II-3: SEM image using BSE mode for 316L/430LNb composite without etching

i) Chemical analysis by EDS

Principle of EDS

EDS analysis is based on the bombardment of the sample with a focused beam of high-energy electrons. The interaction between the electron beam and sample atoms results an X-ray emission whose energy spectrum gives access to the chemical analysis of the bombarded area. EDS uses this X-ray spectrum to determine the localized element composition. All element above atomic number 4 (Be) can be detected based on the characteristic energy of X-ray photons emitting from each element*. Electrons interact with specimen atoms in different way resulting in different products which carry information such as specimen's chemical composition and topography. After inelastic interaction a variety of interaction products are generated, such as back-scattered electrons with small energy loss, secondary electrons of low energy and X-rays [Goldstein et al.1994]. The trajectories of elastic or inelastic scattered electrons determine the volume interaction between beam electrons and specimens atoms. This interaction volume is usually called in the literature as interaction-pear due to its shape taken during scattering. Indeed, when electrons penetrate the material they lose energy and therefore the probability of elastic scattering increases resulting in deviations (or broadening) of the trajectory.

The backscattered electrons coming from this volume are mostly used for SEM imaging whereas the X-rays are used in EDS to determine the chemical composition of the material. Figure II-4.a shows the different parts of the interaction volume (interaction-pear).

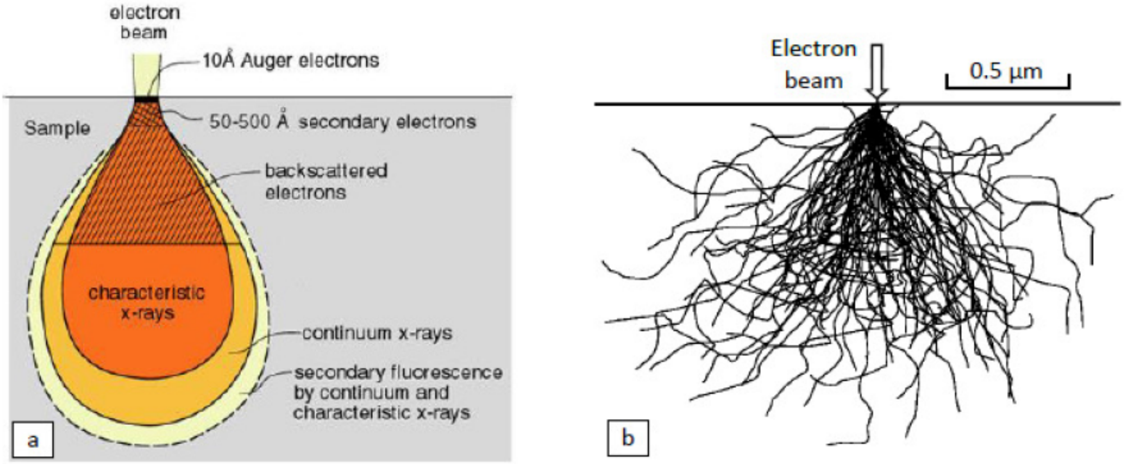

Figure II-4:(a): Schematic beam electrons-specimen interaction volume ; (b): Monte Carlo simulation of electron trajectory in iron for 20 keV beam energy [Goldstein et al.1994]

---

*Introduction to Energy Dispersive X-ray Spectrometry (EDS), micron.ucr.edu/public/ manuals/EDS-intro.pdf, Nov.2011.

The depth(x) and the width (y) in **µm** of the interaction-pear can be determined using an empirical expression [Potts 1987]:

$$x = \frac{0.1 * E_0}{\rho} \text{ and } y = \frac{0.077 * E_0}{\rho}$$

Where E_0 is the beam energy (keV) and ρ is the material density (g/cm^3).

However, there are some theoretical methods based on Monte Carlo simulations for determining the interaction-pear. Figure (5) shows the influence of the SEM accelerating voltage on the size of the interaction-pear in iron using Monte Carlo simulation.

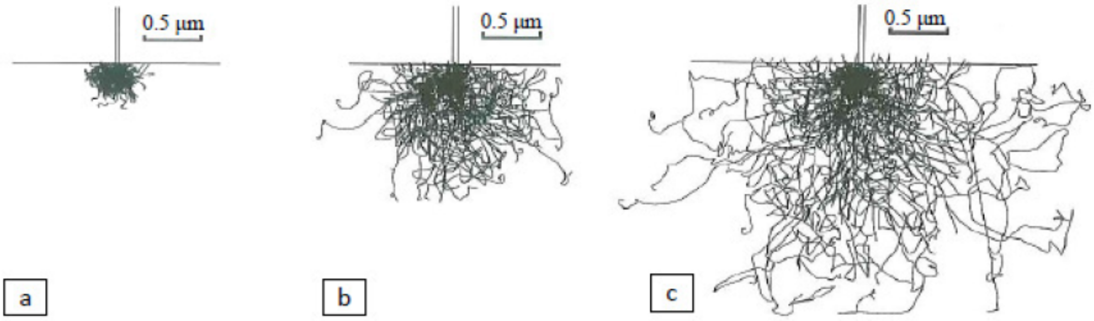

Figure II-5:Monte Carlo simulation of the interaction volume in iron as a function of accelerating voltage, (a): 10 kV, (b): 20 kV, (c): 30 kV [Goldstein et al.1994]

Chemical analysis profile by EDS

For a good chemical analysis using multi-point profile, it is necessary to ensure a sufficient distance between the interaction-pears. This will avoid the interference between the interaction volumes and therefore allow obtaining good accuracy. In our case, the half width of the simulated interaction-pear (x) for beam energy of 20ekV is assumed to be the distance from the centre of the pear to the hard line as shown in Figure II-6. The half width of the pear for our materials is found to be 0.7 µm. Hence we chose a step distance of at least 0.7 µm between the points of the analysis profile. A SEM JOEL JSM 6400 apparatus has been used for all quantitative EDS analysis.

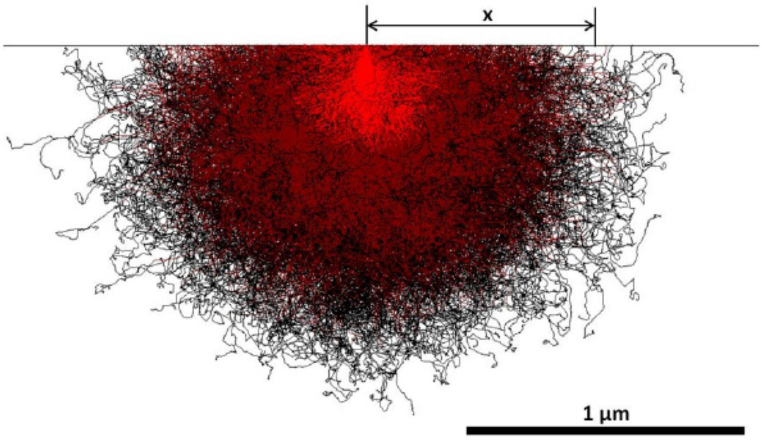

Figure II-6: Simulated pear of interaction for 316L and 430LNb

ii) EBSD analysis

EBSD technique has been mainly used in present work for grain structure and phase evolution analysis in particular for composites with fine microstructure. The resolution of the investigated area depends on the step size. For large and local map, a step size of 1µm and 0.1µm has been taken respectively. EBSD analysis has been carried out with an automated pattern indexation tool (from TeX SEM laboratories) coupled to the FEG SEM Zeiss Ultra 55. After collection, data are post-processed with the OIM software, which offers different possibilities to illustrate the results.

II.III.2.c Transmission Electron Microscopy (TEM)

A JEOL 3010 TEM and JEOL 2100F operating at 200kV have been used for fine microstructure investigation.

Sample preparation:

The TEM samples should be in form of thin foils. The preparation of these thin foils can be realized by two ways; either by mechanical grinding followed by electro-polishing or by using Focused Ion Beam (FIB). The latter is used particularly for fine regions which are inaccessible by the classical methods. This technique allows in fact obtaining thin foils by directly milling the region of interest of the sample in question. It is based on sending a gallium ion beam originating from liquid metal ion source. This beam is accelerated up to 30 kV [Rao et al. 2010]. In our work, we used FIB technique to observe the 316L/430LNb interface of the finest cells in the micro-composites. The thin foils were prepared in the Material Characterization Platform of Grenoble-INP (CMTC-GrenobleINP). The present author would like to thank Florence Robaut for her help in the preparation of FIB foils.

ACOM-TEM:

The Automatic Crystallographic Orientation Mapping (ACOM) is a recently developed tool aiming to obtain crystal orientation maps that couldn't be resolved by the popular EBSD-SEM technique, in particular the severely deformed materials [Mathis and Rauch 2007]. Indeed, the classical EBSD technique is based on the diffraction signals composed of Kikuchi lines indexation whose relative positions are strongly crystal orientation sensitive [Rauch and Véron 2014]. On the other hand, ACOM-TEM technique lies on the indexation of Bragg spot patterns rather than Kikuchi lines and hence it is very efficient for severly deformed metals having high dislocations density. The principle of ACOM-TEM can be resumed on the following steps:

- Bombarding a sample by nano-prop scanning electron beam. The system is coupled with high speed external camera allowing recording diffraction patterns through the TEM from window.

  Once the acquisition of the diffraction pattern is achieved, the recorded diffraction is compared with a calculated diffraction pattern for a specific phase/orientation performed in kinematic conditions. This technique is called a Template Matching Strategy. In fact, a complete data base is setted up by the used with a chosen mis-orientation between the templates. The construction of the calculated template is illustrated in Figure II-8. For more detailed aspects about this technique, interested reader can refer to [Rauch and Véron 2014].

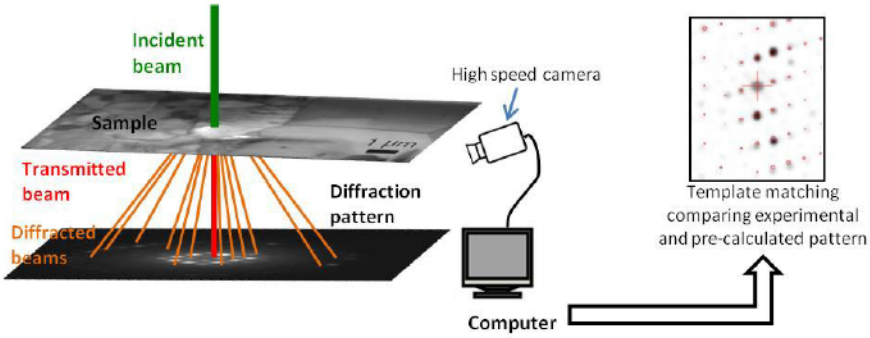

Figure II-7: Schematic illustration of ACOM-TEM system (adapted from [Sallez 2014])

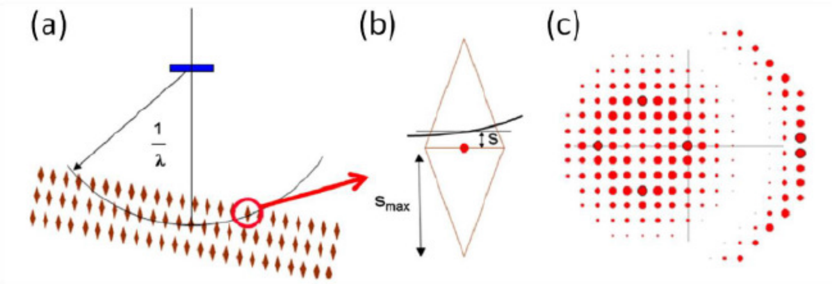

Figure II-8:Schematic view of the template construction: a) the Ewald sphere intercept nodes of the rotated reciprocal lattice; b) the shape of the nodes is representative of the decrease of the spot intensity with increasing deviation fromthe Bragg condition. The decrease is set linear up to a maximumvalue Smax of the deviation fromBragg conditions; c) the resulting template is a first order estimate of the diffraction pattern pertaining to kinematical conditions [Rauch and Véron 2014].

- The final step consists on an orientation identification procedure via image correlation index technique. Indeed, each reflection is characterized by spot positions (x, y) and its intensity. For every pre-calculated template, the following correlation index is calculated for each pixel (x,y).

$$Q_c(i) = \frac{\sum_{j=1}^{m} I(x_j, y_j) T_i(x_j, y_j)}{\sqrt{\sum_{j=1}^{m} I^2(x_j, y_j)}\sqrt{\sum_{j=1}^{m} T^2(x_j, y_j)}}$$ Eq. II-1

Where $I(x, y)$ and $T(x, y)$ are, respectively, the intensity of the recorded pattern and the simulated pre-calculated template i for a point of coordinates (x,y). The highest value of Q is taken as the best template solution.

II.III.3 Quantitative metallography

II.III.3.a Estimation of the recrystallized fraction

The recrystallized fraction has been estimated with a point counting method. A regular grid is placed over the SEM/optical micrographs of the structure revealed by electro-nitric etching. The proportion of nodal points which coincide with recrystallized grains indicates the surface of recrystallized grains. This fraction is also equal to the volume recrystallized fraction [Modin and Modin 2013]. To ensure accuracy a total number of 150 points was counted in three separated fields.

II.III.3.b Estimation of the grain size

The grain size has been estimated using the intercept method. In our recrystallization investigation of bulk wires in Chapter IV, the grain size was estimated on the longitudinal section of the bulk wires. According to [Modin and Modin 2013], as grains are elongated in the longitudinal section (parallel to the drawing direction) but equiaxed in the transverse section (perpendicular to the drawing direction), two characteristic intercept lengths can be evaluated. $L^{\perp}$ and $L^{\parallel}$ designate the intercept length perpendicular and parallel to the drawing direction. Test lines in two directions have been drawn over three different regions of the sample. The number of grains intersected by the line is counted whereas grains that touch the end-points are counted as half grains. The mean intercept length of grains $L^{\perp,\parallel}$ can be calculated as following:

$$L^{\perp,\parallel} = \frac{L_{tot}^{\perp,\parallel}}{mag \times P^{\perp,\parallel}}$$ Eq. II-2

Where $L_{tot}^{\perp,\parallel}$ is the total test-line length in a given direction, mag is the linear magnification and $P^{\perp,\parallel}$ is the number of grain boundary intersection with test-lines in a given direction. Hence, the number of grains per unit volume is:

$$N_V = \frac{0.7}{L^{\parallel}(L^{\perp})^2}$$

Eq. II-3

The equivalent radius of spherical grains is then expressed:

$$r_{eq} = \sqrt[3]{\frac{3}{4\pi N_V}}$$

Eq. II-4

II.III.4 Measurement of martensitic volume fraction

The amount of the martensitic phase susceptible to form during plastic deformation in either duplex or fully austenitic stainless steel has been measured in this work. There are several techniques to measure the volume fraction of martensite. In the current thesis, the evolution of the martensitic phase was measured after drawing (92% of deformation) and after different annealing conditions using a sigmameter. However, for determining the possible martensitic transformation during tensile test, synchrotron X-ray diffraction was used as we will explain in the next section of this chapter.

Sigmametry is a technique used to measure the amount of the magnetic phase (ferrite and martensite) present in the sample in question. The principle of this technique is based on measuring the specific saturation magnetization of a material σ_s. This parameter is measured using SERMAG 35-13 M device by introducing the sample in a uniform magnetic field H of 1.28 Tesla. Hence, the sample gains a magnetic moment M proportional to its mass m. The sample is then driven out from the magnetic field inducing by consequence an electromotive force proportional to the magnetic moment M. σ_s can be then deduced from the following formula:

$$\sigma_s = \frac{(R_i + R_a) \times \theta}{m \times a}$$

Eq. II-5

Where:
θ is the deviation registered by the galvanometer;
R_i is the internal resistance of the circuit (coil and galvanometer);
R_a is the adjusted additional resistance to correct the sensibility when the deviation θ becomes high;
m is the sample mass;
a is the calibration coefficient of the device.

The volume fraction of the magnetic phase is the ratio between σ_s and the magnetization of the magnetic phases σ_0 which can be calculated via the chemical composition of the sample using the following empirical relation:

$$\sigma_0 = 2.17 - (0.12\%C + 0026\%Mn + 0.33\%Ni + 0.0275\%Mo + 0.023\%Cu + 0.06\%V + 0.06\%V + 0.061\%Si)$$

Eq. II-6

II.IV Mechanical testing

II.IV.1 Microhardness

This technique is used to measure the local mechanical properties of a particular region of the material. For example, the softening kinetics of different phases in multi-scale composites can be followed using this technique. In our investigation, microhardness measurements have been performed using a BUEHLER apparatus. Sample preparation for this testing consisted in a mechanical polishing down to OPS finishing. For determination of softening kinetics, 10-15 indents are made on the transverse section of the sample. The applied load used during this work is 10g for the composites and 100g for the bulk wires. A verification test regarding the possible size effect between these two loads on the microhardness value has been made. It showed a slight difference of about 10HV as a function of the applied load, which is within the error bar of our measurements.

II.IV.2 Tensile test

A high capacity 3R-syntech testing machine from UGITECH Research Centre has been used for tensile testing at room temperature. An extensometer has been used for accurate strain measurement with a deformation rate fixed at $2.10^{-4}\ s^{-1}$. The recorded stress strain curves have been used to obtain the elastic limit and strain hardening behavior. All tensile tests have been realized on wires of 1.5 mm of diameter and 300 mm of length.

II.IV.3 In-situ tensile test by synchrotron X-ray diffraction

The aim of this experiment is firstly to determine the stress distribution in the different phases of our designed composites during in situ uniaxial tensile test at room temperature when applying increasing stress until failure. This technique allows also assessing a possible martensitic transformation induced by the plastic deformation during the tensile test.

II.IV.3.a Experimental setup

The experiment was performed at the ID15 beam line of the European Synchrotron Radiation Facility (High Energy X-ray Scattering) in Grenoble-France.

In the optical cabin, three Laue silicon monochromatic crystals are used to select three energy levels: 30, 60 and 90 keV. In the current study, the experiments were performed at an energy around 90 keV for all samples. A flat detector was used to collect the Debye-Scherrer rings. The detector is a Pixium and is part of the family of flat panel detectors developed and long used in medical imaging. These detectors consist of a phosphorous screen which is coupled to an amorphous silicon matrix. They exhibit excellent sensitivity for energies ranging from 30 to 100 keV and a good acquisition rate of 7 frames per second. The main characteristics of this detector are: a pixel size of 154 x 154 μm^2; an image size of 2480 x 1910 pixels. The acquisition time of a picture every four seconds was chosen for all our tests.

The tensile machine (with load sensor of 4.4 kN) is positioned on a moving table that can be translated in z direction, which allows focusing and analyzing always the same area in the center of the specimen during loading. For each acquisition a Debye Scherrer ring, the corresponding force and displacement provided by the tensile machine are recorded automatically. The strain rate was fixed at 2.10^{-4} s^{-1}. A schematic illustration of the experimental setup is shown in Figure II-9.

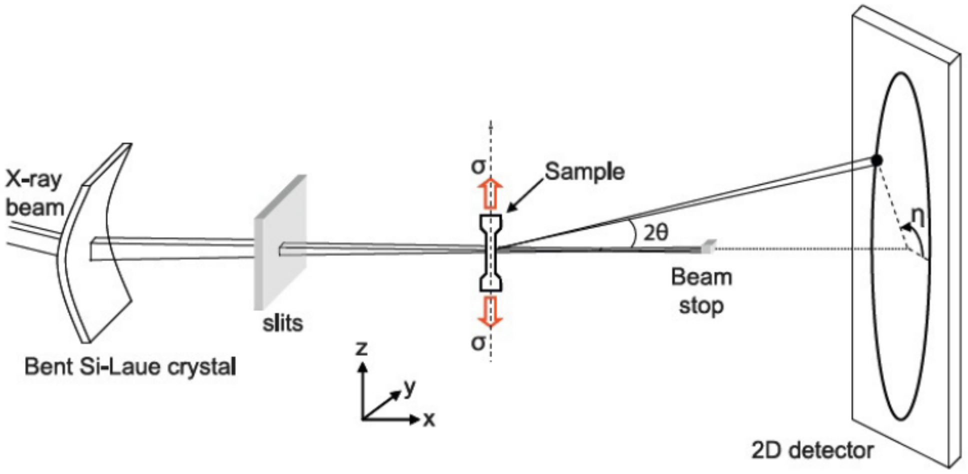

Figure II-9:Schematic representation of the High energy synchrotron X-ray diffraction setup for in-situ tensile test

II.IV.3.b Analysis of the diffraction data

i) Evaluation of phase fraction

In order to analyze the diffraction data, the wavelength of the incident radiation must be known accurately. To do so, the diffraction of a reference oxide cesium powder is used. Since the lattice parameter of this powder is known, it is possible to determine precisely the wavelength of the incident beam λ which is found to be 0.142273Å. The diffraction patterns obtained during the tensile tests were calibrated against this reference. A circular integration is then performed to obtain the conventional diffractograms showing the intensity (I) versus diffraction angle (2θ). The evolution of the phase's amount during deformation was inferred using Rietvield analysis via Fullprof software [Rodriguez 1993]. The present author would like to thank A. Lechartier for her help in using Fullprof software. Figure II-10 shows an example of the analyzed data for cesium oxide.

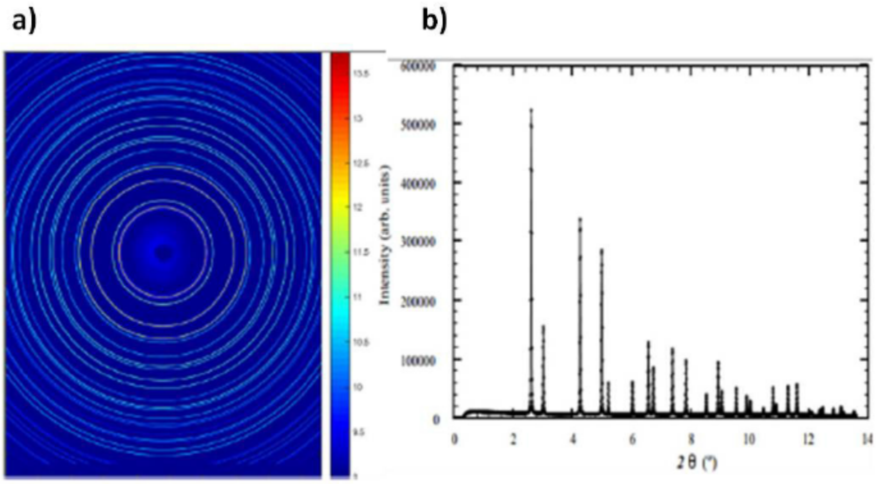

Figure II-10: Result of X-ray diffraction, example of cesium oxide. a) Diffraction pattern of Debye Sherrer b) Polar integration to obtain intensity as a function of Bragg angle

ii) ***Elastic strain measurement***

The principle of strain measurement is based on the change of the inter-planer spacing *(d)* of the chosen references planes during loading. In fact, the d-spacing of the planes can be used as a strain gauge. Indeed, by applying stress σ, a change in d-spacing is induced. This will shift by consequence the angle of the Bragg peaks as shown in Figure II-11.

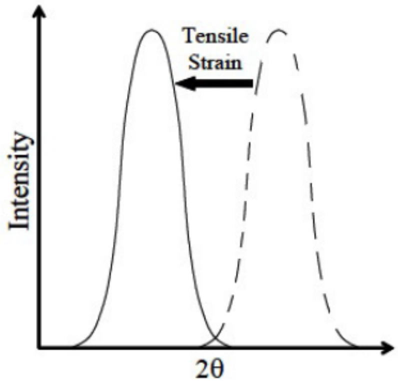

Figure II-11:Shift in Bragg position during tensile testing

This shift can be measured using Bragg law:

$$\lambda = 2d_{hkl}sin\theta \qquad \text{Eq. II-7}$$

Where λ is the wavelength of the incident beam, d_{hkl} is the interplaner spacing for hkl plane. On the other hand, the elastic strain for a give hkl plane (ε_{hkl}) can expressed by the following relation:

$$\varepsilon_{hkl} = \frac{d_{hkl} - d_{hkl}^{0}}{d_{hkl}^{0}} = \frac{sin\theta_{hkl}^{0}}{sin\theta_{hkl}} - 1 \qquad \text{Eq.II-8}$$

Where d_{hkl}^{0} (θ_{hkl}^{0}) represents the interplanar distance (Bragg position) of the plane hkl before loading.

In the unstrained material the diffraction rings are perfect concentric circles. In the deformed condition these circles bend, forming ellipses with semi-axes oriented parallel and perpendicular to the tensile direction; the major axis (a) of the ellipse and the minor axis (b) are parallel and perpendicular to the tensile direction respectively as shown in Figure II-12.a. Indeed, as represented in the work of [Young et al. 2007] the hkl planes parallel to the tensile direction correspond in fact to η=0°/180° (according to our configuration) and those perpendicular to the tensile direction correspond to 90°/270°. See Figure II-12.b. In addition, the wavelength of the high energy X-rays is considerably small and by consequence the Bragg angles of the corresponding planes are small. This implies that the inclination of these planes versus the tensile direction can be neglected (which is not the case for neutron diffraction). Hence, the simplest technique used to measure the elastic deformation from the deformation of the diffraction rings is the discretization of these rings into 8 portions of 45 °, Figure II-12.c, and then make the radial integration. The intensity of a Bragg reflection I_{hkl} is fitted by a Lorentzian function:

$$y(x) = y_0 + \frac{2A}{\pi}\frac{w}{4(x-x_0)^2 + w^2}$$

Eq. II-9

Where:

$y_0$the baseline offset

A total area under the curve from the baseline

x_0 center of the peak

w full width of the peak at half height

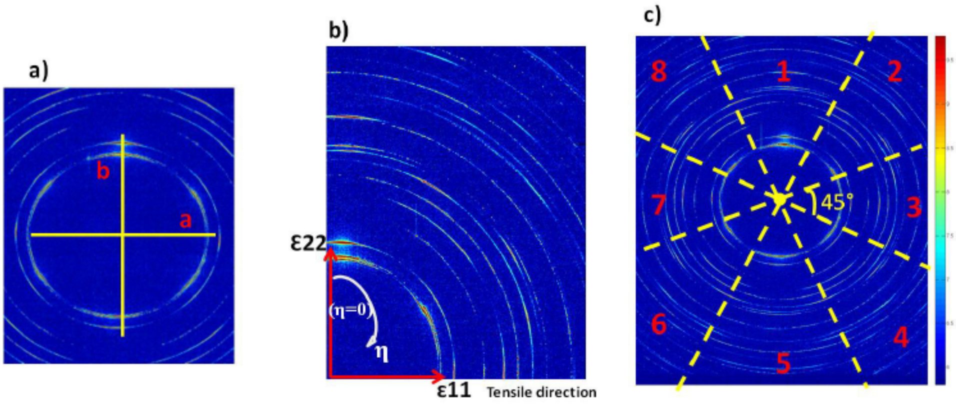

Figure II-12: a) The elliptic shape of thediffraction pattern after deformation b) quadrent of the diffraction pattern showing the tensile direction c) The discretization of the diffraction pattern

Figure II-13 shows an example of the fitted diffractogram using Lorentzian function for diffraction parallel (portion 3 and 7) and perpendicular (1 and 5) before loading. An algorithm was implemented using MATLAB language to fit and determine at each acquisition the position of the peak during plastic deformation. The present author would like to thank Frédéric De Gueser for his help in the implementation of this algorithm.

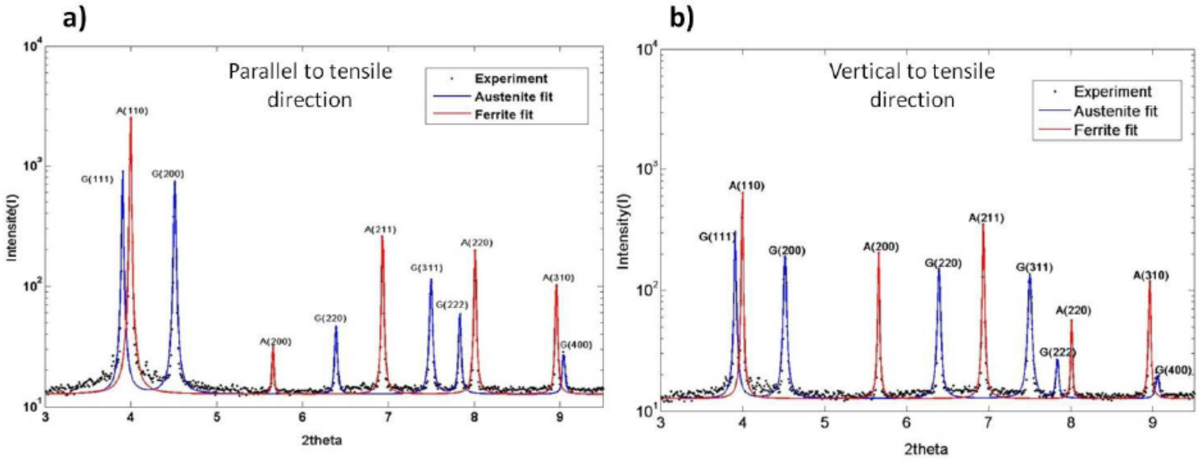

Figure II-13:Example of diffractogram before loading and after discretization a) parallel to tensile direction b) vertical to tensile direction

References

[Goldstein et al.1994]
Goldstein J. I., Romig A. D., Newbury D. E., Lyman C. E., Echlin P., Fiori C., Joy D. C., Lifshin E., Scanning electron microscopy and X-ray microanalysis, Second edition, Plenum Press, 1994, ISBN 0-306-44175-6.

[Máthis and Rauch 2007]
Máthis K. et Rauch E.F. (2007) MICROSTRUCTURAL CHARACTERIZATION OF A FINEGRAINED ULTRA LOW CARBON STEEL. Materials Science and Engineering: A, 462, 248‐52.

[Modin and Modin 2013]
Modin, H., & Modin, S., Metallurgical microscopy. Elsevier,2013.

[Potts 1987]
Potts, P.J., A Handbook of Silicate Rock Analysis. Chapman and Hall, New York,1987, (p. 336 and p. 37).

[Rao et al.2010]
Rao, D. S., Muraleedharan, K., & Humphreys, C. J., TEM specimen preparation techniques. Microscopy: Science, Technology, Aplications and Education, FORMATEX Research Center, Extremadura Es,2010, 1232-1244.

[Sallez 2014]
Sallez, N. (2014). Recrystallization, abnormal grain growth and ultrafine microstructure of ODS ferritic steels (Doctoral dissertation, Grenoble).

[Rauch and Véron 2014]
Rauch E.F. et Véron M. (2014) AUTOMATED CRYSTAL ORIENTATION AND PHASE MAPPING IN TEM. Materials Characterization, 98, 1‐9.

[Rodriguez 1993]
Rodriguez-Carvajal, J., FULLPROF 98. Program for Rietveld Pattern Matching Analysis of Powder Patterns, unspublished results, Grenoble, 1998.(b) Rodriguez-Carvajal, J. Physica B,1993, 55, 192.

[Young et al. 2007]
Young, M. L., Almer, J. D., Daymond, M. R., Haeffner, D. R., & Dunand, D. C., Load partitioning between ferrite and cementite during elasto-plastic deformation of an ultrahigh-carbon steel. Acta materialia, 2007, 55(6), 1999-2011.

III Manufacturing process: ADB

Contents

Introduction

Since the aim of this research is to develop a new architecture of duplex stainless steel wires by the **Accumulative Drawing and re-Bundling (ADB)** process, it was necessary to prepare the ground for the manufacturing process. It should be noted here that it is the first time to our knowledge that a duplex stainless steel is fabricated using this technique. Thus, our first concerns were the feasibility and the reproducibility of this process applied to our specific couple of materials. Controlling the process parameters is necessary not only to ensure its reproducibility but also to allow understanding in some way the resultant microstructure. Therefore, establishing the necessary know-how in this kind of manufacturing requires certain knowledge primarily related to:

- Assembling two metals at room temperature by severe plastic deformation. Achieving such "cold welding" requires solving bonding problems between the two constituents.
- Wire drawing for stainless steel which deals especially with process parameters such as lubrication, die, etc.

The first section of this chapter is devoted to the bonding problem in cold welding. This issue has been, and still is, the subject of a lot of research. The major investigations about this problem were performed on Cold Rolling Bonding (CRB) process. However, the outcomes of these investigations can be extended to other cold welding processes such as drawing or extrusion.

The second section presents a very brief literature review on wire drawing of stainless steel and the most important parameters for a successful wire drawing. This review focuses mainly on the PhD work of [Levrau,2006] which was realised in UGITECH Research Centre (CRU) using the same drawing machine (Marshall) that we will use for our composite manufacturing.

The third section will be devoted to the implementation of all this acquired knowledge into the establishment of a sound methodology of ADB process for our system. The resultant composite microstructures will be finally presented and discussed.

III.I General issues about cold welding for multi-metallic assemblies

One of the major issues of multi-metallic assemblies at room temperature is to find ways to create a metallurgical bonding only by pressure and plastic deformation. Numerous researchers since the late 1950s have tried to i) verify the feasibility of this process on some metallic materials; ii) study empirically the influence of various parameters governing bonding; iii) understand bonding mechanisms; iv) establish theoretical models to predict bonding initiation and quality (i.e. strength).

III.I.1 Main parameters affecting bonding

III.I.1.a Surface preparation

Surface preparation is one of the most determinant parameters for a successful adhesion between two metals. In fact, both plated surfaces must be clean from any oxide film or external contamination such as oil, grease or water vapour which can be considered as a physical obstacle for the cohesion between the two metals [Cave 1973], [Mohamed 1975], [Wright 1978]. Hence, numerous researchers [Wright 1978], [Clemensen 1986], [Rollason 1958], [Tylercote 1958], [Vaidyanath et al. 1960] and [Wadora 1963] have extensively investigated and discussed the influence of surface preparation on the quality of the metals adhesion. They classified surface preparation techniques into three categories:

- Chemical treatments [Vaidyanath et al. 1960], [Wadora 1963]:

It consists on using acids or solvent solutions which allows eliminating any grease from the metal surface. However, it was found that these solutions can be absorbed by the metal causing by consequence an inhibition of adhesion.

- Mechanical treatment [Wadora 1963]:

This method consists on brushing the metal surface with a steel brush. [Wadora 1963] found that a mechanical treatment is more efficient, in terms of adhesion quality, than a chemical treatment.

- Mixed treatment:

This category is a combination of the two former processes; chemical cleaning followed by brushing using steel brush. This technique showed a better adhesion quality [Cave 1973], [Cantalejos 1972], [Bay 1983 &1986].

Figure III-1 shows the effect of different methods of surface preparation on the bond strength of aluminium composites. It is interesting to notice that, in mixed treatment technique, the order of the combination has a significant influence on the bonding quality. Indeed, degreasing followed by scratch brushing give better bonding properties than the reversed procedure (i.e. scratch brushing followed by degreasing) while electropolished surfaces do not bond even with 80% of deformation.

It is important to notice that brushing does not only result in cleaning but also creates additional surface asperities, which promote a localized shear stress and also mechanical bonding. This shear stress causes an unavoidable rupture of the oxide films initiating the bonding of the two metals [Tylercote 1958].

Generally speaking, surface roughening by scratch brushing can improve the bonding quality, reduce the pressure needed to initiate bonding and give the highest bonding strength.

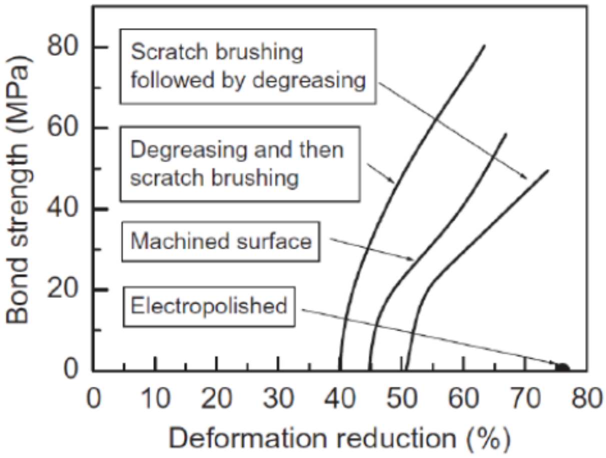

Figure III-1: Effect of different methods of surface preparation on bonding of aluminum composites [Vaidyanath et al. 1960]

III.I.1.b Deformation reduction

[Vaidyanath et al. 1959] are the first who studied the influence of the deformation reduction on the resistance of a welded joint made by cold assembling. Figure III-2 shows the relation between the ratio of reduction and the strength of different cold rolled assemblies [Vaidyanath et al. 1959, Milner 1960].

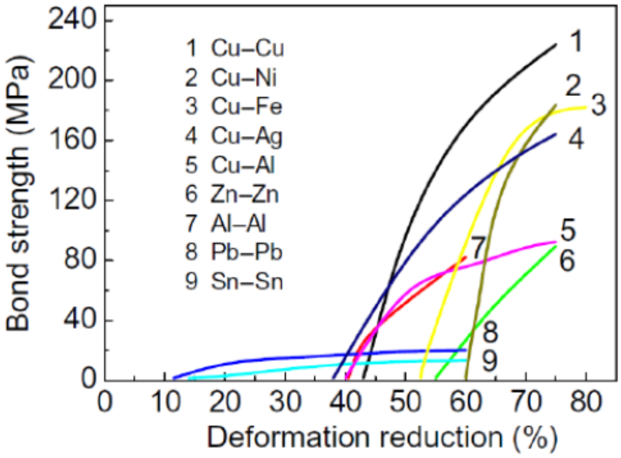

Figure III-2: Bond strength-Deformation reduction relationship for assemblies produced by cold rolling [Bay 1983]

Three important points can be concluded fromFigure III-2:

i) Bonding is not achieved until a certain threshold deformation reduction (R_t) is reached. Beyond this value the bond strength increases rapidly with deformation and then increases more slowly, corresponding to the strength of the weaker phase [McEwan et al. 1962].

ii) Bonding strength and threshold deformation (R_t) are highly dependent on the nature of the metals.

iii) It seems to be very difficult to obtain a very high bond strength even with high deformation reduction

Moreover, it is important to note that in order to initiate bonding, R_t must be reached in a single deformation step. Indeed, [Vaidyanath et al.1959] investigated one pass rolling and multi-pass rolling of aluminium and copper and evaluated the threshold deformation value allowing the initiation of metal bonding. They found that no bonding could be obtained if the first pass was not sufficient to initiate bonding.

III.I.1.c Metals' hardness

Metals' hardness can be also considered as one of the key parameters on bond initiation by pressure and plastic deformation at room temperature between two metals. Numerous researchers have studied the relationship between metal hardness and critical deformation for bonding R_t. [Tylercote 1958] was among the first who investigated the influence of pre-straining on metal bonding. He showed that increasing the metal hardness by pre-straining made small assembly-clip bonding easier. However, one year later [Vaidyanath 1959] investigated the effect of pre-straining on the bond strengths of copper and aluminium and found the opposite trend; increasing aluminium's initial hardness had no effect while increasing copper's initial hardness made bonding very difficult to initiate.

Figure III-3 shows the relationship between hardness and R_t of different metals pre-strained at different level and cold rolled with the same metal. In contrast, Figure III-4 shows the relationship between Rt and hardness ratio for different cold rolled copper coupled with another metal.

Thus, it was concluded that the results of [Tylercote 1958] were specific only for assembly-clip welding and can't be generalized to explain the mechanism of pressure welding. This was attributed to the alteration in the deformation pattern and/or the joint area [Vaidyanath 1959].

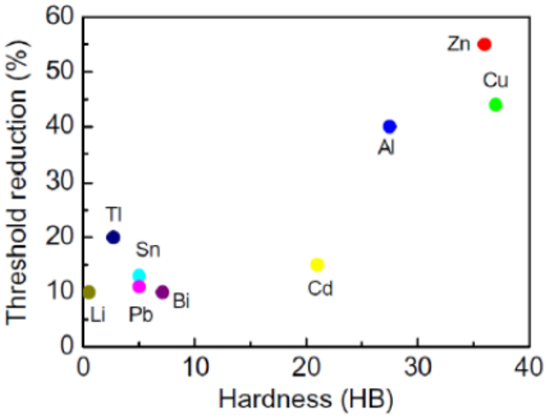

Figure III-3: Relation between threshold reduction and hardness for assemblies of the same metal [Long 2008]

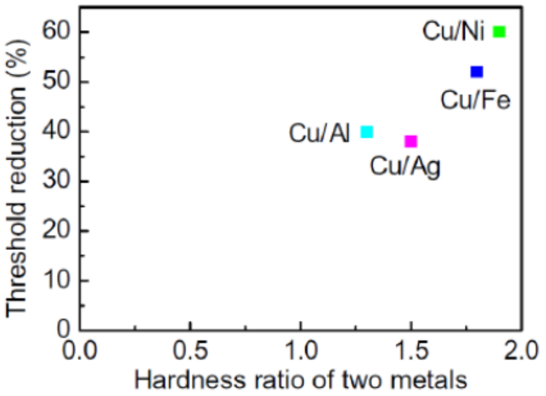

Figure III-4: Relationship between threshold reduction and hardness for assemblies of different metals [Long 2008]

III.I.1.d Annealing treatment

In general, cold rolling is followed by a heat treatment often called “consolidation heat treatment” which aims, in the first place, at enhancing the cohesion between the two plated metals. Naturally, the choice of time and temperature will depend on the metal’s properties.

Annealing treatment can enhance the adhesion between the plated metals not only after deformation but also before. Indeed, [Vaidyanath et al. 1959] again performed a test on aluminium sheets and showed that increasing the temperature of the Al-Al assemblies before rolling reduces the reduction deformation value (Rt) Figure III-5. In fact, [Vaidyanath et al. 1959] showed that annealing before rolling helps to eliminate any absorbed surface contaminations.

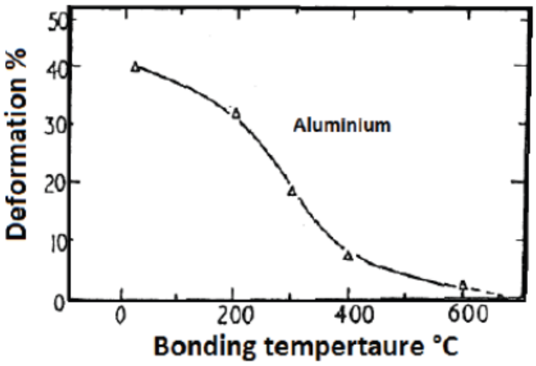

Figure III-5: Temprature influence on the threshold reduction deformation [Vaidyanath et al.1959]

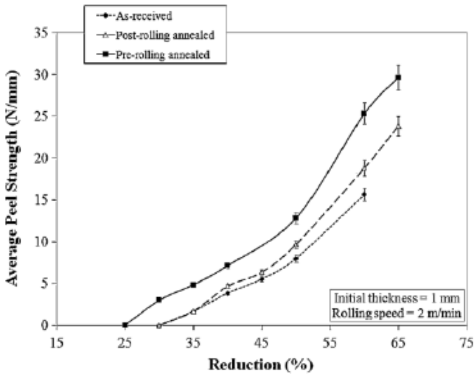

Figure III-6: Variaition in the average peel strength of aluminum versus reduction for as-recieved, pre- and post-rolling annealing [Jamaati 2010]

Recently, [Jamaati 2010] studied the effect of the heat treatment before rolling (pre-rolling annealing) and after rolling (post-rolling annealing) on the bond strength of Al-Al strips. Figure III-6 reveals that the effect of the annealing treatment on the bond strength is significantly higher when annealing is performed before rolling than after it, which was interpreted by the fact that annealing before rolling reduces the hardness and thereby increases the bond strength.

According to numerous researches, four mechanisms can explain the enhancement of the adhesion by heat treatment:

- The first mechanism is based on the concept of atomic transport by diffusion from both sides within the interface. New bonding regions between both metals are built up.
- The second mechanism, which is the most common among authors, is based on surface diffusion of atoms, similarly to the sintering mechanism.
- The third one consists on recrystallization and/or grain growth within the interface, which may form a new grain structure on both sides of the former interface. This mechanism helps and facilitates also the creation of a metallurgical bonding. However, special attention should be given for some parameters governing this mechanism such as time and temperature.
- The idea of the fourth mechanism is based on the dissolution of the oxide film in the metal by annealing. Indeed, oxide film plays an important role on the inhibition of a metallurgical bonding.

III.I.1.e Other parameters

[Li et al.2002] evaluated the possibility of two metals to be cold welded and found some correlation with the crystallographic structure. Their findings are classified in a diagram (see Figure III-7). Other parameters are more related to the manufacturing process itself. In the case of Cold Rolling Bonding (CRB) for example, authors have investigated the influence of rolling velocity, friction between rolls and metals, friction between the two metals, rolls diameter...etc.

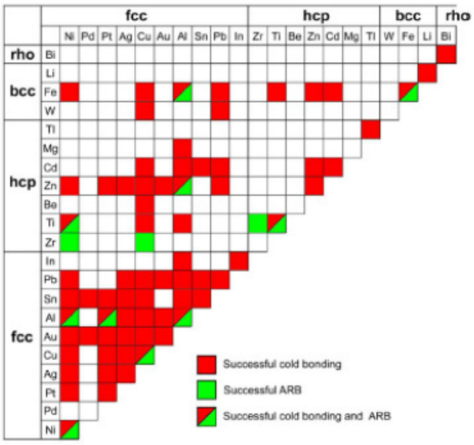

Figure III-7: Diagram showing the capacity of different metal couples to be cold welded [Long 2008]

III.I.2 Bonding mechanism and quality

III.I.2.a Mechanism

Having investigated the major parameters governing the bonding initiation and strength, researchers tried to establish a theory that explains the adhesion mechanism between two metals during cold rolling. Today, four theories have been proposed to explain this mechanism i) the film theory [Cave 1973] [Mohamed 1975] [Lukaschkin 1997] [Manesh 2004] ii) energy barrier theory [Cave 1973] [Mohamed 1975] iii) diffusion bonding theory [Mitani 1984] iv) recrystallization theory [Parks 1953]. These theories are based either on microstructural observations by optical microscopy and scanning electron microscopy (SEM) or numerical/analytical calculations. In this paragraph only the film theory, which is the most widespread, will be briefly presented.

The film theory was established for the first time for rolling by [Vaidyanath et al. 1959]. According to this theory, the pressure of the rolls causes the fragmentation of the micro strips (also called “tongues” by Vaidyanath) created on the metal’s surface during brushing. A so called “virgin surfaces” appear and enter into contact and the bonding is hence initiated. Tested on Al-Al, Cu-Cu, Pb-Pb and Zn-Zn the theory is based on the mechanism of fragmentation-extrusion-bonding, illustrated in Figure III-8. Indeed:

- Brushing with steel brush the metal’s surface will eliminate the oxide layer and contamination issued during chemical treatment and create in the same time a work-hardened surface (with almost 10 µm of thickness in the case of an aluminium sheet)
- The work-hardened layer, which is hard and relatively brittle, breaks up into “coherent fragments” under the pressure of the rolls.
- The fragmentation of this hard and fragile layer gives a “virgin” surface without any contamination or oxide, which makes the extrusion of the two metals easier. The adhesion of the two metals is then established.

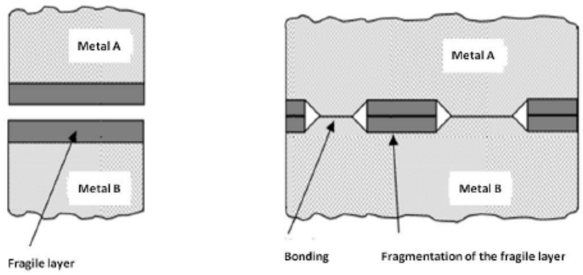

Before plating

After plating

Figure III-8: Schematic illustration for Vaidyanth’s bonding mechanism

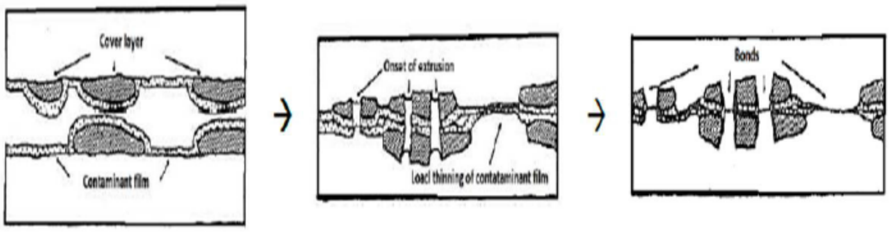

a) Fragmentation b) Extrusion c) Adhesion

Figure III-9:Schematic illustration for Bay's bonding mechanism

[Bay 1983] gathered all previous work on this theory especially the work of [Vaidyanath et al.1959] and proposed a more enhanced model. Unlike [Vaidyanath et al. 1959], Bay showed that brushing results in brittle and localized “tongues” on the metal surface and not a “coherent layer”. While plating, three different regions can be distinguished: i) zone without strips ii) zone with only one strip iii) zone with superimposed strips. The mechanism proposed by Bay can be summarized in two points:

- In regions with strips, when the threshold deformation is reached, the hard strips break up giving a “clean and virgin” surface. Under pressure the extrusion is established between these new surfaces.
- Concerning the region without strips, when the threshold deformation is achieved, the contamination film, rich in oxide and water vapour, fractures. Thanks to roll’s pressure, the adhesion with underlying surface is built up.

Bay’s model is considered as the most complete theory providing a realistic description of the bonding initiation during cold rolling.

III.I.2.b Bond quality: prediction models

When adopting the film theory, many authors tried to give a mathematical description of the bonding mechanism and in particular a strength prediction. The first mathematical model was proposed by [Vaidyanath et al. 1959]. Based on several assumptions, he wrote the adhesion strength σ_{adh} as follows:

$$\frac{\sigma_B}{\sigma_{adh}} = R_f(2 - R_f) \tag{Eq. III-1}$$

Where σ_B is the bond strength, σ_0 is the strength of the base metal, assuming that it is the same on the two sides of the bond, and R_f is the final reduction at the end of the rolling pass.

[Wright, 1978] proposed another model by introducing the threshold reduction deformation of Vaidyanath’s Model. The bonding strength can be then written:

$$\frac{\sigma_B}{\sigma_0} = H\left(1 - \frac{\left(1 - R_f\right)^2}{(1 - R_t)^2}\right)$$ Eq. III-2

Where H is an empirical hardening factor and R_t is the threshold reduction deformation.
In contrast, Bay proposed a theoretical model based on a probabilistic approach. Indeed, he defines the probability to produce the extrusion mechanism by strips fragmentation by the parameter $(1-\beta)$. If we define φ as the fraction of the film layer with respect to the total area, the parameter β which is the probability of non occurrence of extrusion-bonding mechanism can be written as follows: $\beta = \varphi^2$. Bay's model is then written:

$$\frac{\sigma_B}{\sigma_0} = (1-\beta)Y\frac{p - p_E}{\sigma_0} + \beta\frac{Y - Y'}{1 - Y'}\frac{p}{\sigma_0}$$ Éq. III-3

Where Y is the surface reduction of the bond area surface, p the normal pressure on base metal surfaces, p_E the extrusion pressure necessary to break the fragile layer (see the paragraph above) and Y' is the threshold surface reduction for the contaminant film.

III.II Wire drawing

III.II.1 Deformation by wire drawing

Wire drawing is, primarily, a forming technique consisting on applying a section reduction to a bar/wire by plastic deformation, by pulling it through a special metallic tool called die (Figure III-10). Repeating this operation several times with different die diameters, wires with very small section (less than one millimetre) are obtained.

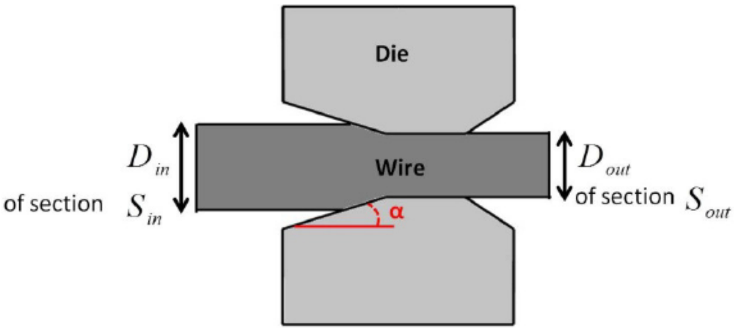

Figure III-10: schematic illustration for a one pass of wire drawing

As explained in chapter 1, this process can also be used as an assembling technique in case of two metals forming. In this case, the matrix and the reinforcement must follow the "three for one" rule; i.e. the ratio between their flow stress must be less than 3 [Russell 2000]. When this ratio is larger than 3, the harder phase deforms only elastically while the softest phase continue deforming plastically around the hardest one causing then a premature fracture. Applying this rule to the case of austenite/ferrite system, the ratio obtained is in favour of co-deforming without any premature fracture.

For both cases of drawing single-phase or dual-phase wires, wire elongation and deformation ratio can be written after using the volume conservation constraint between the input and the output of the die, respectively as following:

$$S_{in}.L_{in} = S_{out}.L_{out} \rightarrow \lambda = \frac{L_{out}}{L_{in}} = \left(\frac{D_{in}}{D_{out}}\right)^{2} \qquad \text{Éq. III-4}$$

$$\eta = ln\lambda = 2\ln\left(\frac{D_{in}}{D_{out}}\right) \qquad \text{Éq. III-5}$$

Where η is the true deformation, λ is the wire elongation and $S_{in(out)}, L_{in(out)}, D_{in(out)}$ are respectively, the input (output) wires section, length and diameter.

Generally, wire drawing cannot be realized without the following three conditions:

- ✓ Wire: it should have the adequate characteristics in terms of mechanical properties (plastic deformability) and undergo some surface preparations to ensure the drawability.
- ✓ Die: is the element that ensures the section reduction.
- ✓ Lubricant: is the most important element in drawing which play the role of a third body between wire and die, thus facilitating the deformation and the whole process.

III.II.2 Key parameters for a successful drawing

A successful drawing will depend on the quality of its three elements which are wire, die and lubrication. However, the latter is the most important for achieving a successful drawing process. Several works, especially the work of [Felder et al. 2011] and [Levrau 2005], showed that the quality of lubrication will depend, in turn, on parameters related to i) the process (wire and die) ii) the type and the quality of the lubricant itself. The work of [Levrau 2005] has been performed using the Marshal drawing machine at Ugitech Research Centre, which is the same one that we will use to elaborate our composite in this work. Similarly to what has been used in her study, the lubrication used in our manufacturing process is solid lubrication by soap.

III.II.2.a Surface preparation

Dry lubricants such as soap are difficult to stick, during drawing, on the wire surface, especially in case of wires with low surface roughness. It is therefore necessary to deposit a support layer on the surface for the lubricant. This coating will also ensure the protection of the wire surface from any kind of wear or seizing caused by bad lubrication. However, the efficiency and the nature of this deposit will depend on the metal; for example for stainless steel wires, it was found, by [Montmitonnet 1983] and [Meignan 1990], that salt deposits is considered as the most efficient.

The influence of the coating by salts on the quality of lubrication, investigated by [Levrau, 2006] can be measured by the weight of the residual soaps film on the wire surface after drawing. Indeed, the more the wire surface contains residual soap at the end of the drawing operation, the more efficient is the lubrication. In this study, the test was performed on wire of 5.5 mm in diameter drawn down to 4.6 mm with and without salt coating. The salt coating was realised by immersing the wires in a hot bath of $K_2\,SO_4$. Two kinds of soaps, XNa80 and XCa35, were used as lubricants. The result showed that the weight of the residual soap on the surface of the coated wire is significantly higher than the non-coated wire as shown in Figure III-11.

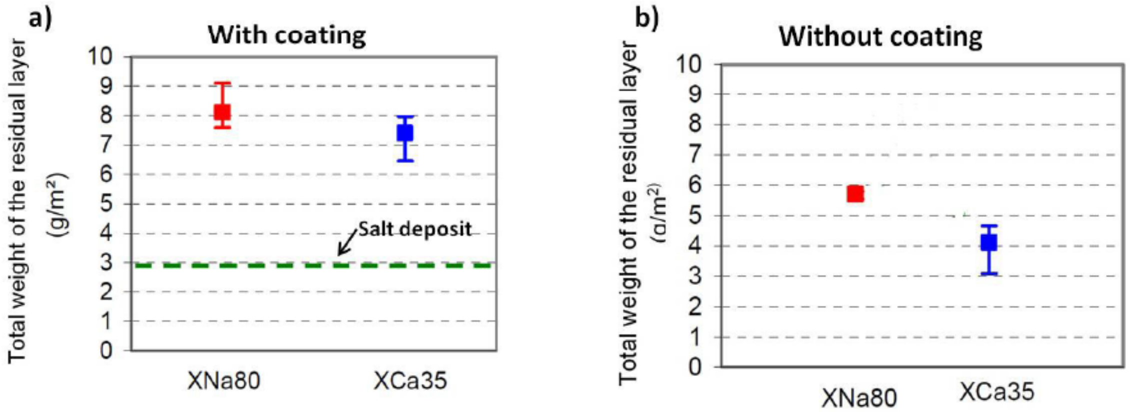

Figure III-11: Influence of the coating on the weight of the residual layer a) with coating b) without coating [Levrau 2005]

The initial surface roughness of the wire also plays a determinant role in enhancing lubrication quality. It is established that the thickness of the residual film increases proportionally with the initial roughness [Dolzhanskiy 2001] [Brison 1978]. This is due to the fact that the surface cavities act like lubricant reservoirs. This trend was also confirmed in [Levrau 2006]'s work on austenitic stainless steel.

III.II.2.b Die angle

Die angle can play a role in the success of wire drawing in two ways; it can influence the metal flow during section reduction and the lubrication process. For the first effect, four flow patterns can be distinguished, which can occur during wire drawing as a function of die angle (see Figure III-12) [Avitzure 1983]:

i) Sound flow: it is the ideal flow configuration
ii) Dead-zone: occurs when the wire shears and develops a dead-metal zone no longer taking part in the flow, which sticks to the die
iii) Shaving: occurs when the material starts to move backward and peel off
iv) Central bursting: it is an internal defect that occurs when the flow field becomes un-steady inside the metal. The internal defects can be in form of "V" cavities. In case of bi-phase drawing, central bursting may cause fracture of matrix/or reinforcement.

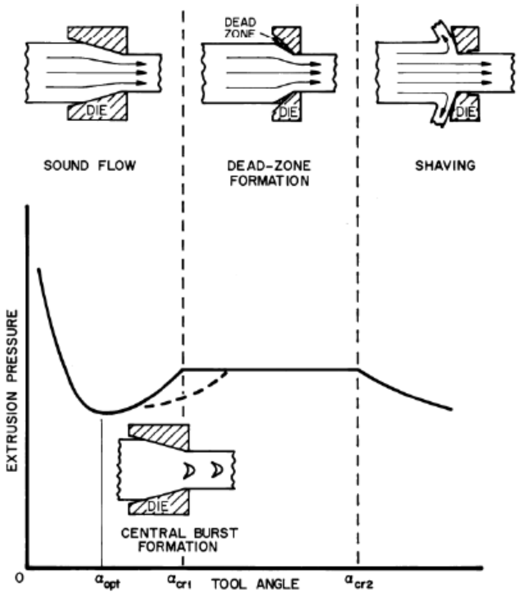

Figure III-12: Influence of the die angle on the pattern flow [Avitzure 1983]

In the region where neither external nor internal defects occur, [Levrau 2006] investigated the influence of the die angle on the lubrication quality. An austenitic stainless steel (304) has been drawn from 2.2 mm down to 1.85 mm of diameter using three different soaps with a die of α=5° and α=8°. The results showed that decreasing the die angle causes an increase of the weight of the residual layer for two sodium soaps content and calcium soap as shown in Figure III-13.

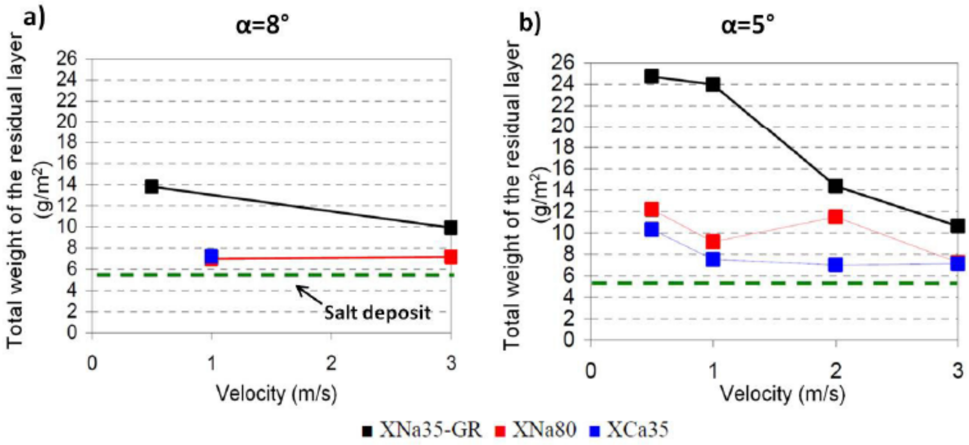

Figure III-13: Influence of the die angle on the weight of the residual layer a) α=8° b) α=5° [Levrau 2005]

III.II.2.c Wire properties

Wire hardness has a direct influence on the lubrication and lubrication quality. Indeed, according to the basic concepts of hydrodynamic lubrication, the effect of the metal's flow stress on the lubricant thickness depends on the rheological properties of the lubricant [Montmitonet, 2002]; lubricant thickness is inversely proportional to the wire's flow stress if the consistency coefficient (in fluid mechanics this coefficient is defined as the viscosity at a shear stress rate of $1s^{-1}$) is independent of pressure.

In order to study the influence of yield stress on lubrication quality, [Levrau 2006] tested two grades of austenitic stainless steel; 304 ($\sigma_{0.2}$ =250 MPa) and 301 ($\sigma_{0.2}$ =400 MPa). Figure III-14 shows that as $\sigma_{0.2}$ increases, the weight of the residual layer decreases for both soaps. One can note that the XNa80 soap is much less sensitive to the increase of $\sigma_{0.2}$ as compared to XCa35, this difference is attributed to their different rheological properties [Felder et al. 2011].

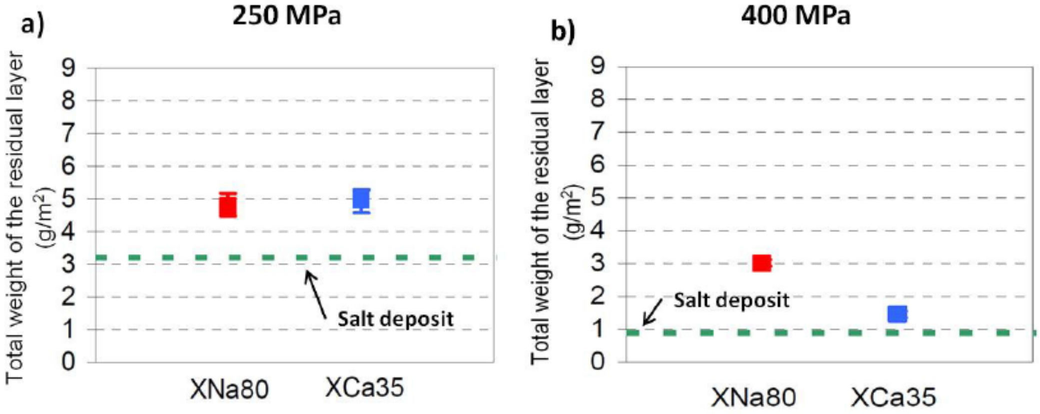

Figure III-14: Influence of wire's hardness on the weight of the residual layer a) yield strength=250MPa b) yield strength=400MPa [Levrau 2005]

III.III Implementation of the ADB process for γ-α system

III.III.1 Manufacturing steps

III.III.1.a Materials

Steels of types 430LNb and 316L whose chemical compositions are detailed in Table II-1, representing respectively the ferritic and the austenitic phases, were chosen for the present work. These two grades have been well-characterized in the literature. In fact, this choice is based on two criteria:

i) Stability: our first concern was to avoid any complexity during manufacturing which could arise due to phase transformation, particularly the strain-induced martensite in the austenitic phase. Indeed, having a phase transformation will make drawing and other manufacturing steps (such as heat treatment) more complicated. On the other hand, we seek to design a model material in which only architecture, volume fraction and scale are allowed to be variable.

ii) The availability: these two types are widely used and can be found easily in construction stainless steel market. This will help us to save time in manufacturing since the ADB process itself is time consuming.

In the 316L grade, [Spencer 2004] showed that the kinetics of the martensite transformation during plastic straining is slow due to its high nickel content. He showed that it is possible to deform 316L at room temperature to large strains without forming any martensite which is also confirmed by our experiments in chapter IV and V. Regarding the stability of 430LNb, it is ensured thanks to the Nb content which prevents a phase transformation α→γ during heat-treatment. In fact, when all carbon and nitrogen in the melt are combined with niobium, the excess quantity of Nb forms high stability Nb(C,N) precipitates. The indicator of the stabilization degree is given by the stoichiometric formula [Mantel et al 1990]: $\Delta Nb = w_{Nb} - 7.66 w_C - 6.57 w_N$.

The as-received wires have been subjected to thermo-mechanical treatments in order to adjust them to the configuration of our composites (see in next paragraph). A 316L wire of 1.8 mm and 430LNb of 2.2mm of diameter were drawn down to 1.5 mm followed by annealing at 1050°C and 900°C respectively for 10 minutes.

The mechanical response of these treated wires is shown in Figure III-15. These two wires will be designated in the present work as the **initial-state**.

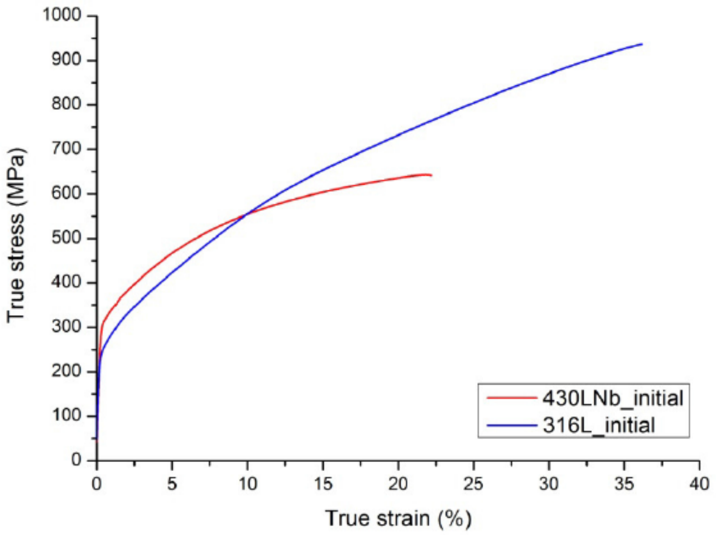

Figure III-15:Tensile behavior of grade 430LNb and 316L used in this work

III.III.1.b Methodology

Architectured Duplex Stainless Steel (ADSS) wires are fabricated starting from individual wires of ferrite 430 LNb and austenite 316L, 1.55 mm in diameter, gathered in a containing tube of 430LNb or 316L, 6 mm in external diameter and 0.4 mm in thickness. The fabrication will proceed with the following successive steps (see Figure III-16):

0) Configuring the first composite starting from individual wires and tube. This composite will constitute the elementary pattern of the following composites structure. The fabrication of this composite will be discussed in the next paragraph.
1) Wire drawing: operation in which the (re-)bundled composite is reduced from φ=6 mm to φ=1,5 mm through 14 steps
2) Annealing: this is one of the most important steps of the manufacturing process. It consists on heat-treating the drawn composite in order to recover the mechanical properties by softening and to recover a capacity of plastic deformation, which allows further drawing.
3) Re-bundling the annealed wire in a containing tube of ferrite or austenite.

The concept of ADB process is based on the repetition of step 1, 2 and 3. However, some intermediate operations are necessary for ensuring the reproducibility of the process and to produce the desired composite without any defects. Some of these operations are inspired from the work realized by [Levrau 2006] in particular surface preparation, coating and lubrication. Other operation such as heat treatment is a subject of investigation in the present work.

Before bundling: the tube is coated by immersing it in a hot bath of potassium sulphate (K_2SO_4) salt serving as a film support for lubrication whereas the wires are cleaned and degreased using an acetone bath to eliminate any surface contamination.

After drawing through 14 steps: the wire's surface is covered by a residual layer of coating and lubricant in the form of powder (soaps). Before introducing the wire into a furnace for heat softening, it is necessary to remove this layer by pickling in a hot bath of phosphoric acid (H_3PO_4).

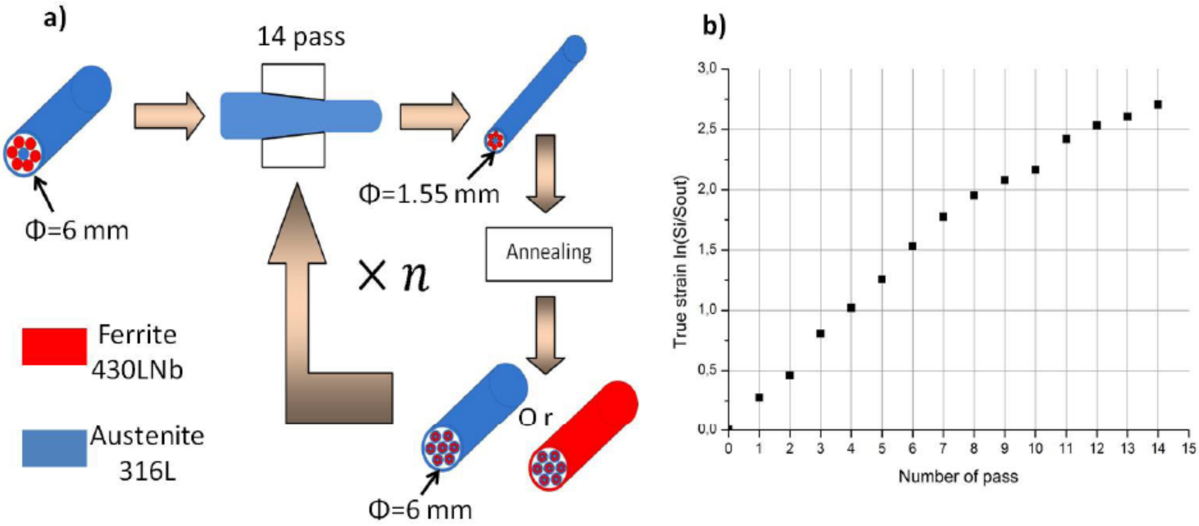

Figure III-16 : a) Schematic illustration of the ADB process b) Evolution of the true deformation in function of the step number where S_i is the global input section and S_{out} is the global output section

Annealing: the wire is then heat treated in a vacuum furnace, using a heating rate of 70°C/hour, which allows avoiding any kind of oxidation whether external i.e. on the composite surface or internal i.e. inside the composite particularly between the constituent wires. The choice of the annealing parameters will be the subject of the next paragraph.

After annealing: despite the use of a vacuum furnace, some localized surface oxidation was observed. As mentioned above, before bundling, the wire should be cleaned and degreased. In case of an oxidized wire, an operation of pickling with a hot bath of hydrochloric acid (HCl) is necessary.

III.III.1.c Fabrication of the elementary pattern: First composite n1

In the last paragraph, the general methodology and the roadmap of how we will proceed in our manufacturing process were presented. Nonetheless, the fabrication of the first composite through which the annealing parameters are determined, needs to be briefly detailed.

i) As-drawn state

The first composite consisted in 6 wires of ferrite 430LNb surrounding one wire of austenite 316L, these 7 wires being inserted inside an austenite tube as shown in Figure III-17. As this is the first step, the austenite and ferrite wires do not need a pickling operation. Only a degreasing operation was necessary. The wires are inserted manually into the tube shown in Figure III-18. It is very important to keep every wire in its place to i) avoid any change of the initial configuration ii) keep wires parallel with each other inside the tube avoiding any junction point between wires.

Figure III-17: Configuration of the first composite

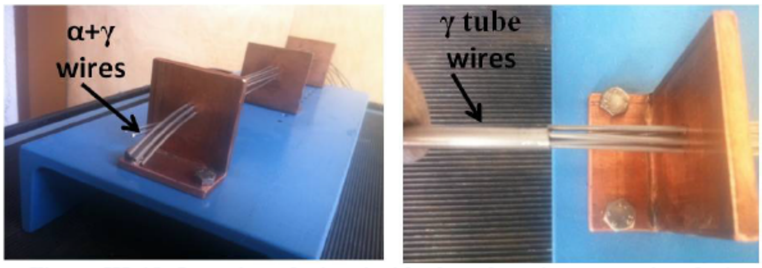

Figure III-18: Insertion of wires inside the tube using a centring devise

Figure III-19 shows the resultant microstructure of the first composite (n1) in the as-drawn state i.e. after drawing without heat treatment. One can notice the change in the shape of wires inside the austenitic tube. Ferrite wires, which are in dark grey, take semi-trapezoidal shapes whereas the austenitic wire in the centre has a semi-hexagonal shape. Moreover, one can distinguish easily the presence of black lines in form of “cracks” representing, in fact, the geometrical interface of components which are not completely adhesive.

Table III-1 shows the dimension of each component before drawing and after drawing as well as the corresponding hardness. Indeed, after almost 92% of section reduction the dimension of wires and tube is divided by almost 3.1 and the hardness increases significantly; from 200 HV to 450 HV for austenite and from 158 HV to 300 HV for ferrite.

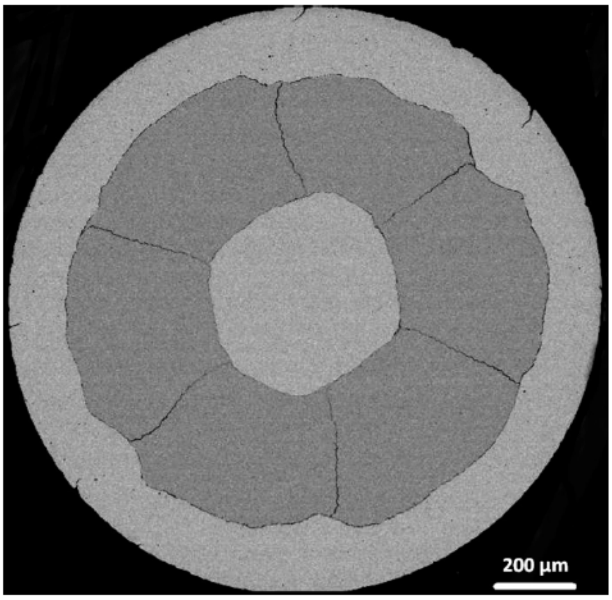

Figure III-19: SEM image in BSE of the microstructure of n1 composite in the work-hardened state (Ferrite: dark grey, Austenite: clear grey)

Table III-1: Comparison between the initial bulk wires and those after drawing

Component		**Initial state Bulk materials**	**Composite n1 As-drawn state**	**Reduction factor**
Ferrite wire	Average Equivalent diameter (µm)	1550	480	3.23
	Hardness (HV)	156	300	
Austenite wire	Equivalent diameter (µm)	1550	501	3.1
	Hardness (HV)	190	450	
Austenite tube	Average Thickness (µm)	400	158	2.5
	Hardness(HV)	200	455	

ii) Annealed state

As presented above, in order to continue the process and the co-deformation, the composite needs to be annealed to gain enough ductility. For n1 composite, we chose 1050°C as annealing temperature with a holding time of 10 minutes in the vacuum furnace using a heating rate of 70°C/hour. Figure III-20 shows the tensile curve of the n1 composite before and after annealing at 1050°C. One can notice that the composite before annealing presents no ductility and its yield strength coincides with its ultimate strength. After annealing, the n1 composite gains a good elongation of 35 %, which seems enough for starting the next step by re-bundling it into ferrite/austenite tube to manufacture the n2 composite.

The microstructure of the n1 annealed composite (Figure III-21.a) shows a significant change compared to the as-drawn state. First, the “crack” lines representing the components geometrical interfaces are locally “welded”. Indeed, Figure 21.b, which zooms on the interface of three wires (ferrite/ferrite wire and ferrite/austenite wire) reveals a partial adhesion between wires interrupted by porosities showing as black points. These porosities mark in fact the place of the older geometrical interface. Secondly, Figure III-21.b also reveals a regression of the austenite phase, shown by the progress of the ferrite towards the austenite from the porosity line. The width of this regression region is between 2-3µm. This regression region is in fact mainly attributed to the inter-diffusion of nickel as shown in Figure III-21.c.

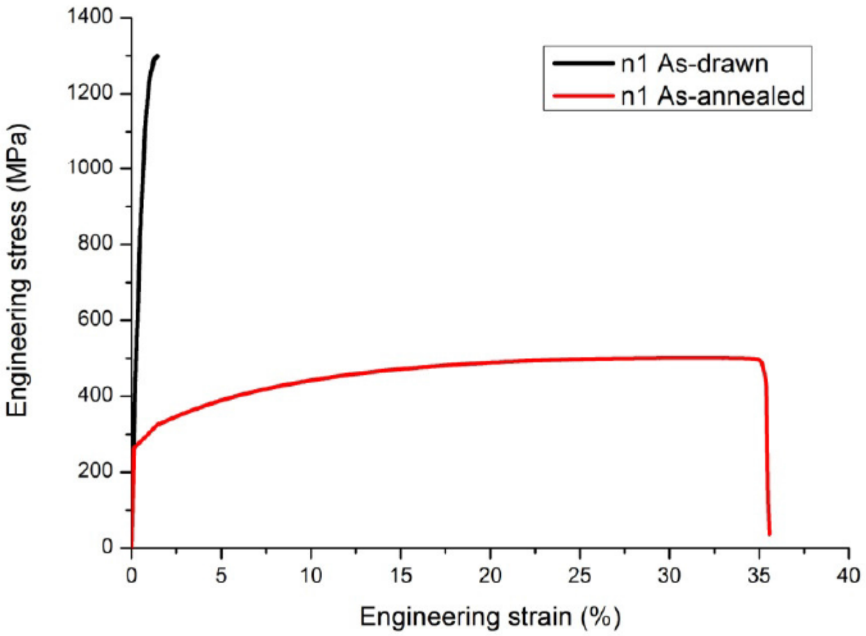

Figure III-20: Tensile curves of n1 composite before and after annealing

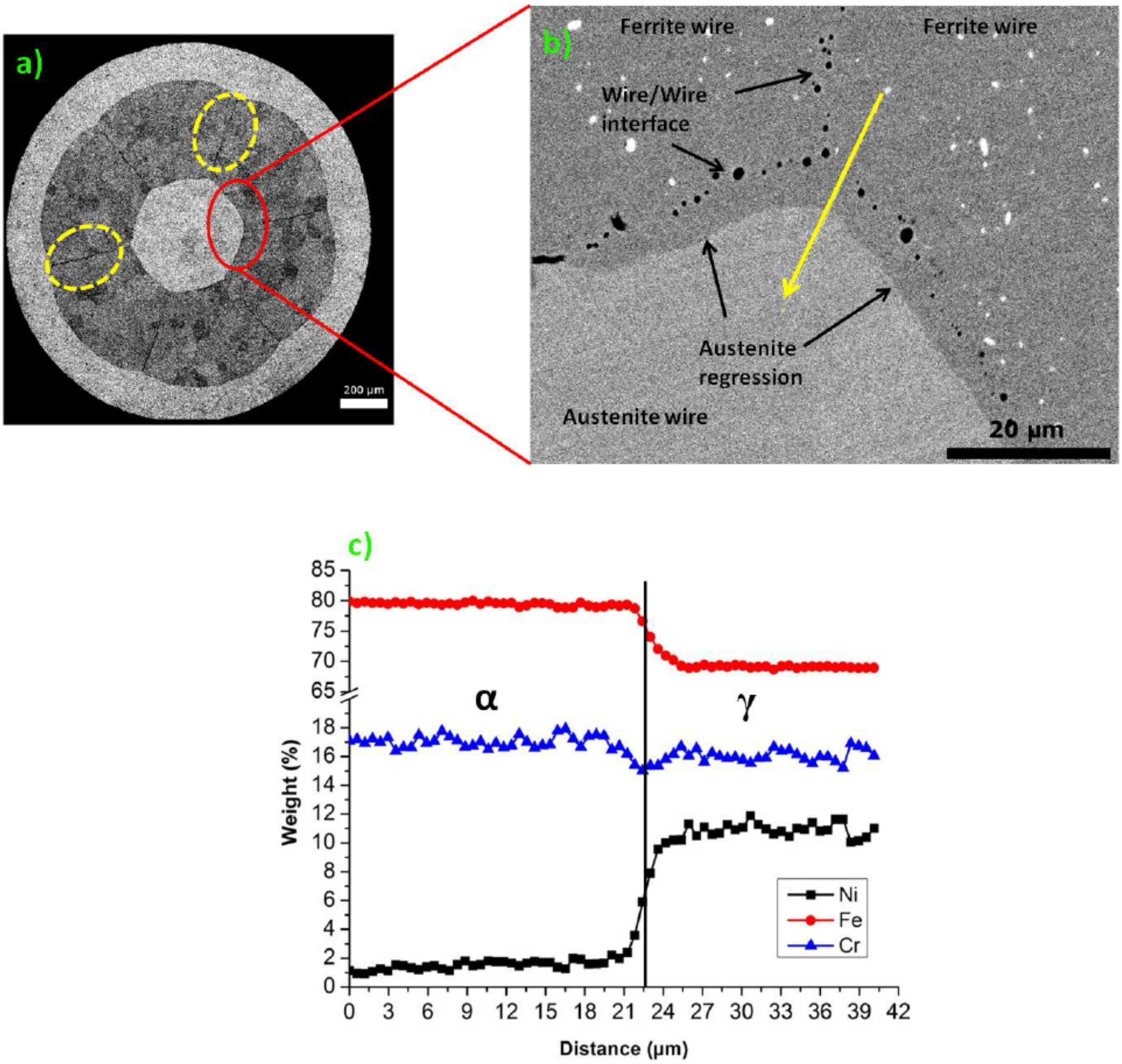

Figure III-21:a) SEM image in BSE of the microstructure of n1 composite after annealing at 1050°C for 10 min holding time; the dashed circles indicates the unbounded interfaces; b) a magnification on the wires interface showing the austenite regression; the arrow indicates the direction in which the EDS analysis profile of c) was performed; c) EDS analysis showing the evolution of Fe, Cr, Ni weight percentage as a function of distance to the interface (marked by the vertical line).

iii) Problem position

Although the chosen annealing parameters (1050°C for 10 minutes as a holding time) provide a sufficient ductility to continue the process, the induced austenite regression cannot be neglected and needs to be minimized. Indeed, allowing such regression will prevent us of obtaining a refined microstructure with micro or sub-micro (<1µm) domains of austenite. It is thus necessary, before launching our repeated processing of composite drawing, to determine the annealing parameters through which the regression is minimized and the ductility is sufficiently maximized to continue the co-deformation process. These two demands are contradictory because the first requires a decrease of temperature and/or time and the latter requires an increase of temperature and/or time, so that an optimization investigation needs to be performed to find the best parameters for our application. This will be the subject of the next section.

III.III.1.d Optimization of process parameters

i) Annealing parameters

The optimization study has been performed on the n1 composite by testing different temperatures ranging from 700°C to 1100°C for holding times of 30 minutes and 1 hour. The annealing treatment was realized in the same furnace used above (i.e. vacuum furnace with 70°C/hour as a heating rate).

> *Notice: The most practical way to determine qualitatively the ductility capacity is by measuring locally ferrite's and austenite's hardness.*
> *Concerning the diffusion measurements of Ni (the element responsible of austenite regression), EDX measurements showed inaccurate results due to the fact that the n1 microstructure presents a lot of interfacial decohesion between the ferrite and austenite components. With this lack of intimate contact, the diffusion does not necessarily take place. Therefore only microhardness results will be presented here which seems to be enough for our purpose.*

An initial hardness value, of at most 220 HV, was fixed for both phases beyond which it is estimated to be very difficult to draw the composite down to 1.55mm. This limit has been empirically fixed after several tests of drawability; i.e. the ability of composite to be drawn down to 92% of section reduction without any premature rupture or an intermediate softening annealing, for different hardness values.
Moreover, it is worth mentioning that drawing process, particularly the case of multi-wires assembly, depends on many interdependent parameters. This makes the process complex and very time consuming; 4 to 6 weeks are needed to manufacture one generation of composite. These reasons lead us to a more conservative choice of acceptable hardness limit to avoid any wires damage during manufacturing and materials losing.

Figure III-22.a and Figure III-22.b show the hardness evolution as a function of temperature for austenite and ferrite inside n1 composite after 30 minutes and 1 hour of holding time, respectively. One can notice that ferrite is the softest phase not only in work-hardened state but also in annealed state for all temperatures ranging from 700°C to 950°C (for 1h as holding time) and from 800°C to 950°C (in case of 30 minutes as a holding time). However, at temperatures 950°C and 1050°C the austenite and the ferrite have almost the same hardness.

After annealing, the hardness value of ferrite, for both holding times (30 minutes and 1h), is always below the pre-fixed hardness value i.e. in the acceptable region whereas the austenite shows a different behaviour. Indeed, in the case of 30 minutes of holding time, only materials annealed at 950°C and 1050°C show an acceptable hardness. However these two temperatures are considered relatively high in terms of inter-diffusion. After one hour of annealing, one can notice from Figure III-22.b that at 850 °C an acceptable hardness is obtained unlike annealing for 30 minutes. Annealing at 850°C for one hour as a holding time seems to be then the best compromise.

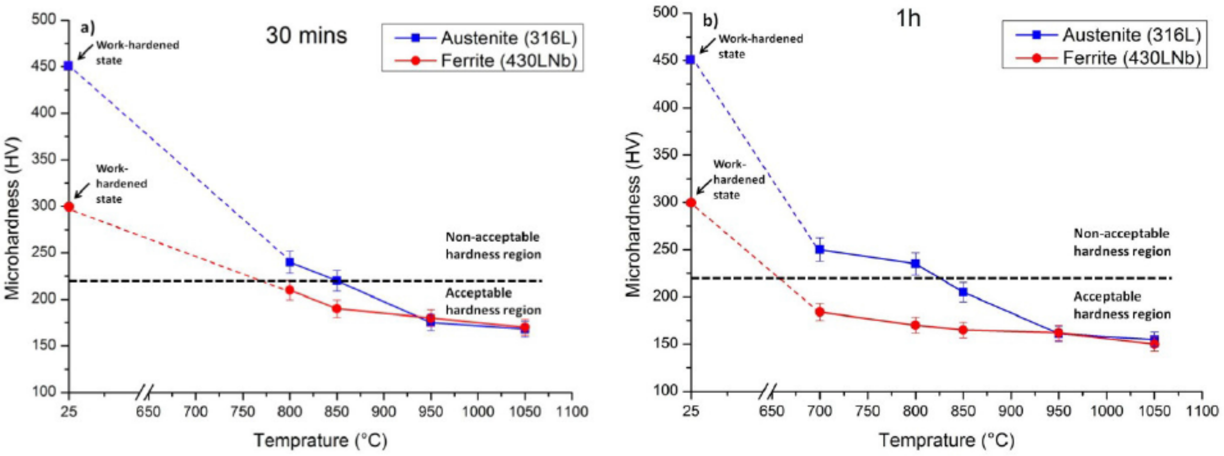

Figure III-22: Microhardness evolution as a function of temperature a) 30 minutes of holding time b) one hour of holding time

ii) Lubrication

The lubrication was also optimized. [Levrau 2006] (See section III.II.2.c) showed that some lubricants are sensitive to wire hardness. Hence, one can deduce that for a multi-pass process lubricant should be changed as the wire hardness increases. In our case, we found that the calcium soap XCa35 is more suitable for the first 5 drawing steps whereas the sodium soap XNa80 shows a good efficiency for the steps from 5 to 14.

III.III.2 Resultant microstructure

III.III.2.a 1st architecture

The first architecture results from re-bundling the produced composite, after annealing it, in only an austenitic tube. Figure III-23 and Figure III-24 show the microstructure of composite n2, which is obtained by re-bundling 7 wires of n1 composite annealed at 1050°C in an austenitic tube, before and after annealing. Before annealing, the microstructure reveals the absence of bonding, between n1 wires themselves and between n1 wires and the austenitic tube, which is represented by the "corrugated" black lines. However, n1's components (i.e. ferrite wires, austenite wire+tube) show a good adhesion despite some local decohesion. After annealing, the bonding between n1 wires is locally enhanced as Figure III-24 shows, or else the microstructure is, generally, quite similar to the one before annealing.

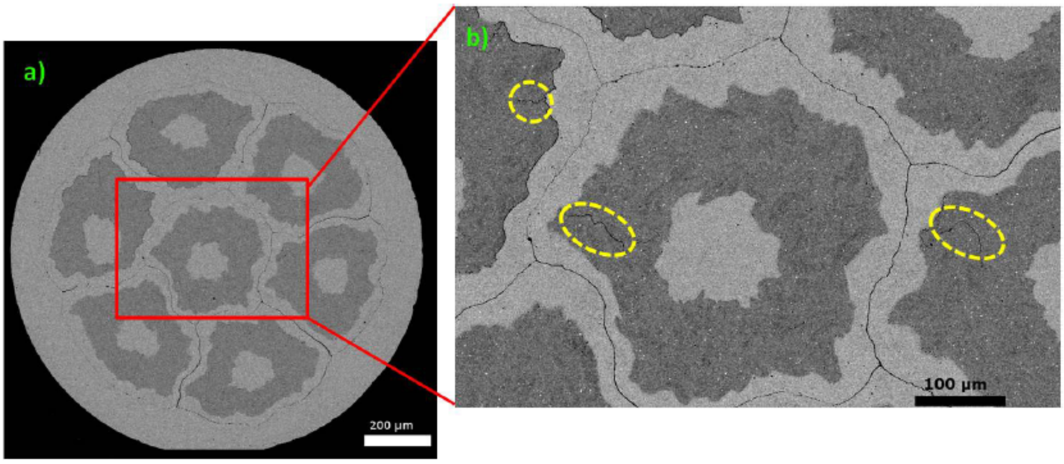

Figure III-23: a) n2 composite at as-drawn state b) detail of the n1 cell inside n2 (dashed circles indicate the debonding between ferrite wires of n1 cell)

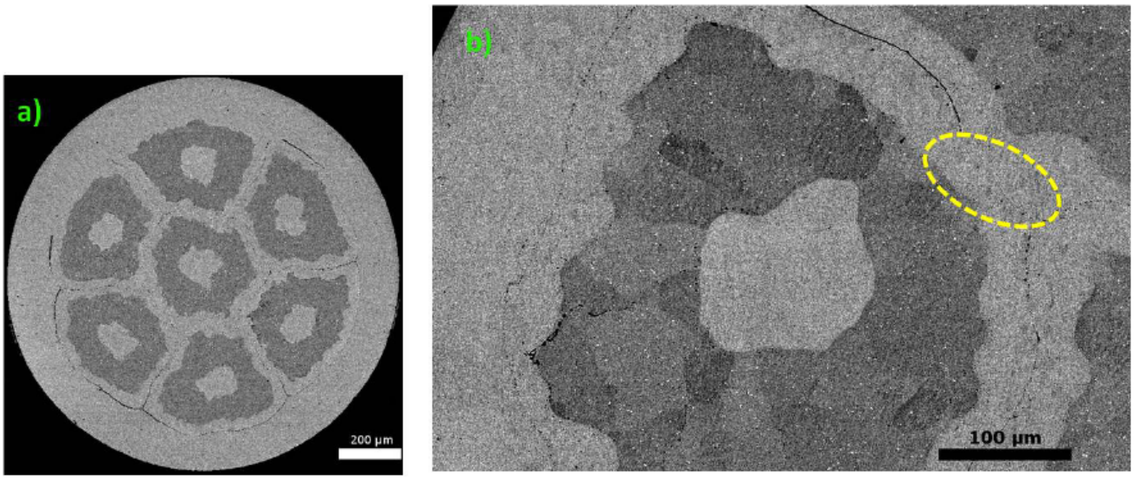

Figure III-24: a) n2 composite after annealing (850°C for a holding time of 1h) b) the detail of n1 cell inside n2 structure (dashed circle highlights the localized bonding between n1 wires)

Once annealed, the n2 composite is cut into 7 wires of 1m of length, re-bundled into an austenitic tube and finally drawn down to 1.55 mm to give n3 composite. The resultant microstructure of this new generation (n3) is presented in Figure III-25.a in work-hardened state. Identically to the precedent generations (n1 and n2), one can distinguish easily the de-bonding between outer tube and wires, and between n2 wires itself. At higher magnification (Figure III-25.b), one can notice that this de-bonding exists also between n1 wires. However, the ferrite and the austenite issued from n1 wires exhibit a perfect cohesion.

The volume fraction of the austenitic phase in n3 composite is estimated by image analysis of the Figure III-25.a to be 75% ±5%. Indeed, one should notice that, for each iteration n, a new austenitic tube is introduced which means that the austenite fraction is increasing continually while the ferrite phase is only issued from n1 step. Moreover, it is also important to notice that the outer tube of every composite n constitutes almost 37% of the whole microstructure which explains this drastic increase of austenite volume fraction. Therefore, in order to manufacture a representative material model of duplex stainless steels (DSS), the volume fraction of both phases should be balanced to almost 50% of ferrite and 50% of austenite by introducing a new ferrite component during re-bundling operation. The idea is in fact re-bundling alternately with a ferrite and austenite tube as we will see in the next section. The produced composite will naturally have a different architecture. It is for this reason that the manufacturing of the first architecture was interrupted at this stage.

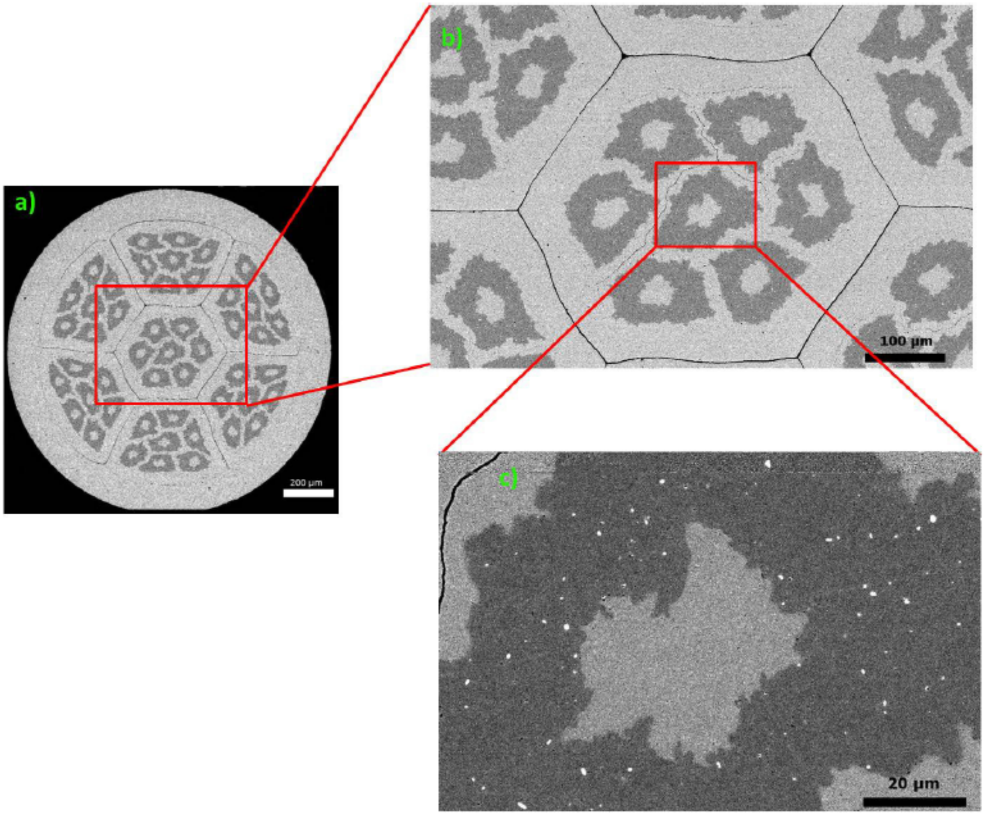

Figure III-25: a) n3 composite microstructure at as-drawn state b) detail of n2 composite (7 wires of n1) c) detail of n1 cell

III.III.2.b 2nd architecture

i) Composite n2

Figure III-26 shows the microstructure of the n2 composite, in the as-drawn state, resulting from re-bundling and drawing 7 annealed wires of n1 in a tube of ferrite (430 LNb). It reveals, in fact, the same debonding problem between each component (n1 wires and tube). By introducing a ferritic tube, the volume fraction of ferrite phase increased significantly compared to composite n2 of the first architecture.

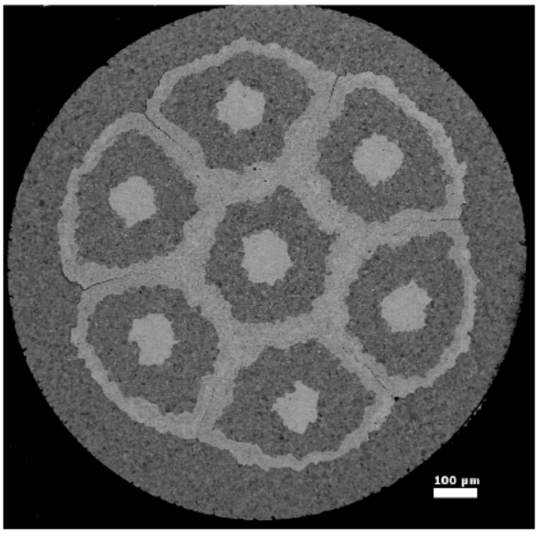

Figure III-26: Microstructure of n2 composite after annealing

Table III-2: Dimension of each component inside n2 composite

	Issued from		Av. Thickness (µm)	Volume fraction (%)
Ferrite 430LNb	n1		79	70
	n2		114	
Austenite 316L	n1	Wire diameter	104	30
		Tube	28	

ii) Composite n3

In the same way, composite n3 is produced by embedding 7 annealed wires of n2 in an austenitic tube. Figure III-27 shows the microstructure of n3 composite in as-annealed state. The same observations regarding debonding problem between this time n2 wires can be made.

Arriving to this stage in which the dimension of n1 cells becomes small, it is interesting to follow the evolution of n1 cells locally after annealing at the optimised annealing parameters via the EBSD technique. Figure III-28.a shows an EBSD map of a n1 cell; for the sake of visibility, only the BCC phase is shown. One can observe the formation of small grains (shown with yellow arrows) at the BCC/FCC interface, inside the FCC region. However, these new grains are not visible in BSE SEM images where the chemical sensitive contrast assimilates them to the austenitic phase (Figure III-28.b).

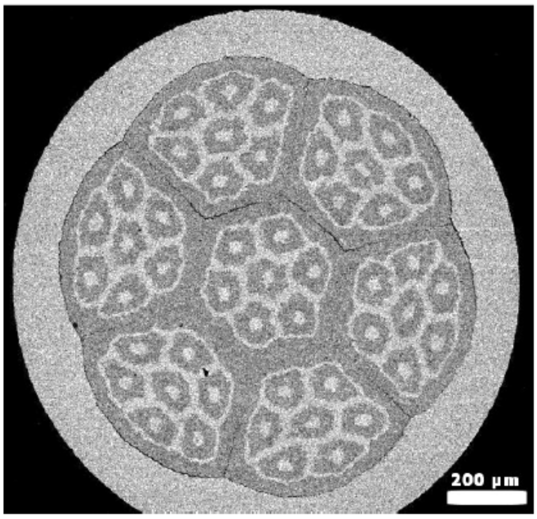

Figure III-27: Microstructure of n3 composite after annealing

Table III-3: Dimension of each component inside n3 composite

	Issued from		Av. Thickness (µm) ±5%	Volume fraction (%)
Ferrite 430LNb	n1		34	52
	n2		39	
Austenite 316L	n1	Wire diameter	37	48
		Tube	11	
	n2		-	
	n3		117	

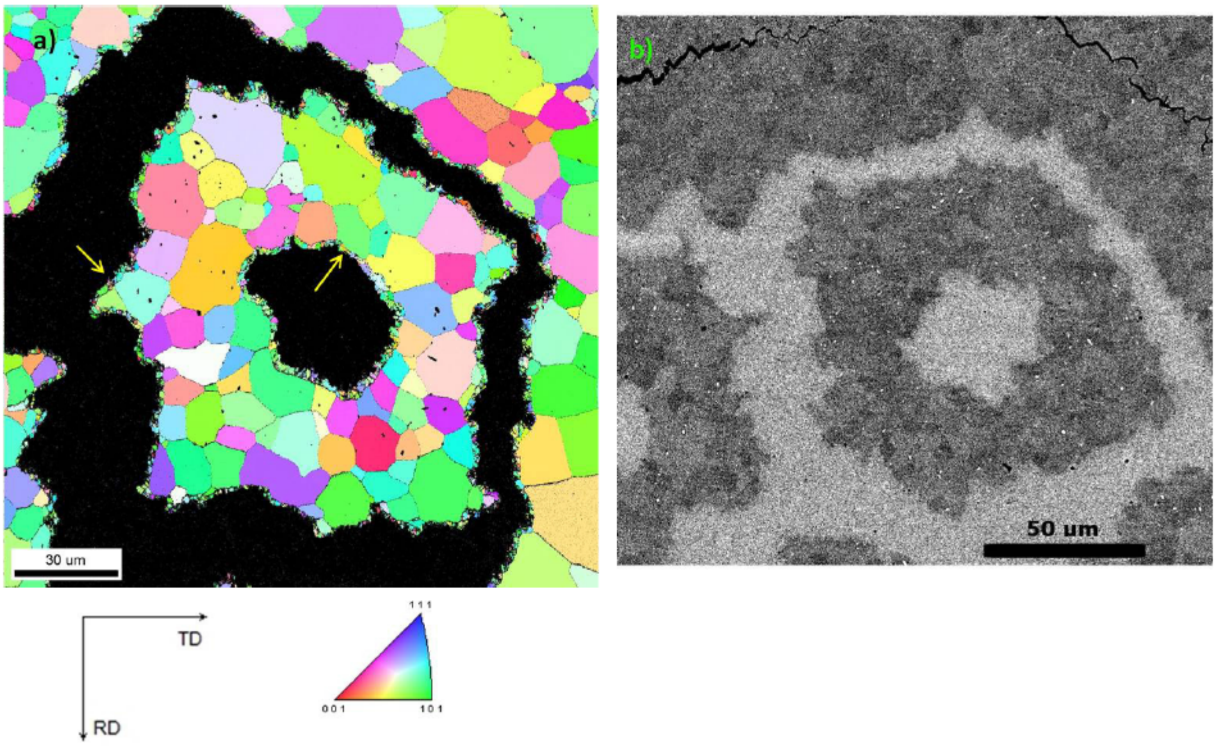

Figure III-28:n1 cell inside composite n3 a) EBSD mapping (yellow arrows indicating the small grains) b) BSE SEM image

iii) Composite n4

At this stage, austenite and ferrite issued from n1 cells (7^3 cells) reach an interesting size around 8-10 µm. Generally, the microstructure in the as-drawn state possesses the same characteristics of the precedent generation n1, n2 and n3 composite in terms of debonding problem.

However, after annealing, the EBSD map of Figure III-28.a shows an increase of the small grains that interrupts the FCC phase already observed in n3 composite. In some regions, one can observe the total regression of the FCC phase in favour of these small grains (see Figure 30.b).

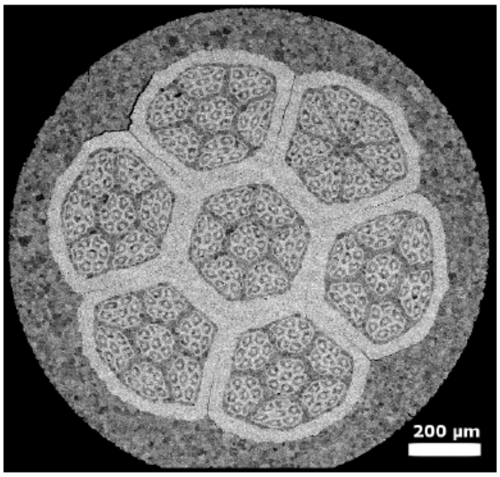

Figure III-29:Microstructure of n4 composite after annealing

Table III-4: Dimension of each component inside composite n4

	Issued from		Av. Thickness (µm) ±5%	Volume fraction (%)
Ferrite 430LNb	n1		8	72
	n2		10	
	n4		132	
Austenite 316L	n1	Wire diameter	10	28
		Tube	5	
	n3		40	

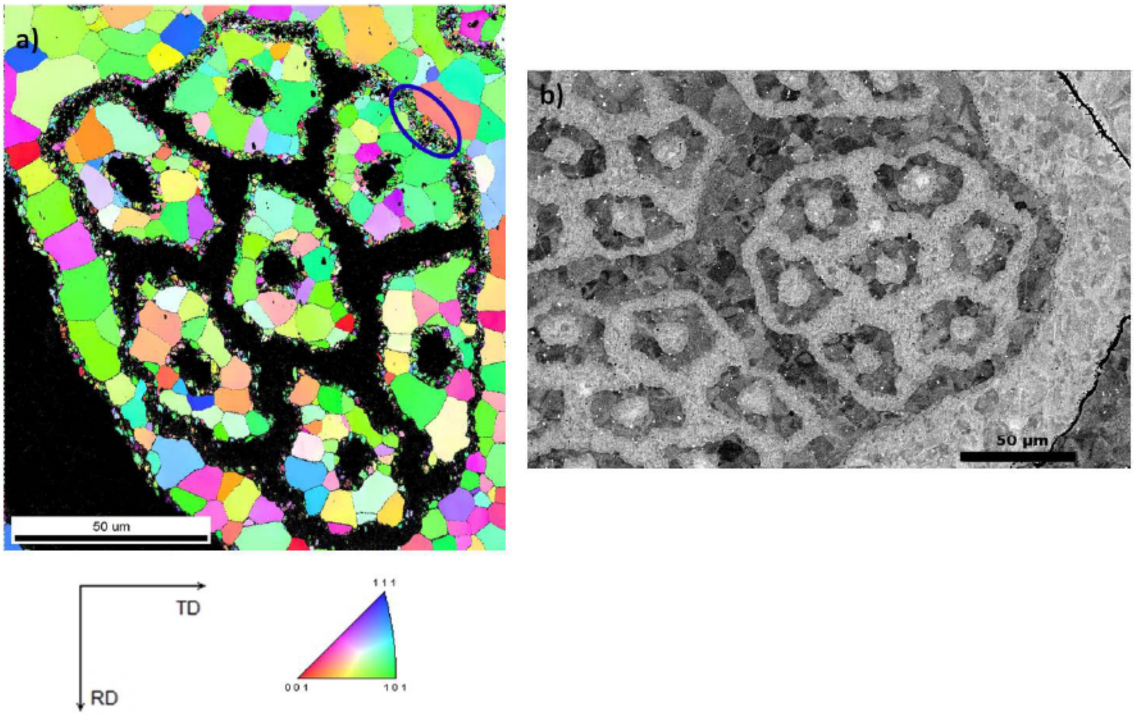

Figure III-30: n1 cells in composite n4 a) EBSD cartography (blue circle indicates the complete regression of the FCC phase) b) BSD SEM image

iv) Composite n5

Figure III-31 shows the as-drawn microstructure of the composite n5, which is composed of 7 wires of n4 (7^4 n1 cells) stacked in an austenitic tube. The dimension of the austenite issued from n1 cells is reduced down to almost 1-3 µm of thickness (see Table III-5). Unlike the precedent composite generations, n1 cells have no longer a cylindrical shape but start to get a wavy shape, which is considered as the signature of the curling structure (Figure 32.a). A curly microstructure is in fact a classical feature of BCC-FCC co-deformation [Sinclair et al. 1999]. This result is in agreement with the work of [Quelennec 2011] on Cu-Fe codeformation where they showed that the curling structure begins when reaching a microstructure of about 3 µm.

After annealing with the optimised parameters (i.e. 850°C; 1h of holding time), the microstructure loses its structure and the architecture is completely disrupted. Figure III-32.c shows a 100*100 µm EBSD map (step=0.7µm) of 2 cells of n2 inside of which 7 cells of n1 should appear. One can observe an almost complete regression of the FCC phase (in dark); the 2 µm austenite wire issued from n1 cells does no longer exist, thereby defining the limit of our refining process. Table III-5 shows the dimension of each component inside n5 measured by image analysis via different local SEM images.

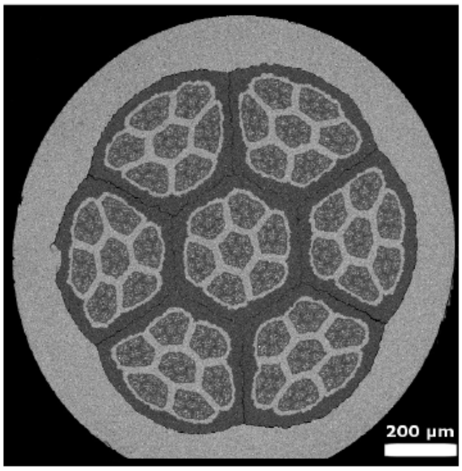

Figure III-31: Microstructure of composite n5 in as-drawn state

Table III-5 : Dimension of each component inside n5

	Issued from		Av. Thickness (µm) ±5%	Volume fraction (%)
Ferrite 430LNb	n1		2.5	45
	n2		3.6	
	n4		37	
Austenite 316L	n1	Wire diameter	2.2	55
		Tube	1.5	
	n3		11	
	n5		152	

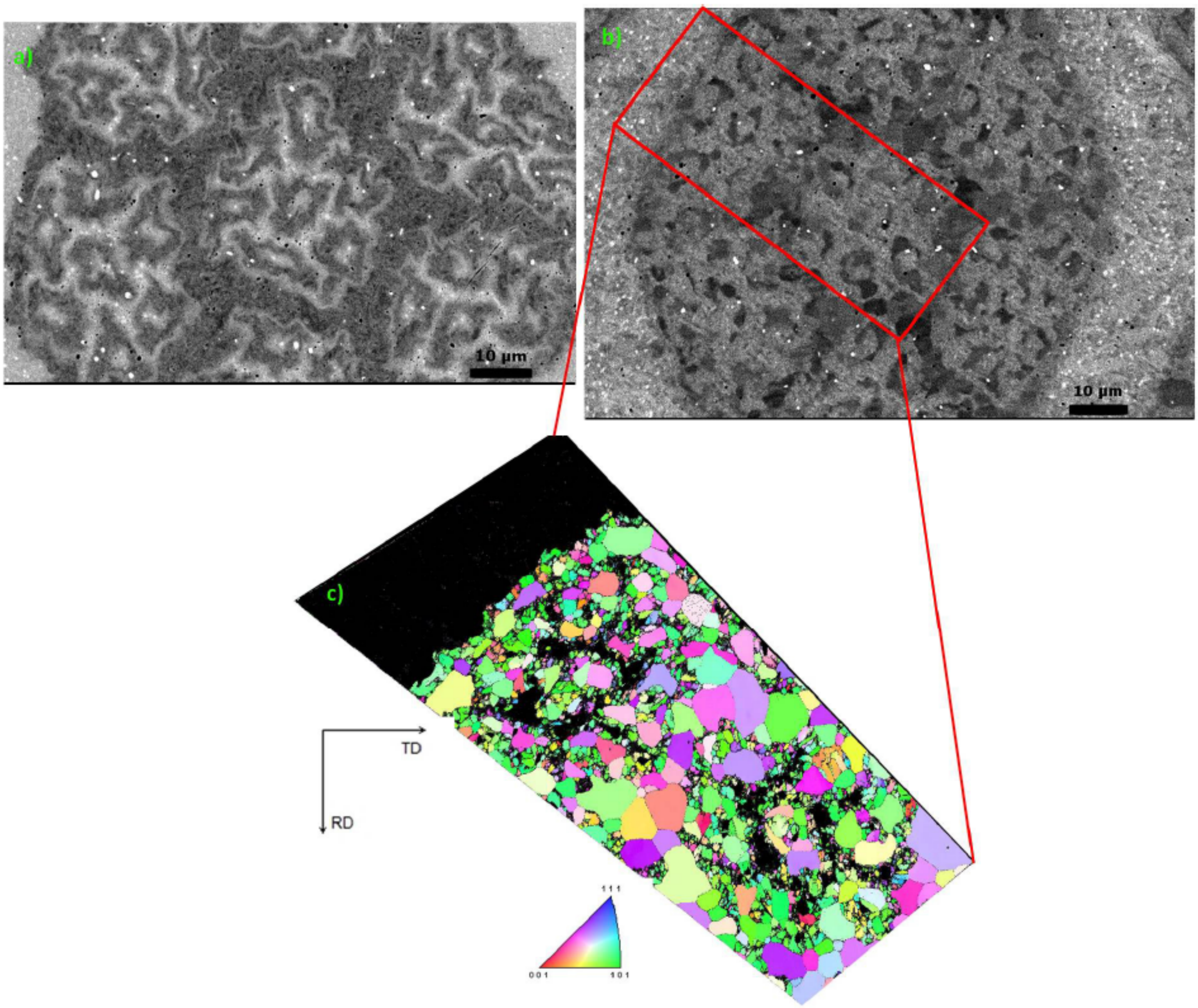

Figure III-32:n2 cells inside n5 composite a) BSE SEM image before annealing b) BSE SEM after annealing at 850°C@1h c) EBSD cartography after annealing

III.III.3 Texture

The texture of each composite after annealing with the optimised parameters has been also followed using EBSD analysis (with a step size of 1µm) on the cross section direction of the composite wire. Figure III-33 and Figure III-34 show the pole figures, where ND (drawing direction) is in the centre, for the three components <100>, <111> and <110> for both austenite and ferrite respectively. The austenite in the three composites develops a duplex fibre texture of <111> and <100>. The distribution of these two components seems to be dependent on the composite. Indeed, as Figure III-33 reveals, composite n3 and n5 have an austenitic texture of <100> as major and <111> as minor component whereas the opposite trend is developed in composite n4.

The ferritic phase developed a <110> fibre texture in the three composites. However, the intensity of this component seems to be also dependant on the composite; composite n5 shows a weak intensity compared to composites n3 and n4.

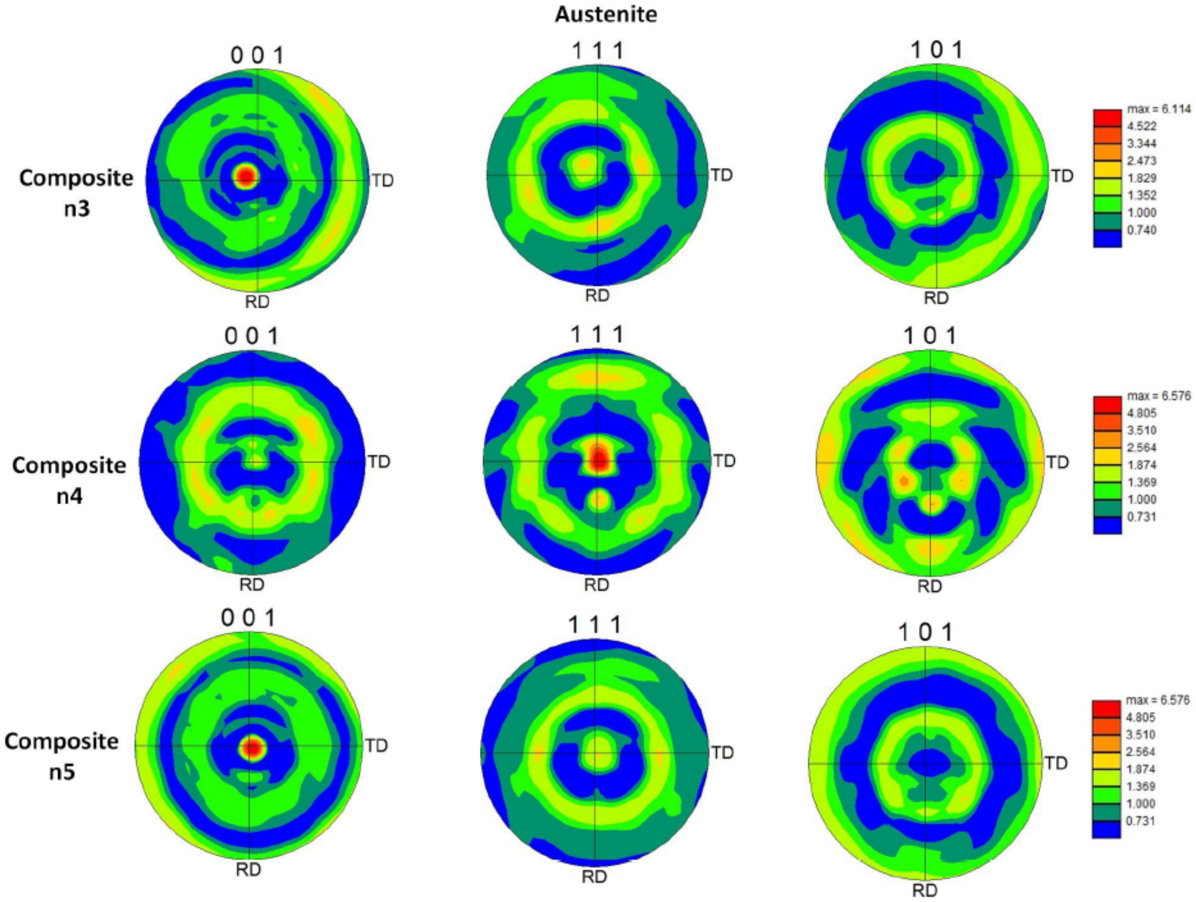

Figure III-33: Austenite texture inside composite n3,n4 and n5 after annelaing at 850°C for 1h as holding time

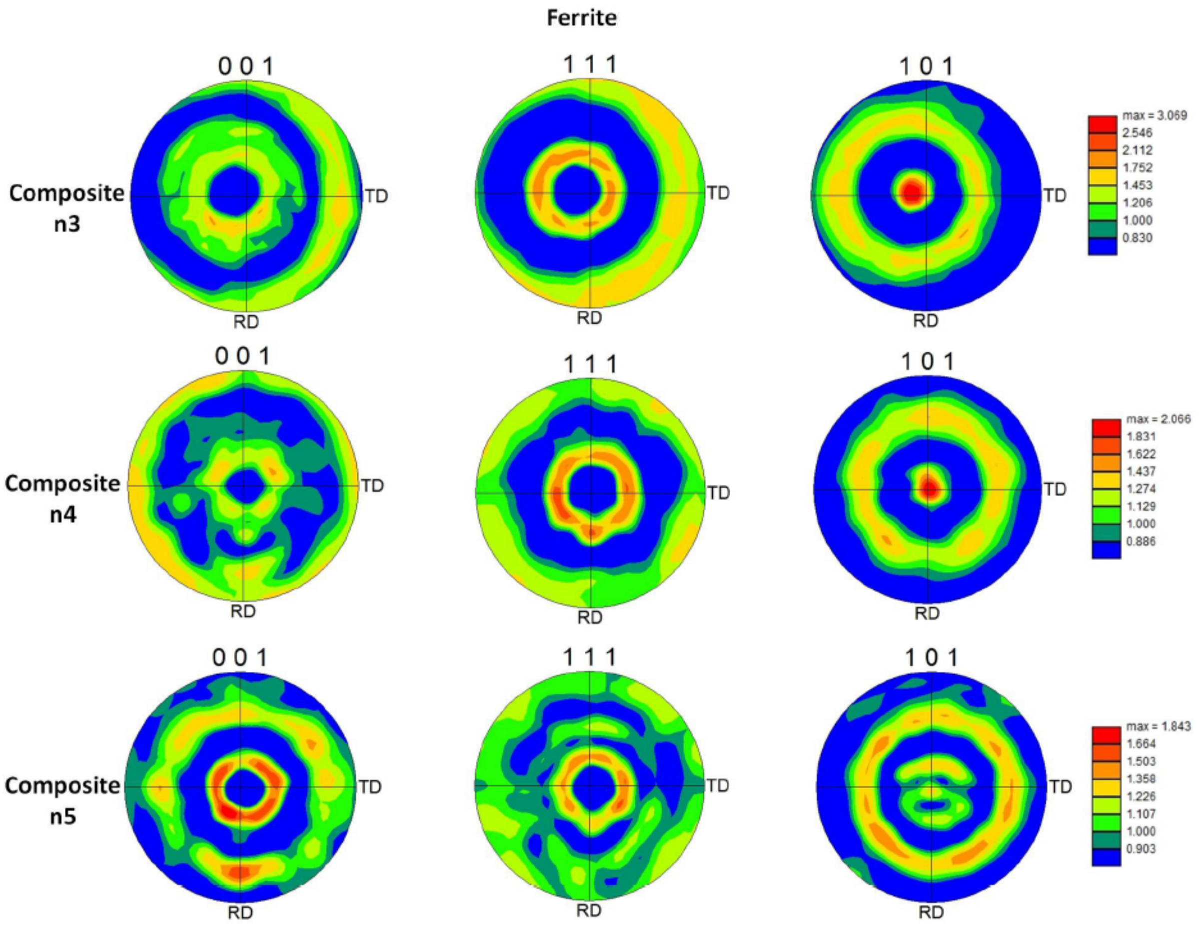

Figure III-34: Ferrite texture inside composite n3,n4 and n5 after annealing at 850°C for 1h as holding time

III.IV Discussion

III.IV.1 Microstructure

Microstructure of both 1st and 2nd architecture has been described in the precedent paragraphs and from Figure III-23-Figure III-31 one can notice that for a given composite of range i (i=1,2,3,4,5), the n(i-1) wires inside that composite are not in complete adhesion. At higher magnification of a composite n(i>2) the same debonding problem is observed, in as-drawn state, between n(i-2) wires. However, the bonding is significantly enhanced after annealing (T=850°C;t=1hour of holding time). This can be explained by the fact that the drawing was performed using 14 steps. Indeed, each pass has a total section reduction of at most 15% which is not sufficient to initiate a metallurgical bonding by plastic deformation only [Vaidnath 1959]. According to the work of [Vaiydnath 1959], if the threshold deformation is not reached during the first pass, it becomes too hard to initiate bonding because the metal's hardness will increase causing, in turn, an increase of the threshold reduction deformation (see Figure III-3 and Figure III-4). Hence, the metallurgical bonding between ferrite and austenite occurred only during annealing if the two surfaces are in an intimate contact. It is for this reason that the n(i-1) wires inside a composite of range i are not bonded even after annealing.

When the metallurgical bonding is achieved, all geometrical boundaries disappear and form a unique entity between ferrite/ferrite or ferrite/austenite components which means that the surface preparations and heat treatment in a vacuum environment were efficient in a manner that neither inter-phase contamination nor oxidation have been observed.

Although the annealing is realised with the optimum parameters, the regression of austenite seems to be unavoidable. Indeed, EBSD maps in Figure III-30 show the austenite phase interrupted continually by small grains having the same crystallographic orientation as BCC phase in case of composite n3 and n4. Arriving to n5 composite, most of the austenite inside 2 cells of n2 has reverted. Four hypotheses could explain this:

1) The complete dissolution of the austenitic regions with micrometric dimensions (1-5 µm) into the ferritic phase forming a ferrite with different chemical composition than the initial one. This hypothesis is plausible since Figure III-32.c shows that austenite is destabilized by the diffusion of the Ni from the austenite toward the ferrite.
2) Martensitic transformation of the austenite during cooling. This hypothesis is also plausible since, the martensitic phase has the same crystallographic structure as the ferrite that is why in EBSD maps it has the same crystallographic orientation.
3) Both hypotheses 1) and 2); dissolution and transformation can be the origin of the architectural perturbation especially for composite n5 in which a 2.2 µm of austenitic phase rich in Ni is surrounded (in some region squeezed) by almost 3-5 µm of ferritic phase.
4) The variability of the optimum annealing parameters with the composite generation (n). Indeed, the optimization was performed basing on n1 composite in which the finest component is about 158 µm. Thus, for composite n4 or n5 we could have a size

effect on the kinetics of the softening annealing which means a different optimum annealing parameters for every step.

The respective influence of these four hypotheses will be investigated in the next chapter (chapter IV).

III.IV.2 Texture

The ferrite developed the expected <110> fibre texture of the BCC metals recrystallized after an axisymetric deformation. In the case of the austenite, the texture evolution showed also the classical duplex fibre texture <100> and <111> of FCC metals. However, one can observe that the relative proportion <100>/<111> depends on the composite generation. Indeed, n5 and n3 showed the same fibre texture which is <100> as a major fibre, while n4 have <111> as a major component. This might be due to the thermo-mechanical history [Hu 1974] of the austenite. In fact, both composites n3 and n5 have an outer austenitic tube which constitutes almost 37% of the composite’s microstructure. This tube underwent exactly the same process during the manufacturing of n3 and n5 composites i.e. drawing followed by annealing at 850°C and 1h as a holding time whereas in n4 composite, an outer ferritic tube was introduced and though the austenitic phase is only issued from n3 and n1 wires.

Conclusion

- The ADB process has been successfully implemented for austenite/ferrite stainless steel system by which multi-scale micro-composites with different architectures and volume fractions are obtained.

- The refining process is limited when one of the phases starts to regress significantly by inter-diffusion.

- As drawn n5 composite is the finest microstructure obtained via this process in which micro-domains (1-3 µm) of austenite and ferrite produced.

References

[Avitzure 1983]
Avitzure B,Handbook of Metal-forming Processes Hardcover – May 4, 1983

[Bay 1983]
Bay N., "Mechanisms producing metallic bonds in cold welding", Welding journal research supplement, 1983, 62, mai, p. 137s-142s.

[Bay 1986]
Bay N., "Cold welding II, process variants and applications", Metal construction, 1986, 18, p. 486-490.

[Cantalejos 1972]
Cantalejos N.A., G. Cusminsky, "Morphology of interface of roll-bonded aluminum", Journal of the institute of metals, 1972, 100, p. 20-23.

[Cave 1973]
Cave J.A., J.D. Williams, "Mechanism of cold pressure welding by rolling", Journal of the institute of metals, 1973, 101, p. 203-207.

[Felder et al. 2011]
Felder, E., Levrau, C., Mantel, M., & Dinh, N. T. Experimental study of the lubrication by soaps in stainless steel wire drawing. Proceedings of the Institution of Mechanical Engineers, 2011, Part J: Journal of Engineering Tribology, 225(9), 915-923.

[Jamaati 2010]
Jamaati, R., & Toroghinejad, M. R., Manufacturing of high-strength aluminum/alumina composite by accumulative roll bonding. Materials Science and Engineering, 2010, A, 527(16), 4146-4151.

[Levrau 2005]
Levrau, C. , Compréhension et modélisation des mécanismes de lubrification lors du tréfilage des aciers inoxydables avec des savons secs (Doctoral dissertation, École Nationale Supérieure des Mines de Paris), 2005.

[Li et al.2002]
Li Y.T., Z.Y. Du, C.Y. Ma C Y, "Interfacial energy and match of cold pressure welded Ag/Ni and Al/Cu", Transactions of nonferrous metals society of China, 2002, 12, p. 814-817.

[Long 2008]
Long L., N. Kotobu, Y. Fuxing Y. "Progress in cold roll bonding of metals", Science and technology of advanced materials, 2008, 9, p. 11-23.

[Lukaschkin 1997]
Lukaschkin N.D., A.P. Borissow, A.I. Erlikh, "The system analysis of metal forming technique in welding processes", Journal of materials processing technology, 1997, 66, p. 264-269.

[Manesh 2004]
Manesh H.D., A.K. Taheri, "Study of mechanisms of cold roll welding of aluminium alloy to steel strip", Materials science and technology, 2004, 20, p. 1064-1068.

[Mantel et al 1990]
Mantel, M., Baroux, B., Ragot, J., & Chemelle, P., Mémoire et Etudes Scientifiques. Revue de Métallurgie, 1990, 637-648.

[McEwan et al. 1962]
McEwan, K. J. B., & Milner, D. R., Pressure welding of dissimilar metals. British welding journal, 1962, 9, 406-420.

[Meignan 1990]
MEIGNAN, P. Contribution des traitements de surface et des lubrifiants dans une démarche de qualité en tréfilage. Fils, Tubes, Bandes, Tréfilés. 1990, p.19-22

[Milner 1960]
Milner D.R., G.W. Rowe, "Fundamentals of solid-phase welding", Metallurgical reviews, 1962, 7, p. 433-480.

[Mohamed 1975]
Mohamed H.A., J. Washbush, "Mechanism of solid state pressure welding", Welding journal, 1975, 9, p. 302s-310s.

[Montmitonnet 1983]
MONTMITONNET, P. (1983). Contribution à l'étude de la lubrification par les savons métalliques en tréfilage (Doctoral dissertation).

[Parks 1953]
Parks J. M., "Recrystallization in welding", Welding Journal, 1953, 32, p. 209-222.

[Quelennec 2011]
Quelennec X. Nanostructuration d'un composite Cu-Fe par deformation intense : vers un mélange forcé à l'échelle atomique (Doctoral desseration), 2011.

[Russell 2000]
Russell, A. M., Chumbley, L. S., & Tian, Y., Deformation processed metal–metal composites. Advanced Engineering Materials, 2000, 2(1-2), 11-22.

[Sinclair et al. 1999]
Sinclair, C. W., Embury, J. D., & Weatherly, G. C., Basic aspects of the co-deformation of bcc/fcc materials. Materials Science and Engineering, 1999, A,272(1), 90-98.

[Tylercote 1958]
Tylecote R.F., D. Howd, J.E. Furmidge, "The influence of surface films on the pressure welding of metals", British welding journal, 1958, 5, p. 21–38.

[Vaidyanath et al. 1959]
Vaidyanath L.R., M.G. Nicholas, D.R. Milner, "Pressure welding by rolling", British welding journal, 1959, 6, p. 13-28.

[Vaidyanath et al. 1960]
Vaidyanath L.R., D.R. Milner, "Significance of surface preparation in cold pressure welding of metals", British welding journal, 1960, 7, p. 1-6.

[Wadora 1963]
Wodara J., "Einfluss der Oberflächenvorbereitung auf die Kaltpressschweissbarkeit von Metallen", Schweisstechnik, 1963, 13, p. 548.

IV Microstructural evolution

Contents

Introduction

A literature review about the annealing phenomena is first presented. A particular attention is paid to the physical mechanism and the influence of the different parameters on the annealing kinetics. This is treated in the first section of this chapter. This chapter is then devoted to give an understanding about the microstructure of the architecture composite described in Chapter III in particular the limitation of the process for further structure refinement. As discussed in Chapter III, different possibilities could be behind this limitation. The softening behavior of the composite after annealing, which is a fundamental step in the manufacturing process, has been investigated by comparing it with that of the bulk wires 316L and 430LNb. The second section of this chapter is dedicated to this study.

The third section deals with the diffusion behavior which could occur during softening annealing. An experimental investigation has been performed in parallel with a simulation study using DICTRA software. This allowed to rationalize the experimental results and to use DICTRA as a predictive tool with confidence for such specific applications.

IV.I Literature review

IV.I.1 Recovery

IV.I.1.a Basic phenomena

Recovery is a thermally activated phenomenon in which some of the stored energy present as elastic internal stresses inherited from the preceding plastic deformation is released. At this stage, the structure of the deformed metal shows **no significant changes in terms of grain structure**. However, the energy relief, caused mainly by dislocation relaxation or point defect motion, causes **changes in properties either mechanical, such as hardness, or electrical resistivity**, which can therefore be used to follow the degree of recovery during annealing treatments. Some direct measurements of the stored energy can be also performed using calorimetry (DSC: Differential Scanning Calorimetry). However, one should keep in mind that other energy release phenomena, particularly recrystallization, result in the same signatures. For example, Figure IV-1 shows the evolution of hardness, resistivity and stored energy of pure nickel deformed by torsion as a function of temperature. The first peak of stocked energy release is attributed to recovery whereas the second corresponds to recrystallization. One can notice also the slow decrease of resistivity in the recovery stage followed by a significant diminution associated with recrystallization. However, before the recrystallization stage, hardness seems to be unaffected. Generally speaking, the change in mechanical properties during recovery is quite limited.

When a recovery phenomenon occurs during cold working, it is referred then to as dynamic recovery. Static recovery (i.e. occurring after plastic deformation) is observed at temperatures ranging from 1/3 to 1/2 of the absolute melting point.

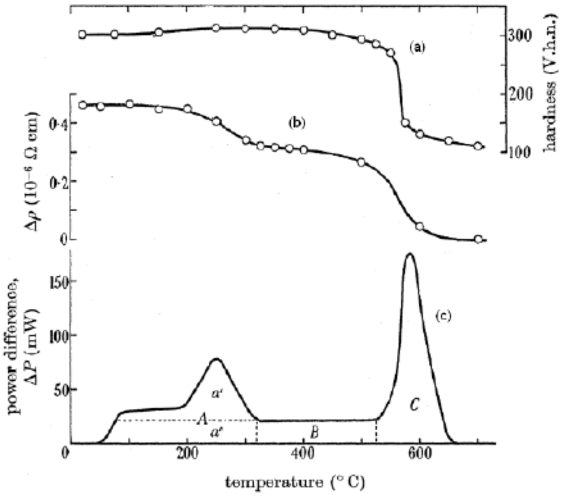

Figure IV-1: Recovery and recrystallization of cold-worked nickel: evolution of a) hardness b) electrical resistivity c) stored energy as a function of temperature [Clarebrough 1955]

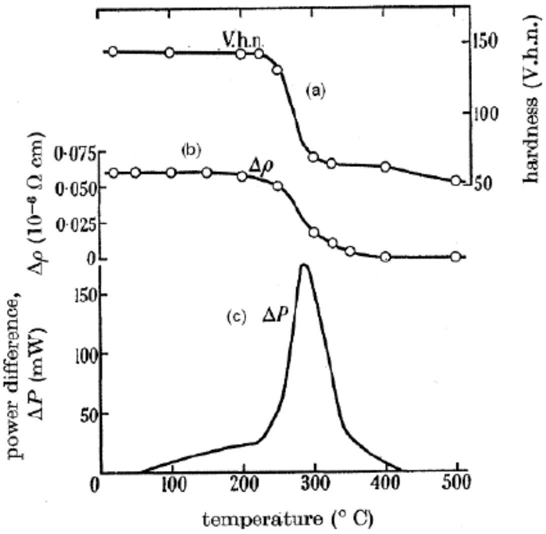

Figure IV-2: Recovery and recrystallization of pure copper deformed by torsion during annealing (6°C/min): a) hardness b) electrical resistivity c) stored energy evolution as a function of annealing temperature [Clarebrough 1955]

IV.I.1.b Parameters influencing recovery

Recovery can be affected by the following parameters:

- Strain level: typically the higher the strain the higher the stored energy, which promotes the occurrence of recovery. However, the opposite trend can be obtained in case of highly deformed material wherein the recrystallization is in competition with recovery and starts very quickly.
- Annealing temperature: in case of isothermal treatments, more complete recovery occurs at high temperature.
- The nature of the material: Staking Fault Energy (SFE or γ_{SFE}) is one of the most determinant parameter. Indeed, γ_{SFE} determines the extent to which the dislocations dissociate into partials and therefore are capable of reorganizing their structure. In metals with low γ_{SFE} such as austenitic stainless steel and copper, cross-slip and climb are difficult and recovery is hardly observed before recrystallization (see Figure IV-2). On the other hand, in metals with high γ_{SFE} such as ferritic stainless steel and aluminum, cross-slip and climb are rapid and recovery develops before recrystallization causing large relative changes in properties as shown in Figure IV-1.

IV.I.1.c Structural modification during recovery

Recovery is defined as the annihilation and reorganization of stored dislocations inherited from previous plastic strain (usually cold work). These two phenomena generate microstructural changes. Figure IV-3 shows the different stages of recovery and the associated structural change.

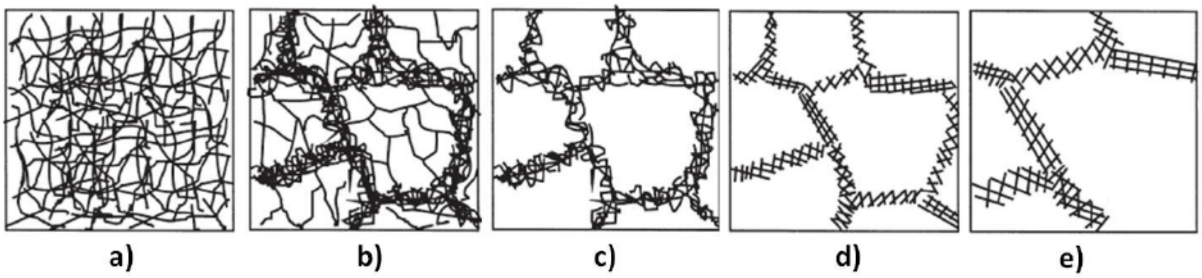

Figure IV-3: Recovery stages of a cold worked material [Humphreys 1995] a) Dislocation tangles b) Cell formation c) Annihilation of dislocations within cells d) Subgrain formation e) Subgrain growth

i) Dislocation migration and annihilation

During recovery annealing, a decrease in the total dislocation density is primarily observed by migration followed by annihilation. This stage is controlled by the mutual interaction of the dislocations through their elastic fields. The resultant force of this interaction causes the migration of dislocations. For example, dislocations of opposite sign and parallel (dipoles) in the same slip plan glide toward each other and may annihilate. This mechanism can be observed at low temperatures or during straining (dynamic). Dipole situated in different glide planes may annihilate by a combined process of gliding and climbing. Climb mechanism is thermally activated because it requires point defect diffusion.

ii) Rearrangement and sub-structure

After annihilation, all glide planes contain dislocations of the same sign, which are in fact in excess and cannot be removed by annihilation. These dislocations will arrange in configuration of lower energy forming then boundaries with low misorientation (Low Angle Grain Boundaries LAGBs). [Cahn 1949] demonstrated that in case of a single crystal where dislocations of only one Burgers vectors are present, dislocations will arrange in a way causing a crystal bending. This produces, in fact, a polygonal crystal. This mechanism is thus called ***Polygonization***. Figure IV-4 sketches the successive stages of annihilation, rearrangement and polygonization.

In the case of polycrystals in which several slips systems are activated when subjected to large strains, the dislocation structure becomes more complex. Indeed, during annealing, the same phenomena of dislocations annihilation by gliding and climbing followed by dislocations rearrangement are observed. Since the dislocations present different Burgers vectors, the cells boundaries are not formed by simple bent sub-boundaries. Nonetheless, TEM study conducted by [Humphreys 2004] on a recovered 10% deformed aluminum sample, shows that dislocation tangles can rearrange in the same manner as the polygonization in single crystals. Figure IV.5 reveals that the tangled cells A and B have become more regular dislocation networks (Low angle grain boundaries) and the number of dislocations has diminished.

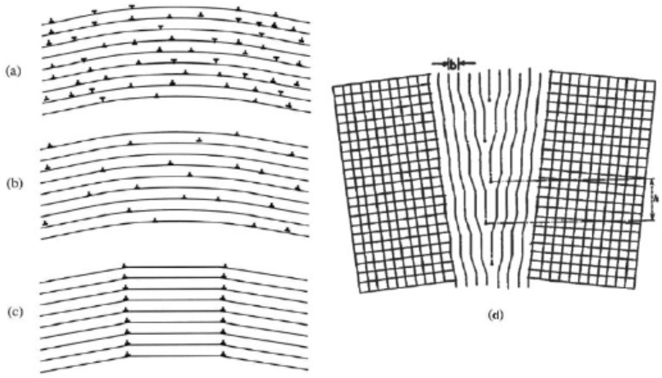

Figure IV-4:Polygonization of a single crystal containing edge dislocations a) As-deformed structure b) After dislocation annihilation c) Formation of tilt boundaries [Humphreys 2004] d) Structure of bent sub-boundary [Cahn 1996]

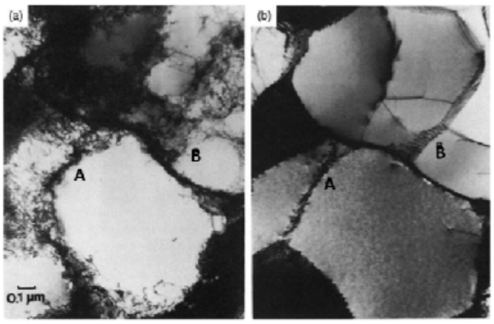

Figure IV-5: Sub-boundary formation of aluminum deformed 10% a) deformed state b) annealed state at 250°C [Humphreys 2004]

iii) Sub-grain coarsening

Following the formation of a sub-grain structure, the last stage of recovery is coarsening of this structure. Two mechanisms of sub-grain growth have been proposed by [Sandström 1977] a) sub-boundary migration b) sub-grain rotation and coalescence.

a) Sub-grain migration

The concept of this mechanism is based on the growth of the large sub-grains at the expense of the small ones. Thanks to boundary energy, the sub-grain structures will be modified by the movement of a triple junction point. Indeed, in case of "Y" configuration Figure IV-6, the movement of point A is realized by dislocation disassociation of sub-boundary AB (highly misoriented and thus of high energy). Sub-grain III grows at the expense of I and II.

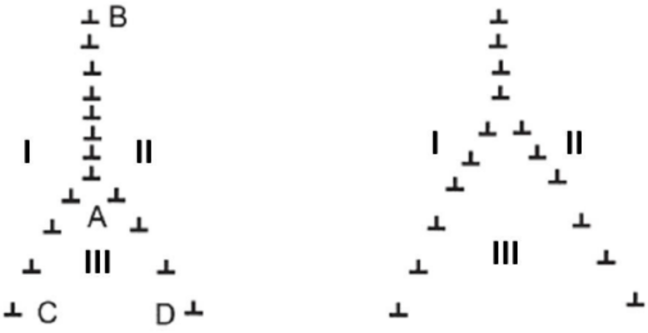

Figure IV-6:Sub-boundary "Y" configuration

It is found that the growth rate of sub-grains v_{SG} is proportional to the **driving pressure P** and **sub-grains mobility** M_{SG}.

$$v_{SG}=M_{SG}P \qquad \text{Eq. IV-1}$$

The expression of these two quantities, M_{SG} and P is as following:

- **Expression of driving Pressure**

While annealing, the sub-grains tend to grow by releasing the stored energy inherited from cold working. The driving force arises from this stored energy. If we imagine a microstructure with an array of spherical sub-grains of radius R and boundary energy γ_{SG}, then the stored energy per unit volume E_d will be expressed as follows:

$$E_d \approx \frac{3}{2}\frac{\gamma_{SG}}{R} \qquad \text{Eq. IV-2}$$

The driving force is then written as the derivative of the stored energy E_d :

$$F = -\frac{dE_d}{dR} = \frac{d}{dR}\left(-\frac{3}{2}\frac{\gamma_{SG}}{R}\right)$$ Eq. IV-3

$$P = \frac{F}{A} = R\frac{d}{dR}\left(-\frac{3}{2}\frac{\gamma_{SG}}{R}\right)$$ Eq. IV-4

Where A is the area of sub-grain per unit volume. In general, γ_{SG} is independent of the sub-grain size (R). It depends however on the misorentation angle. Thus, we have two cases

- case where the misorientation is constant during subgrain growth. The driving pressure will be simply expressed then as follows:

  $$P = \frac{3}{2}\frac{\gamma_{SG}}{R}$$ Eq. IV-5

  The growth rate of the sub-grain is then expressed:

  $$v_{SG} = M_{SG}\frac{3}{2}\frac{\gamma_{SG}}{R}$$ Eq.IV-6

  Since the sub-grains are assumed to be spherical, the growth rate of a sub-grain is then defined as the change of its radius R with time. Thus we can write the growth rate as following:

  $$\frac{dR}{dt} = M_{SG}\frac{3}{2}\frac{\gamma_{SG}}{R} \rightarrow R^2 - R_0^2 \propto t$$ Eq. IV-7

- case in which the misorientation varies with R

  [Furu et al. 1992] have studied the relation between the sub-grain size and misorientation in commercially pure aluminium and found that as subgrain growth proceeds, the misorientation increases. Identically, [Huang et al.2000] observed the same trend, i.e. the accumulation of the misorientation as the subgrains grow, in a hot deformed aluminium.

  [Furu et al.1992] proposed a simple linear relation between misorientation θ and subgrain radius R: $\theta = \beta R$. The growth rate of sub-grains can be written then as:

  $$v_{SG} = M_{SG}\frac{3}{2}\frac{\gamma_m\beta}{\theta_m}$$ Eq. IV-8

- **Expression of mobility**

Mobility is a term introduced in both subgrain growth and grain growth. However, both mechanisms are completely different; subgrain growth as presented above occurs by glide and climb of dislocations in the sub-boundary whereas grain growth is based on the atomic diffusion through the grain boundary. As a result, the mobility of low angle grain boundaries is generally lower than that of high angle grain boundaries by several orders of magnitude. [Sandström 1977, Ørsund et al. 1989] discussed the theory of mobility and suggested the following expression for the mobility of sub-grains:

$$M_{SG} = \frac{D_S b}{k_B T}$$ Eq.IV-9

Where D_S is the coefficient of self-diffusion. Nevertheless, the mobility is still the subject of various investigations in order to establish the influence of the misorientation on the mobility (interested reader can refer to [Humphreys 1995]).

b) Sub-grain rotation and coalescence

The concept of this mechanism is explained by the fact that the migration of dislocations from a sub-boundary induces a rotation of the neighbouring subgrains, which can lead to coalescence as shown in Figure IV-7. This mechanism was firstly introduced by [Hu 1962] based on a TEM study on Si-Fe alloys. [Li 1962] provided a quantitative explanation by suggesting a theoretical coalescence kinetics. For a symmetric tilt boundary of height H, the rate of change of the misorientation during coalescence is given by :

$$\frac{d\theta}{dt} = \frac{3\gamma_m \theta B b}{H^2} ln \frac{\theta}{\theta_m}$$ Eq. IV-10

Where B is the dislocation mobility per unit length and b is the Burger vector of the dislocation. θ_m and $\gamma_m$the limiting values (of misorientation angle and specific energy respectively) beyond which the description of the subgrain by a dislocation array is not possible because dislocation cores overlap. However, no experimental evidence has shown yet that this mechanism is behind the sub-grain growth [Jones 1980].

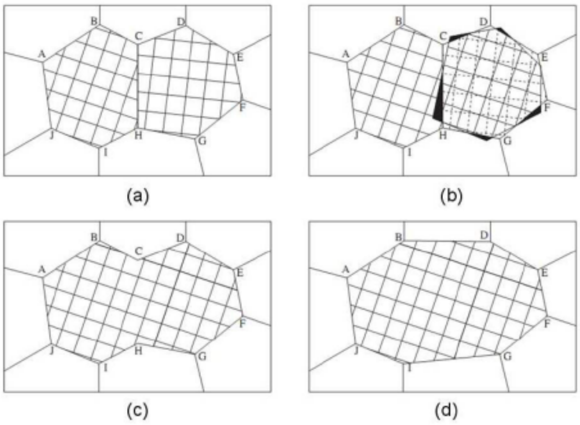

Figure IV-7: Schematic illustration of sub-grain coalescence as proposed by [Li 1962]

IV.I.1.d Recovery kinetics and model

i) Friedel model

The kinetics of recovery can be determined by observing the time dependant evolution of a structural or microstructural parameter such as hardness, yield strength, dislocation density etc. [Friedel et al. 1964], for example, proposed a model, in which the evolution of the internal stress with time is rationalized, by assuming that the dislocation annihilation during recovery is governed by thermally activated cross-slip under the action of the internal stress field from neighboring dislocations. The expression of this model is as following:

$$\frac{d\sigma_i}{dt} = -Kexp\left(-\frac{U_{CS}(\sigma_i)}{k_B T}\right) \qquad \text{Eq. IV-11}$$

Where σ_i is the internal stress, U_{CS} is the activation energy for cross slip, which is, in turn, a decreasing function of σ_i. K is a constant. If we consider the first order development of U_{CS}, the above expression can be re-written as following:

$$\frac{d\sigma_i}{dt} = -Kexp\left(-\frac{U_0 - V\sigma_i}{k_B T}\right) \qquad \text{Eq. IV-12}$$

Where U_0 is the activation energy and V the activation volume. By integration of both sides of this last equation, the internal stress is expressed as a logarithmic decreasing function with annealing time:

$$\sigma_i = \sigma_{i0} - \frac{k_B T}{V} \ln\left(1 + \frac{t}{t_0}\right) \qquad \text{Eq. IV-13}$$

Where σ_{i0} is the internal stress before recovery. t_0 is a characteristic time constant dependant on activation parameters and temperature:

$$t_0 = \frac{k_B T}{KV} exp\left(-\frac{U_0 - V\sigma_{i0}}{k_B T}\right) \qquad \text{Eq. IV-14}$$

ii) Verdier model

A more recent description of the recovery kinetics has been proposed by [Verdier et al. 1998]. This model is based on the assumption that the rate of the internal stress is a proportional function of the plastic strain-rate induced by the internal stress relaxation.

$$\frac{d\sigma_i}{dt} = -E\dot{\varepsilon}_p \qquad \text{Eq. IV-15}$$

The plastic strain rate can be related to the dislocation slip via the Orowan law:

$$\dot{\varepsilon}_p = \frac{\rho b \bar{v}}{M} \qquad \text{Eq. IV-16}$$

Where $\bar{v}$ is the average dislocation velocity:

$$\bar{v} = 2v_D b exp\left(-\frac{U_0}{k_B T}\right) sh\left(\frac{V\sigma_i}{k_B T}\right) \qquad \text{Eq. IV-17}$$

The final expression of the internal stress evolution rate according to this model is then written as following:

$$\frac{d\sigma_i}{dt} = -\frac{2Ev_D}{M^3(\alpha\mu)^2}\sigma_i^2 exp\left(-\frac{U_0}{k_B T}\right) sh\left(\frac{V\sigma_i}{k_B T}\right) \qquad \text{Eq. IV-18}$$

[Verdier et al. 1998] developed this model based on a recovery study of cold-rolled Al-Mg alloys. This model has been then used successfully for the study of ferritic stainless steel (BCC) [Meyer 2008] and micro-alloyed austenite (FCC) [Zurob 2002].

IV.I.2 Recrystallization

IV.I.2.a Basic phenomena

Unlike the recovery process, recrystallization of a cold worked metal is characterized, not only by changes of structural properties but also by an evolution of the grain structure. A new microstructure is formed, causing significant modifications of texture, grain size and the complete release of internal stress when recrystallization is complete. Formation and motion of new High Angle Grain Boundaries (HAGBs) allow, in fact, the growth of new grains.

The driving pressure for recrystallization is provided by the stored deformation energy. The recrystallization process can occur either during annealing after cold working (Static Recrystallization (Rex)) or during deformation at high temperature (Dynamic Recrystallization (DRX)). There are two stages of Rex; primary recrystallization and secondary recrystallization. The later is characterized by the abnormal grain size growth; some numbers of grains grow to dimension that exceeds more than 100 times the average grain size. Our current study deals with the primary static recrystallization.

Many researchers through the past 50 years carried out series of investigations on various metals in order to rationalize recrystallization behavior. [Tunbull et al. 1952] are the first who sketched out the so-called “recrystallization laws”. These laws have been experimentally verified through various investigations:

- Recrystallization initiates above a minimum deformation. Indeed, the deformation must be sufficient to provide the necessary driving force for nucleation and growth.
- Recrystallization is a thermally activated phenomenon. Thus, the necessary annealing time for recrystallization decreases with increasing temperature.
- The temperature necessary for recrystallization decreases as strain increases. By increasing the strain, the stored energy providing the driving force for recrystallization increases.
- After recrystallization, the resultant grain size, for a given temperature, depends primarily on the amount of prior strain. The higher the strain, the smaller the grain size. This is attributed to the fact that nucleation of new grains is more affected by strain than the growth rate.
- For a given amount of deformation, a larger initial grain size increases the recrystallization temperature. Indeed, since the grain boundaries are favored sites for nucleation, fewer nucleation sites can be found when the initial microstructure has a large grain size. Hence, the nucleation rate is lowered and therefore the recrystallization is slower.

IV.I.2.b Nucleation

It is well known that the classical nucleation theory of phase transformations cannot be applied to the formation of recrystallization nuclei. As shown by [Christian 2002] and [Rollett 1997] this theory would lead to a considerable underestimation of the nucleation rate because recrystallization, as compared to phase transformations, is characterized by a very low volume driving force, and a relatively high interfacial energy.

A model for nucleation of recrystallization was proposed by [Beck and Sperry 1995] called Strain Induced grain Boundary Migration (SIBM). As its name indicates, the concept of this model is based on the migration of the boundary of the most misoriented grain pre-existing in the microstructure. This boundary separating two deformed grains will migrate to the most deformed one leaving a region behind the migrating boundary with a lower dislocation density. This migration results in a special grain shape called boundary bulge, which has been widely observed by TEM as shown in Figure IV-8. This mechanism is also sketched in Figure IV-8. [Bailey and Hirsh 1961] assumed that there is a critical length L^* (R bulge radius) beyond of which nucleation of recrystallization occurs.

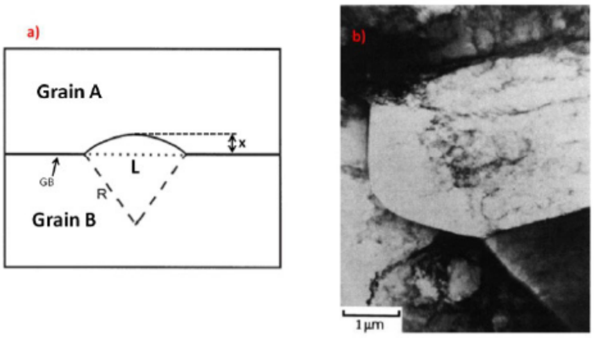

Figure IV-8:Scheme of nucleation by bulging (SIBM) under the difference of stored energy b) TEM observation of SIBM in copper [Bailey and Hirsch 1961]

$$L > L^* = \frac{\gamma_{GB}}{\Delta E_s}$$

Eq. IV-19

Where ΔE_s is the difference between the stored energy between the grains A and B (see Figure IV-8). According to Eq. IV-19, nucleation recrystallization will occur earlier if L^* is small i.e. when ΔE_s is sufficiently large. Therefore, the extent of recovery influences the nucleation process since:

- L(t) increases during recovery (subgrain growth) if we take L as the distance between the dense region of dislocations
- The net driving pressure acting on the bulge decreases during recovery.

However, the expression of the driving pressure on the bulge depends in fact on the bulging mechanisms observed. This will lead naturally to different expression for L^*:

- The first bulging mechanism was proposed by [Bailey and Hirsh 1961]. Based on the assumption that the dislocation density is independent of the boundary displacement, the driving pressure exerted on the bulge is written as following:

$$\Delta E_s = E_S^A - E_S^B = \frac{1}{2}\mu b^2(\rho^A - \rho^B)$$

Eq. IV-20

If we define f as the heterogeneity factor of stored energy between the two grains A and B $f = E_S^A / E_S^B$, then L^* becomes:

$$L^* = \frac{4\gamma_{GB}}{\mu b^2 \rho^A (1 - f)}$$ Eq. IV-21

- A second mechanism was proposed by [Bate and Hutchinson 1997]. Based on experimental observations, they suggest that the substructure is dragged behind the bulge. Hence, they assume that when the bulge grows, the stored energy in the concave side of the bulge decreases proportionally to the inverse of the bulge area. Thus, when the bulge is moved by a distance x the driving pressure becomes:
-

$$\Delta E_S = E_S^A - E_S^B = \frac{1}{2}\mu b^2 \left(\rho^A - \rho^B \frac{L^2}{L^2 - x^2}\right)$$ Eq. IV-22

$$\rightarrow L^* = \frac{4\gamma_{GB}}{\mu b^2 \rho^A \sqrt{1 - f}}$$ Eq. IV-23

- The third mechanism is based on the assumption that the movement of the boundary during bulging eliminates dislocations and generates a volume free of dislocations on one side of the boundary (i.e. $\rho^B = 0$). By consequence the energy difference is maximised allowing the development of strain induced boundary migration (SIBM). The nucleation criterion becomes then:

$$L^* = \frac{4\gamma_{GB}}{\mu b^2 \rho}$$ Eq. IV-24

Other nucleation mechanisms have been observed such a nucleation within grains. Similarly to the subgrain growth mechanism by rotation and coalescence, intergranular nucleation of a new grain consists in a transition from LAGB into HAGB.

IV.I.2.c Growth

The growth of a recrystallized grain within a deformed microstrutcure occurs by migration of a HAGB whose mobility M_G is higher than that of LAGB. The mobility is controlled by the thermally activated transfer of atoms across the grain boundary. The velocity is then related to the difference of stored energy across the grain boundary and the frequency of atomic transfer across it. This can be described as the following relation:

$$v_B = M_G \Delta E_S \quad \text{Eq. IV-25}$$

Where:

$$M_G = \frac{bv}{k_G T} \exp\left(-\frac{Q}{k_G T}\right) \quad \text{Eq. IV-26}$$

IV.I.2.d Recrystallization kinetics

Recrystallization kinetics is controlled by nucleation followed by grain growth. Typically, the recrystallization kinetics is measured by the volume fraction of the recrystallized grains (X_r) as a function of time. The evolution of X_r as a function of $\ln(t)$ is found to be sigmoid. Following this form, the function can be decomposed in three parts and interpreted as follows: i) the first part is attributed to the incubation time before any observed recrystallized grains corresponding to the necessary time for nucleation; ii) a brutal increase in the recrystallization velocity (dX_r/dt) is then observed corresponding to the grain nucleation and growth; iii) full recrystallization is achieved and the rate decreases.

i) Parameters affecting the recrystallization kinetics

Recent investigations have shown that recrystallization is a very complex process, especially in multi-phase materials. In fact, many factors can affect the proceeding of this phenomenon. However, three parameters are considered as the most significant in recrystallization behavior:

- Strain amount:

As mentioned above, the influence of the previous strain on the rate of recrystallization is very significant. Indeed, nucleation is highly dependent on the energy stored in the metal. The higher the stored energy, the more nucleation is stimulated. This was experimentally shown in the work of [Anderson and Mehl 1945] on aluminum tensile strained at different amount and annealed at 350°C as shown in Figure IV-9. It is also necessary to note that there exists a minimum amount of strain around 1-3% below which recrystallization cannot occur [Humpherys 2004].

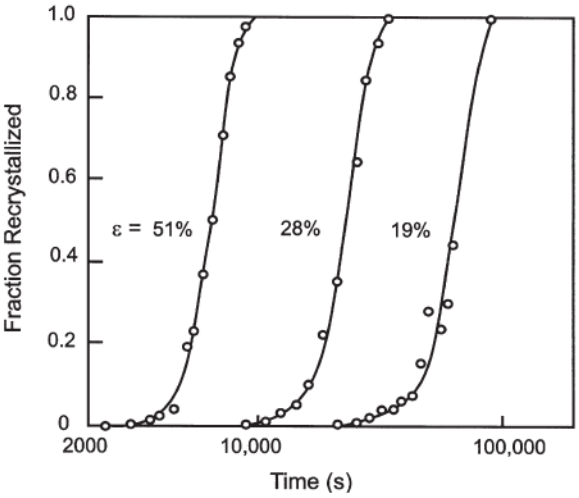

Figure IV-9: Influence of the tensile strain on the recrystallization kinetics of aluminium annealed at 350°C [Anderson and Mehl 1945]

➢ Annealing temperature:

Since nucleation and grain growth are both thermally activated processes as Eq. IV-26 shows, the recrystallization rate is very sensitive to the change in annealing temperature. [Speich 1966] showed, in 60% deformed Fe-3.5%Si, that the increase of temperature accelerates the recrystallization rate (See Figure IV-10).

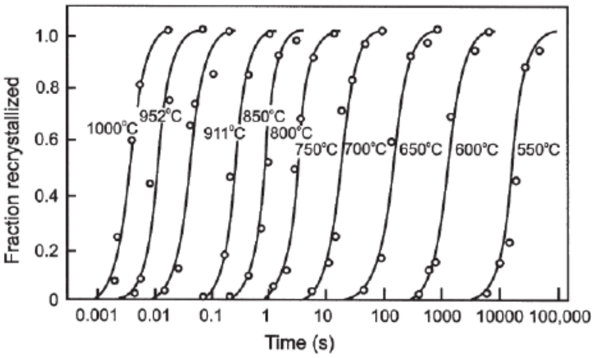

Figure IV-10:Effect of annealing temperature on the recrystallization rate of Fe-3.5%Si deformed 60%[Speich and Fisher 1966]

➢ Initial grain size:

In different ways the initial grain size can affect the recrystallization kinetics. However, we will cite here only two aspects (interested readers can refer to [Humphreys 2004] for more detailed aspects):

- The stored energy tends to increase with a decrease in grain size
- Since nucleation is promoted at grain boundaries, the number of nucleation sites is higher in a fine-grained material.

[Hutchinson et al. 1989] have investigated the influence of the initial grain size of copper cold-rolled 93% and found that the growth rate of the grains in the fine-grained material was 20 times faster than that of coarse grains at the same temperature (Figure IV-11).

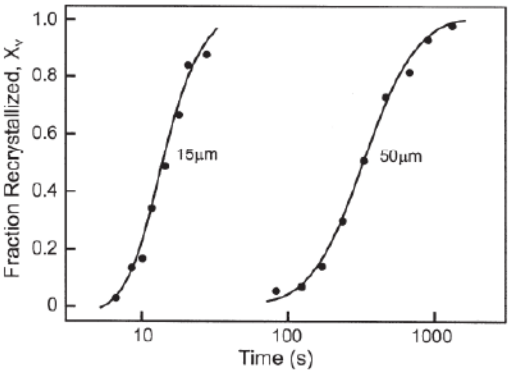

Figure IV-11: Influence of the initial grain size on 93% cold-rolled copper annealed at 225°C [Hutchinson et al. 1989]

ii) Recrystallization model

The sigmoidal curves of recrystallization kinetics are classically modeled by an Avarami (or JMAK) equation:

$$X(t) = 1 - \exp(-kt^n) \qquad \text{Eq. IV-27}$$

Where $X(t)$ is the recrystallization fraction, t is time, n is the recrystallization exponent and k is a constant whose expression depends on the mobility, stored energy and nucleation rate.

For constant growth rate and site saturation: $k = \frac{4\pi}{3}(n_0 \pi v^3)$ where n_0 is the effective number of nuclei per unit volume. In this case the Avrami kinetic exponent n=3.

For constant growth rate and nucleation rate ($\dot{\eta}$): $k = \frac{\pi}{3}(\dot{\eta}\pi v^3)$ with a kinetic exponent n=4

A generalized JMAK model has been developed by [Dunlop et al. 2007] for estimating k taking into account the influence of recovery and of nucleation rate for the case of SIBM.

IV.I.3 Summary

The structural changes observed during annealing of a cold worked metal are well understood and documented: many theories and mechanisms based on experimental observations have been proposed to explain the recovery, recrystallization and grain growth. Thus, it is now possible to interpret, at least on a qualitative level, the microstructure obtained after annealing.

It is shown that recovery is a thermally activated phenomenon based on the release of the elastic internal stresses. For a given amount of strain, the most influential parameters on this process are temperature and SFE. However, the latter can be considered as an intrinsic property of a material. Indeed, SFE determines the extent to which the dislocations dissociate into partials. Therefore, one can qualitatively measure the evolution of the recovery process by measuring the change in mechanical properties such as the hardness of a metal.

Different mechanisms can describe recrystallization process. Namely, nucleation and growth constitute the main features of recrystallization mechanism. Hence, in contrast to recovery process, other parameters are involved in recrystallization. The history of the microstructure of a metal, in particular its initial structure before cold working and annealing, could be considered as one of the key parameters.

Based on this brief literature review, we will attempt to understand the recovery and the recrystallization behavior of 316L austenite stainless steel (low SFE) and 430LNb ferrite stainless steel (high SFE) after heavy drawing. Several parameters may play significant roles in the recovery and recrystallization of both metals inside the composite during manufacturing process of the composite. Indeed, both phases undergo different thermomechanical treatments and therefore their initial microstructure varies from one step to another of the process. In the next section, we present the investigation carried out on the recovery and recrystallization of both metals, which is based on the hardness and microstructural evolution at different annealing conditions.

IV.II Annealing kinetics

IV.II.1 Presentation

The goal of this section is to compare the softening kinetics of the austenitic 316L and ferritic 430LNb alloys within the fine cells up to the n4 composite (i.e. n1 cell) with that of individual wires of each type (i.e. bulk alloys). To do so, bulk alloys should undergo the same deformation as the n1 cell phases of the composite during drawing. In fact, each component of n1 cells (i.e. 316L wire and 430LNb channel) underwent a section reduction of almost 92% compared to its initial size in n3 composite. Therefore, in order to ensure the same conditions, bulk alloy wires are subjected to the same deformation, they were drawn from 5.5mm of diameter down to 1.5mm. Bulk and composite wires are then heat treated in salt bath at tempraturs 750°C, 850°C and 950°C for duration ranging from 5 seconds to 1 hour.

The initial microstructure of both alloys is presented in Figure IV-12. The initial average grain size for 430LNb and 316L is 17 µm and 22 µm respectively. The 316L alloys contains a large amount of growth or annealing twins, illustrating its low stacking fault energy (SFE).

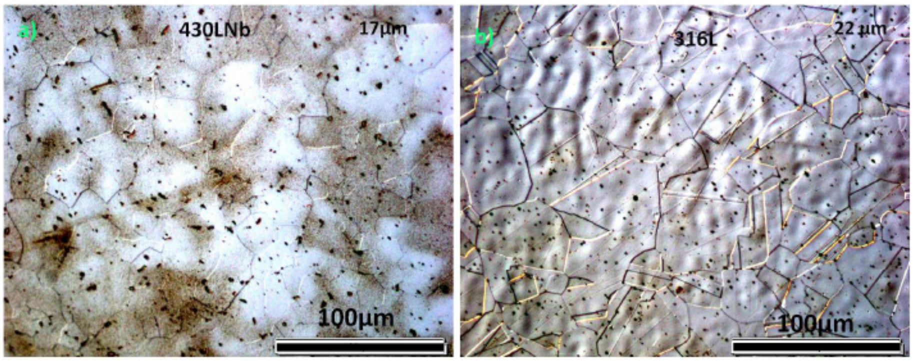

Figure IV-12:Initial microstructure (before drawing) of a) 430LNb b) 316L

On the other hand the initial microstructure of n1 cells in the n4 composite is in fact that inside n3 composite after annealing at 850°C. The averaged grain size diameter for 316L and 430LNb channel is 1.7 µm and 11 µm respectively.

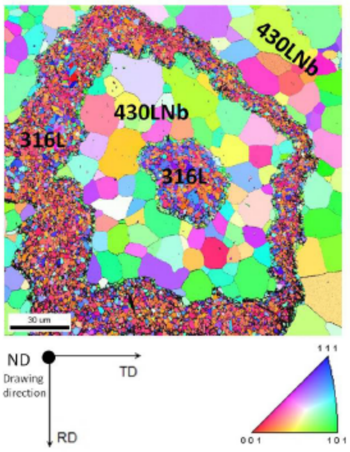

Figure IV-13: Microstructure of n1 cell inside n3 composite after annealing at 850°C

IV.II.2 Annealing kinetics of 316L and 430LNb: bulk wires

IV.II.2.a Annealing at 750°C

i) Grain structure evolution

Figure IV-14 shows the evolution of the grain structure for 316L and 430LNb annealed at 750°C after 92% deformation. It reveals that no large change in grain structure appears after 15 minutes of annealing. After 1 hour the structure of both types shows a slight evolution. Indeed, a significant change can be observed in 316L structure. However, no evidence of the presence of recrystallized grains was found.

On the other hand, some recrystallized grains were observed in 430LNb after 1 hour of annealing. The volume fraction of these recrystallized grains is estimated to be around 5%.

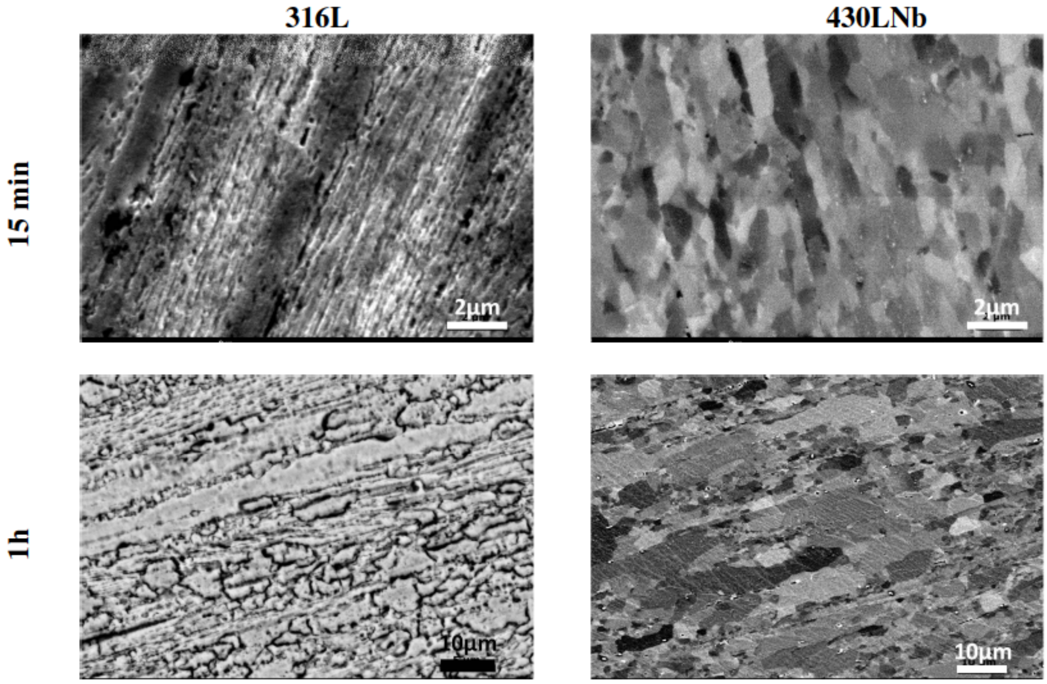

Figure IV-14: Grain structure revealed by electronitric etching and observed in SEM. The left column shows the evolution of the austenite 316L after 15 min and 1 h annealing at 750°C. The right hand side column shows the grain evolution of the ferrite 430LNb after 15 min and 1h.

ii) Softening kinetics

Figure IV-15 presents the softening kinetics of austenite 316L and ferrite 430LNb annealed at 750°C after 92% deformation. One can notice:

- A significant difference in term of hardness in the as-drawn state (t=0 s) between 316L and 430LNb; the austenite is almost 1.5 times harder than the ferrite.

- 316L shows a gradual decrease of hardness as a function of time. However, after 1 hour annealing a step decrease in hardness is observed.

- A linear decrease in hardness is observed in 430LNb despite the unchanged grain structure shown in Figure IV-14.

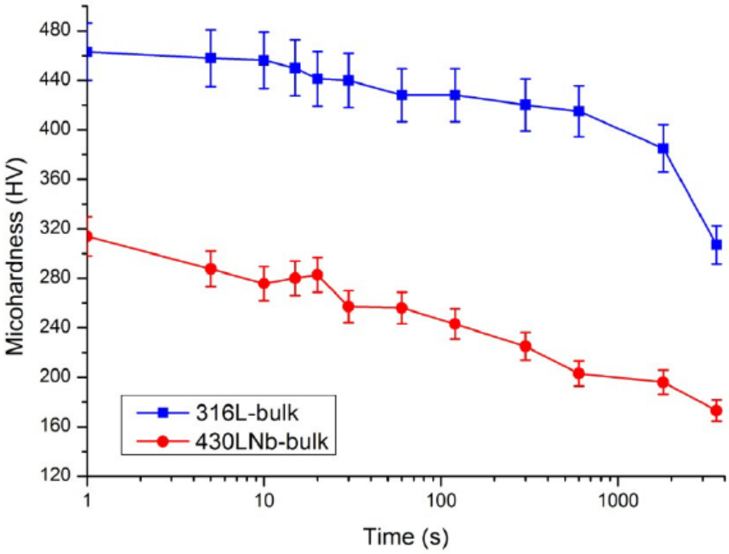

Figure IV-15: Softening kinetics during 750°C annealing treatment in salt bath for 316L and 430LNb deformed by drawing to 92%

IV.II.2.b Annealing at 850°C

i) Grain structure evolution

The evolution of 316L and 430LNb microstructure after annealing at 850°C is illustrated in Figure IV-16. After 5 seconds of annealing, recrystallized grains appear, interrupted by "lamella" which represents the non recrystallized region. Although 316L is more recrystallized than 430LNb after 5 seconds of annealing, the recrystallization fraction evolves faster for 430LNb than it does for 316L. Indeed, for 430LNb, the recrystallization fraction reaches almost 90% after only 15 seconds of annealing and a fully recrystallized structure after 20 seconds whereas 316L starts to get a fully recrystallized microstructure only after 1 hour of annealing (see Figure IV-17).

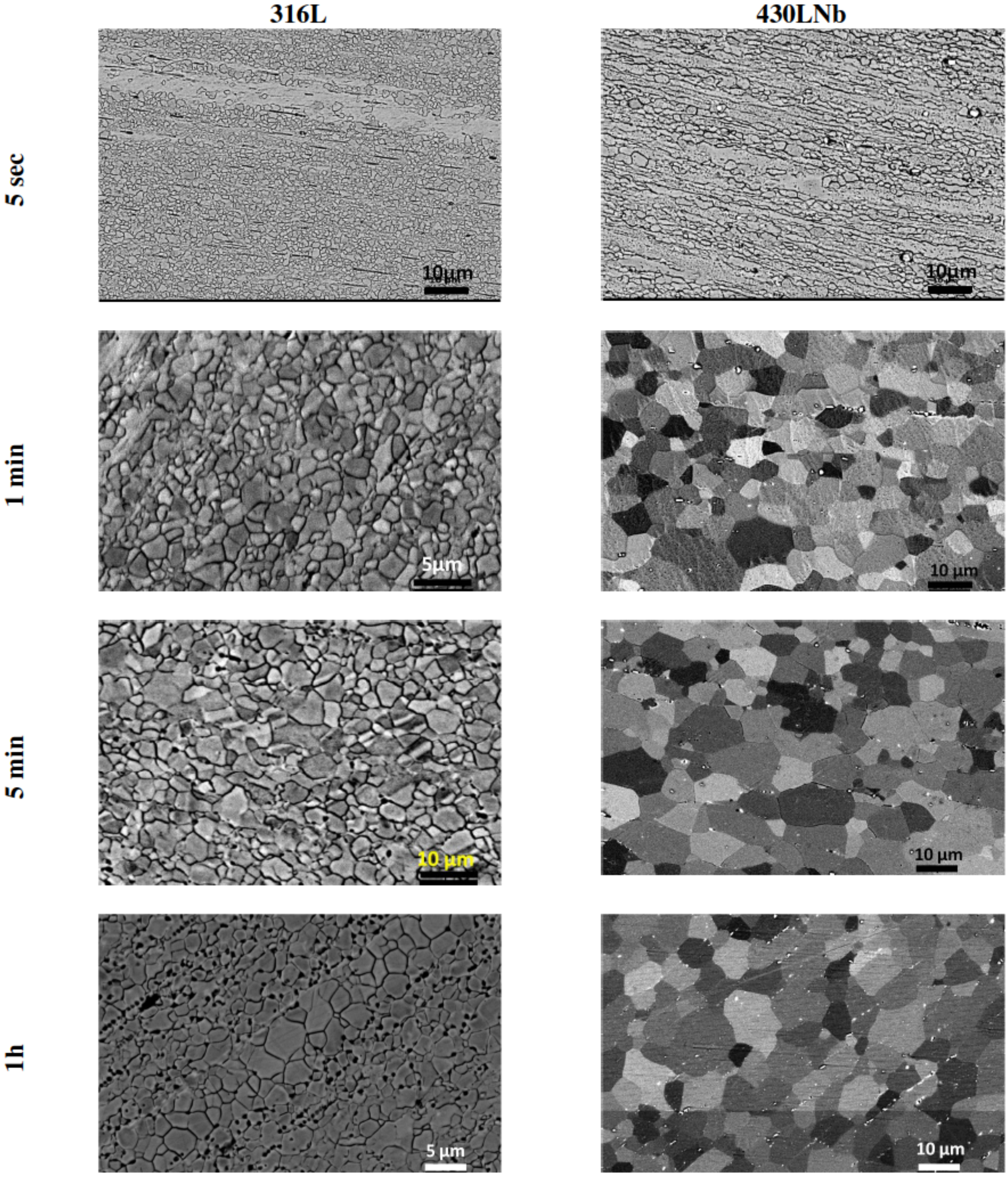

Figure IV-16: Grain structure revealed by electronitric etching and observed in SEM. The left column shows the evolution of 316L (left column) and 430LNb (right column) after annealing at 850°C.

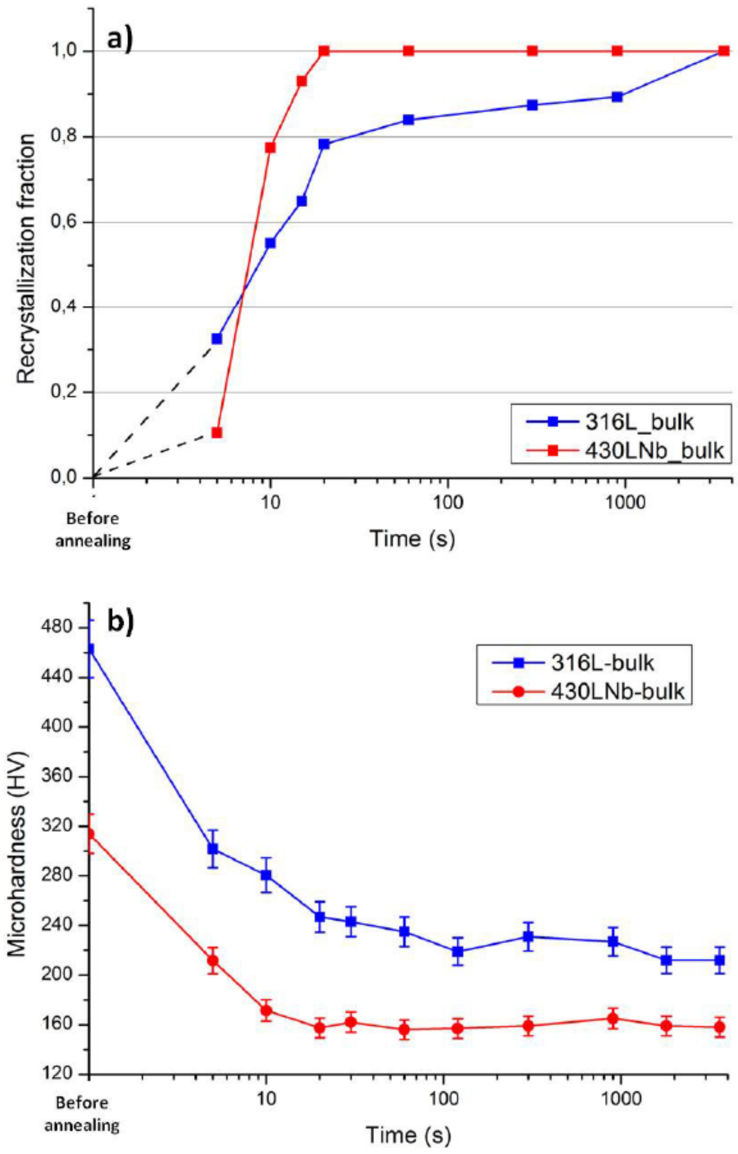

Figure IV-17:Softening kinetics for both 430LNb and 316L (deformed to 92%) after annealing at 850°C in salt bath a) Rex. fraction b) microhardness evolution

ii) Softening kinetics

Figure IV-17.b presents the evolution of the hardness for 430LNb and 316L as a function of time. Both alloys show two distinct stages. A first stage corresponds to the completion of recrystallization where the hardness drops quickly. This stage takes 2 min in the 316 L and only 20s in the 430LNb alloy. Afterwards, the hardness is stable during the investigated annealing time, where the grain growth is not sufficient to result in a significant hardness drop. In addition to the difference in recrystallization kinetics, the austenite is significantly harder than the ferrite during the whole annealing process.

IV.II.2.c Annealing at 950°C

i) Grain structure evolution

Figure IV-18 shows the evolution of the microstructure of both 430LNb and 316L after annealing at 950°C. One can notice that the recrystallization for both materials is very rapid. Indeed, after only 5 seconds of annealing, the recrystallization fraction reaches almost 90%. One can notice also that after full recrystallization the 316L alloy undergoes grain growth whereas the grain size of 430LNb remains stable.

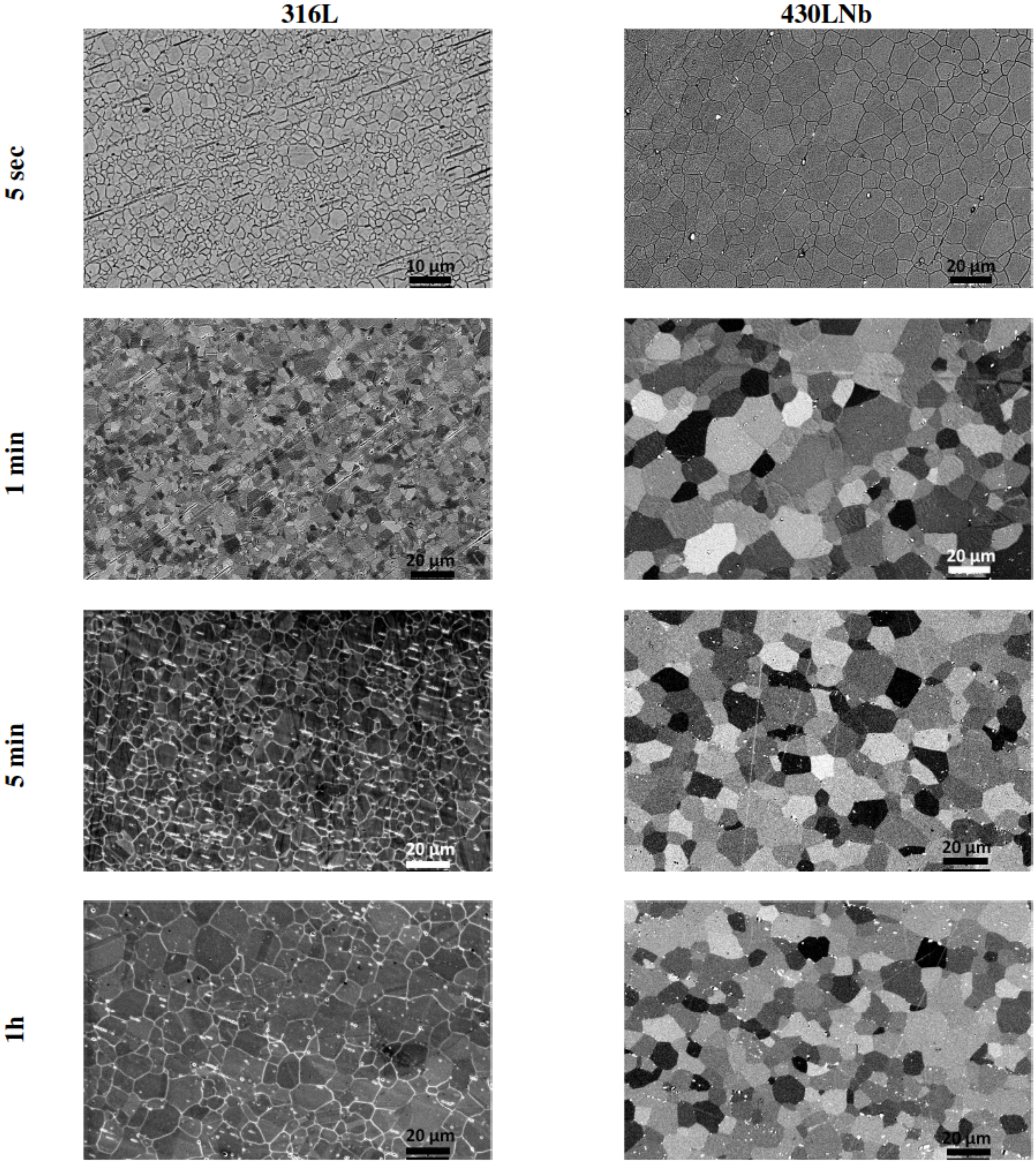

Figure IV-18: Microstructure revealed by electronitric etching and observed in SEM. The left column shows the evolution of 316L (left column) and 430LNb (right column) after annealing at 950°C.

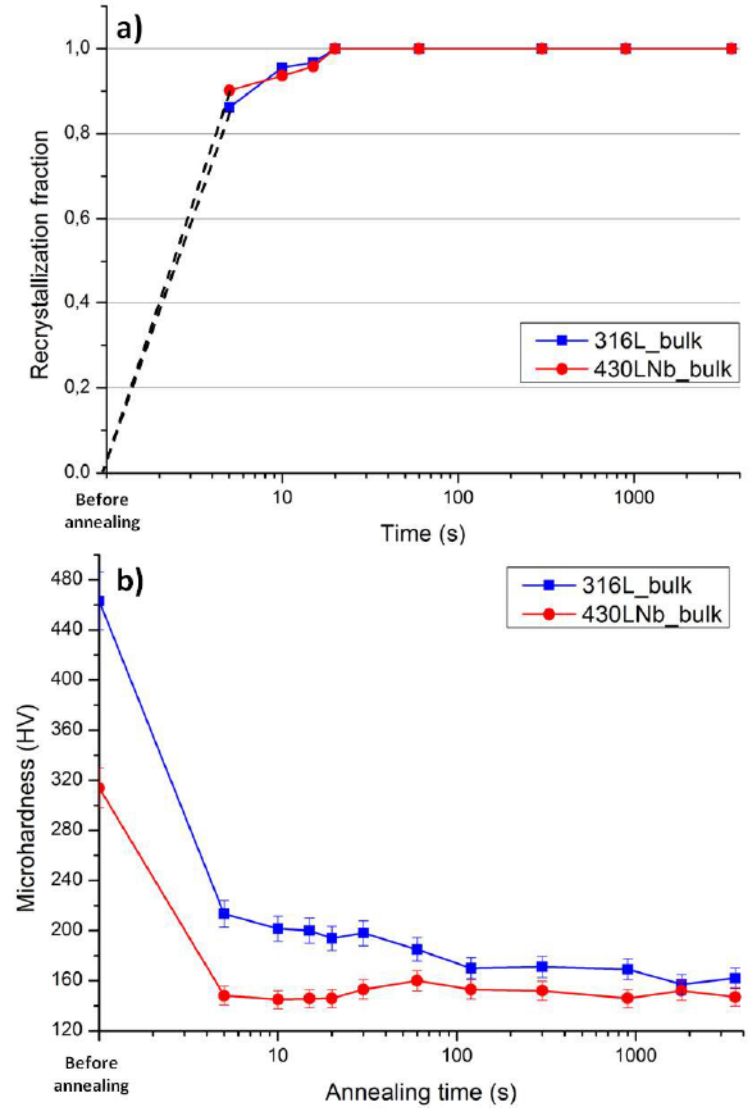

Figure IV-19: Softening kinetics for both 430LNb and 316L (deformed to 92%) after annealing at 950°C in salt bath a) Rex. fraction b) microhardness kinetics

ii) Softening kinetics

The softening kinetics of 316L and 430LNb is presented in Figure IV-19.b. For both materials, one can notice the drastic decrease of hardness after 5 seconds of annealing. Contrarily to the last two cases (750°C and 850°C) the two curves get closer. However, 316L is still slightly harder than the 430LNb even for long annealing duration (1h).

IV.II.2.d Summary

The effect of temperature on recrystallization and softening kinetics of both alloys 316L and 430LNb is summarized in Figure IV-20. One should bear in mind that one of the purposes of this investigation is to find the optimized annealing conditions, for both 316L and 430LNb drawn 92%, for which the ductility is sufficient to continue the process and for which diffusion is minimized to preserve the chemical composition of each phase. In this view, the results show two “extreme” temperatures; 750°C and 950°C. The first is too low i.e. the hardness of both phases, in particular 316L, remains high (above the acceptable hardness value imposed in chapter III for drawing). In addition, no recrystallized grains were revealed in the two alloys except for long ageing times. The second (950°C) shows an instantaneous recrystallization in 316L and 430LNb (almost 90% of recrystallization fraction is reached after 5 seconds of annealing).

However, 850°C represents the intermediate temperature at which the structure of both alloys, particularly 316L, recrystallizes and softens gradually with increasing annealing time. Indeed, only after 1hour of annealing the 316L is fully recrystallized and its hardness value is slightly less than the imposed drawing hardness i.e. 225 HV.

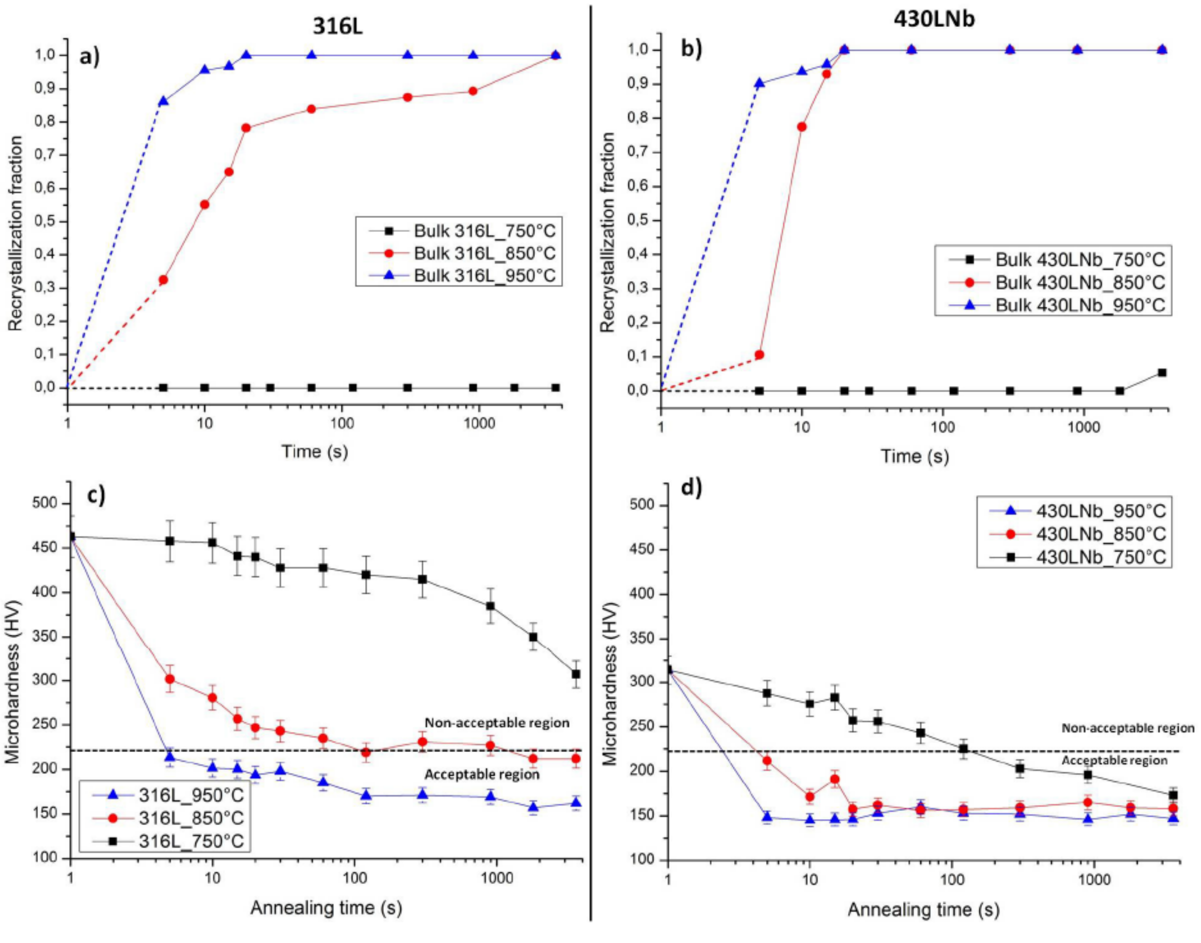

Figure IV-20: Summary of the temperature effect on the recrystallization and softening kinetics, respectively, of 316L; a) and c) and 430LNb; b) and d)

IV.II.3 Annealing kinetics of ADSS composite: n4

In this section, the grain structure and the softening kinetics of the 316L (wire+tube) and 430LNb wires issued from the n1 composite inside the n4 composite are followed during annealing treatments performed on the as-drawn composite. Due to difficulties to reveal the grain boundaries of both austenite and ferrite of the first generation (i.e. n1) inside the composite n4 by chemical etching, EBSD technique was used to evaluate the microstructure evolution. It is necessary to note here that EBSD analysis does not enable to evaluate highly deformed samples, which do not provide usable Kikuchi patterns. This is why only recrystallized microstructures will be presented.

IV.II.3.a Annealing at 750°C

i) Grain structure evolution

Figure IV-21 presents the evolution of the microstructures of the 316L and 430LNb alloys issued from n1 generation inside n4 composite after annealing at 750°C. Both phases are fully recrystallized after 10 minutes of annealing.

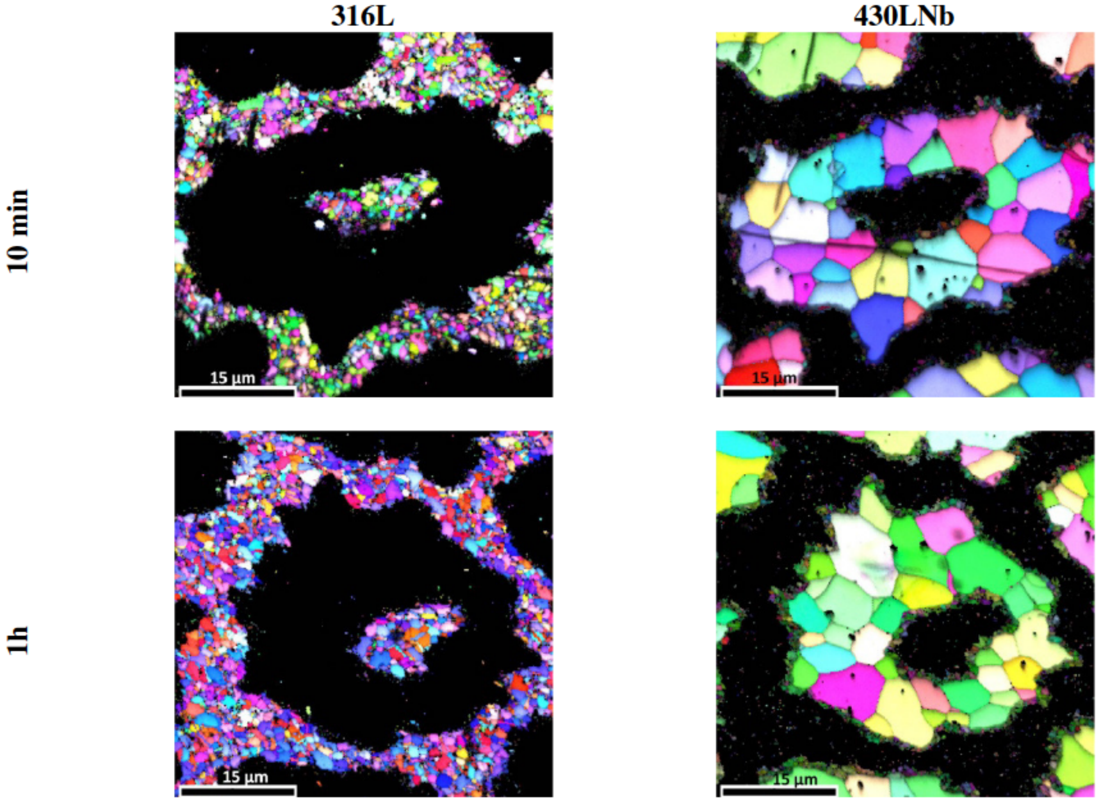

Figure IV-21:EBSD maps of n1 inside n4 composite after annealing at 750°C: the left column is the austenitic phase (colored region) and the right column is the ferritic phase (colored region)

ii) Softening kinetics

The evolution of microhardness as a function of time for 316L and 430LNb inside n4 composite is shown in Figure IV-22. The austenitic phase shows a three stage curve. First the hardness decreases very slowly (HV≈420 HV), the recrystallized fraction being close to 0, which corresponds to a stage of very slight recovery. After 100s, recrystallization starts and results in a large hardness drop. After 300 to 1000s, recrystallization is complete and translates in a new hardness plateau (≈285 HV) with a slow decrease caused by grain growth. The hardness evolution of the ferritic phase, on the other hand, is more gradual. Moreover, the ferrite, in this configuration, is largely softer than the austenite.

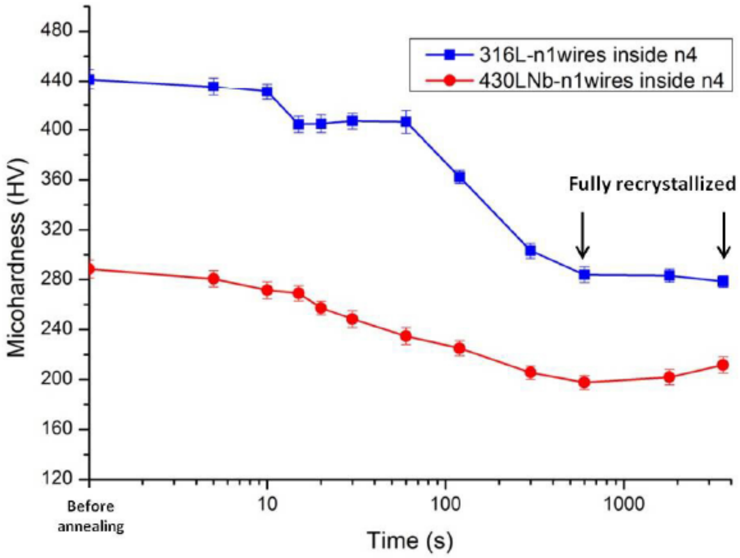

Figure IV-22:Softening kinetics of austenitic and ferritic phase inside the composite n4 after annealing at 750°C

IV.II.3.b Annealing at 850°C

i) Grain structure evolution

The recrystallization of both phases is complete already after 5 second of annealing. One can notice also from EBSD maps in Figure IV-23, the significant increase of grain size of the austenitic phase after 1 hour of annealing. In the ferritic phase, the grain size is from the completion of recrystallization, of the order of the phase size, so that it does not evolve significantly with annealing time. Besides, the small ferritic grains surrounding the large ferrite grains, already observed in Chapter III, increase significantly in size as annealing time increases. This aspect will be treated in the next section of this chapter.

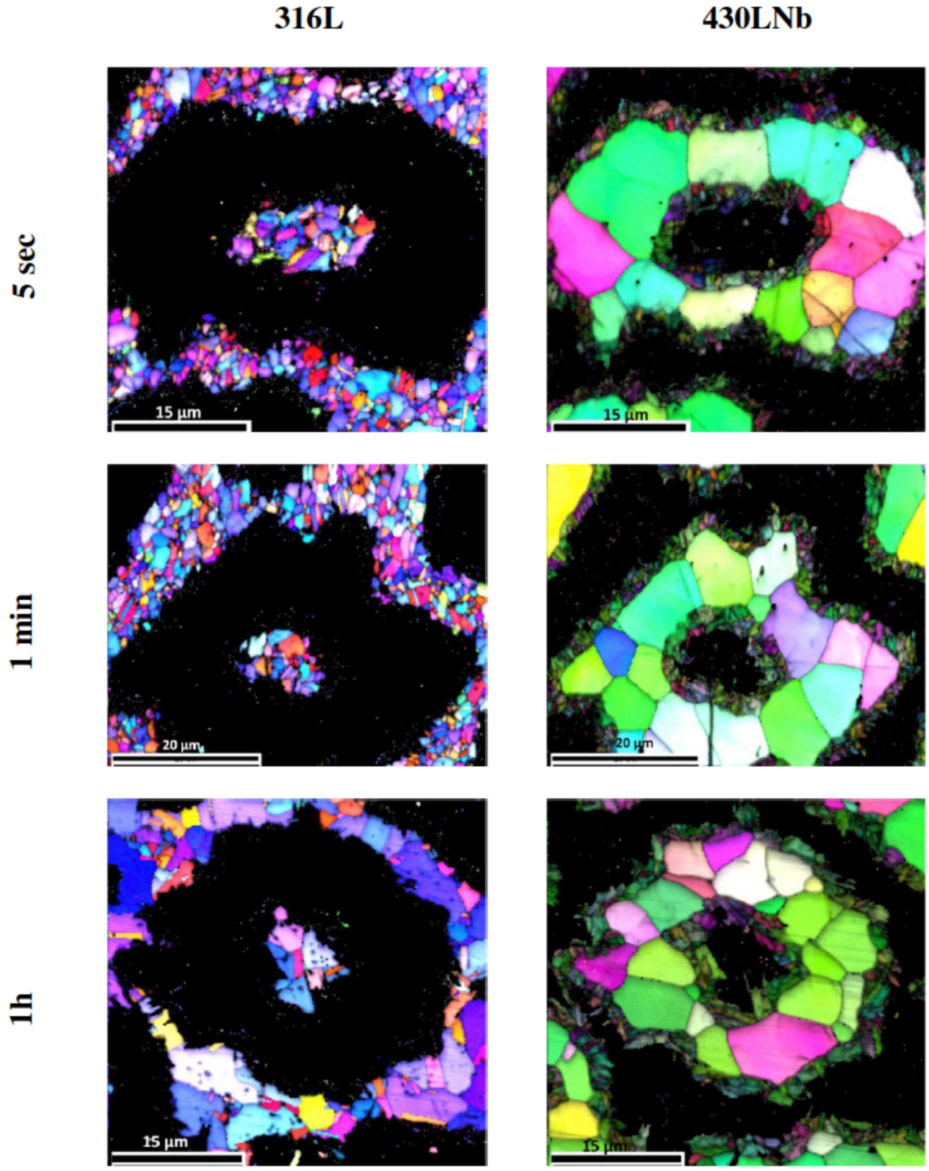

Figure IV-23:EBSD maps of n1 inside n4 composite after annealing at 850°C: the left column is the austenitic phase (colored region) the right column is the ferritic phase (colored region)

ii) Softening kinetics

Figure IV-24 reports the softening kinetics of ferrite and austenite phase. In accordance with the evolution of recrystallized fraction shown in Figure IV-24.a , the hardness drops rapidly to that of the recrystallized materiel, and the austenite and ferrite show a constant hardness of 300HV and 220HV respectively.

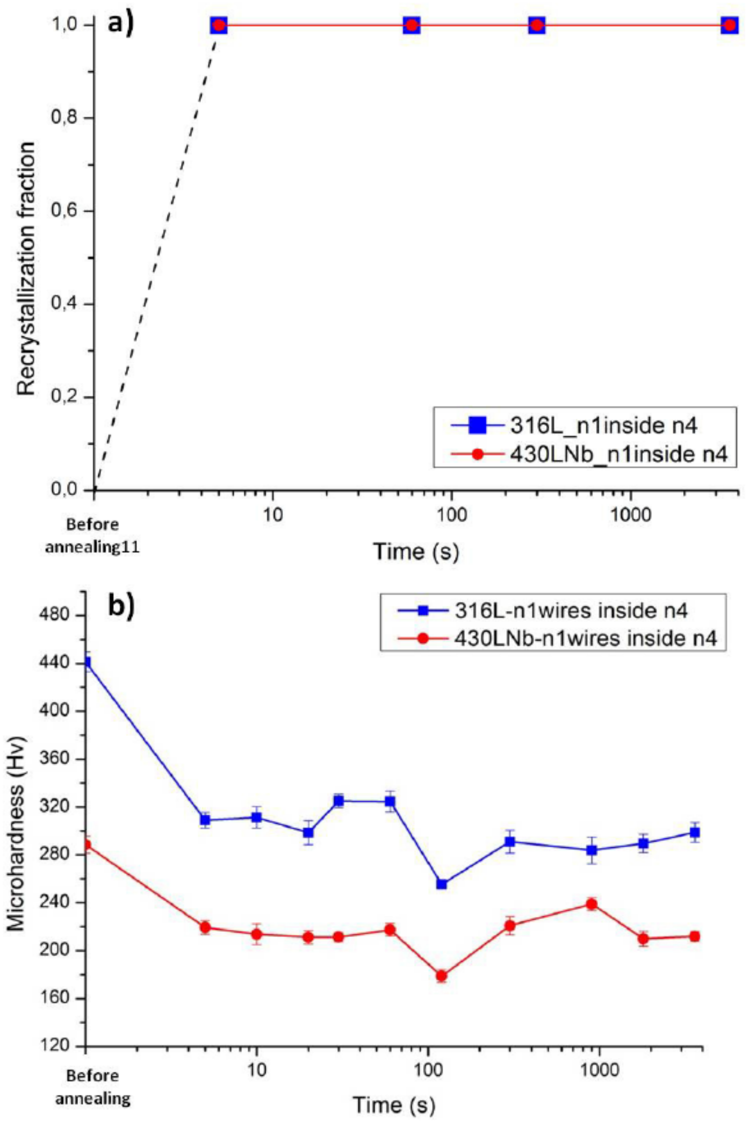

Figure IV-24:Softening kinetics of austenitic and ferritic phase inside the composite n4 after annealing at 850°C

IV.II.3.c Annealing at 950°C

i) Grain structure evolution

Similarly to the 850°C case the recrystallization of both phases at 950°C is complete after 5 seconds of annealing. A significant increase in grain size within the austenitic phase is also observed.

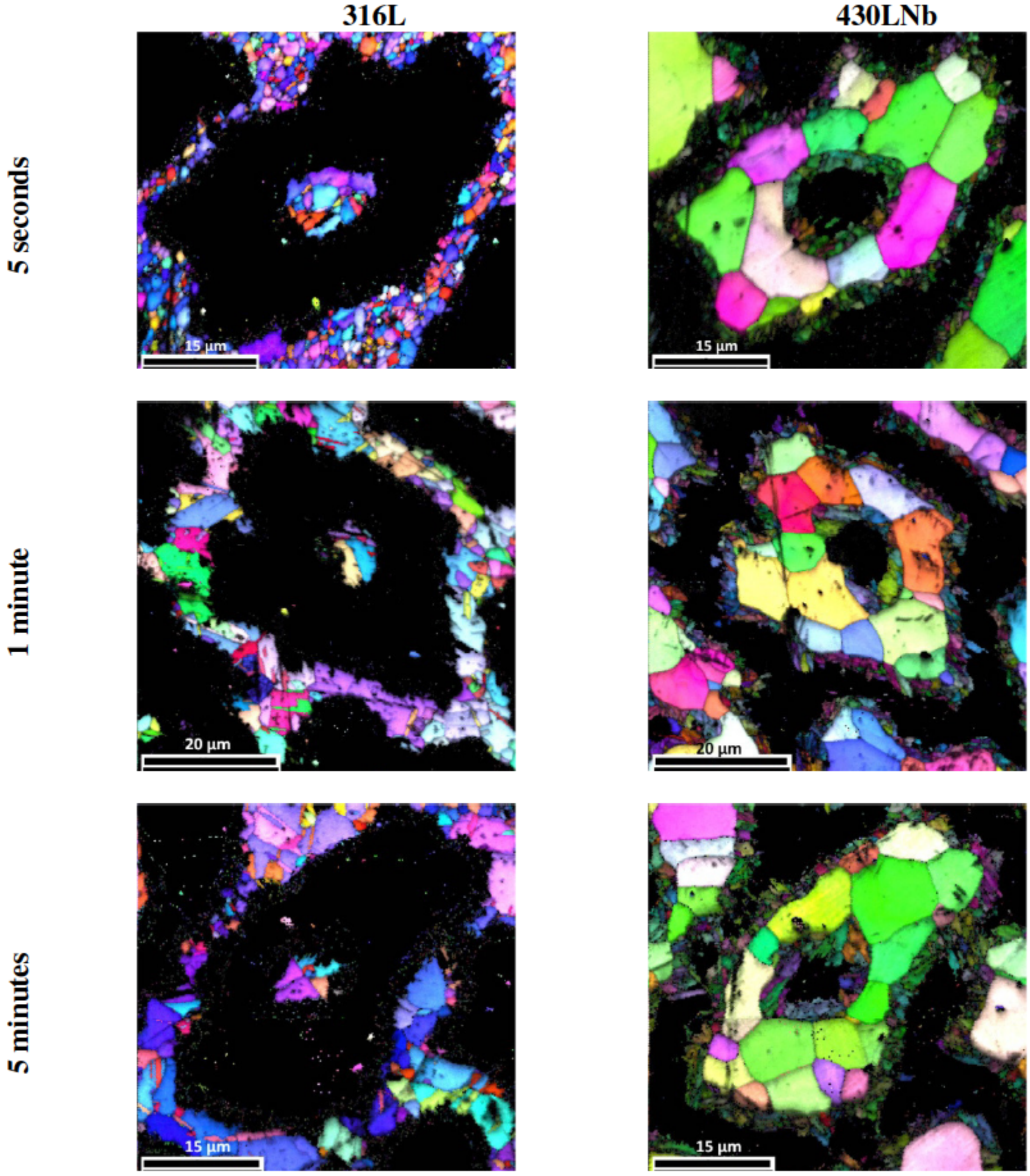

Figure IV-25:EBSD maps of n1 inside n4 composite after annealing at 950°C: the right column is the austenitic phase (colored region) left column is the ferritic phase (colored region)

ii) Softening annealing

The ferritic phase shows constant hardness evolution as a function of time after 5 seconds of annealing whereas the austenitic phase remains stable after 20 seconds. Generally, the austenite is the hardest phase at 950°C for annealing times ranging from 5 seconds to 1 hour.

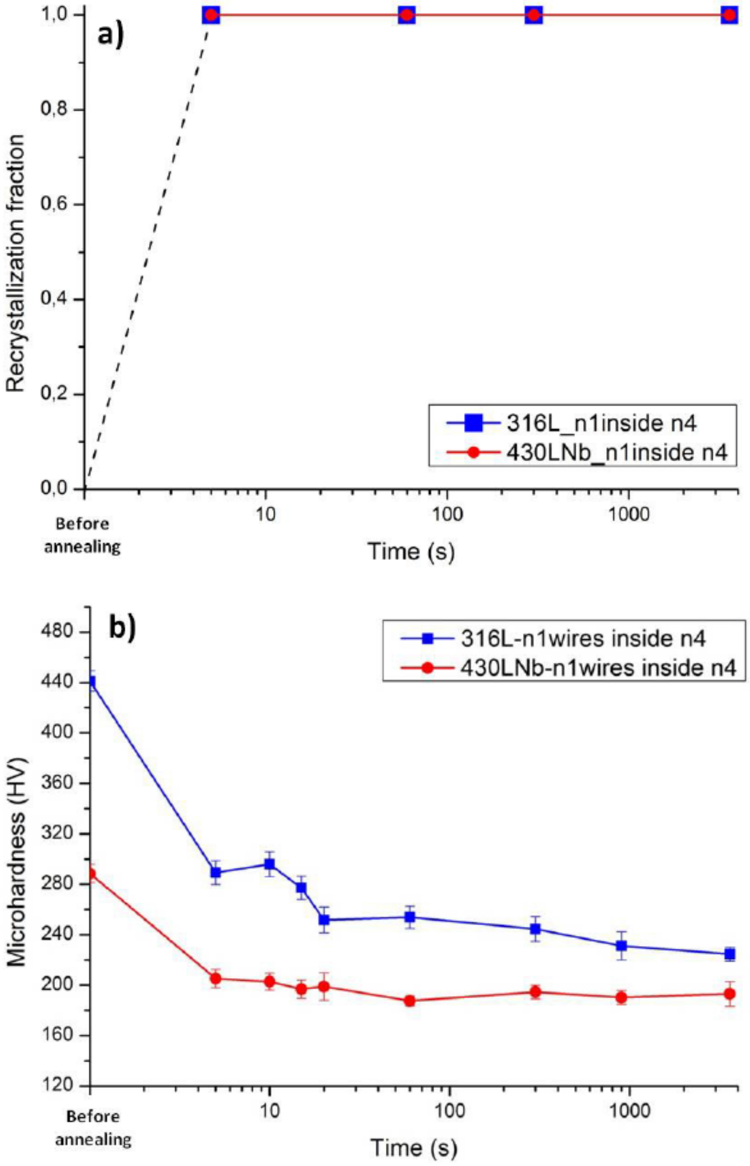

Figure IV-26:Softening kinetics of austenitic and ferritic phase inside the composite n4 after annealing at 950°C

IV.II.4 Comparison and discussion

Before comparing the softening behavior between the bulk wires (individual wires) and those inside the composite n4 issued from n1 generation, the softening curves of bulk state need to be commented first.

IV.II.4.a Individual 316L and 430LNb wires

At 750°C, the microstructure of 316L and 430LNb (Figure IV-14) showed no evidence of complete recrystallization which is confirmed by the softening curves. Indeed, 316L, along the whole annealing times except the longest time (1h) showed a gradual decrease in hardness which is a typical behavior of FCC metals of low SFE during recovery; the slow recovery kinetics is attributed to the low mobility of dissociated dislocations. However, the sudden hardness decrease after 1 hour of annealing shows the onset point for recrystallization.

On the other hand, the ferrite showed a significant and logarithmic decrease of hardness during its recovery despite the mostly unchanged grain microstructure at this temperature even after 1 hour of annealing. This is a typical behavior of BCC metal with high SFE [Humphery 2004].

After annealing at 850°C, both wires (316L and 430LNb) showed a drastic decrease in hardness after only 5 seconds of annealing time, associated to the development of a partially recrystallized microstructure (see Figure IV-17). Before arriving to a fully recrystallized microstructure (15 seconds for ferrite and 1 hour for austenite), 316L and 430LNb are both under the influence of recovery and recrystallization.

At 950°C, the microstructure of 316L and 430LNb is immediately governed by recrystallization process which is in agreement with hardness evolution showing single-stage curves.

Figure IV-27 shows the evolution of the average size of recrystallized grains as a function of annealing time after annealing at 850°C and 950°C. The graphs show only the grain size evolution in completely recrystallized conditions. After annealing at 850°C, the recrystallization of 316L is completed only after 1 hour of annealing time. Its grain size is, however; significantly lower than the initial grain size prior to cold-drawing (22 µm).

For 430LNb, the grain size increases first very quickly and then stabilizes after 20s with a subsequent slow increase. This stabilization could be attributed to the presence of particles pinning the grain boundaries. Indeed, it is found, in ferritic stainless steel stabilized by niobium, that the niobium precipitates first at high temperature as carbonitrides Nb(N,C) in form of relatively large "rod-like" particles ≈10µm in length [Mantel et al. 1990] [Meyer 2008]. The excess of the precipitated Nb forms subsequently very fine (<1µm) intermetallic compounds Fe_2Nb_3 at the grain boundaries. These intermetallic particles have an important recrystallization delaying effect and can hinder the grain growth. This phenomenon is known as Zener pinning. The stabilization by Zener effect is explained by the equilibrium of the competing driving pressure for grain growth against the retarding pressure. Assuming that the precipitates are uniformly distributed at grains boundaries and there is no precipitates coalescence during heat treatment, the equilibrium between the two pressures can be translated by the following formulation:

$$\sum P_i = P_C - P_Z = \gamma \left(\frac{2}{R} - \frac{3f_p}{2r_p}\right) = 0 \qquad \text{Eq. IV-28}$$

Where: $P_C$is the capillary pressure governed by the grain boundary curvature effect, P_Z is the Zener pinning pressure, $f_p$and r_p is the volume fraction and mean radius of the precipitates and γ is the grain boundary energy. This equation allows deriving the critical grain size (R_C) reached by the microstructure as follows:

$$R_C = \frac{4}{3}\frac{r_p}{f_p} \qquad \text{Eq. IV-29}$$

The mass fraction of the Nb precipitated in form of intermetallic can be estimated from the amount precipitated in the carbo-nitrides using the formula given by [Mantel et al. 1990]:

$$\Delta Nb = w_{Nb} - 7.66w_C - 6.57w_N \qquad \text{Eq. IV-30}$$

Direct application of this formula, for our case 430LNb, gives a Nb available for intermetallic precipitation corresponding to $f_{Nb}^{mass} = 0.277\%$ which means a significant effect of Nb on the recrystallization process and the grain growth. Using thermodynamic calculations by Thermo-calc, [Sello 2010] estimated the mass fraction of iron (Fe) present in lave phase for ferritic stainless steel rich of niobium to be around $f_{Fe}^{mass} = 0.522\%$. Assuming that the critical size has been already reached after annealing at 850°C and 950°C, one can calculate the mean radius of the precipitates r_p using Eq. IV-29. The mean radius r_p corresponding to critical grain size of 10.5µm and 17.5µm is 58.2nm and 97nm respectively. The size of the precipitate seems to be reasonable for our annealing conditions.

Generally speaking, the grain size obtained for 430LNb after recrystallization is lower than the initial one as shown in Figure IV-27.

At 950°C, both grades (316L and 430LNb) reached a fully recrystallized state after 15 seconds of annealing. The ferrite shows no increase of grain size during all annealing durations and its size almost equal to the initial grain size, consistently with a limitation by particle pinning, whereas the austenite presents a significant increase of grain size as a function of annealing time, with the ½ time exponent usual of normal grain growth. However, the recrystallized grains of 316L remain lower than the initial ones.

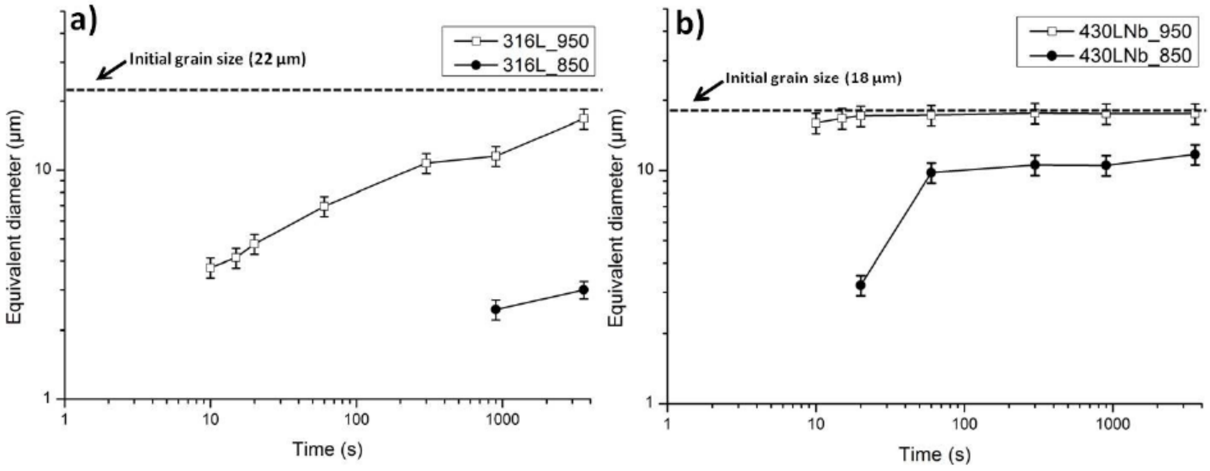

Figure IV-27:Grain size evolution of individual wires as a function of annealing time and temperature a) 316L b) 430LNb

IV.II.4.b Individual wires vs. composite phases

- Annealing at 750°C:

Figure IV-28.a shows the softening behavior in terms of hardness evolution of both phases, ferrite and austenite, in individual wires and inside the composite n4. The austenite inside the composite shows a different behavior than it does as an individual wire. Indeed, while the individual wire 316L at 750°C shows a typical recovery curve as it is indicated in the last section and only starts to recrystallize after 1 hour, the austenite phase inside the composite recrystallizes much earlier; initially it follows almost the same behavior as the individual wire along the recovery process whereas the hardness drop starts after 2 minutes of annealing and stabilizes between 10 minutes and 1 hour of annealing marking, hence, the recrystallization process which has been confirmed by EBSD maps of the grain structure. Therefore, one can conclude that the recrystallization of 316L issued from n1 generation inside n4 composite is faster than it is in the individual wire. This may be attributed mainly to the initial grain size effect. As discussed in the literature review above, smaller grains have a large grain boundary area per unit volume, which promotes the nucleation of recrystallization, since grain boundaries are preferred nucleation sites. In our case, the initial grain size of the austenite in the individual wire (22µm) is in fact much larger than it is in the composite before drawing (1.5µm), due to the recrystallization treatment performed on the drawn n3 wire.

Concerning 430LNb, the hardness evolution of the ferrite phase inside the composite follows the same evolution of the individual ferrite wire until 10 minutes of annealing time where the ferrite starts to stabilize as the austenite phase. Moreover, comparing the microstructure evolution of the individual wire with that inside the composite after 10 minutes and 1 hour of annealing (Figure IV-14 and Figure IV-21), one can notice that the ferrite inside the composite is already recrystallized whereas the grain structure of the individual wire is still deformed. Hence, it can be concluded that the recrystallization of the ferrite inside the composite is also accelerated.

- Annealing at 850°C:

Similarly to 750°C, the onset of recrystallization is accelerated for both phases inside the composite compared to the individual wires. The EBSD maps in Figure IV-23 show that full recrystallization is already reached after 5 seconds of annealing whereas it is of 20% in the individual wires. However, the hardness of both phases (316L and 430LNb) inside the composite is significantly higher than it is in the case of individual wires as Figure IV-23.b shows. This is mainly attributed to a difference in grain size developed in the two cases for both phases. Indeed, the grain size of 316L individual wire in the fully recrystallized conditions is between 2-3 µm whereas the austenitic phase inside the composite is between 1.5-1.7 µm for duration between 5 seconds and 5 minutes. After 1h of annealing, the grain size increases suddenly to 3 µm (See Figure IV-29.a). Despite this increase at 1hour the austenitic phase inside composite remains harder than the 316L in the individual wire. This may be attributed to the change in the chemical composition within 316L wire especially after 1 hour of heat treatment at which a significant diffusion of elements of substitution or even interstitial elements such as N has occurred between 316L and 430LNb (see next section).

On the other hand, the effect of grain size on the hardness evolution is more obvious in ferrite than austenite. Figure IV-29.b shows the evolution of the grain size in the individual 430LNb wire and 430LNb inside the composite. Once both phases are completely recrystallized, the grain size of the latter is slightly lower than that of the individual wire. As the grain size of the 316L inside the composite shows almost a power-law increase with the annealing time, the grain size of 430LNb inside n4 composite, similarly to that of individual wire, tends to stabilize. As discussed above, this could be attributed to the particles pining within the grain boundaries. The grain size in both cases is quite close (10µm in bulk and 8µm in composite).

- Annealing at 950°C:

The same observation can be noticed in the case of annealing at 950°C; recrystallization is accelerated for both phases inside the composite, and the two phases are harder than the individual wires. The difference in grain size in this case is clearer than at 850°C. For 316L, the grain size inside the composite is around 5 µm at most whereas the grain size of the fully recrystallized wire ranges between 5-17 µm, see Figure IV-29.c.

A stabilization of the grain size of 430LNb inside the composite is also noticed. However, the grain size of the bulk wire (17µm) is significantly larger than 430LNb in n4 composite (10µm). In addition to the particle pining effect, in the composite, the size and the shape of the 430LNb channel could also play partly a role in this stabilization.

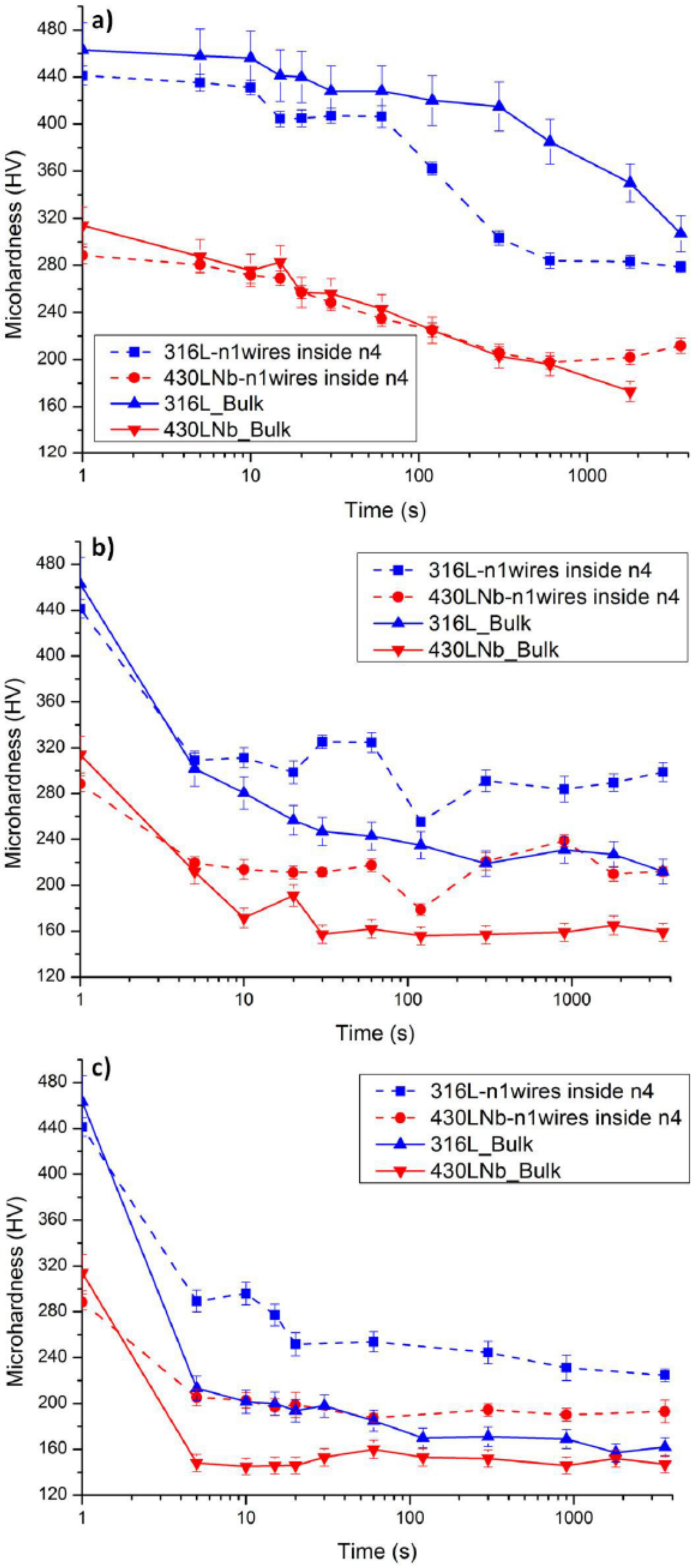

Figure IV-28:Hardness evolution as a function of annealing time and temperature of 316L and 430LNb in both cases bulk state and n4 composite a) 750°C b)850°C c)950°C

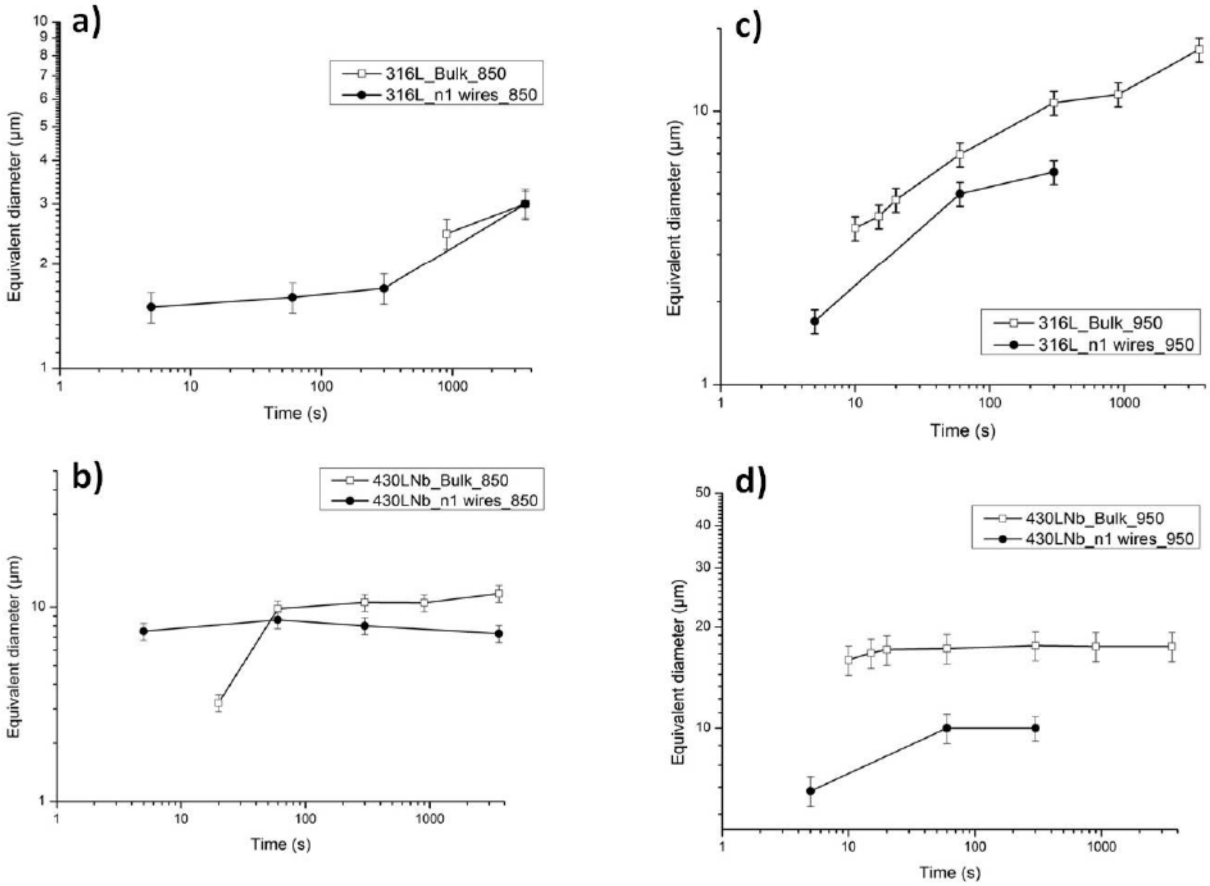

Figure IV-29:Grain size evolution as a function of annealing time and temperature of 316L and 430LNb in both cases bulk state and n4 composite a) 316L at 850°C b) 430LNb at 850°C c) 316L at 950°C d) 430LNb at 950°C

IV.II.4.c Complementary investigation

Until now we have presented the recrystallization kinetics of bulk 316L and 430LNb wires subjected to the same thermomechanical treatments as the 316L and 430LNb issued from n1 generation inside n4 composite. It is interesting also to compare the softening kinetics of individual wires and composite phases but issued from other generation of composites. As presented in Chapter III, the n4 composite contains different generations of austenite and ferrite, which have each undergone a different sequence of thermo-mechanical treatments. The n2 channels issued from the 2nd generation (that underwent 3 co-deformation and 3 softening annealing) are chosen for the ferritic phase, and the n3 channels issued from the 3rd generation (that underwent 2 co-deformation and 2 softening annealing) for the austenitic phase. Figure IV-30 shows the hardness evolution of these generations compared with the bulk state and the n1 wires, during recrystallization treatments.

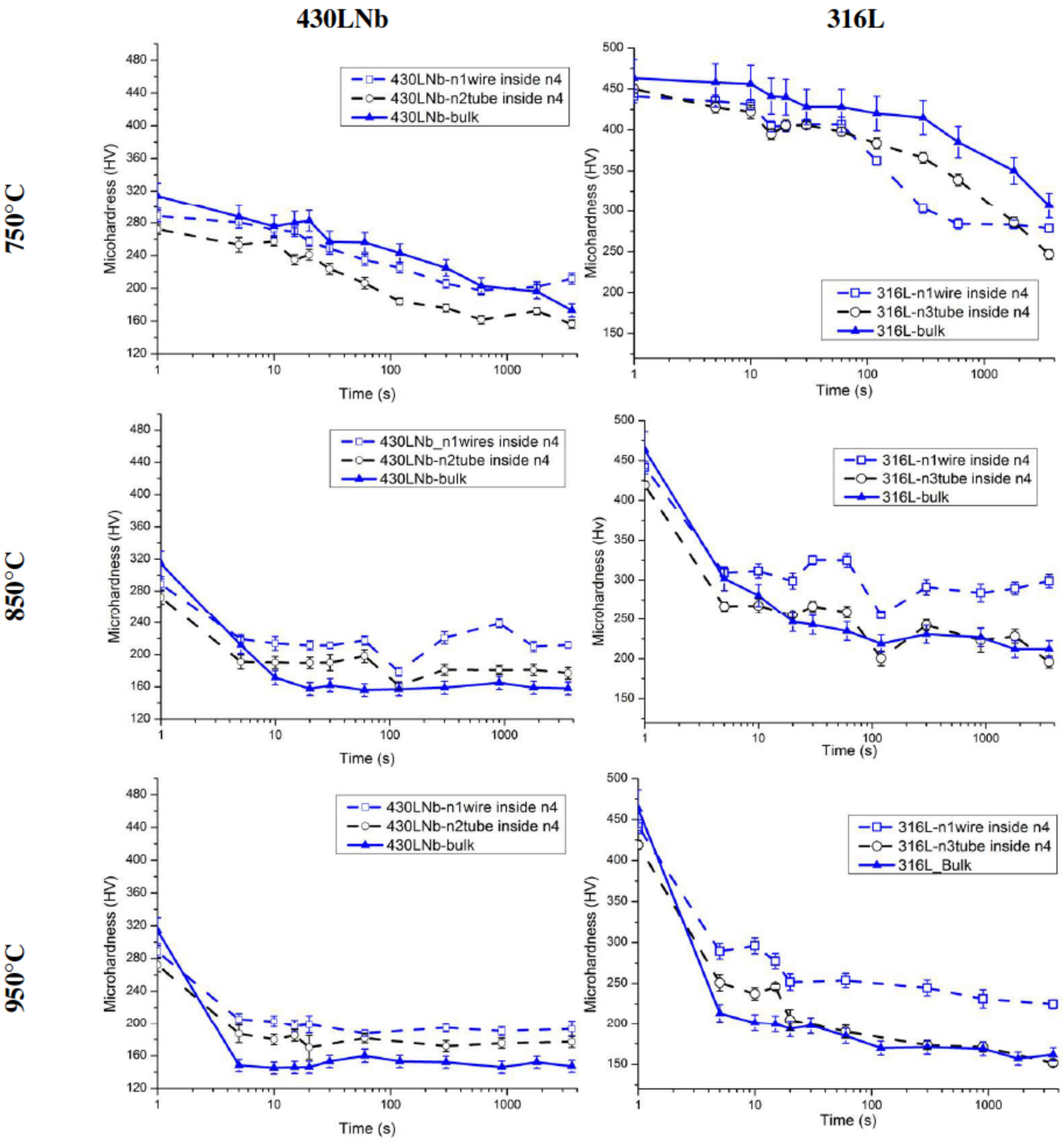

Figure IV-30: Softening kinetics comparison between individual 316L and 430LNb wires and different generation of the same phases inside n4 composite: right hand 316L and left hand 430LNb

The following comments can be made on the graphs shown in Figure 30:

- 430LNb:

At 750°C, the n2 channels follow almost the same trend as the ferrite phase of the first generation (n1) and bulk wire. However, after 850°C and 950°C, one can notice i) a significant decrease of n2 channels hardness and the stabilization of hardness value around 180HV for both temperatures and ii) the hardness curve of n2 channels is observed to be perfectly between the ferrite issued from n1 generation and the bulk 430LNb wire. This result is expected and may be mainly attributed to the grain size effect of the recrystallized grains between i) ferrite of n1 generation and n2 channels ii) both ferritic generations inside n4 composite and bulk 430LNb wire.

- 316L:

Although, the softening behavior of the n3 channels, at 750°C, has the same trend as the bulk wire, the curve is significantly lower. One can deduce from the shape of the graph that recovery plays a major role for n3 channels similarly to the bulk wire. Recrystallization occurs at times intermediate between the n1 generation and the bulk wire. After 850°C and 950°C, the n3 channels takes more and more the same curve as the bulk state in particular at 950°C where the curves are almost similar.

Even though, the initial grain size of n3 channels before drawing is much smaller (4.5 µm) compared to the one of the bulk wire (22µm), it does not seem critical for the softening kinetics.

IV.II.5 Summary

- ✓ For individual 316L and 430LNb wires drawn to 92%:
  - No recrystallization evidence has been observed at 750°C for both 316L and 430LNb except after 1 hour of annealing time. The softening kinetics is governed mostly by recovery.
  - At 850°C, 430LNb shows a faster recrystallization rate than 316L. The latter is fully recrystallized only after 1 hour of annealing time.
  - At 950°C, the recrystallization of both wires is very fast; 90% of recrystallization has been reached after 5 seconds.

- ✓ 316L and 430LNb issued from n1 generation inside n4 composite:
  - Compared to the bulk wires, the softening kinetics is accelerated. Evidence of recrystallization has been found by EBSD maps for durations between 10 minutes and 1 hour at 750°C.
  - At 850°C and 950°C, the recrystallization rated is also accelerated and very fast at these temperatures. However, the n1 phases are harder than the bulk wires.

- ✓ Comparison between other generations of 316L and 430LNb inside n4 composite shows that softening kinetics, for a given phase, is dependent on its generation.

- ✓ The effect of the grain size is found to be very significant either in rate of recrystallization or in the softening kinetics.

IV.III Diffusion analysis

IV.III.1 Presentation

In chapter III, we have shown that due to the recrystallization heat treatments necessary for repeating the drawing between each generation of composite, interdiffusion between the two phases occurred, resulting in a loss of the initial two phase microstructure and therefore in a limitation of the microstructural refinement achievable to the n5 generation. The strategy we adopted to understand the microstructure perturbation of n5 composite is first to go back to each manufacturing step and analyze them; second to rationalize these experiments using thermo-kinetic Dictra simulations for understanding and predicting the final n5 microstructure.

For this, diffusion analysis using EDS technique was performed to measure the concentration profile through 316L wire and 430LNb from the initial step (i.e. n1 composite) up to n4 composite. Figure IV-31 shows the region of interest for both experimental and modeling analysis.

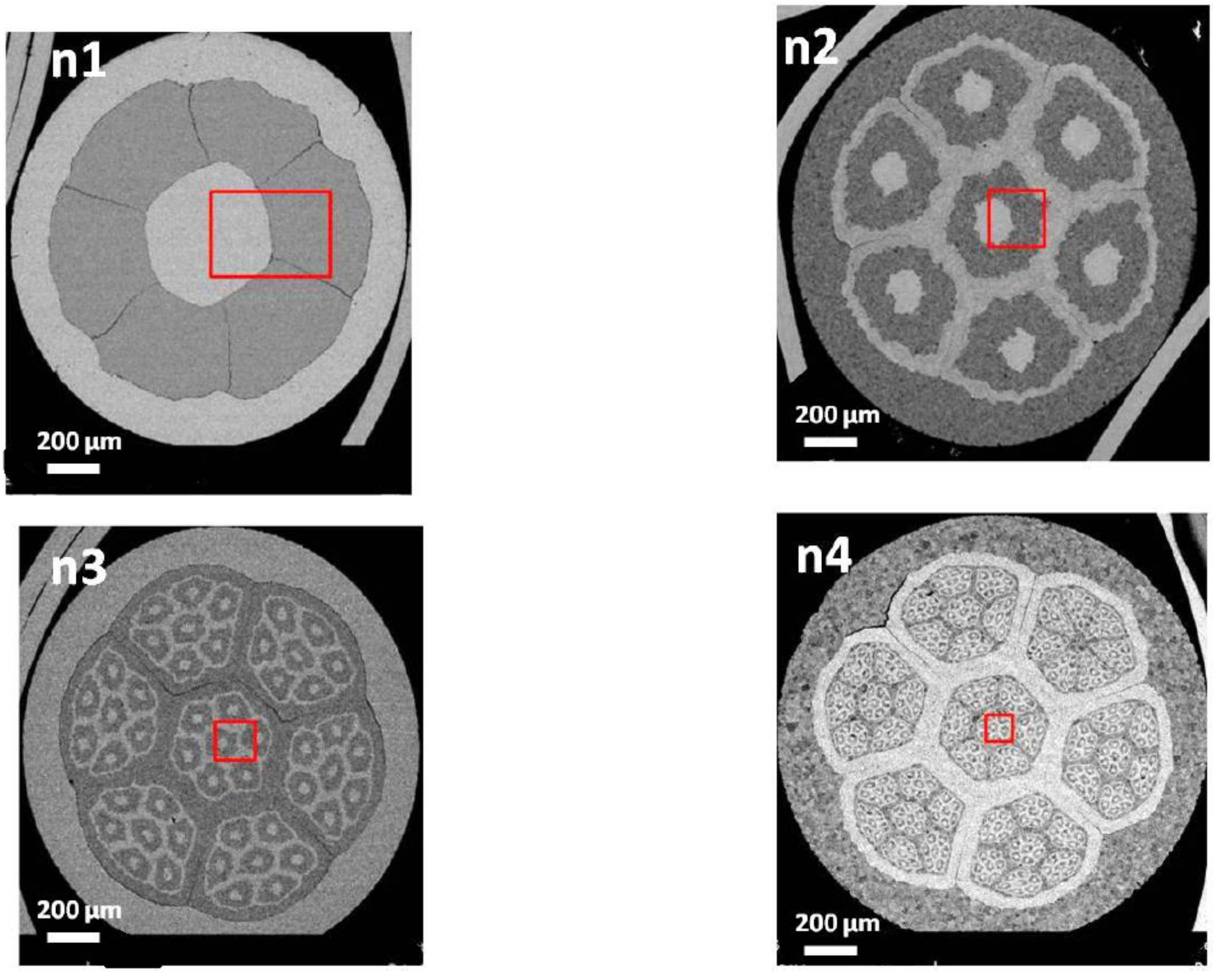

Figure IV-31:Composites n1, n2,n3 and n4 : the red square indicates the zone of interest for our analysis in two cases before and after annealing

IV.III.2 Experimental results

IV.III.2.a Ni diffusion during manufacturing steps

Figure IV-32 illustrates the experimental measurements of the Ni concentration in the diffusion couple 316L/430LNb of n1 composite and n1 cell inside composite ni (i=2,3 and4) before and after annealing during manufacturing steps.

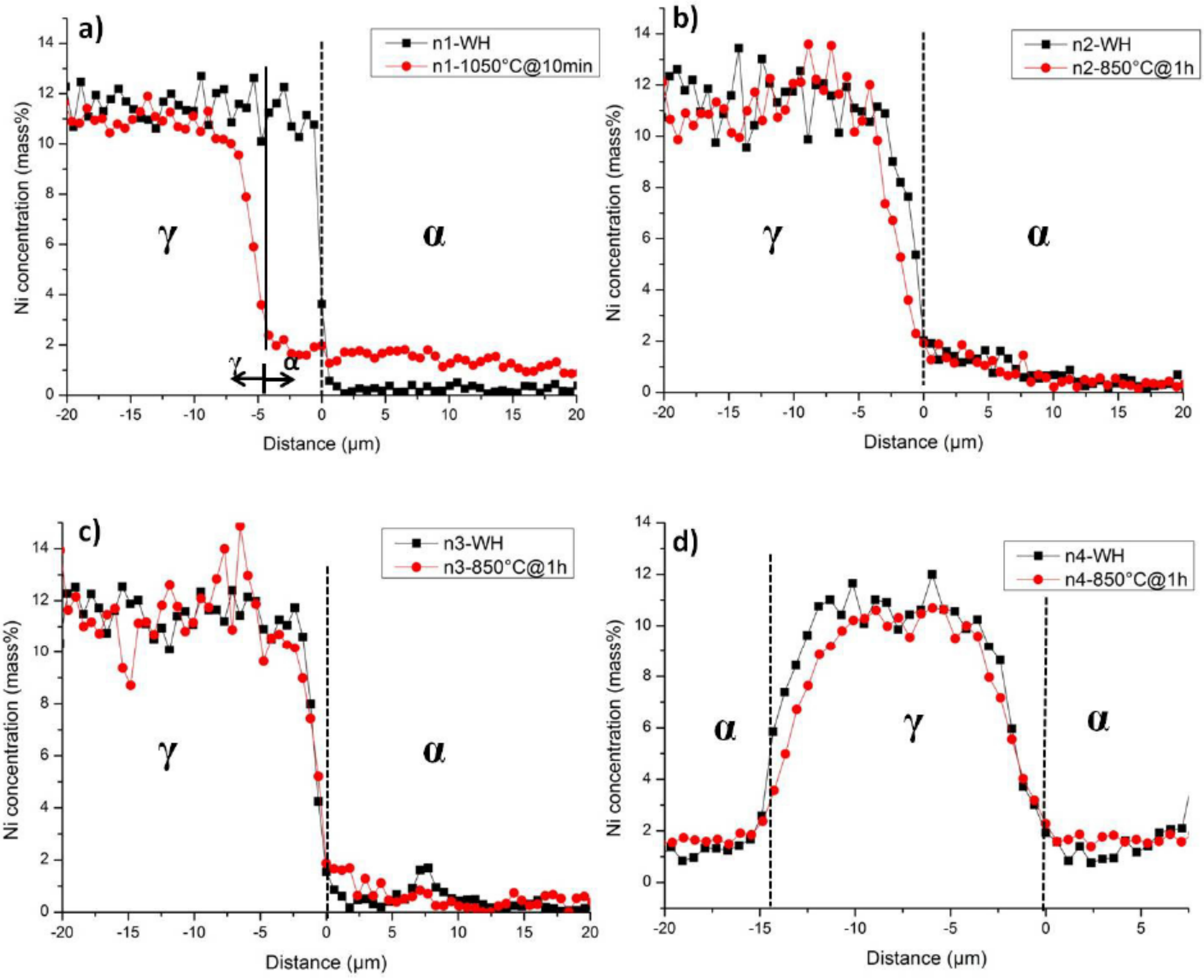

Figure IV-32:EDX profiles for Ni along 316L/430LNb interface at each step of manufacturing before and after annealing treatment: a) n1 composite b) n1 cell inside n2 c) n1 cell inside n3 d) n1 cell inside n4

The nickel composition profile of the first composite n1 is shown in Figure IV-32.a. The as-drawn (Work-hardened WH) concentration profile reveals a sharp interface between both phases α and γ which is considered as the initial state. As discussed in Chapter III, the n1 composite was annealed at 1050°C (1323 K) for 10 minutes holding time in a vacuum furnace with a heating rate of 70°C/h. The resultant nickel concentration evolution is reported in Figure IV-32.a. As a result of this annealing treatment, a significant migration of the α/γ interface towards the austenitic phase (almost 4-5 µm) is observed; i.e. 4-5µm of the austenitic phase is transformed into ferrite. Within the vicinity of the migrated interface, one can notice a gradient of Ni concentration. Besides, a significant increase in terms of Ni concentration in the α phase is clearly observed. Indeed, Ni concentration, across the analysis distance jumps from 0.2% (initial Ni concentration in 430LNb) to 2%. However, the bulk concentration can still be reached beyond 20µm of the ferritic phase.

A different behavior is noticed in composite n2. In the work hardened state, the profile corresponds to the profile after heat treatment of the n1 composite, scaled by the drawing deformation of 92% experienced by the n2 composite. Due to the decreasing scale of the microstructure, annealing parameters were changed compared to the n1 composite. After heat-treatment at 850°C for 1 hour, only a small migration of the α/γ is observed in Figure IV-32.b. However, the diffusion profile of the as-drawn state shows already a concentration gradient within the vicinity of the interface. This gradient becomes larger once n2 composite is heat-treated. In addition, one can observe the diffusion gradient of nickel into the ferritic side; Ni concentration reaches 2% near the interface and decreases smoothly to the nominal concentration (0.2%) beyond 10µm from the interface. This trend is quite similar between as-drawn and annealed state.

Similarly to n2 composite, a region of depleted Ni is developed in the austenitic phase near the interface with ferrite in the n3 composite. This region appears in both cases before and after annealing. However, contrary to n2, the gradient of Ni concentration seems to be unchanged after annealing compared with that of the as-drawn state. On the other hand, in α side and near the interface, Ni concentration is higher in the annealed state (it reaches 2% along 5µm from the interface) than that before annealing (<1%).

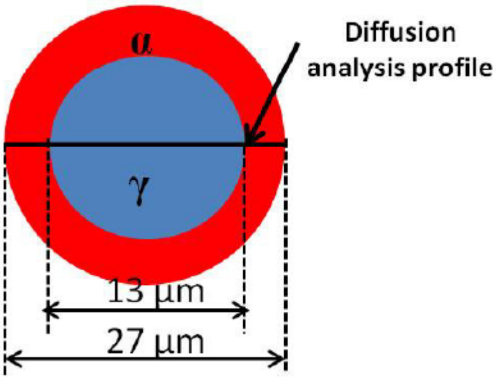

Figure IV-33:Schematic illustration for n1 cell inside n4 with the diffusion analysis profile

Arriving to n4 composite where n1 cells are smaller, the diffusion analysis distance (30 µm) covers the entire n1 cell (i.e. Ferritic channel and 316L wire) contrarily to the last steps (see Figure IV-33). In this case, the difference in concentration gradient before and after annealing is clear. As observed in n2, the gradient of Ni concentration at both interfaces with γ is larger after annealing treatment. The concentration of Ni in α channel is significantly higher for both cases (before and after heat treatment) than that of bulk concentration (1.5-2% compared to 0.2%).

IV.III.2.b Martensite formation

i) ***Ms evolution***

We showed in the last paragraph that for all manufacturing steps, the γ phase is depleted, in terms of Ni content, near the α/γ interface, causing a destabilization of the 316L. This depleted region promotes a transformation into ferrite but also a transformation into martensite upon cooling from the recrystallization treatment when still in austenite, but when Ms is above room temperature. [Pickering 1984] developed the following formula to predict Ms for austenitic stainless steels:

$$Ms=502-(810*\%C+1230*\%N+13*\%Mn+30*\%Ni+12*\%Cr+54*\%Cu) \qquad \text{Eq. IV-31}$$

Using the values of the different elements measured by EDS, the evolution of MS temperature across α/γ is calculated with the above equation. Regarding carbon and nitrogen, in addition to their low content in both 430LNb and 316L, they are considered as "light" elements and not easily detectable by standard EDS measurement. Therefore, in the current analysis, carbon and nitrogen content is assumed to be unchanged during the heat treatment (realized in vacuum furnace). Thus, the nominal compositions of these two elements have been used in the calculation of Ms.

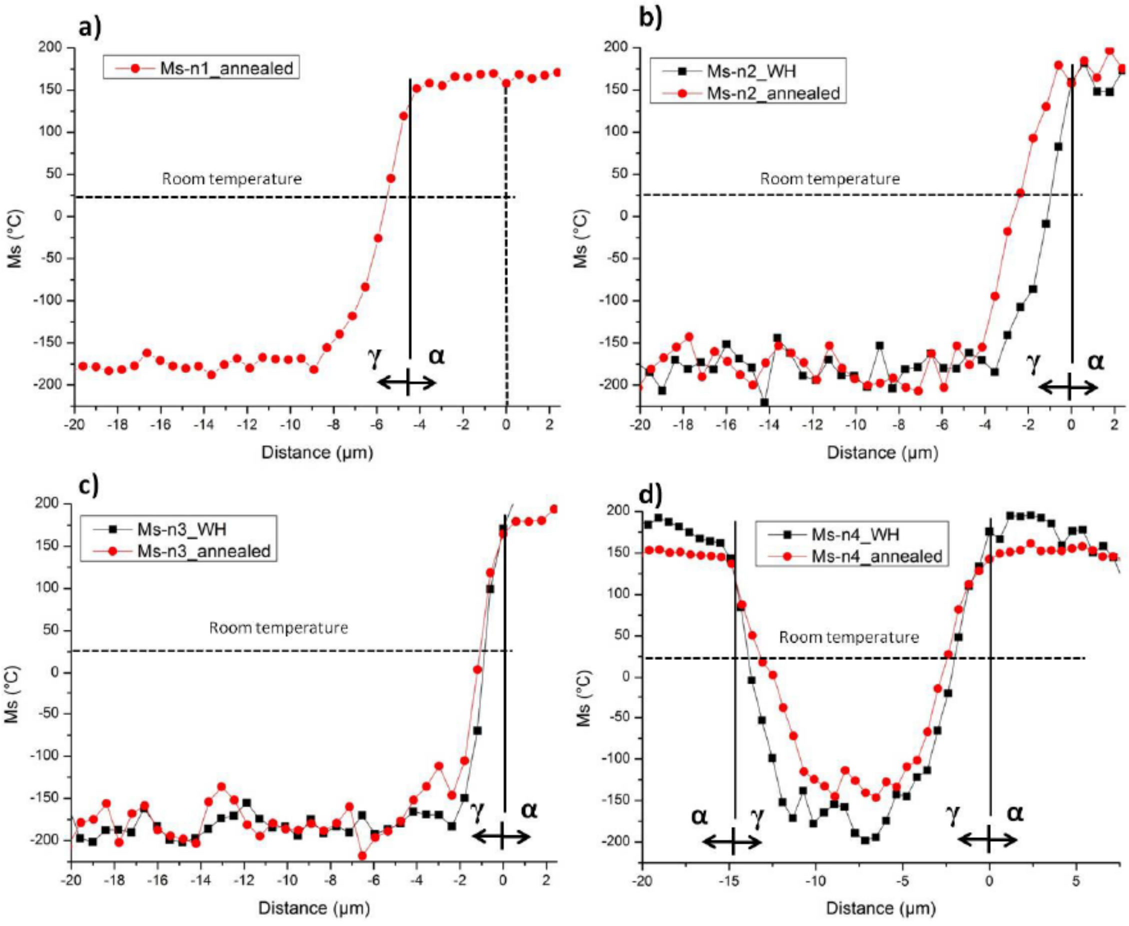

Figure IV-34:Ms evolution as a function of distance at each manufacturing step

Figure IV-34 shows the evolution of Ms as a function of distance for each step before and after annealing. These results show that a martensite layer is expected to form at the interface between austenite and ferrite during cooling following the annealing treatment.

Table IV-1 shows the thickness of the martensite layer predicted from the diffusion measurements after each step. These values are measured as the distance between the start of Ni concentration gradient near α side and the point where Ms crosses room temperature beyond which the martensite will stop forming. One can notice from the thickness values reported in Table IV-1:

- The martensite thickness is almost constant and ranges between 1-2.5 µm for all manufacturing step.
- The martensite layer is larger after annealing.

Table IV-1: Martenisite thickness within 316L/430LNb interface at each manufacturing step

	Martensite thickness (µm)	
	As-drawn	Annealed
n1	0	1.3 (1050°C@10 min)
n2	1	2.3 (850°C@1h)
n3	1	1.2 (850°C@1h)
n4	1-1.5	2-2.3 (850°C@1h)

ii) TEM observations 316L/430LNb interface

In order to confirm the predicted martensite formation within the vicinity of the interface α/γ, TEM observations were performed within the n4 composite. Using FIB preparation, thin foils were cut from n1 cells inside the n4 composite as illustrated in Figure IV-35. The TEM samples were observed in the wire direction. Two samples were prepared; before and after annealing.

Figure IV.35 shows a TEM image of the α/γ interface after annealing. One can notice from figure Figure IV.35.a that the martensite is located on the left side of α grains. The martensite layer exhibits a lenticular structure. Thanks to ACOM-TEM, this layer is identified as BCC phase. We can notice also from Figure IV.35.c the expansion of BCC phase towards the austenite. The thickness of this layer is not constant along the interface. It varies from 1 to 3 µm. Besides, TEM-EDS maps have been also performed to analyze elements distribution (in particular Ni) across 316L/430LNb interface (Figure IV-36). The nickel gradient within the martensite layer is higher compared to the ferritic phase. These maps reveal also the formation of some precipitates rich in chromium and molybdenum. These precipitations seem to be formed in the γ phase and in the vicinity of the martensite layer.

316L/430LNb interface in the as-drawn state, Figure IV-37, also shows clearly the presence of a martensite layer, which has an elongated lamellar structure along the wire axis. The thickness of this layer, according to ACOM images in Figure IV-37.c, reaches 3 µm. similarly to the annealed case, chemical analysis shows that the martensite layer is richer in terms of Ni content than the ferritic phase. Moreover, the same precipitation observed in as-annealed state appeared in the as-drawn case Figure IV-38.

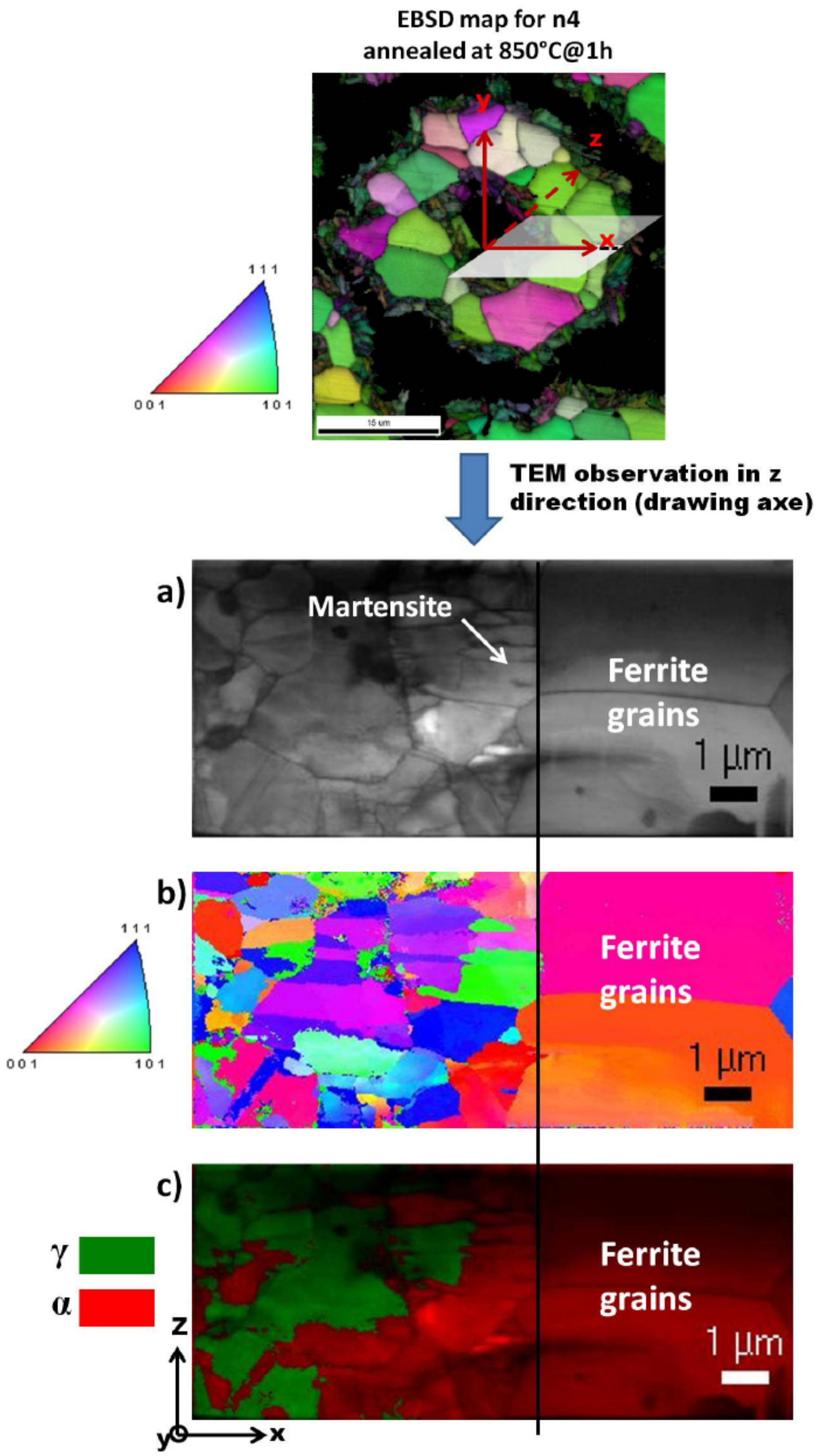

Figure IV-35:ACOM images of 316L/430LNb interface in n4 composite after annealing within n1 cell: a) indexed image b) orientation map along drawing axis c) combined indexed and phase distribution

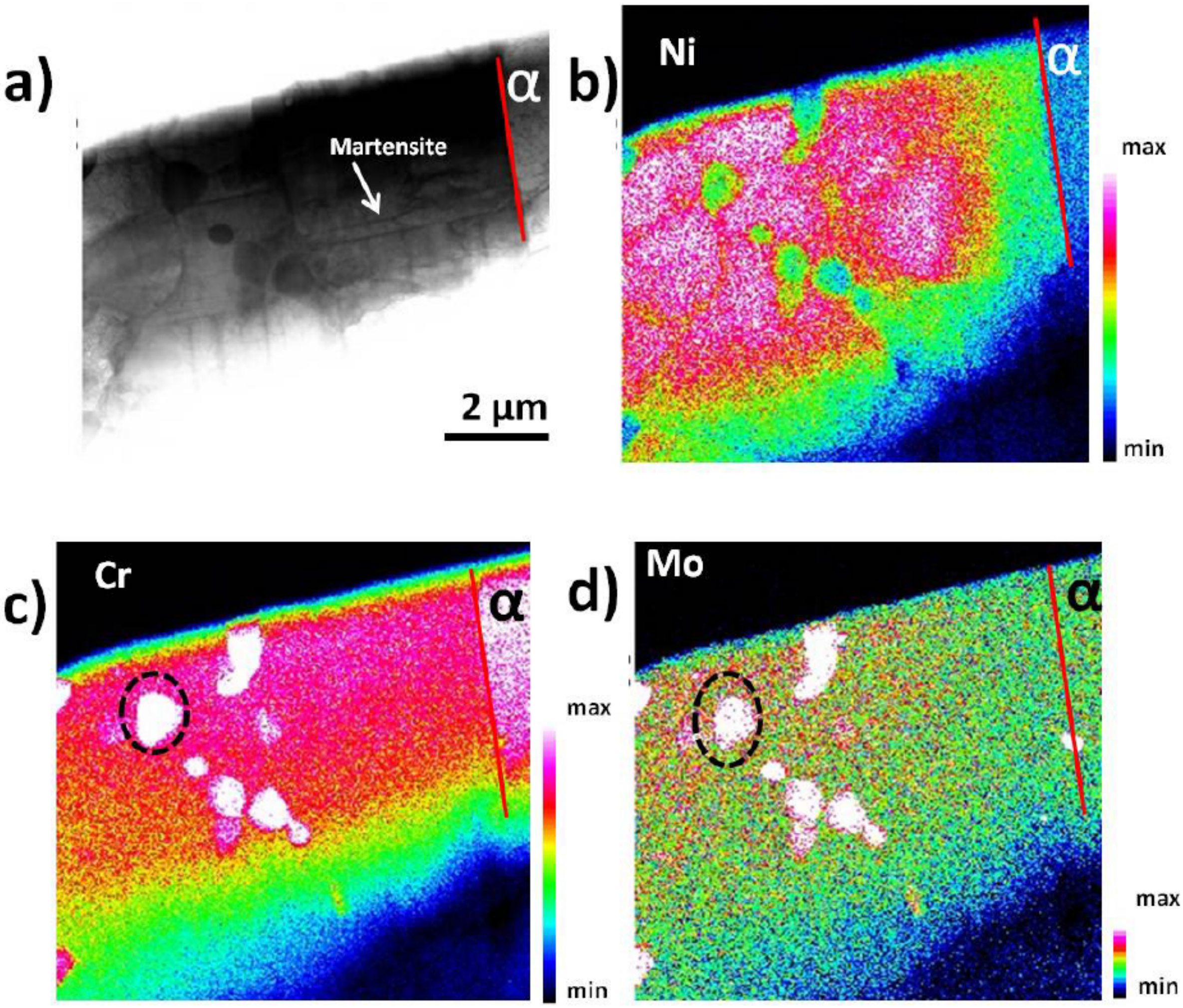

Figure IV-36:TEM-EDS maps of 316L/430LNb interface in n4 composite after annealing within n1 cell; a) indexed image. Chemical concentration maps of b) Ni ; c) Cr ; d) Mo (dashed circle indicates precipitates)

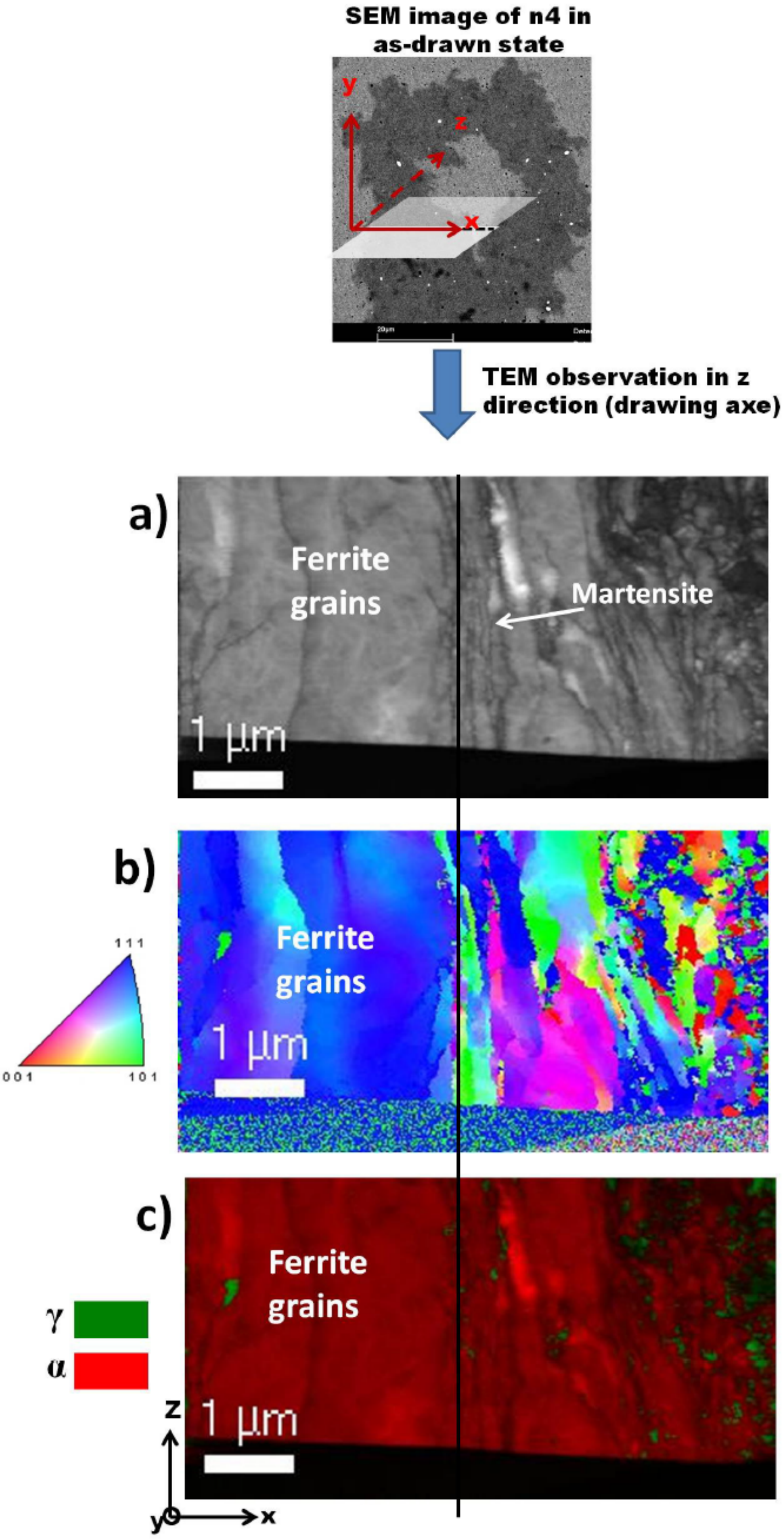

Figure IV-37:ACOM images of 316L/430LNb interface in n4 composite before annealing within n1 cell: a) indexed image b) orientation map along drawing axis c) combined indexed and phase distribution

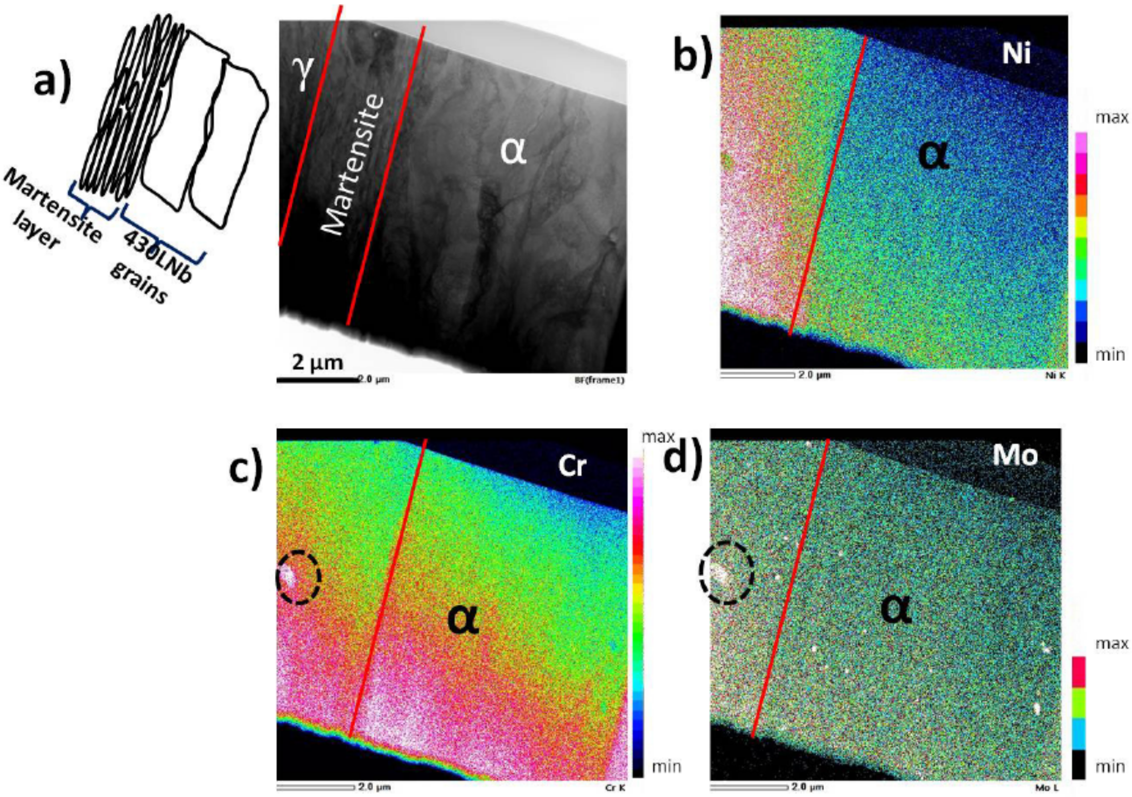

Figure IV-38:TEM-EDS maps of 316L/430LNb interface in n4 composite before annealing within n1 cell; a) indexed image. Chemical concentration maps of b) Ni ; c) Cr ; d) Mo (dashed circle indicates precipitates)

IV.III.3 Rationalization by Dictra modeling

In the view of the previous results, in chapter III and section IV.III.2, one can deduce that the interdiffusion across interfaces plays an important role not only in bonding of two-phase materials but also in phase transformations during the manufacturing process. Providing an analytical model, which aims at describing the interdiffusion paths and interface migration for multiphase systems, has been the subject of many studies. Most of the known analytical solutions are based on very simplifying assumptions (such as the geometry of phases, number of components….). It is within this scope that simulation tools such as DICTRA have been developed. Nowadays, DICTRA software is considered as one of the most important numerical tools, in describing the complex behavior that materials interfaces exhibit and in modeling multicomponent and multiphase systems [A. Engström et al.1997] [H.Larsson 2006]. In recent studies such as [A. Seki, 2013], DICTRA demonstrated its efficiency in simulating and predicting diffusion paths and interface migration during heat bonding of industrial materials (316L(γ)/ 444(α) stainless steels).

In this section we attempt to understand the resultant microstructure of n5 (in particular the architecture perturbation and the regression of the finest 316L phase inside the n1 cells) after annealing during manufacturing step using DICTRA simulations. Therefore, it seems to be necessary to give a rough description of the numerical calculation used by DICTRA before presenting our results. For more details on the numerical methodology and mathematical models of the different approaches used to solve diffusion problem in mutlicomponent multiphase system, the readers can refer to [A. Schneider and G.Inden 2004][U.R. Kattner and C.E. Chambell 2009] [J-O. Andersson and J. Argen 1992][L.Kaufman and H. Bernstein 1970].

IV.III.3.a DICTRA software

i) Concepts of calculation

DICTRA employs finite difference methods to simulate one-dimension diffusion in multicomponent alloys using Thermo-calc [B.Sundman et al 1985] databases, which contain data for multi-component thermodynamics and diffusion.

It is well established that diffusion and diffusion-controlled transformation can be described on the basis of Fick's law, which relates the mass flux to the gradient of chemical composition proportionally to coefficient D (called diffusion coefficient). However, from a thermodynamic point of view, the chemical potential of an element represents in fact the salient parameter for diffusion rather than concentration therefore the previous relation cannot be applied to multicomponent alloys [L.S Darken 1948]. Thus, the solute flux has to be related to the gradient of chemical potential of each species present in the system and Onsager's equation [L. Onsager 1931] should be then considered:

$$J_k^K = -\sum_{i=1}^{n} L_{ki} \nabla \mu_i \qquad \text{Eq. IV-32}$$

Where:

J_k^K is the flux of species k in mol/(m^2.s^1)

L_{ki} is a kinetic factor related to the diffusion of species k under the gradient of chemical potential i

μ_i is the chemical potential of species i in J/mol

The L-matrix is symmetric i.e. $L_{ik} = L_{ki}$

If the flux is defined as the number of species crossing a unit area per time, a reference frame has to be introduced defining the position of this unit area, starting with the lattice fixed (or Kirkendall) reference frame. In this reference frame the net flux of atoms is countered by the flux of vacancies and the kinetic factor of species k under its own chemical potential gradient L_{kk} can be expressed as the product of the atomic mobility M_k and the concentration C_k.

In general, solving a diffusion problem in multicomponent system consists in finding the solution of the following two equations:

- First Fick's law of the diffusion species k in the mass conservation form:

$$\frac{\partial C_k}{\partial t} = -div(J_k)$$

Eq.IV-33

- The so-called Fick-Onsager law

$$J_k = -\sum_{j=1}^{n-1} D_{kj}^n \nabla C_j$$

Eq. IV-34

Where

D_{kj}^n is the chemical diffusion coefficient. Since the n concentration gradients are not independent, the summation is reduced to (n-1) concentration. Thus, D_{kj}^n can be expressed as [J.O Anderson and J. Agren 1992]:

$$D_{kj}^n = \sum_i (\delta_{ik} - C_k) L_i \left(\frac{\partial \mu_i}{\partial C_j} - \frac{\partial \mu_i}{\partial C_n} \right)$$

Eq. IV-35

Where δ_{ik} is the Kronecker detla ($\delta_{ik} = 1$ if i=k; otherwire $\delta_{ik} = 0$), C_i is the concentration, μ_i is the chemical potential of element i.

ii) Boundary conditions and hypothesis

The geometry of the problem is represented in DICTRA by a single closed cell. The cell is subdivided into two regions (or more). The diffusion is then treated separately in each of these regions (Figure IV-39). Different geometries are possible in DICTRA such as linear, cylindrical, and ellipsoidal of spherical geometry. The discretization of these regions is realized by grid points which can be either equidistant or with increasing density as obtained by a geometric series [S.Crusius et al. 1992]. In linear geometry, the symmetry can reduce diffusion calculations to the half cell.

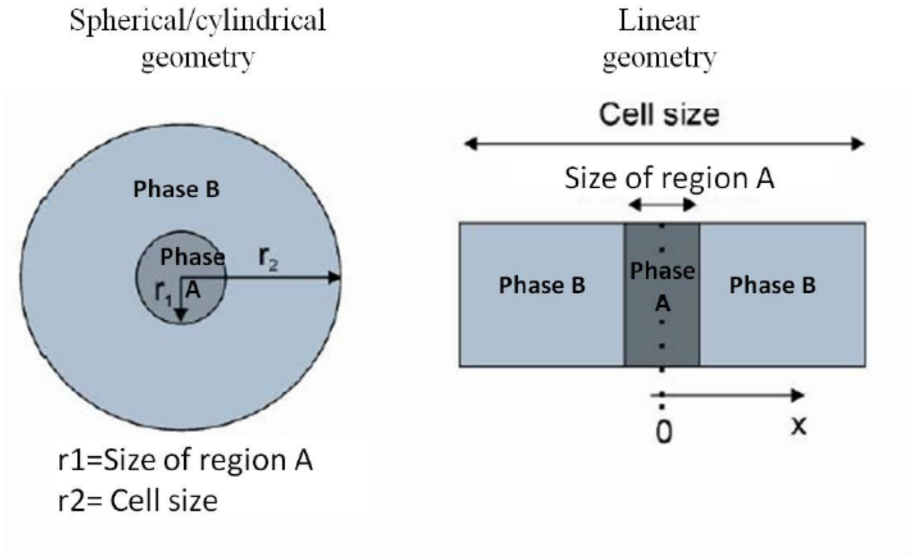

Figure IV-39:Definition of the various geometries in DICTRA [A. Schneider and G.Inden 2004]

The hypothesis that is widely used and successfully applied in the numerical calculation of controlled-diffusion transformation of a couple of diffusion is the Local Equilibrium (LE). This assumption imposes that chemical potentials of all components should be equal on each side of the phase boundary [G. Inden 2003].

For the case of substitutional elements, the local diffusional equilibrium condition is met with a parallel tangent construction Figure IV-40. For selected values of $\varnothing_B^\gamma = \mu_B^\gamma - \mu_A^\gamma$ corresponding to a composition $x^{\gamma/\alpha} > x_0$ at the interface, the corresponding composition $x^{\gamma/\alpha}$ in α phase at the interface is obtained by a parallel tangent. The driving force for diffusion in γ phase is related to the difference $\varnothing_k^{\gamma/\alpha} - \varnothing_{k0}^\gamma = \mu_k^{\gamma/\alpha} - \mu_{k0}^\gamma$. It is clear from the figure that the more $x^{\gamma/\alpha}$ approaches x_e^γ (or further) the more the driving force increases.

In case of interstitial component (such as C and N), the diffusion equilibrium, based on the local equilibrium in the interface, is reached when $\mu_C^{\gamma/\alpha} = \mu_C^{\alpha/\gamma}$. See Figure IV-41.

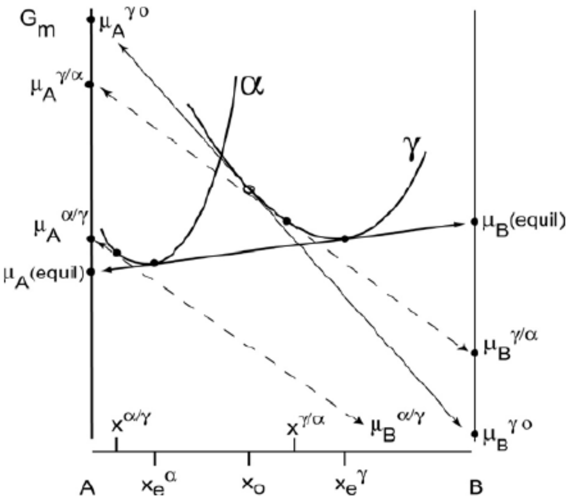

Figure IV-40:Boundary condition in the case of a binary substitutional alloy (dashed lines define a local equilibrium at the interface) [A. Schneider and G.Inden 2004]

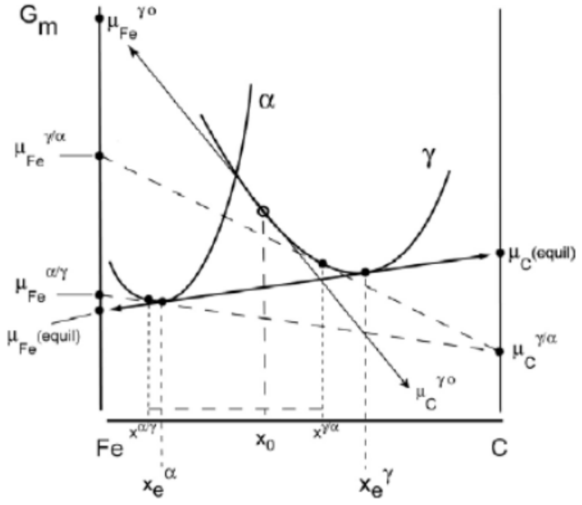

Figure IV-41:Boundary condition in the case of a binary interstitial alloy (dashed lines define a local equilibrium at the interface) [A. Schneider and G.Inden 2004]

For all calculations realized in the current section, a cylindrical geometry is used representing the most realistic configuration for case study. Moreover, the assumption is made of local equilibrium at the interface. The thermodynamic and kinetic databases used were TCF6 and MOB2 respectively.

IV.III.3.b Simulation results

i) n1 composite annealed at 1050°C

The configuration of the simulation of n1 composite is given in Figure IV-42. It is a 2D representation of the cylindrical geometry. The dimensions of 316L and 430LNb are taken to be the same as the real n1 composite; the diameter of 316L wire is 500µm and the thickness of the 430LNb is 402 µm.

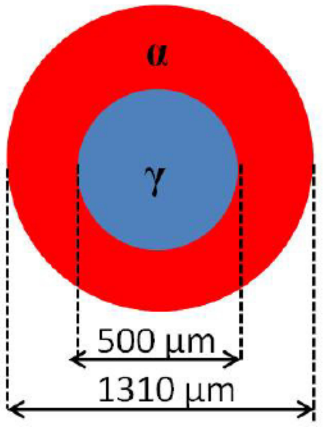

Figure IV-42:Two-dimension representation of the cylindrical configuration of n1 composite for simulation with Dictra

The chemical composition of each phase for this composite corresponds to the nominal chemical composition (see chapter II), which fits also with experiments of n1 composite at as-drawn state. For both phases, each solute is assumed to have a constant concentration along the phases at the beginning of this simulation.

The annealing cycle used during manufacturing is first considered, namely 70°C/hour heating rate up to 1050°C followed by 10 minutes of holding time as shown in Figure IV-43. For the sake of calculation speed, the anisothermal annealing is assumed to start from 650°C instead of 25°C.

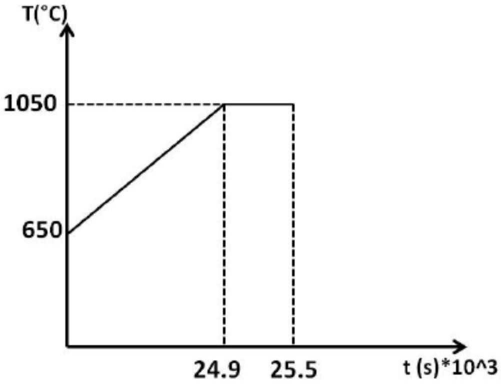

Figure IV-43:Heat-treatment cycle introduced in Dictra simulation for n1 composite

Figure IV-44 shows the simulation results of Ni diffusion through 316L/430LNb interface compared with experimental measurements. A very good agreement between simulation and experiments is obtained. Dictra succeeded to predict the γ transformation into α and the migration of the interface as a consequence.

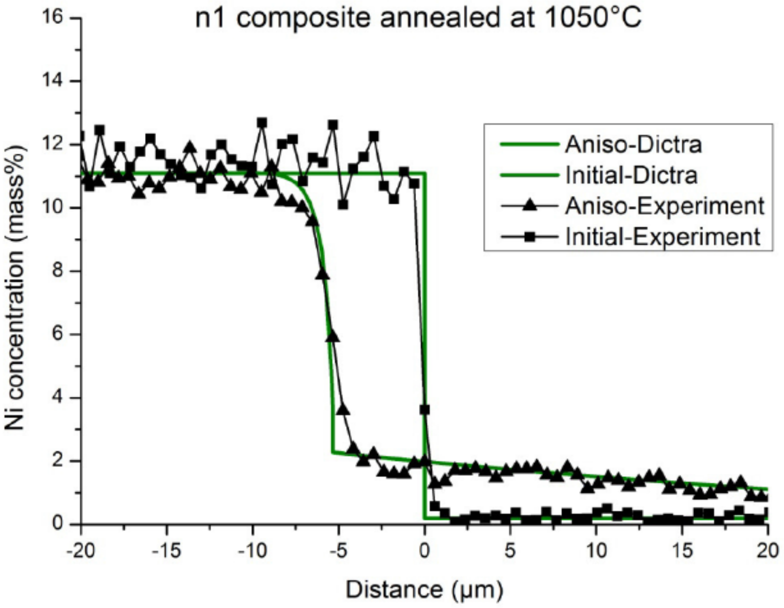

Figure IV-44:Nickel diffusion profiles in the vicinity of 316L/430LNb interface obtained from Dictra simulation with a heating cycle as presented in Figure IV 43 together with EDS measurements

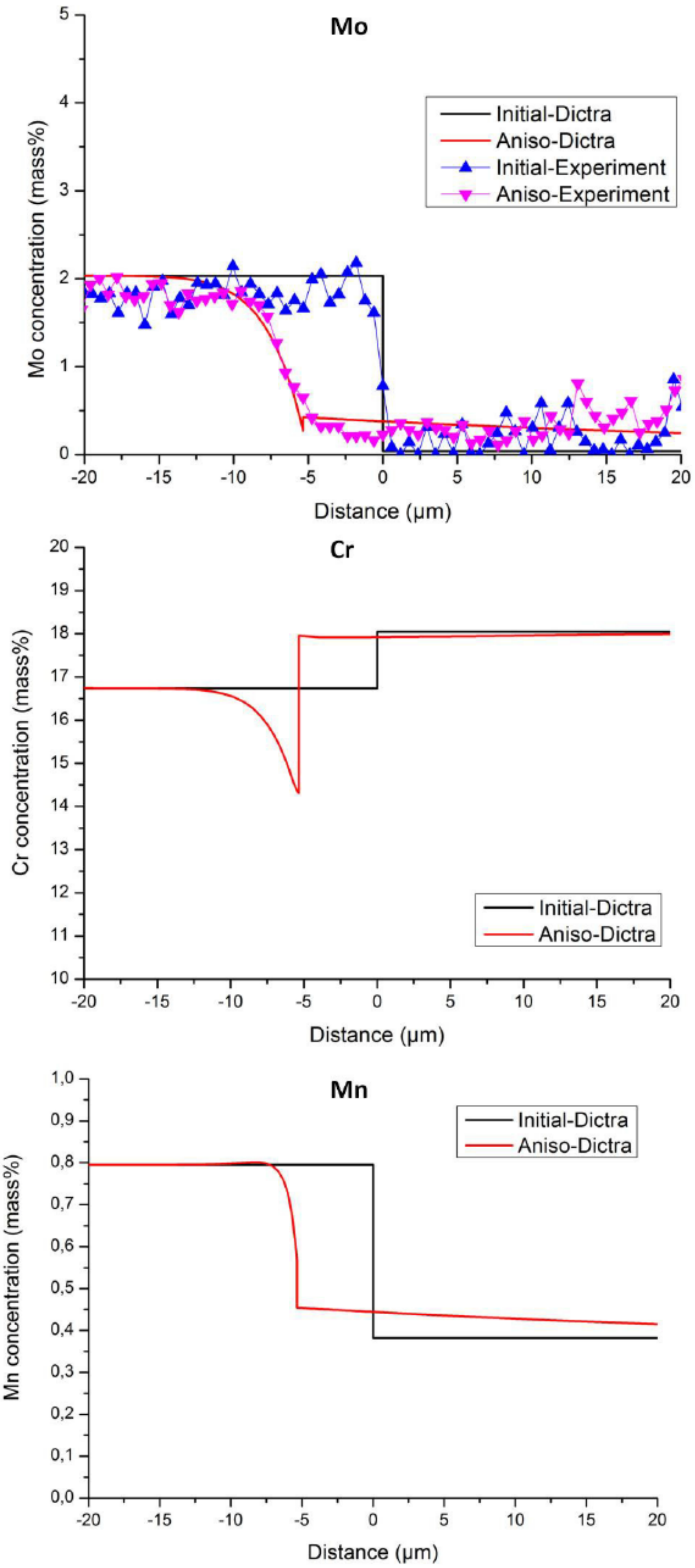

Figure IV-45:Diffusion profiles in the vicinity of 316L/430LNb interface of n1 composite obtained from DICTRA simulation with a heating cycle as presented in Figure 43 for elements: Mo, Cr and Mn

The diffusion profiles for the other elements taken into account in the simulation are shown in Figure IV-45.

> *Notice: The concentration content of Cr and Mn in both phases 316L and 430LNb is close and therefore the experimental EDS profiles don't have a good resolution. It is for this reason that only simulated profiles are shown in* Figure IV-45.

The value of Ms is estimated using Pickering's formula. In Figure IV-46, we compare the Ms evolution in n1 composite after anisothermal annealing using diffusion profiles obtained by EDS measurements and those obtained by DICTRA simulation. Very good superposition between the simulated and experimental curve of Ms is obtained.

The simulation results obtained above make us confident not only in using DICTRA for our specific application but also in our calculations hypothesis particularly the heating cycle which starts from 650°C rather than 25°C.

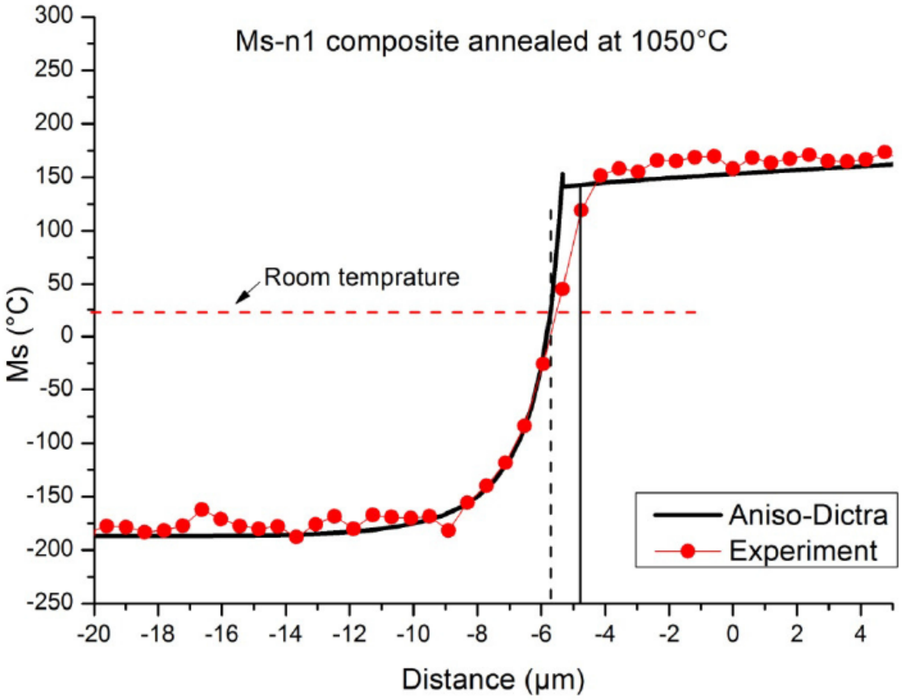

Figure IV-46:Ms evolution calculated from Dictra simulation and experimental measurements using Pickering formula

ii) *n(1<i<5) composites annealed at 850°C*

Before presenting simulation results obtained by Dictra for composites n(i>1), it seems very important to note, that for a given volume fraction of both phases and chemical concentration, no evidence of the influence of the geometrical size on the diffusion behavior has been observed. Thus, for sake of simplicity, only n1 cell inside n4 and n5 composite will be treated in the following two sub-sections.

Figure IV-47 shows the geometrical configuration of n1 cell inside n4 where the diameter of 316L wire is 13µm and the thickness of 430LNb channel is 11µm. An anisothermal annealing is considered starting from 650°C up to 850°C for 1 hour as holding time and 70°C/hour as heating rate. As proven above, these heat treatment conditions give a very good prediction close to the experiments.

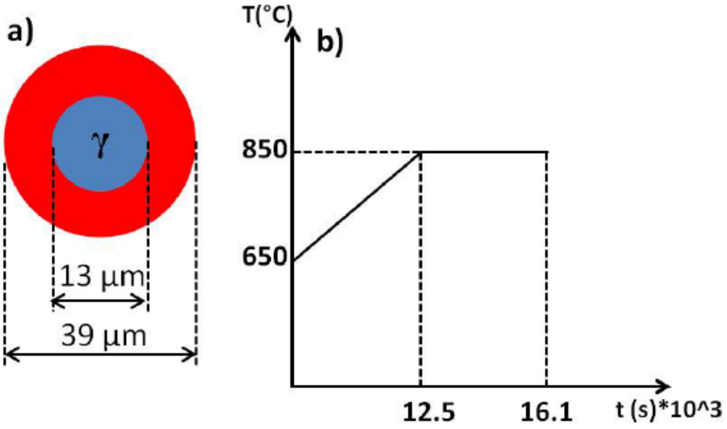

Figure IV-47:a) schematic illustration of the geometry of n1 cell inside n4 composite b) annealing cycle used for Dictra simulation

- *Constant concentration:*

A constant concentration in both phases is first assumed. Figure IV-48 shows nickel diffusion profile issued from Dictra simulation compared with the EDS measurements. A significant difference between experiment and simulation has been observed. Indeed, one can notice from this figure that the experimental curve has a larger concentration gradient in γ side than the simulated diffusion profile.

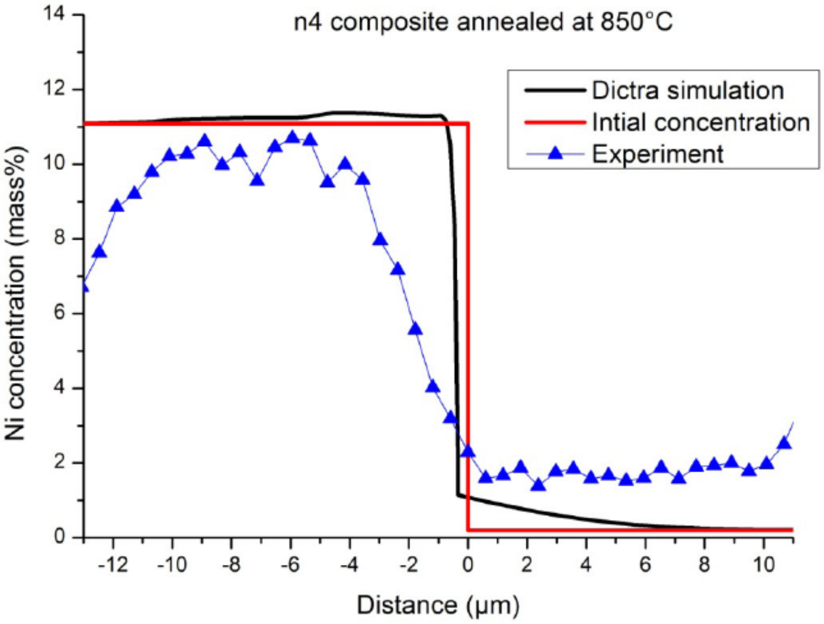

Figure IV-48:Nickel diffusion profiles in the vicinity of 316L/430LNb interface obtained from Dictra simulation with a constant concentration with EDS measurements

- *Gradient of concentration:*

In view of the above results, it is more realistic to introduce the experimental initial concentrations; i.e. the diffusion profile in the as-drawn state for n4 composite as Figure IV-32 shows.

For the sake of simplicity, the diffusion profiles of Ni, Mo, Cr and Mn for each phase of n4 at as-drawn state were fitted and then introduced as an initial concentration into Dictra. The simulation results compared with the experiments are reported in Figure IV-49. Good agreement between Dictra simulation and experiments is obtained. These results allow us to extend the investigation to n5 in order to understand the perturbation of the microstructure.

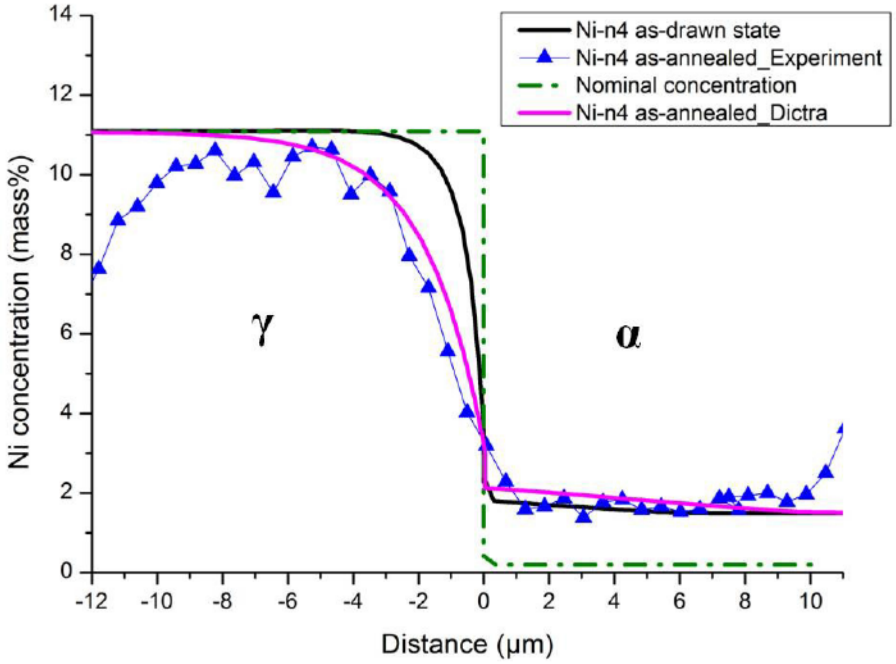

Figure IV-49:Nickel diffusion profiles in the vicinity of 316L/430LNb interface obtained from Dictra by introducing an experimental diffusion profiles as initial concentration with EDS meausurments

iii)<u>n5 composite annealed at 850°C</u>

After drawing of the n4 composite, n1 cell is reduced to 10-12 µm in which the diameter of the 316L wire becomes 3µm and the thickness of 430LNb is reduced to almost 4µm. the configuration of this cell is illustrated in Figure IV-50. Similarly to n(i>1) composites, an anisothermal annealing is envisaged.

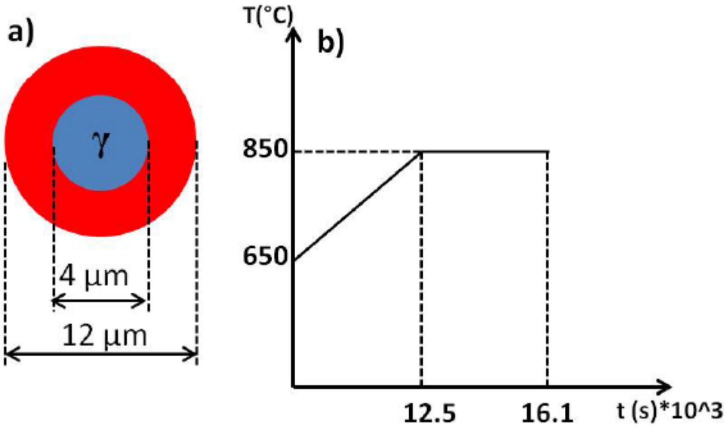

Figure IV-50:a) schematic illustration of the geometry of n1 cell inside n5 composite b) annealing cycle used for Dictra simulation

The initial chemical concentrations are taken to be exactly the same initial concentrations as n4 composite at as-drawn state. Indeed, as we presented in IV.III.2.a, the slope of the Ni profile within the vicinity of the interface is similar for n2, n3 and n4 which allows us to extrapolate the concentration profiles for n5 at as-drawn state by taking into account the section reduction.

These diffusion profiles are introduced into Dictra model to predict the diffusion behavior, in particular, Ni profile within the fine cells in n5 (i.e. n1 cell). The resultant diffusion profile of Ni for n5 after annealing is presented in Figure IV-51. A significant decrease of Ni concentration in γ side compared to the initial one is observed. Concerning the α a deep diffusion of Ni has occurred.

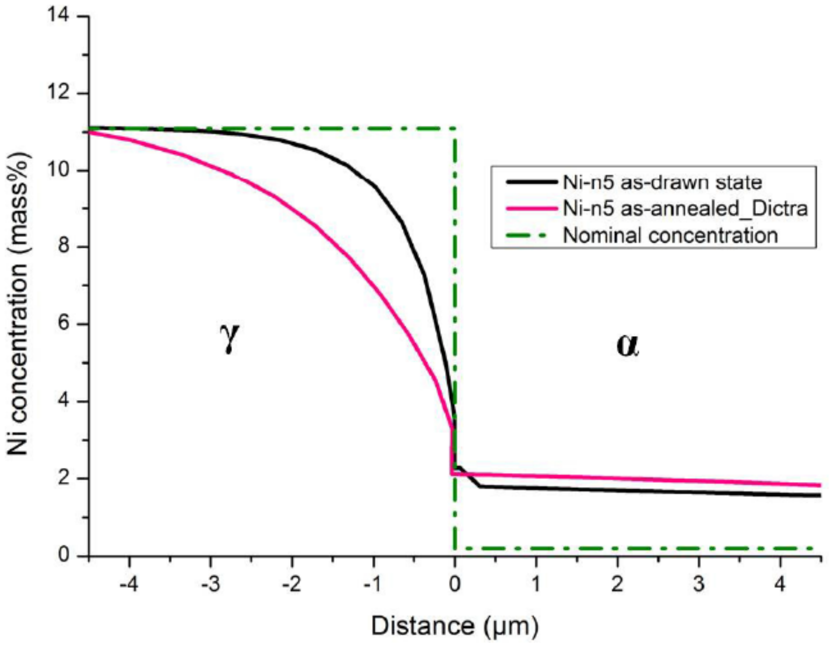

Figure IV-51:Nickel diffusion profile after annealing at 850°C predicted by Dictra

IV.III.4 Discussion

In sub-section IV.III.2, diffusion profiles of Ni for 316L/430LNb wires in n1 composite were presented. The EDS measurements confirm the SEM observations in terms of γ-phase transformation into α-phase after an anisothermal annealing (70°C/h up to 1050°C held for 10 minutes). Recently, [Seki 2013] made the same observation by studying diffusion bonding of couples 316L/444. Similarly to our case, [Seki 2013] observed a significant interface migration toward γ-phase side after isothermal annealing starting from 1343 K (1050°C). Using Dictra simulation, Seki rationalized the interface migration distance (i.e. the amount of γ phase transformed into α). He found that the migration distance increased proportionally with square root of time holding.

However, within the vicinity of the new migrated interface, a depleted region in γ-phase side is formed. Using a usual formula for the Ms temperature, a martensite layer is predicted to form in the composite wires upon cooling, consistently with the experimental observations. The wires of n1 composite were then drawn to fabricate n2 composite in which the 316L and 430 LNb issued from n1 composite were reduced by factor of 3. The nickel profile in the as-drawn state of n2 composite shows already a depleted region in γ-phase side, which is attributed to the inherited concentration profile from the previous step (i.e. n1 annealed). After annealing at 850°C (the optimized annealing conditions see chapter III), no significant interface migration has been observed, due to the lower temperature. However, the concentration gradient of the nickel in γ-phase side after annealing is wider as compared to the as-drawn state whereas the Ni concentration in α-phase increases significantly. This trend was also observed in n3 and n4 composites. In fact, at each step of co-deformation the gradient is steepened by the section reduction (factor of 3) and is flattened again by the annealing treatment, resulting in a width of the interdiffusion layer, which is relatively constant for each step. The Ni depleted layer in austenite results for all steps in the formation of a martensite layer upon cooling. TEM observations of the γ/α interface of a n1 cell inside n4 composite confirmed the formation of this martensite layer within the interface before and after annealing. In the as-drawn state, an elongated structure within the interface and along drawing direction was found.

Since the concentrations gradient in γ-phase before annealing are similar in all manufacturing steps (n2, n3 and n4), it is possible to extrapolate the diffusion profile of n1 cell inside n5 composite by considering the section reduction of n1 cell of n4 composite (before annealing) of the γ-phase having 10-11% of Ni concentration as Figure IV-52 shows which is in coherence with SEM observation and EDS measurements shown in Figure IV-53.

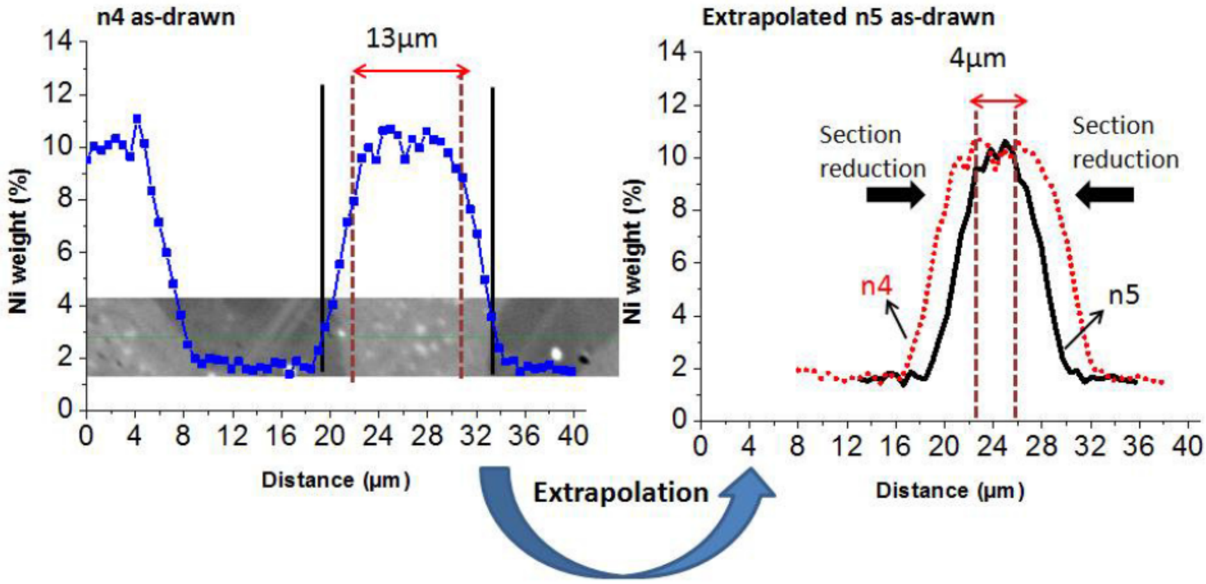

Figure IV-52:Extrapolation of Ni diffusion profile in n5 composite from n4 EDS measurements before annealing

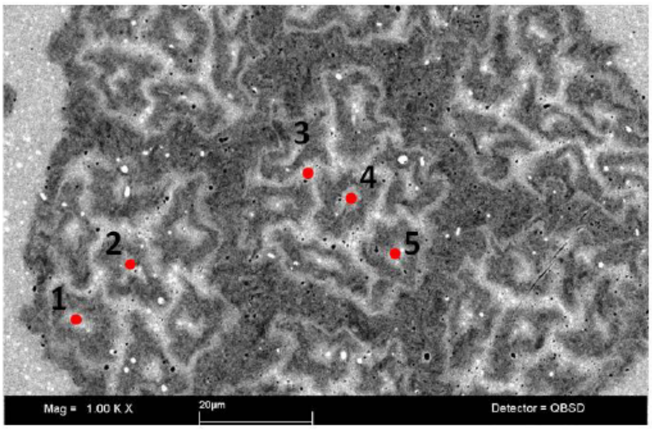

Point	Ni(mass%)
1	9,71
2	13,14
3	12,29
4	8,74
5	11,36
Average	11.02

Figure IV-53:BSD-SEM image of n5 composite before annealing (red points indicate the point EDS measurements of Ni concentration of 316L in n1 cells)

Dictra simulations reproduced successfully the experimental results obtained by EDS measurements for n1, n2, n3 and n4 composite. Using an anisothermal annealing similar to the experimental conditions, the interface migration in n1 composite is well reproduced. [Seki 2013] showed also the efficiency of Dictra simulation to reproduce interface migration in 316L/444 diffusion couples.

For n (1<i<5) the annealing temperature is reduced to 850°C after optimization. Good agreement between simulations and experiment was obtained for these composites after introducing the experimental initial concentration profiles.

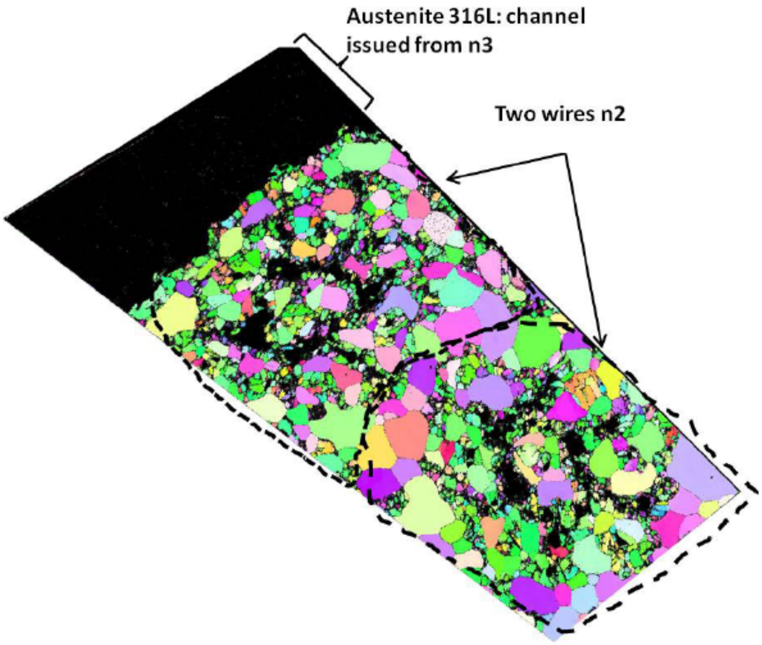

Figure IV-54:EBSD map of n5 composite after annealing at 850°C: black: austenite; colored: ferrite

The experimental and simulation results show that the nickel diffusion is controlled by the austenitic phase. Indeed, generally speaking, the diffusion coefficient of Ni (substitution element) in BCC phases is much higher than in FCC phases so that the gradient of Ni in the γ-phase side is much higher than in the α-phase. This was clearly observed from diffusion profiles where the Ni concentration in the α-phase increases and flattens much faster than in the γ-phase.

IV.III.5 Summary

- EDS analysis showed a significant interdiffusion of chemical elements between 316L and 430LNb in particular Ni leading to a destabilization of the austenite phase in n1 composite after annealing at 1050°C leading to a martensitic formation during cooling which has been predicted by Ms formula.

- For composites n(i>1), they inherited the martensite layer from n1 composite during manufacturing process. TEM observations confirmed the presence of the martensite in the vicinity of 316L/430LNb interface of n1 cell inside n4 composite before and after annealing at 850°C.

- DICTRA simulation has successfully predicted the experimental EDS profile analysis for composites n1 and n4. Therefore, the resultant microstructure of n5 composite has been rationalized using this simulation tool.

IV.IV General conclusion

Let us recall the hypotheses raised in chapter III regarding the limitation of the Accumulative Drawing and re-Bundling (ADB) process for our specific couple materials 316L and 430LNb which was translated by the significant regression of the austenite phase (316L) during annealing step necessary for processing:

i) Variability of the optimum annealing parameters with the composite step (n).
ii) The dissolution of the austenite regions with micrometric dimensions (1-5 µm) into the ferritic phase forming a ferrite with different chemical composition than the initial one.
iii) Martensitic transformation of the austenite during cooling
iv) Both hypothesis ii) and iii)

Concerning the first hypothesis, an investigation on the softening kinetics was carried out using composite n4. The softening kinetics of the finest phases in composite n4 (i.e. 316L and 430LNb issued from n1 cells) was compared with that of individual wires having being subjected to exactly the same section reduction as that of 316L and 430LNb cells. The result showed that the phases of n1 cells inside n4 composite recrystallize faster than that of individual wires for temperatures 750°C, 850°C and 950°C. At 750°C for example the phases of n1 cells were already recrystallized after 1 hour whereas the individual bulk wires were hardly recrystallized. This was attributed to the initial grain size. These results may lead to decrease the optimal temperature. However, the other recent generations of both phases (such as the austenite issued from n3 and the ferrite issued from n2) particularly the austenite has almost the same softening kinetics as the bulk wires. This suggests that the softening behavior of a given phase differs from one generation to another within the same composite. However, the volume fraction of the austenite issued from n1 cells (is small) represents only 1.9% whereas the austenite volume fraction issued from n3 is about 24%. Therefore the global softening kinetics of the composite is unaffected since the finest scale represent low volume fraction.

Hence, the variability of the optimal annealing conditions as a function of manufacturing step can be neglected.

Hypotheses ii) and iii) have been investigated through a diffusion analysis across the γ/α interface at each manufacturing step n1, n2, n3 and n4. This analysis was performed using EDS technique. Indeed, a significant inter-diffusion of elements of substitution, in particular Ni, was observed in composite n1 annealed at 1050°C for 10 minutes. At this temperature a transformation $\gamma \rightarrow \alpha$ resulting in a significant interface migration has been observed. In the interface region following the inter-diffusion, a martensitic layer was formed during rapid cooling, of thickness around 1.3µm, which was found to be consistent with the composition profiles based on the existing formulae for martensite start temperature. However, for composites ($i \geq 2$) subjected to the optimal annealing conditions (850°C for 1hour), the following features have been made from EDS diffusion profiles:

- The martensitic layer within the vicinity of 316L/430LNb interface is always preserved.

- The martensitc layer is maintained even in as-drawn state.
- The thickness of this layer is constant for all composite.

In addition, TEM observations confirmed the presence of the martensite layer at the interface 316L/430LNb of n1 cells inside n4 composite before and after annealing at 850°C for 1h. TEM observations revealed that the thickness of this martensite layer is almost similar before and after heat treatment.

On the other hand, we attempted to rationalize the microstructure of n5 composite after annealing using DICTRA software. Simulation results showed a significant diffusion of Ni from the austenite region (4µm) to the ferrite one (4µm) of n1 cell inside the composite n5. This diffusion was considered as the origin behind the dilution of the austenite. Moreover, the chemical composition of the ferritic phase has been significantly changed in particular the nickel content which increased from 0.198 wt% to almost 2 wt%.

It can be therefore concluded that the austenite regression of the n1 cells inside n5 composite can be explained by the coupled effect of : a) inter-diffusion, in particular Ni, between 316L and 430LNb and the martensitic transformation (hypotheses iv); b) section reduction during drawing process.

References

[Anderson and Mehl 1945]
Anderson, W. A., & Mehl, R. F., Recrystallization of Aluminum in Terms of the Rate of Nucleation and the Rate of Growth. Trans. Aime, 1945,161, 140.

[Andersson and Argen 1992]
Andersson J.O. and J. Ägren., Models for numerical treatment of multicomponent diffusion in simple phases. Journal of Applied Physics, 1992, 72:1350_1355.

[Bailey and Hirsh 1961]
Bailey J.E., Hirsch, P.B., The recrystallization process in some polycrystalline metals. Proceedings of the Royal Society of London A267, 1961, 11-30.

[Bate and Hutchinson 1997]
Bate, P. and Hutchinson, B., A re-evaluation of the mechanism of SIBM. Scripta Materialia,1997, 36, 195-198.

[Beck and Sperry 1950]
Beck, P.A. and Sperry, P.R. Strain Induced Grain Boundary Migration in High Purity Aluminum. Journal of Applied Physics, 1950, 21, 150.

[Cahn 1949]
Cahn, R. W., Recrystallization of single crystals after plastic bending.Journal of the Institute of Metals, 1949, 76(2), 121.

[Cahn 1996]
Cahn, R. W., & Haasen, P., Physical metallurgy. Vol. 2. North-Holland,1996.

[Christian 2002]
Christian, J. W., The theory of transformations in metals and alloys. Newnes,2002.

[Clarebrough 1955]
Clarebrough, L. M., Hargreaves, M. E., & West, G. W., The release of energy during annealing of deformed metals. In Proceedings of the Royal Society of London A: Mathematical, Physical and Engineering Sciences, 1955, (Vol. 232, No. 1189, pp. 252-270). The Royal Society.

[Crusius et al. 1992]
Crusius, S., Inden, G., Knoop, U., Höglund, L., & Ågren, J. (1992). On the numerical treatment of moving boundary problems. Zeitschrift für Metallkunde,1992, 83(9), 673-678.

[Darken 1948]
Darken, L. S., Diffusion, mobility and their interrelation through free energy in binary metallic systems. Trans. Aime,1948, 175(1), 184-201.

[Dunlop et al. 2007]
Dunlop, J. W. C., Bréchet, Y. J. M., Legras, L. and Zurob, H. S., Modelling isothermal and non-isothermal recrystallisation kinetics: Application to Zircaloy-4. Journal of Nuclear Materials,2007, 366, 178-186.

[Engström et al.1997]
Engström, A., & Ågren, J., Simulation of diffusion in multicomponent and multiphase systems. In Defect and Diffusion Forum, 1997, (Vol. 143, pp. 677-682).

[Friedel et al. 1964]
Friedel, J. (1964). Dislocations Pergamon, 1964, New York, 274.

[Furu et al. 1992]
Furu, T., Modelling of recrystallization applied to commercial aluminium alloys. PhD dissertation, 1992, pp. 148. NTH Trondheim.

[Hu 1962]
Hu, H. (1962) Transactions of the Metallurgical Society A.I.M.E.,1962, 224, 75.

[Huang et al.2000]
Huang, Y., & Humphreys, F. J., Subgrain growth and low angle boundary mobility in aluminium crystals of orientation {110}< 001>. Acta Materialia, 2000, 48(8), 2017-2030.

[Humphreys 1995]
Humphreys, F.J. and Hatherly, M. (1995) Recrystallization and related annealing phenomena,1995, Pergamon Press.

[Humphreys 2004]
Humphreys, F. J., Rohrer, G. S., & Hatherly, M. (2004).Recrystallization and related annealing phenomena,2004, Elsevier.

[Hutchinson et al. 1989]
Hutchinson, B., Jonsson, S., & Ryde, L., On the kinetics of recrystallisation in cold worked metals. Scripta metallurgica, 1989, 23(5), 671-676.

[Jones 1980]
Jones A. R., Grain boundary phenomena during the nucleation of recrystallization. In Grain Boundary Structure and Kinetic, 1980, pp. 379-425. American Society for Metals.

[Kattner and Chambell 2009]
Kattner, U. R., & Campbell, C. E., Invited review: Modelling of thermodynamics and diffusion in multicomponent systems. Materials Science and Technology, 2009, 25(4), 443-459.

[Kaufman and H. Bernstein 1970]
Kaufman, L., & Bernstein, H., Computer calculation of phase diagrams. With special reference to refractory metals, 1970.

[Larsson 2006]
Larsson, H., & Engström, A., A homogenization approach to diffusion simulations applied to α+ γ Fe–Cr–Ni diffusion couples. Acta materialia, 2006, 54(9), 2431-2439.

[Li 1962]
Li, J.C.M., Possibility of Subgrain Rotation during Recrystallization. Journal of Applied Physics, 1962, 33, 2958.

[Meyer 2008]
Meyer, N., Etude de la recristallisation d’un acier inoxydable ferritique au niobium. Conséquences sur les propriétés magnétiques en régime statique et dynamique,2008, PhD thesis.

[Onsager 1931]
Onsager L. Reciprocal relations in irreversible processes. II. Phys. Rev., 1931, pages 2265-2279,1931.

[Ørsund et al. 1989]
Ørsund, R., Hjelen, J., & Nes, E., Local lattice curvature and deformation heterogeneities in heavily deformed aluminium. Scripta metallurgica, 1989, 23(7), 1193-1197.

[Rollett 1997]
Rollett, A. D., Overview of modeling and simulation of recrystallization.Progress in materials science, 1997, 42(1), 79-99.

[Sandström 1977]
Sandström, R., On recovery of dislocations in subgrains and subgrain coalescence. Acta Metallurgica,1977, 25(8), 897-904.

[Schneider and Inden 2004]
Schneider A. and G. Inden. Computer simulation of di_usion controlled phase transformations. Continuum Scale Simulation of Engineering Materials, 2004.

[Seki, 2013]
Seki, A., Ogawa, K., & Nishibata, T., Analysis of Diffusion-controlled Phenomena at the Interface of α/γ Diffusion Couples of Stainless Steels. ISIJ international, 2013, 53(12), 2242-2249.

[Sello 2010]
Sello, M. P. Laves phase embrittlement of the ferritic stainless steel type AISI 441, 2010, PhD thesis.

[Speich 1966]
Speich, G. R., & Fisher, R. M., Recrystallization, grain growth and textures. Am. Soc. Metals, 1966, Metals Park, Ohio, 563.

[Sundman et al 1985]
Sundman, B., Jansson, B., & Andersson, J. O. (1985). The thermo-calc databank system. Calphad, 1985, 9(2), 153-190.

[Tunbull et al. 1952]
Turnbull, D& Burke, J. E., Recrystallization and grain growth. Progress in metal physics, 1952, 3, 220IN11245IN13267IN15275-244IN12266IN14274292.

[Verdier et al. 1998]
Verdier, M., Brechet, Y. and Guyot, P., Recovery of AlMg alloys: flow stress and strain-hardening properties. Acta Materialia, 1998, 47, 127-134.

[Zurob 2002]
Zurob, H. S., Bréchet, Y. and Dunlop, J., Quantitative criterion for recrystallization nucleation in single-phase alloys: Prediction of critical strains and incubation times. Acta Materialia, 2006, 54, 3983-3990.

V Mechanical behavior

Introduction

In the previous chapter (IV), we have studied the microstructure resulting from ADB (Accumulative Drawing and re-Bundling) process of the 2nd architecture composites and tried to answer the questions posed in chapter III about the limits of this process.

The present chapter will be devoted to answer the next question of this work which is: *What is the resultant mechanical response of these composites?*

In the first section of this chapter, the macroscopic behavior of each composite is investigated. An analysis based on the; i) mechanical behavior of individual wires of both phases 316L and 430LNb; ii) the resultant composites' microstructure, is developed.

However, since a better understanding of the effective behavior of a composite requires the knowledge of the behavior of its individual constituents, in-situ tensile tests were performed with high energy X-ray diffraction measurements. These tests enable the measurement of the stress in the austenite and the ferrite. The results and the discussion of these tests are the subject of the second section.

Contents

V.I Macroscopic behavior

V.I.1 Bulk materials

Before going through the mechanical response of the produced composites, in particular the 2nd architecture (see Chapter III), it is essential to first examine the mechanical response of 316L and 430LNb wires separately.

As presented in chapter III, the mechanical response of the 316L and 430LNb in as-received state is shown in Figure V-1.a. Plot of work-hardening rate (θ=dσ/dε) of both types are compared in Figure V-1.b. Both 316L and 430LNb in as-received state obeys the Considère criterion, which states that necking occurs when the load in tension reaches θ=σ in tension. θ-σ curve of 316L is observed to be above that of 430LNb and the elastic-plastic transition is sharper. Nevertheless, the decrease of the work-hardening rate of the ferrite is faster than 316L.

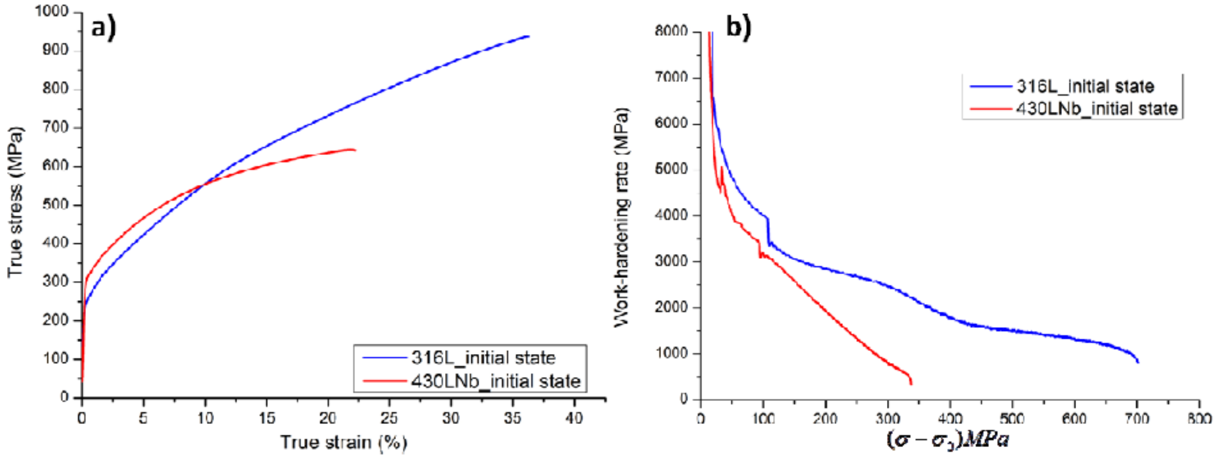

Figure V-1: Mechanical response of 316L and 430LNb wire at as-received state a) uniaxial tensile curves b) work-hardening rate

Besides, it is also useful to compare the stress-strain behavior of 316L and 430LNb wires heat-treated isothermally after 92% of section reduction by drawing (see Chapter IV). Figure V-2.a presents the mechanical response of both types after 850°C and 950°C of heat treatment for duration of 1hour. Comparing with the as-received state, the mechanical response of both types, after cold-drawing followed by annealing treatment, has significantly changed. Indeed, 316L becomes significantly harder than 430LNb for the same thermomechanical conditions. Similarly to the as received case, the elasto-plastic transition is sharper in 316L than 430LNb. The work-hardening rate of 316L is higher than that of 430LNb in both cases; after 850°C and 950°C of annealing.

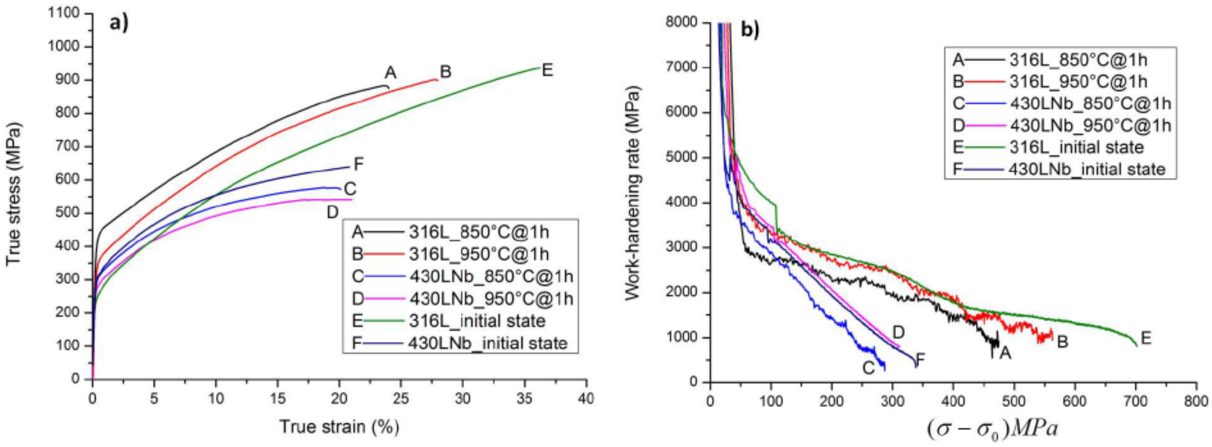

Figure V-2: Mechanical response of 316L and 430LNb wires drawn down to 92% a) uniaxial tensile curves b) work-hardening rate

V.I.2 Composites

V.I.2.a n1 composite annealed at 1050°C

The tensile behavior of composite n1 (45% of austenite and 55% of ferrite), after heat treatment for 10 minutes at 1050°C, is shown in Figure V-3. The stress-strain curve of n1 annealed is here compared with austenite and ferrite wires in as-received state. Although the yield strength is situated between that of both 316L and 430LNb, the work hardening, immediately after the yield strength point, remains significantly below the work-hardening curve of both constituents.

Hence, it seems more adequate to compare the stress-strain curve of the n1 composite with that of wires of 316L and 430LNb being subjected to similar thermomechanical conditions (as studied in chapter IV for softening kinetics). Figure V-3.b compares the tensile curve of n1 annealed with that of austenitic and ferritic wires heat-treated with the same annealing conditions as n1. In these annealing conditions, 430LNb type becomes significantly softer than 316L. The stress-strain curve of the composite n1 is closer to that of 430LNb than 316L.

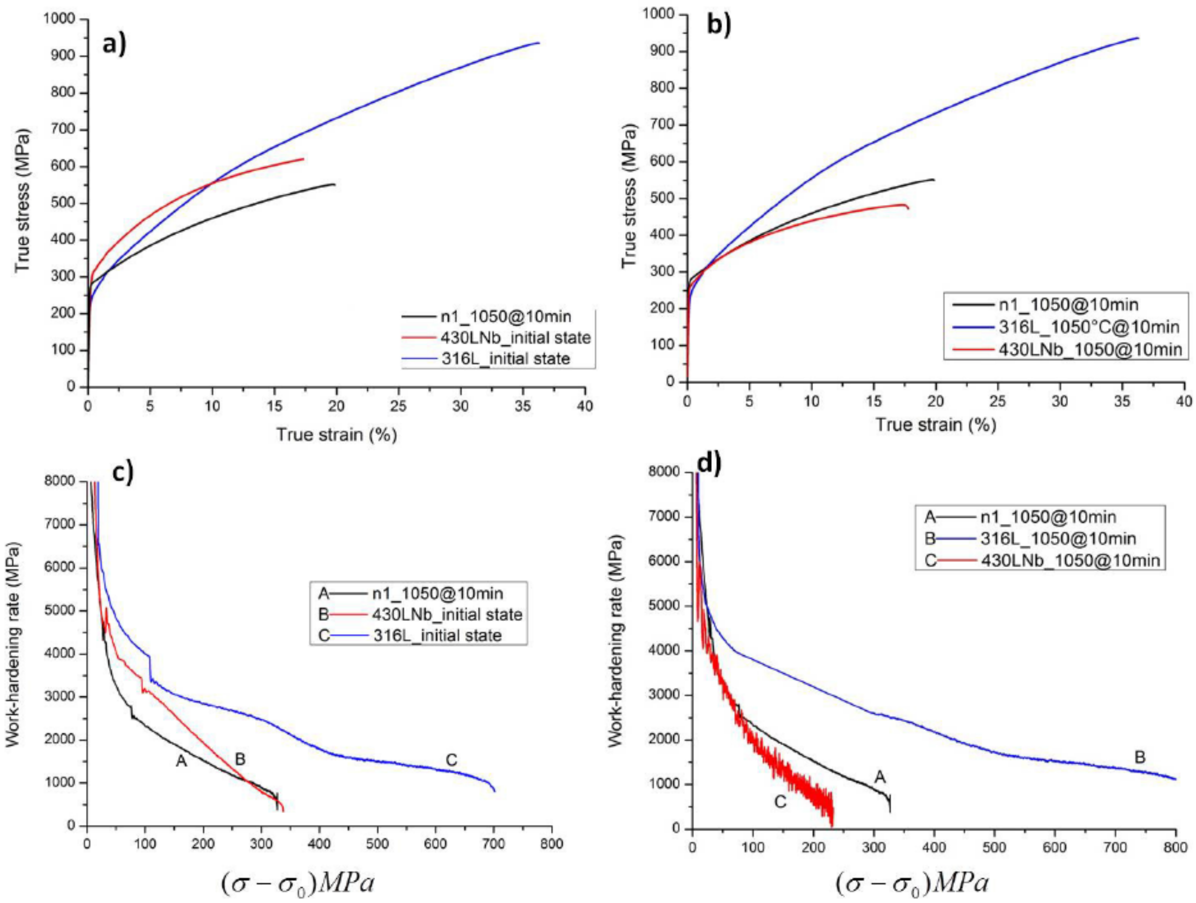

Figure V-3: Mechanical response of n1 composite after annealing at 1050°C@10min compared with initial wires a), c) and Annealed wires b), d)

V.I.2.b Composites n(i>1)

Unlike n1 composite, the tensile behavior of n2, n3 and n4 composites was examined after annealing with the optimized parameters (i.e. 1h at 850°C with a heating rate of 70°C/h). The composites tensile curves were compared with those of individual wires of 316L and 430LNb isothermally treated at 850°C for duration of 1h after cold drawing down to 92% of section reduction (similar drawing conditions as composites). See Figure V-4.

Despite the fact that the volume fraction of each phase varies for each composite, one can notice the increase of the flow stress at each step. Indeed, the n2 and n4 composites have the same volume fraction of ferrite (73% measured by image analysis), however, the flow stress of n4 composite is significantly higher than that of n2. Similar trend is observed in n3 and n5 composite (55% of calculated austenite not taking into account the austenite reversion). The evolution of yield strength, tensile strength and uniform elongation are summarized in Figure V-5. One can notice the strong increase of yield strength between n2 and n3. However, the increase of yield strength becomes relatively slow between n4 and n5.

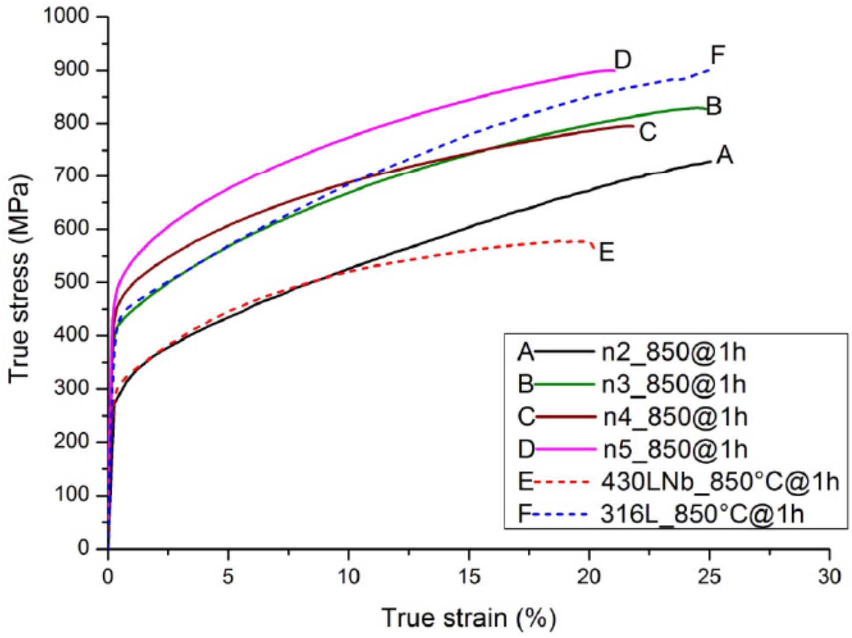

Figure V-4: Mechanical response of composites n(i>1) compared with 316L and 430LNb wires after annealing at 850°C

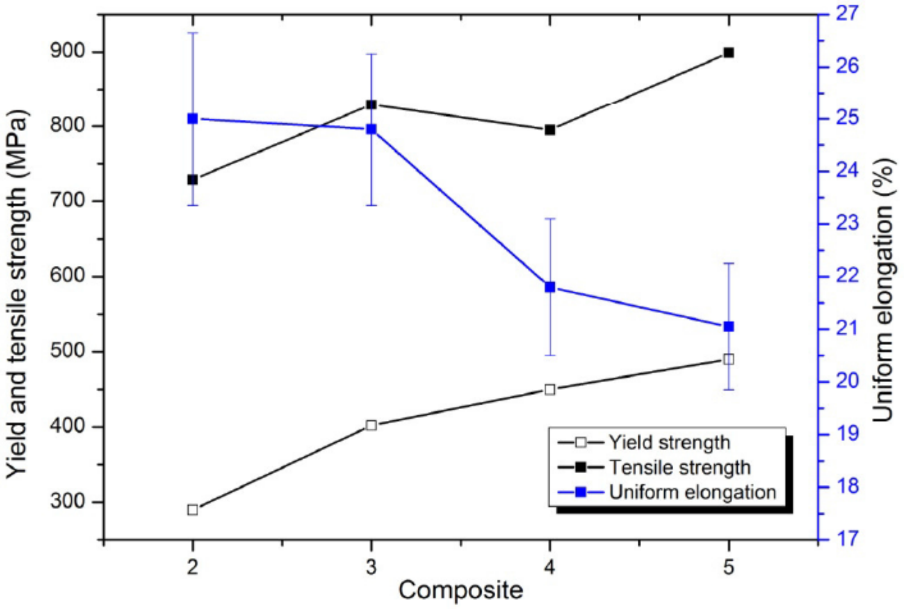

Figure V-5: The evolution of the mechanical properties as a function of composite n

Compared to the individual wires of 316L and 430LNb, it is interesting to notice that none of the composites' flow stress is situated between that of 316L and 430LNb wires. Indeed, the flow stress of n2 composite, with 73% of ferrite, fits perfectly with the flow stress curve of 430LNb wire up to 10% strain beyond which the work hardening of n2 composite starts to increase. The same trend is observed between n3 composite and 316L wire. However, the flow stress of n3 decreases after 10% of deformation. On the other hand, the flow stress of n4 (27% of γ) and n5 (55% of γ) exceeds that of 316L wire.

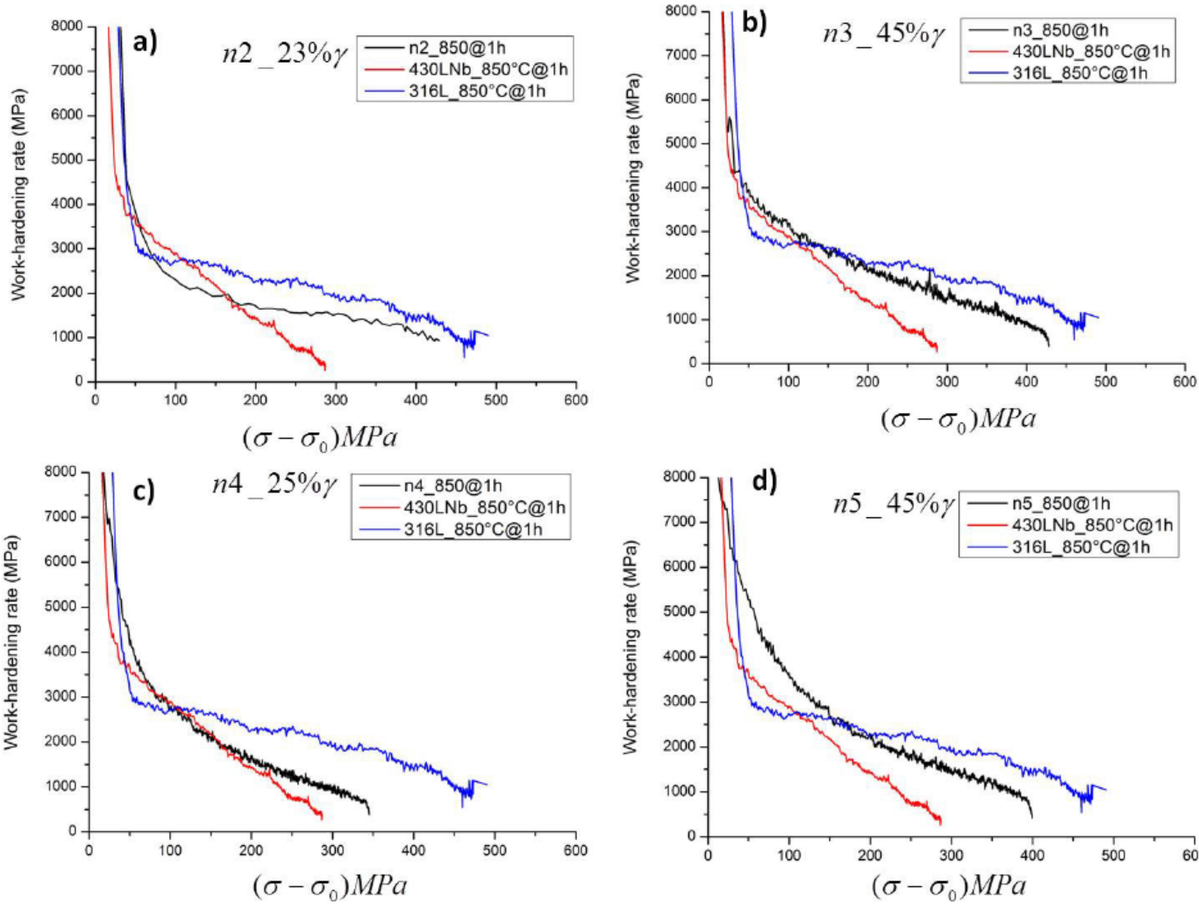

Figure V-6: Work-hardening rates of the composites n (i>1) compared with those of individual wires of 316L and 430LNb after annealing at 850°C a) n2 b) n3 c) n4 d)n5

The work-hardening rate of composites n2, n3, n4 and n5 annealed at 850°C is compared with that of individual wires of 316L and 430LNb (heat-treated isothermally at 850°C for 1h). Unlike the flow-stress curves, the work hardening rate versus the flow stresses curves of composite are always situated between those of 316L and 430LNb wires. It is also interesting to notice that the phase volume fraction influence the trend of work-hardening rate. Indeed, composites with 55% of volume fraction of γ phase such as n3 and n5 possess θ-ε curves similar to that of 316L despite sharper elasto-plastic transition for the latter. The same trend is observed between composite n4 (72% of α) and 430LNb wire. However, a slight difference is observed between n2 (72% of α) and 430LNb.

V.I.3 Discussion

V.I.3.a Tensile curves

i) Bulk materials

316L is, at room temperature, a slightly metastable austentite in which a limited amount of martensitic transformation can occur during plastic deformation. In our case, the tensile curves at room temperature of 316L in either the as-received state or after thermomechanical treatment exhibit no evidence of a possible martensite formation which results generally in a change of slope of the flow stress during plastic deformation [Spencer 2004]. However, the change in strain hardening rate may be visible only if a large fraction of martensite is formed during deformation. In fact, [Spencer 2004] found that for 316L only 9% of martensite formation occurred at large strain during an uniaxial tensile test at ambient temperature, and that the martensitic transformation starts after 30% of strain, see Figure V-7.

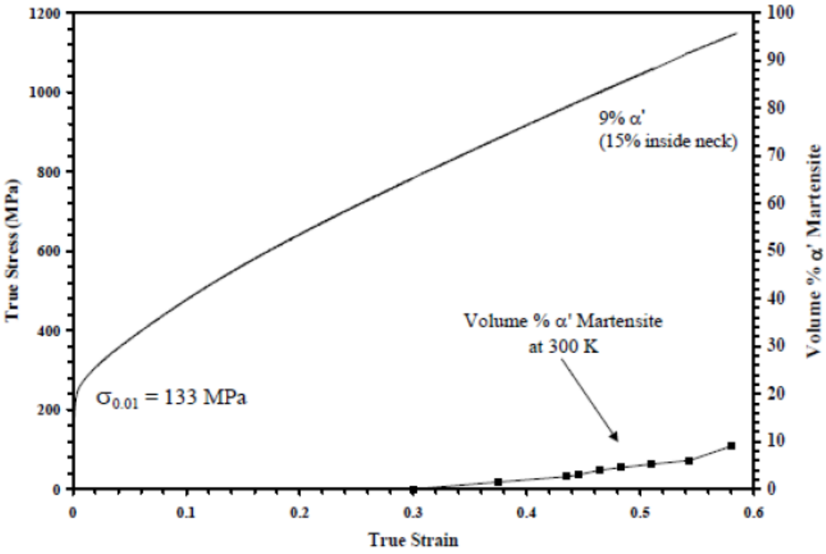

Figure V-7: Stress-strain response of 316L stainless steel at 300 K, with the volume fraction of α' martensite superimposed [Spencer 2004]

In our case, the possible presence of martensite α' was evaluated during two steps; i) after cold drawing of 316L wire and annealing treatment ii) during the uniaxial tensile test.
Using a sigmameter (See Chapter II), the martensite evolution has been followed in the as-drawn state (92% of section reduction) and after annealing at temperatures 750°C and 850°C for annealing durations 30 seconds, 3 minutes and 1h. It is interesting to notice that only 0.7% of magnetic phase is present in the deep drawn state whereas after annealing this amount decreases to 0.2-0.4%. In both cases (drawn and annealed), the amount of the magnetic phase present in 316L is insignificant and negligible.

Besides, no evidence of a possible strain-induced marteniste transformation was found during in-situ uniaxial tensile test using synchrotron diffraction (the methodology of determination of the evolution of γ phase using this technique is detailed in Chapter II). Figure V-8 shows the diffraction peaks parallel to tensile direction (see Chapter II) for bulk wire 316L annealed for 1h at 850°C after 26% of section reduction which shows no presence of the formation of hexagonal ε martensite during deformation. The quantitative analysis of the phase fractions does not show either any evolution of the fraction of the (α+ α') peaks.

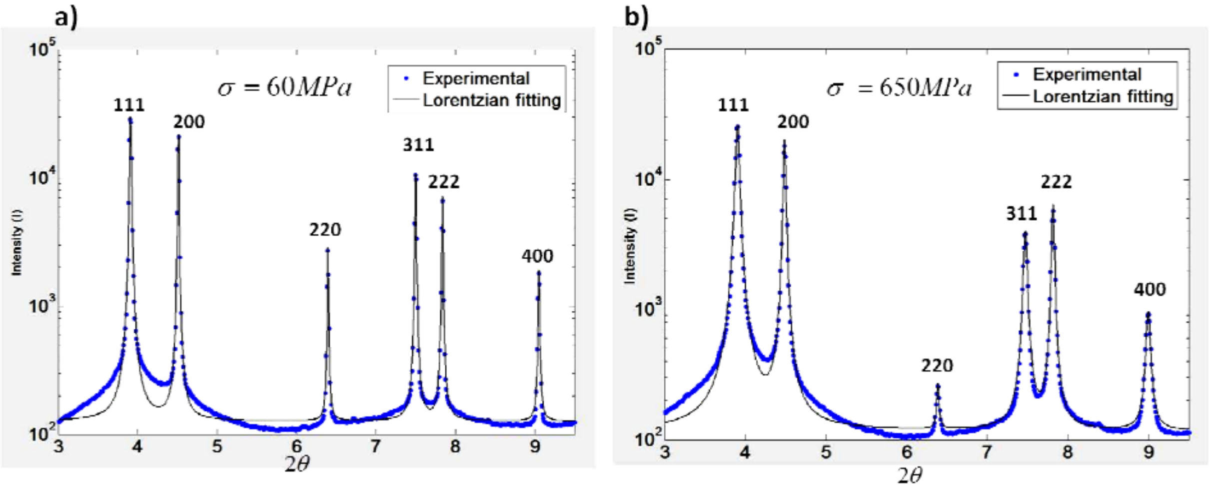

Figure V-8: Diffraction peaks parallel to the tensile direction of bulk 316L annealed for 1h at 850°C a) diffraction at 60MPa of loading b) diffraction after 650MPa of loading

The difference between the present results and that of [Spencer 2004], in terms of a possible strain-induced martensite formation in 316L, is due to differences in chemical compositions, particularly the Ni content. In fact, the 316L type used in the present work has a Ni content of 11.09% against 10.02% in 316L type used in [Sepencer 2004] work, see Table V-1. This significant difference seems to contribute efficiently to the stabilization of 316L wires we have used in this work.

Table V-1: Chemical composition of 316L

	C	N	Cr	Ni	Mn	Si	Cu	Mo	Co
316L [Spencer 2004]	0.02	0.08	16.19	10.02	1.68	0.5	0.34	2.03	0.13
316L Present work	0.019	0.029	16.734	11.09	0.795	0.505	0.344	2.034	0.158

ii) Composites

Since the aim of this study is to explore the mechanical properties of the produced composites, it is essential to, primarily, compare the mechanical behavior of the composites with that of its constituting phase; i.e. 316L and 430LNb wires. Of course, this approach will help us to understand and rationalize the resultant properties of the obtained composites.

- *n1 annealed at 1050°C for 10 minutes*

As presented above, it is more realistic to compare n1 after annealing with individual wires of 316L and 430LNb which have undergone similar annealing conditions as the n1 composite. Wires of 316L 430LNb drawn down to 25% and 53% respectively and annealed for 10 minutes at 1050°C have been used for this purpose. In order to predict the mechanical behavior of n1 composite, the classical law of mixture can be applied. Indeed, if the flow stress σ is modeled according to an isostrain rule of mixtures (ROM), the flow stress of the composite σ_c can be written as a function of the flow stress of the two constituents and their volume fraction as following:

$$\sigma_c(\varepsilon) = V_{316L}\sigma_{316L}(\varepsilon) + V_{430LNb}\sigma_{430LNb}(\varepsilon) \qquad \text{Eq.V-1}$$

Where ε is the strain, σ_c, σ_{316L} and σ_{430LNb} are the flow stress of the composite and of the 316L and 430LNb wires, respectively. V_{316L} and V_{430LNb} are the volume fractions of the constituting phases (316L and 430LNb respectively) present in composite n1.

A good approximation is obtained between experimental result and modeling with the simple law of mixture expressed in Eq.V-1, despite the slight difference in the yield strength, namely 263 MPa in experiment against 230 MPa predicted by ROM. The applicability of the ROM is expected for this composite since no significant changes in terms of microstructure, have occurred between the individual wires and those of the n1 composite.

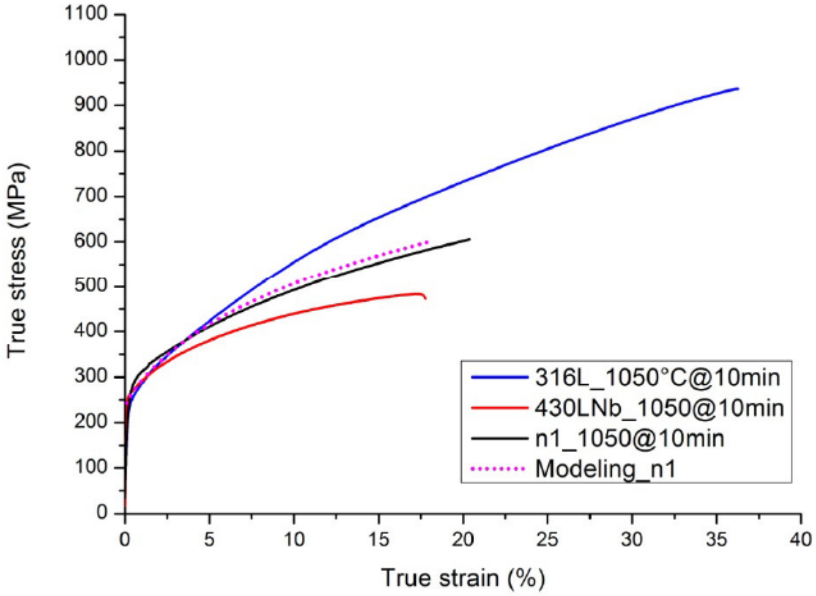

Figure V-9: Mechanical response of composite n1 compared with bulk wires

Indeed, if we compare the average grain size of ferrite inside the n1 composite (measured from EBSD maps) and that of the individual wire (calculated by interception method on optical micrographs) we find a similar average grain size ≈ 55µm. On the other hand, the average grain size of the individual wire of 316L is slightly higher (60µm) than that inside the n1 composite (50µm), which could explain the slightly larger yield strength in the composite.

Regarding the possible influence of the martensite formed in the vicinity of 316L/430LNb interface inside the composite (see chapter IV), one can expect it to be negligible because of its volume fraction that we calculate to be at most 0.6%. This fraction was calculated by assuming that the martensite is formed within a constant layer inside 316L wire and tube as illustrated in Figure V-10. The thickness of this layer was taken to be the maximum observed, namely 3µm (see chapter IV). In fact, the good agreement obtained by ROM with the experiment confirms that there is no contribution of a third phase.

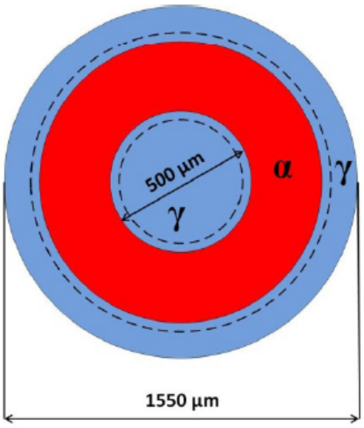

Figure V-10: Illustration of n1 composite with the martensite layer (dashed line) of 3µm thickness formed within 316L/430LNb interface

- *Composite n(i>1) annealed at 850°C for 1 hour*

As described above, a systematic increase in flow stress in composites n(i>1) is observed as a function of manufacturing steps. Three hypotheses could explain this increase:

i) <u>Volume fraction of the hard phase and/or strain-induced martensite transformation</u>

In view of the hardness measurements before and after annealing for both phases (see chapter IV) and also the tensile curves shown above, austenite is the hard phase in our composites 316L/430LNb, except for the thin layer of thermal martensite. However, during the different steps of the process we do not see a correlation between strength and volume fraction of austenite (as for the n4 composite which has a lower fraction of this phase)

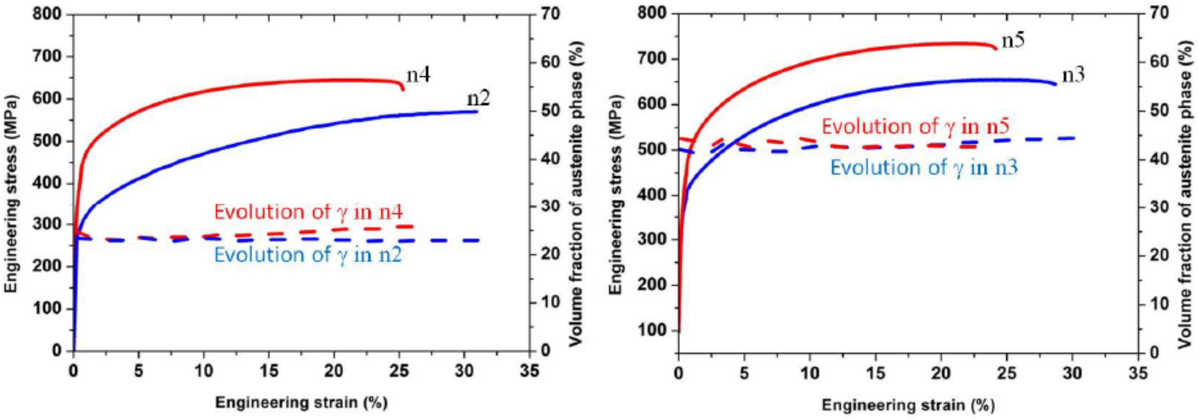

Figure V-11: In-situ tensile tests for n2; n4, n3 and n5 composites, and austenite fractions as a function of strain, determined by high energy synchrotron X-ray

On the other hand, thanks to in-situ tensile test by synchrotron X-ray diffraction, the evolution of the austenite volume fraction was evaluated during plastic deformation in order to examine a possible martensitic transformation. One can deduce from Figure V-11 that the austenitic phase inside all composites is stable and that no transformation to martensite has occurred. Therefore, this first hypothesis does not seem to be the origin of the systematic increase in strength with processing step.

ii) Strengthening by mismatch

The strength ratio (or hardness ratio) of the two constituents (C^*) was found to be one of the most important factors that control the mechanical properties of two-phase alloys [Tamura 1982] [Tamura 1973]. C^* is defined according to [Tamura 1973] as following:

$$C^* = \frac{\sigma_{II}}{\sigma_I} \qquad \text{Eq. V-2}$$

Where σ_{II} and σ_I are referred to the 0.2% proof stresses of the hard and soft phases respectively. [Tamura et al. 1973] have examined the effect of C^* on the yield strength of the alloy (σ_s) as a function of the volume fraction (f) of the hard phase (which is the ferrite in their case) under the same grain size (d). Their investigations were performed on three α-γ alloys: Fe-C, Fe-Ni-C, and Fe-Cr-Ni. Figure V-12 shows the result of C^* relationship with σ_s and volume fraction of the hard phase f. Two interesting results can be obtained from Figure V-12:

- σ_s is almost independent of C^* in the region where f is small
- σ_s increases significantly in the case of high C^*. However, in the case of low C^*, linear relationship is obtained between σ_s and f which is well approximated by the classical ROM.

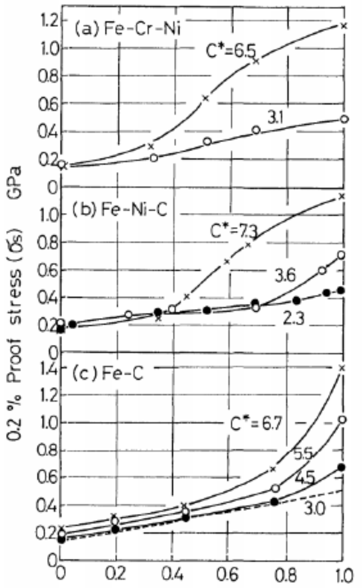

Figure V-12: Effect of parameter C* on relationship between σ_s and volume fraction f [Tamura 1973]

In our case, the strength ratio between ferrite 430LNb and austenite 316L is approximated by their hardness ratio. In sight of the above results and those of chapter IV, the austenite is the hard phase. Hence, C^* can be written as following:

$$C^* = \frac{\sigma_{316L}}{\sigma_{430LNb}} = \frac{HV_{316L}}{HV_{430LNb}} \qquad \text{Eq. V-3}$$

In chapter IV, we showed that within the same phase, different hardness value are obtained as a function of the generation. For example, in composite n4 annealed at 850°C, all 316L generations are harder than 430LNb wires and tubes. If we take the ratio between the hardest generation of 316L and the softest generation of 430LNb, the value obtained doesn't exceed 1.7 which is, based on the results of [Tamura 1973], very low. Thus, the influence of C^*on the increasing of the composites' flow stress could be negligible and doesn't explain this trend.

iii) Shape of constituents and grain size

The influence of the shape of the hard phase in two-phase alloys on the overall strength has been, and is still, a subject of various investigations. The geometry of the second phase inclusions was found to have a determining role in load transfer, between the constituents, which is, in turn, an important factor determining the strength of alloys [Fischmeister and Karlsson 1977].

[Gurland 1979] proposed a model combining the strength of an alloy with its microstructural morphology by introducing the concept of contiguity which expresses the extent of contact between adjacent particles of a phase. This parameter is expressed as the fraction of the internal surface area of a phase that is shared by particles of the same phase. For phase γ for example, the contiguity can be written as following:

$$K = \frac{2S_{\gamma\gamma}}{2S_{\gamma\gamma} + 2S_{\alpha\gamma}} \qquad \text{Eq. V-4}$$

Where $S_{\gamma\gamma}$ is the shared boundary area between γ particles and $S_{\alpha\gamma}$ is the area of the interphase boundary between α and γ per unit volume [E.E Underwood 1969]. A modified ROM taking into account the geometrical aspect of the hard phase was proposed. According to [Gurland 1979], the contiguity parameter for an alloy containing fiber-like hard phase is taken to be 1. Thus, a continuous filamentary alloy obeys always the simple ROM. The strength of particles reinforced microcomposite alloys such as ferrite-martensite has been successfully modeled by a simple law of mixtures in the recent work of [Embury 2010]. The discussion on the influence of phase shape on the alloy strength is rather complicated and therefore is beyond the scope of the current discussion. However, the composites of the present work have a continuous filamentary structure. Hence, the hypothesis of a possible strengthening beyond the ROM under the influence of phase shape seems to be unrealistic.

Therefore, the grain size of each constituent of the composites seems to be the most influential parameter on the systematic strengthening of the composites at each manufacturing step. Indeed, using local and global EBSD maps, the grain size of each component in n3, n4 and n5 were measured. As shown in Figure V-13, one can notice two features:

- Within the same composite, the grain size for a given phase is smaller in the old generations than the new ones. In other words, a decrease of grain size is noticed for a given phase moving from external tube toward the core of the wire.
- For a given generation and phase, one can notice a systematic decrease of grain size when I (number of composite) increases.

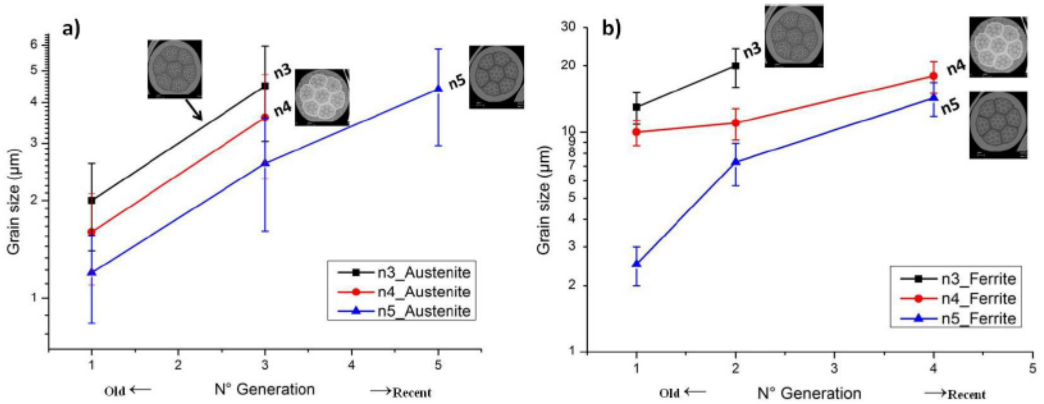

Figure V-13: Grain size evolution of each component (generation) for composite n3, n4 and n5 after annealing at 850°C for 1 hour: a) austenite (316L) , b) ferrite (430LNb)

In order to examine the possible influence of the grain size on the yield strength of the composites, Hall-Petch relation and ROM can be used. The HP relationship for both phases austenite and ferrite has been constructed using individual wires of 316L and 430LNb. These wires were subjected to different thermo-mechanical operations as Table V-1 shows. Figure V-14 shows the relation between the yield strength measured by tensile testing and microhardness as a function of square root of grain size for individual wires 316L and 430LNb.

Table V-2: Experimental data of 316L and 430LNb wires used for HP relationship

316L						
Wire	Deformation	Heat-treatments*	Yield strength (MPa)	Micro-hardness (HV)	ave. diameter d (µm)	$1/\sqrt{d}$
1	Section reduction from Φ=5.5mm down to 1.5mm	850@1min	470	227	1.8	0.745356
2		850@5min	440	215	2.1	0.690066
3		850@1h	410	212	2.6	0.620174
4		950@1h	312	162	16.7	0.244704
5	Section reduction from Φ=1.8mm down to 1.5mm	1050@10min	233	150	50	0.141421
430LNb						
1	Section reduction from Φ=5.5mm down to 1.5mm	850@1h	266	162	11.6	0.29361
2	Section reduction from Φ=2.2.mm down to 1.5mm	900@10 min	293	165	8	0.353553
3		1050@10min	224	150	55	0.134284

The HP for both bulk wires is then expressed as following:

$$\sigma_y^{316L} = 201.42 + \frac{351.35}{\sqrt{d}} \qquad \text{Eq. V-5}$$

$$\sigma_y^{430LNb} = 181.48 + \frac{305.05}{\sqrt{d}} \qquad \text{Eq. V-6}$$

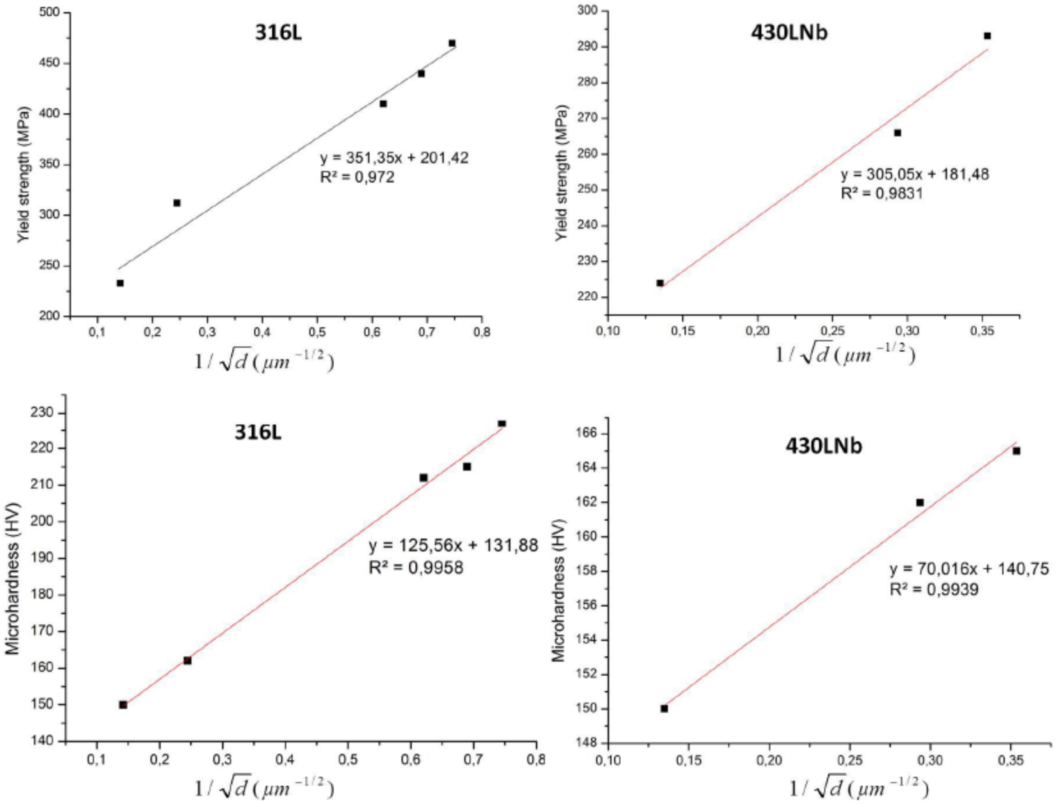

Figure V-14: Yield strength as a function of inverse square root of grain size for a) 316 c) 430LNb; Microhardness as a function of inverse square root of grain size for b) 316 and d) 430LNb

Hence, one can calculate the yield strength of the composite n(i) σ_c taking into account the contribution of each generation. The ROM can then be written as following:

$$\sigma_c = \sum_{j=1} V_j^{316L}\sigma_j^{316L} + \sum_{j=1} V_j^{430LNb}\sigma_j^{430LNb} \qquad \text{Eq. V-7}$$

Where V_j^{ph} and σ_j^{ph} are the volume fraction and the yield strength of the phase *ph* issued from generation *j* respectively.

Table V-3 shows the calculated yield strength of each generation of composite n3 and n4 , after annealed at 850°C for 1h, using the empirical HP relationship of 316L and 430LNb in Eq. V-5 and Eq. V-6. Indeed, in composite n3 two generations of austenitic phase are present: generation issued from n1 (the central 316l wire and the tube) and the second issued from n3 (tube). Concerning the ferritic phase, two generations are also present: the first generation issued from n1 (wires) and the second issued from n2 composite (tube).

In composite n4, the austenitic phase is issued from the same generation as n3 composite. However, in this composite a new generation of ferritic phase is added to those of n3 composite due to the re-bundling with 430LNb tube.

It should be noticed also that it is possible to find similar grain size in different generation. For example from EBSD maps, the grain size of ferrite issued from n2 tube and n1 wire is found to be 10.5µm for both of them.

Table V-3: Data of each generation inside composite n3 and n4 after annealing at 850°C for 1h

n3 composite				
phase	generation	d (µm)	Calculated HP σ_y	Volume fraction%
316L	n1 (tube+wires)	2	449.2	15.4
	n3 tube	4.5	366.5	29.6
430LNb	n1 wires	20	250	26
	n2 tube	13	266	29
n4 composite				
316L	n1 (tube+wires)	1.65	474	1.9
	n3 tube	3.65	384.7	24
430LNb	n1 wires+n2 tube	10.5	275	44.5
	n4 tube	18	253.4	29.6

Applying Eq. V-7 for these two composites, we can obtain the calculated yield strength for n3 and n4 which takes into account the contribution of each component. Table V-4 compares the experimental yield strength and that calculated from using HP and Eq. V-7. Interesting observations can be made here: 1) the calculated yield strength of n3 composite is close to that of n4 composite 2) a significant difference between the calculated and the experimental yield strength can be noticed.

Table V-4:Comparison between ROM and experience for composites n3 and n4

composite	σ_y Calculated ROM (MPa)	σ_y Experimental (MPa)	Error
n3	318	402	20%
n4	298.4	450	33%

This difference between the ROM and the experiments can be attributed to the fact that the HP relationship is derived from individual bulk wires, which are not representative for the austenitic and ferritic phase in the composites. Indeed, as we presented in chapter IV, a strong interdiffusion occurs during annealing which changes significantly the chemical composition. This may lead to a change in mechanical behavior and therefore HP coefficients could change also due to this interdiffusion. [Takeda et al 2008], for example, investigated the influence of the interstitial elements of ferritic steel, namely carbon and nitrogen, on the HP coefficients.

They found that the HP increase significantly as the carbon content is increased whereas the nitrogen has a limited influence on this increase.

iv) Influence of the chemical composition

As discussed in chapter IV, the change in the chemical composition of both phases inside the composite n(i) is significant in particular within phases' interface and the very fine components. Indeed, the concentration of substitutional elements like Ni and Mo has been increased from 0.2% to 2% (for Ni) and 0.039% to 0.5% (for Mo) in α side. The influence of this significant change in chemical composition on the yield strength can be qualitatively estimated using Figure I-4 in which the evolution of the stress change as a function of concentration of different alloying elements are illustrated. One can notice that when the Ni concentration increases, a negative change in stress is obtained. This implies that the ferrite of the finest cells is softer than its initial state. On the other hand, the change in the yield strength induced by a gain in Mo concentration is relatively high which means, in turn, that the ferrite should be stronger than its initial state.

Although the change in chemical composition for Ni and Mo in both phases is significant, its influence on the yield strength remains very limited according to Figure I-4.

Regarding the possible influence of the interstitial elements such as C and N, their concentrations are initially low (<0.02%) and hence the change in strength induced by their interdiffusion can be neglected.

v) Influence of the thermal martensite

In composite n1, the fraction of thermal martensite is estimated to 0.6% which has a negligible effect. However, in composites n (i>1), the fraction of martensite increases together with the increase of the interface area between ferrite and austenite. In addition, the re-bundling process accumulates the martensite from the previous step; n(i-1).For example, in composite n2, the martensite (calculated in the same way as presented in the previous paragraph), reaches 1.6%.

Identically, the martensite formed within the vicinity of the interface γ/α increases to reach 5.1, 5.6 and 6% in composite n3, n4 and n5 respectively. This systematic increase in martensite volume fraction can be explained by the fact that the martensite present in the current composite n(i) is not only issued from the previous one, i.e. composite n(i-1) but also during the current step (i). Indeed, at each step a new intimate contact between 316L and 430LNb is created (see chapter III) as we can see in Figure V-15. In this Figure we can notice the formation of small grains between 430LNb (issued from n2) and 316L (issued from n3) tube in composite n4.

In order to have an idea about the possible contribution of the thermal martensite to composites strengthening, we can assume that the flow stress of this martensite in composite n3 and n4 for example is about 1.2GPa. By including this new hard phase to Eq. V-7, the new calculated yield strength of n3 and n4 is increased by 61 MPa and 67 MPa respectively. The following table summarizes this result:

Table V-5: Comparison between ROM including martensite contribution and experience for composites n3 and n4

composite	σ_y Calculated ROM (MPa) Without martensite	σ_y Calculated ROM (MPa) with martensite	σ_y Experimental (MPa)	Error
n3	318	379	402	5.6%
n4	298.4	365	450	18.8%

If we consider now that the small grains, with 0.8 µm of diameter, formed within the interface ferrite/austenite (see Figure V-15) are ferritic phase rather than martenstic. Hence, one can predict its strength from HP relation Eq. V-6 to be around 522 MPa. Similarly, by taking into account this new ferrite phase in Eq. V-7, the new calculated yield strength of n3 and n4 is increased by 27 MPa and 33 MPa respectively.

Table V-6: Comparison between ROM including fine ferrite (instead of martensite) and experience for composite n3 and n4

composite	σ_y Calculated ROM (MPa) Without fine ferrite	σ_y Calculated ROM (MPa) with fine ferrite	σ_y Experimental (MPa)	Error
n3	318	345	402	14.6%
n4	298.4	331	450	26.4%

The results reported in Table V-5 show that the martensite may contribute significantly to the strengthening of composite n3 whereas its contribution is less pronounced in composite n4. This could be explained by the fact that by introducing a new generation, more fine structures with fine grains are obtained and the difference in grain sizes from generation to another for a give phase will be more pronounced.

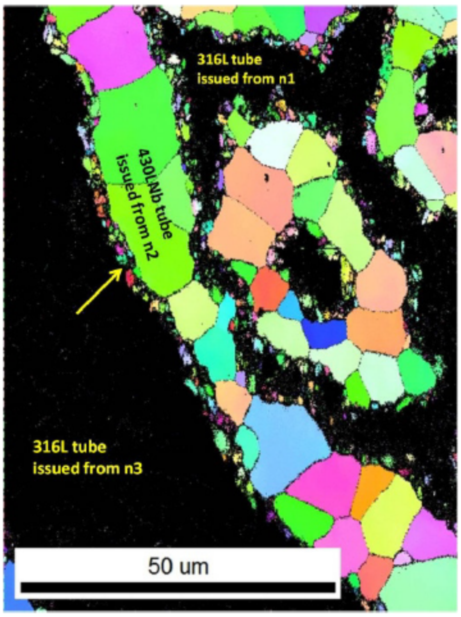

Figure V-15: EBSD map of the detailed microstructure in composite n4: the colored region is the ferritic phase and the black region is the austenitic phase; the arrow indicates the small grains between ferritic and austenite tube

V.I.3.b Work-hardening rate (θ)

The work-hardening rates of wires of 316L and 430LNb heat treated at different temperatures and different durations, are compared in Figure V-6. It is noticed that systematically the ferrite presents a lower hardening capacity than the austenite; θ-ε curves of 316L are always above those of the 430LNb whatever the annealing conditions.

The analysis developed by [Kocks and Mecking 2003] may explain this trend. In fact, their approach treats work hardening as being a function of the net rate of dislocation accumulation with imposed plastic strain ε. They divided the work hardening processes into two groups: those which are athermal and those thermally dependant. This can be mathematically expressed as following:

$$d\rho = \frac{d\varepsilon}{b\Lambda} - d\rho_r \qquad \text{Eq. V-8}$$

Where b is the dislocation Burgers vector and Λ is their mean free path, ρ is the dislocation density. The first term of the right hand side of equation ($d\varepsilon/b\Lambda$), is the athermal term. It represents the accumulation of dislocations due to the reduction in the free path for slip. Since this accumulation is based on geometry, it is thermally independent. The second term $d\rho_r$ represents the annihilation of dislocations due to dynamic recovery processes.

According to [Kocks and Mecking 2003] both terms are operative at all work hardening stages. However, these stages can be distinguished by the extent to which athermal *vs* thermal processes are dominant. For example, in stage II, it is argued that the work-hardening rate is very high due to the dominant effect of the athermal process of dislocation accumulation. On the other hand, in stage III, dynamics recovery begins to offset the dislocation accumulation of the stage II.

The athermal term in Eq. V-8 leads to a constant work hardnening rate and thermally dependant work-hardening θ_r. Thus, the Eq. V-8 may be re-written as :

$$\theta = \theta_0 - K(\sigma - \sigma_0) \qquad \text{Eq. V-9}$$

Where K is the coefficient of dynamic recovery, σ and σ_0 is the stress and the yield strength respectively.

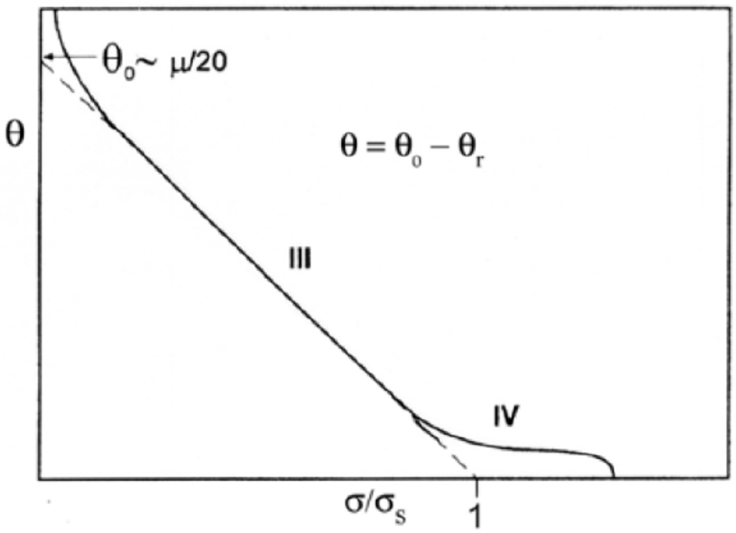

Figure V-16: Schematic sketch of an idealized θ-σ plot for polycristalline FCC metals: σ is normalised by σ_s the stress where the extrapolated stage III work hardening rate goes to zero (adapted from [Kocks 2003])

Where θ_0 represents the maximum possible work-hardening rate in stage II which is to say $\mu/20$ in FCC polycrystals. The idealized behavior is illustrated in Figure V-16.

It is important to notice that the magnitude of θ_r may be influenced by different material parameters [Kocks and Mecking 2003]. One of the most important parameter is the stacking fault energy (SFE). Indeed, as SFE decreases, dynamic recovery processes such as cross-slip become very difficult [Friedel 1964], thus θ_r will be smaller. When θ_r is small, the resultant θ becomes higher. This analysis is valid for all FCC polycrystals. According to [Kocks and Mecking 2003], the result of this analysis can be also extended to BCC metals by assimilating them to FCC metals with high SFE such as aluminum.

For austenitic stainless steels, the stacking fault energy is known to be dependent on the chemical compositions [Rhodes and Thompson 1977] [Brofman and Ansell 1978]. Several empirical equations have been proposed to calculate the SFE based on the chemical composition of the austenitic stainless steel. It is noteworthy that these equations have been determined by regression analysis by taking into consideration a limited number of alloying elements. The effect of the interstitial elements, for example, such as nitrogen was not included in these empirical equations. However, [Talonen 2007] has shown a good correlation between the empirical equation proposed by [Brofman and Ansell 1978] and the experimental measurement on grades 301LN and 304. The equation of [Brofman and Ansell 1978] is written as following:

$$\gamma_{SFE}(mJ.m^{-2}) = 16.7 + 2.1\%Ni - 0.9\%Cr + 26\%C \qquad \text{Éq. V-10}$$

Where γ_{SFE} is the stacking fault energy and %X is the weight percentage of the element X.

Direct application of this equation for our 316L using the nominal composition data shown in chapter II gives SFE of about 25 mJ.m^{-2} which is in consistent with the typical values for 316L found in the literature (30 mJ.m^{-2}) [Feaugas 1999].

In the view of the above discussion, the SFE can explain the trend obtained in Figure V-6. Indeed, when α increase (for example n4 75% of α) the working hardening rate of the composite get closer to that of 430LNb. Similar behavior is observed between composites n3 and n5 with 316L.

Concerning the influence of grain size on θ, it is well known, at least for pure FCC, that the dominant influence is by texture rather than by the grain size [Kocks and Mecking 2003]. However, in the recent work of [Huang 2004] and [Sinclair 2004], it was shown that the grain size dependence can be distinguished into : a) strongly grain size dependant; b) weakly grain size dependant regimes. The first was found to exist over the initial 5% tensile strain whereas the second was shown at large strain where the work hardening rate of fine grained structure converges to that of coarse grain. These features were observed in recent work of [Sinclair et al. 2006] in fine grained copper with grain size of 1-5µm. They provided a physical framework for investigating these grain size effects on yield and work hardening explaining the dependence of the initial work hardening behavior with grain size and the lack of dependence at large strain. The proposed model attributed the grain size dependence to the storage of dislocations at the grain boundaries. This storage contributes in turn to a) forest hardening giving an isotropic hardening b) building up a back stress leading to kinematic hardening contributions. At small strains, grain boundaries act perfectly as barriers to dislocations and impede the progress of similar dislocations [Sinclair et al. 2006]. However, this grain size dependence disappears at large strains owing to dislocation screening and dynamic recovery effects at grain boundaries. This model has successfully predicted the work hardening behavior of fined structure copper with 2 µm of grain size. See Figure V-17.

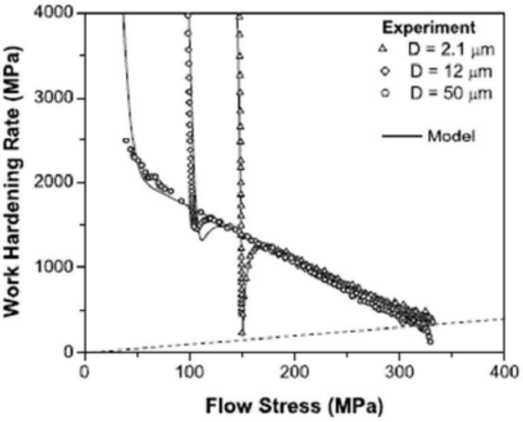

Figure V-17: Comparison with respect to work hardening rate as a function of flow stress between experimental data of copper with diffrent grain sizes (D) from [Lloyd 1980] with physical model [Sinclair et al. 2006].

The same trend has been observed in dual phase steels (DP) of ferrite and martensite in the recent work of [Calcagnottto et al. 2010]. Figure V-18 shows the plots of work hardening rate as a function of applied strains for three DP samples having different ferrite grain size for almost the same volume fraction of martensite. The grains refinement promotes initial work hardening rate. This was attributed to the dislocation interaction and the back stresses exerted by both martensite islands and ultra-fined ferrite grains.

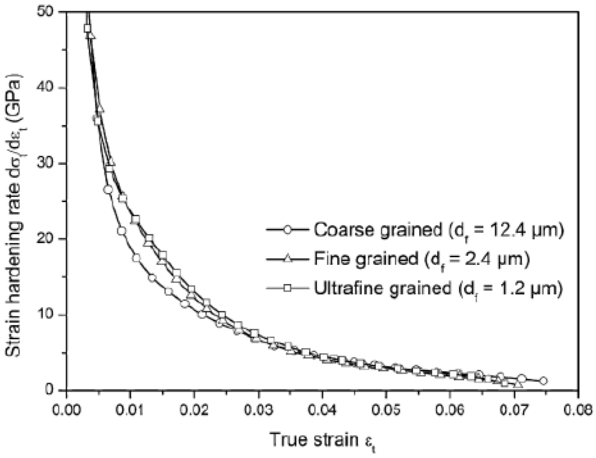

Figure V-18: strain hardening rate as a function of true strain of three DP samples with different ferrite grain size d_f [Calcagnotto et al. 2010]

Nevertheless, some materials such as Ag [Al-fadhalah et al. 2008] and Al-Mg [Sinclair 2004] and steels [Gubierrez 2008] [Bouaziz 2008] do not show this feature. Indeed, it was experimentally found in these cases that the grain size dependence continues at high stress. Particularly, it was observed that for an equivalent flow stresses a structure with fine grain size has a higher work hardening rate compared with larger ones. A very recent work of [Shadkam and Sinclair 2015] attributed this grain size dependence at large strain to the additional contribution of the storage of geometrically necessary dislocations rather than the persistent back stress. They provided a physical model, which takes into account the contribution of the geometrically necessary dislocations, capable of predicting the work hardening rate of fine grained FCC material. This model has successfully predicted the experimental work hardening rate curves of Cu-Ni alloys in which a strong grain size dependence at large strain has been observed.

In our case Figure V-19 shows the work hardening rate of composites n2 (23%γ), n3 (45%γ), n4(25%γ) and n5(45%γ) after annealing at 850°C for 1h. Interesting features can be observed; n5 composite has a higher initial work hardening rate than that of n3 composite. However, both work hardening rate curves overlap at high flow stress (>150MPa). This feature can be mainly attributed to the influence of the grain size (as discussed above) albeit significant chemical composition occurred within n2 cells inside composite n5 as presented in chapter IV. On the other hand, for composites n2 and n4, the same trend is observed at low stress (<150 MPa); the initial work hardening rate of composite n4 is higher than that of composite n2. However, beyond this, the work hardening rate of composite n2 starts to increase rapidly. Generally, one can attribute the difference in work hardening rate between composites n3 and n5 from one hand and from other hand n2 and n4 to the i) grain size effects; ii) volume fraction of the austenite and therefore to the stacking fault energy.

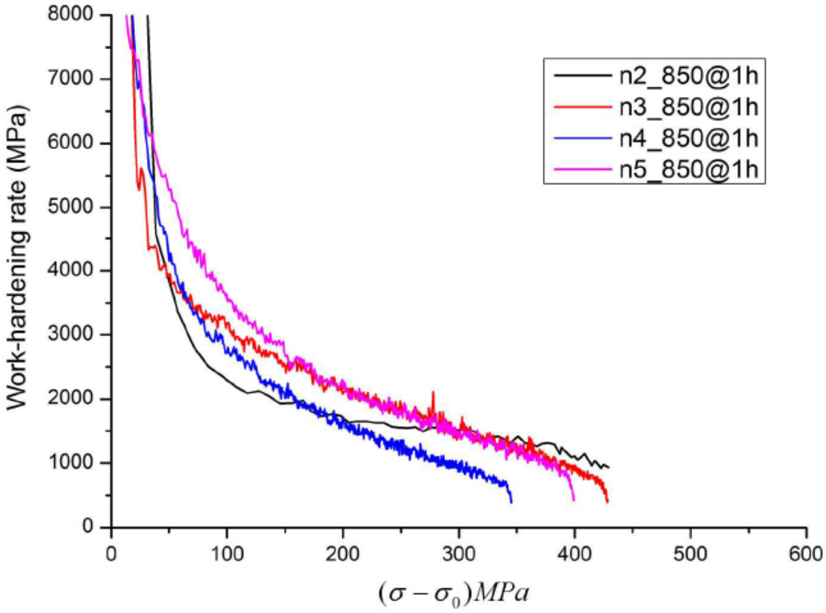

Figure V-19: Work hardening rate as a function of flow stress for composite n2, n3, n44 and n5 after annealing at 850°C for 1h

V.I.3.c Summary

- The austenite 316L is always the hard phase, in particular inside composites n(i>1).
- Good agreement is obtained between experiment and ROM prediction of the composite n1 annealed at 1050°C for duration of 10 minutes.
- An increase in mechanical properties is observed for the composites n(i>1) annealed at 850°C for 1 hour. Different hypotheses have been discussed to explain this systematic increase as a function of manufacturing step while at each one the proportion of the phases change by alternating 316L/430LNb tubes.
  The influence of grain size and chemical composition change seem to be the most plausible hypothesis. In addition, the contribution of the inherent martensite may not be negligible.

V.II Local mechanical behavior: in situ high energy synchrotron X-ray diffraction during tensile tests

V.II.1 Introduction

In-situ uniaxial tensile tests with continuous high energy synchrotron X-ray diffraction measurements were performed on the second architecture composites. The aim of these measurements was to determine the stress partitioning between the different phases during the tensile tests. The detailed methodology of the synchrotron X-ray diffraction experiments is explained in Chapter II. This technique associated with an in-situ applied stress allows quantifying and following the different deformation regimes within each phase of two-phase alloys [Sinclair et al. 2006] [Clausen et al. 1999] [Daymond et al. 2005].

This information is obtained by means of the diffractograms in which the diffracted intensity is plotted against the Bragg angle 2θ. The observed shift in position of a specific {hkl} plan results from a change in the average lattice plane strain ($<\varepsilon_{hkl}>$) which can be calculated using the expression:

$$\varepsilon_{hkl} = \frac{d_{hkl} - d_{hkl}^{0}}{d_{hkl}^{0}} \qquad \text{Eq. V-11}$$

Where $d_{hkl}$and d_{hkl}^{0} correspond to the lattice plane spacing at a given deformation step and at zero deformation, respectively.

In other words, the distribution of the applied stress inside the composite can be estimated thanks to the elastic strain of each phase. In fact, when a multi-phase alloy plastically deforms, the relative contribution of the individual phases to the overall load-carrying capacity can vary depending on their respective plastic behavior, shape, etc. Many representations have been used in the literature in order to analyze stress distribution problems in two-phase metals. The analysis reported by [Harjo et al. 2001] for α-γ Fe-Cr-Ni alloys, shows three distinct stages by plotting lattice strain *vs.* applied stress (or applied stress *vs.* lattice strain). These stages have been also observed in iron-copper experiments reported by [Han et Dawson, 2005] and schematized in Figure V-20:

- Stage I is characterized by an elastic behavior of both phases: a linear relationship between lattice strain and applied stress is found.
- Stage II: the deviation from the linearity marks the beginning of plastic deformation in one of the phases; the softer phase deforms plastically. As Figure V-20 illustrates, the plastification is characterized by a decrease of the slope of the lattice strain evolution in the soft phase. The increase of the slope, on the other hand, of the hard phase indicates a load-transfer from the soft to the hard phase.
- Stage III: both phases have yielded and a new redistribution is observed.

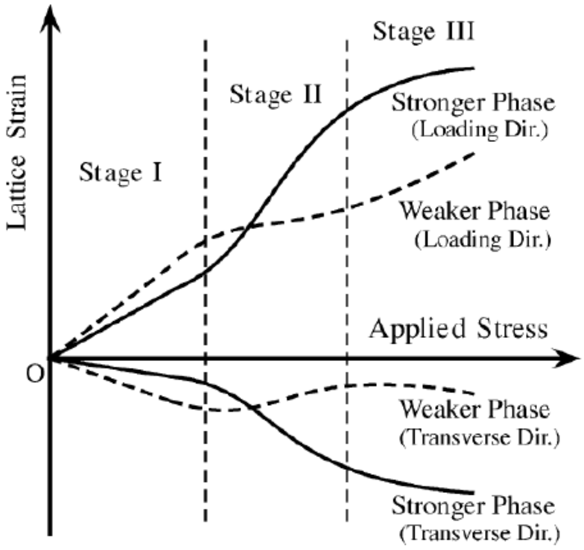

Figure V-20: Schematic illustration of lattice response in two-phase material [Han et Dawson, 2005]

The configuration shown in Figure V-20 is widely used, in the literature, for load partitioning analysis of two-phase alloys assisted by in situ neutron or high energy X-ray diffraction. By using this kind of representation, [Tomota et al. 2004] for example provided a good understanding of the influence of TRIP effects on the tensile behavior of different samples of γ/α steel subjected to different thermo-mechanical processes. Figure V-21 shows an example of [Tomota et al. 2004] results where the lattice strain of (200)γ, (110)α and (200)α are plotted as function of the applied stress. Identically to Figure V-20 , one can distinguish the three regions where the harder phase (γ) carries more load than the softer phase (α) after the deviation from the linear elastic line in point P1. Point P2 marks in fact the onset of strain induced-martensitic transformation determined a priori by texture analysis. Point P3 is the point where both phases α and γ deform plastically.

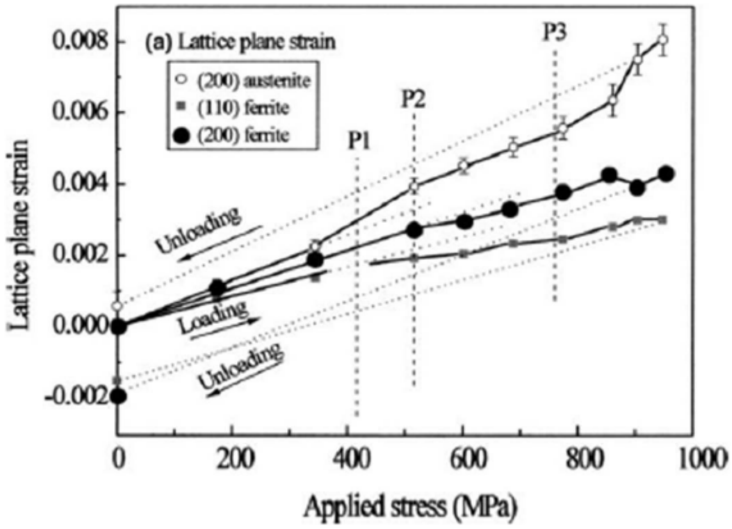

Figure V-21: Lattice plane strain as a function of applied stress for γ/α steel obtained by in situ neutron diffraction tensile test [Tomota et al. 2004]

In order to provide better understanding, it is necessary to highlight, in this kind of analysis, the importance of the choice of the suitable (hkl) reflection to be representative of both phases BCC and FCC during straining.

In the next section we will analyze the experimental results of for each composite n2 (23%γ), n3 (45%γ), n4(25%γ) and n5(45%γ) after annealing at 850°C for 1h. The choice of the suitable reflection for 430LNb and 316L will be also discussed.

V.II.2 Experimental Results

V.II.2.a Data presentation

The data for each composite (n2, n3, n4 and n5) annealed at 850°C is plotted in two different ways: Lattice strain *vs.* Applied stress and Lattice strain *vs.* Macroscopic strain. The calculation of the average stress will be discussed in the discussion sub-section.

Figure V-22 shows the diffraction peaks of ferrite and austenite phase inside composites from the second generation annealed 1 hour at 850°C. The diffraction profiles were fitted with a Lorentzian function. The diffraction peaks were first recorded before straining of a preload of 10 MPa to set up the sample and to ensure its alignment. This acquisition was taken as the initial diffraction state.

One can notice that under the measuring conditions, 6 Bragg peaks are accessible for the γ phase; reflections (111), (200), (311), (222) and (400). The most intense families of planes are (111) and (200).Regarding α phase, 5 Bragg peaks are accessible as shown in Figure V-22; (110), (200), (211), (220) and (310) of which the family of planes (110) and (211) are the most intense.

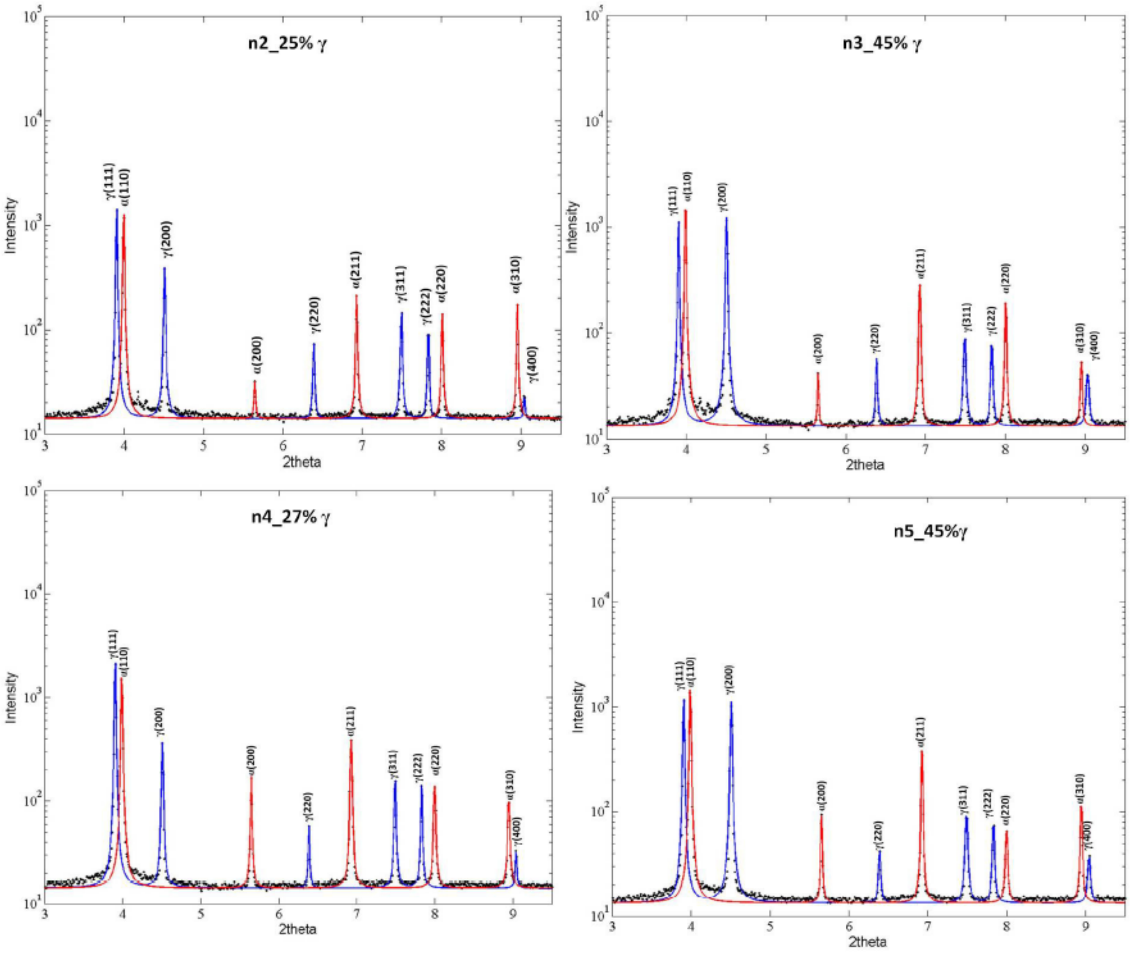

Figure V-22: 2θ diffractograms representing austenite (blue) and ferrite (red) peaks fitted with Lorentzian function at initial state (before straining) for composites n2, n3, n4 and n5 after annealing at 850°C for 1hour

It can be noticed from Figure V-22 that the intensity level of each reflection plane varies from one composite to another. For example, peak γ(200) shows a higher intensity in composites n3 and n5 than in composite n2 and n4. Identically, the intensity of a given reflection varies as a function of the composite. Indeed, one can notice the significant increase in intensity of α(200) in composite n4 compared with that in n2 composite. Nevertheless, reflection α(110) represents the most intense plane among the five ferritic Bragg peaks in all composites.

The calculated lattice strain of each hkl reflection, for both phases ferrite and austenite, is given as a function of true macroscopic strain in Figure V-23 and Figure V-24 respectively. In these figures, one can evaluate qualitatively the anistropic level of both phases. In our composites, the ferrite (bcc) shows less pronounced anisitropic behavior during deformation than the austenite. That is, the choice of a suitable hkl plane to be the most representative for austenitic phase becomes more complex.

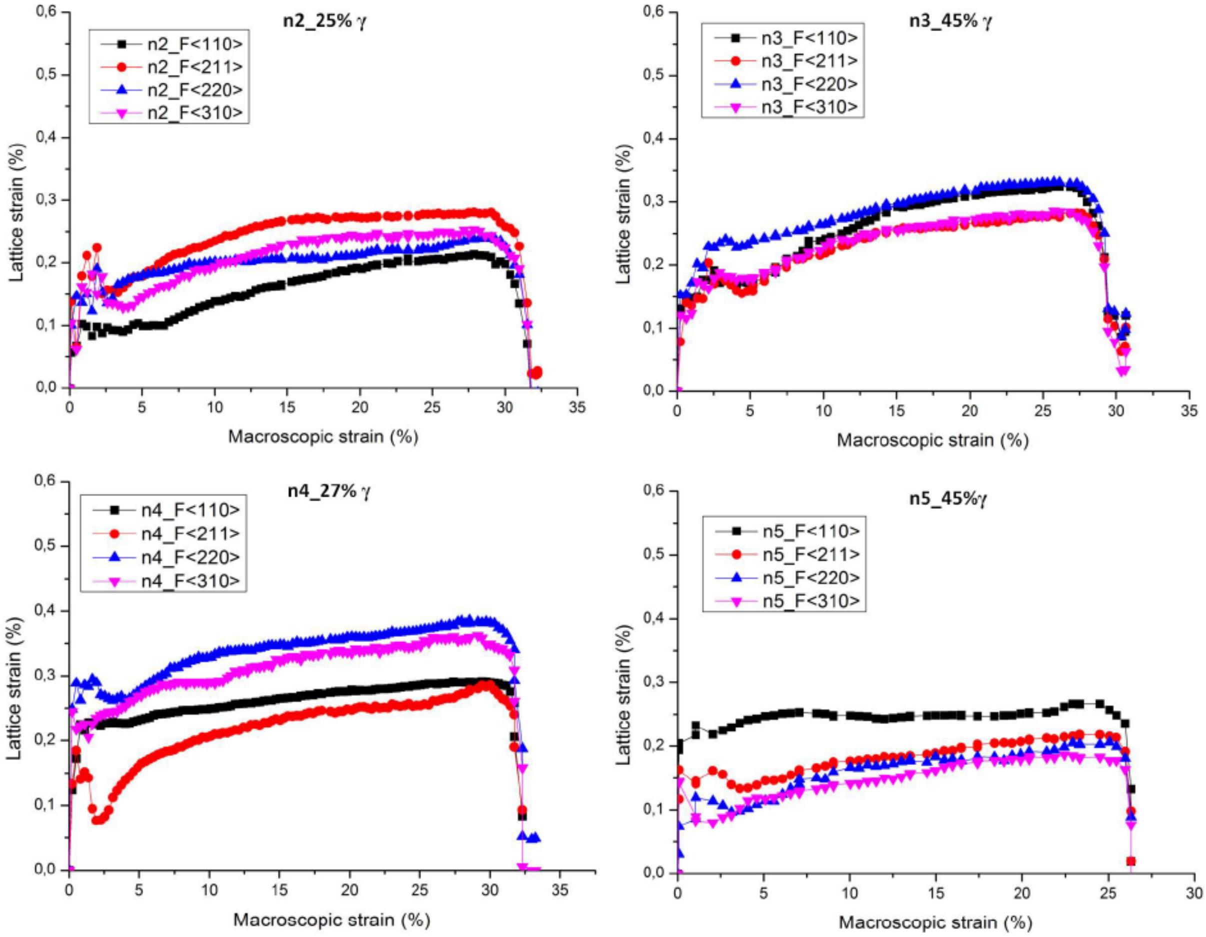

Figure V-23:Lattice strain for different hkl reflection of ferrite phase as a function of True macroscopic strain for composites n2, n3, n4 and n5

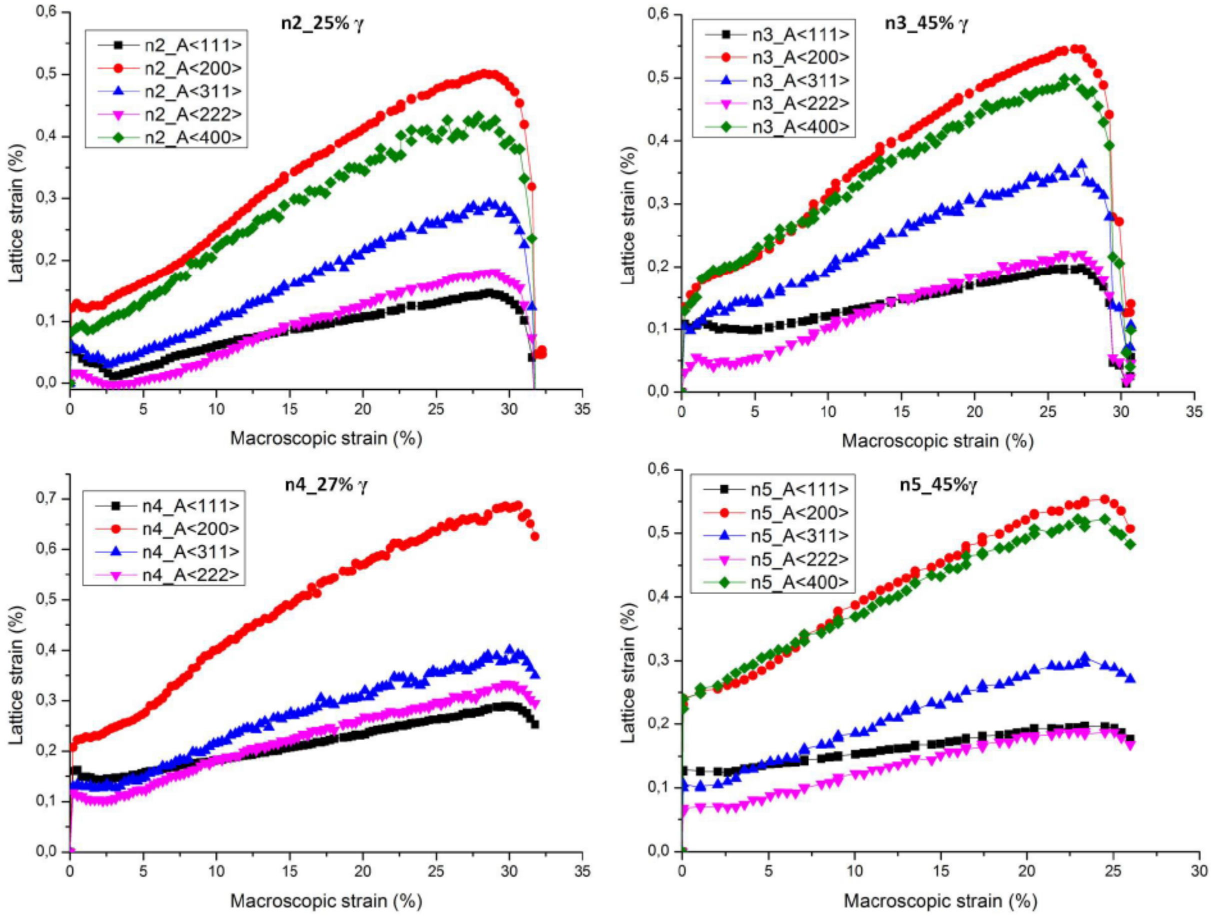

Figure V-24:Lattice strain for different hkl reflection of austenite phase as a function of True macroscopic strain for composites n2, n3, n4 and n5

V.II.2.b Choice of peaks reflection

The use of in-situ tensile tests for either single or multi phase material can be regarded as being of major importance in engineering applications for their significant ability to compare diffraction measurements with macroscopic response. However, the choice of a suitable hkl plane for macrostrain representation is one of the most discussed issues in the literature. It can be deduced from several works that there is no absolute criterion for the selection of a suitable plane of a given phase for the average phase strain. Indeed, several authors have used different planes to be representative for the same phase. Their choice was often based on experimental conditions and the materials in question. In the Cu/Mo composites [Wanner and Dunand 2000], for example, obtained by powder metallurgy and investigated by high energy synchrotron X-ray diffraction, (111) and (200) reflections have been chosen to represent the Cu phase (FCC) and (110) reflection for Mo (BCC). The choice of (200) reflection for FCC phase and (110) for BCC has been also made for steels such as: hot rolled sheets of γ/α alloys [Tomota et al. 2004] (see Figure V-21); and cold rolled TWIP steels [Yan 2012]. [Spencer 2004] in his analysis in single phase austenite stainless steels (304 and 316L) and their mixture with martensite (α') chose (311) and (211) reflections to represent fcc and bcc (martensite) phases respectively. This choice was made essentially basing on the linear response of planes lattice strain with the applied external stress. Indeed, it is found that the best hkl reflection to choose for estimating average stress is one that less affected by intergranular strain [Daymond 2004]. This allows properly converting a measured lattice strain into an equivalent stress by Hook's law.

On the other hand, peak intensity is one of the most important criteria in selecting the most suitable (hkl) reflection to analyze. In the literature, the choice of the (hkl) based on the intensity level is usually confirmed by texture analysis to ensure the representativeness of the chosen plane. According to this criterion, the choice of the reflection for FCC and BCC phase will therefore depend on the sample.

In the present work, the linearity between lattice strain and applied true stress is relatively assumed for ferritic phase (bcc). Regarding the austenitic phase (fcc), all hkl plans deviate significantly from linearity which means that the different grain subsets accumulate elastic strain at different rate while plastic deformation leading therefore to the build-up of intergranular strain. Figure V-25 shows an example of lattice strain calculated by Eq. V-11 for each hkl plane of both phases (austenite and ferrite) in composite n3 as a function of applied stress. The ferrite phase, Figure V-25.b, shows almost an isotropic behavior. Indeed, the elastic strains of planes (110), (211) and (310) have similar response with respect to macroscopic stress. However, plane (220) shows a softer behavior than the others.

On the other hand, in the austenite phase, the response with respect to the macroscopic stress varies significantly from hkl reflection to other. Plans (200) and (400), as expected, have similar response and are significantly softer than planes (111) and (222). This makes, naturally, the choice of the suitable reflection to represent the austenitic phase more complex.

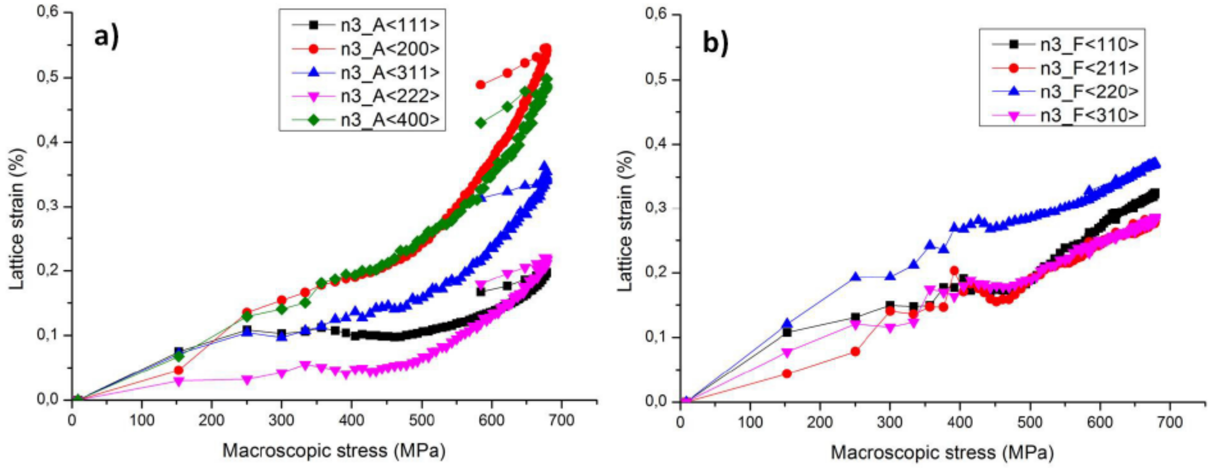

Figure V-25: Evolution of the lattice strain as a function of applied stress for all measured reflections of composite n3 after annealing a) austenite b) ferrite

On the other hand, the texture results presented in chapter III show that the ferritic phase developed a <110> fiber texture which is the most dominant component whereas the austenitic phase developed a duplex fiber texture <100> and <111>. The distribution of these two components depends on the composite generation. See paragraph III.III.3.

In view of the above discussion the choice of (100) reflection for ferritic phase seems to be the most adequate. For austenitic phase, regarding the texture results, planes (111) and (100) should be taken into consideration to estimate stress average although their response as a function of macroscopic true stress is not assumed. In order to simplify the analysis, one of these reflections should be selected. In our analysis, in order to determine the suitable hkl plane to represent the austenite phase, we plotted the lattice strain as a function of macrostopic true stress for planes (111) and (200) and compare it with that of plane (110) (i.e. ferritic phase). Figure V-26 illustrates the evolution of the lattice strain of γ(111), γ(200) and α(110) in the loading direction as a function of the applied stress for composite n3 (<100> fiber texture more dominant Figure III-33) and composite n4 (<111> fiber texture more dominant Figure III-33) . Three regimes can be differentiated by the slope change of one of the phases. As schematized in Figure V-20, one can qualitatively estimate the load partitioning and determine phases behavior. On the other hand, we know, from hardness measurements of both phases of the composites that the austenitic phase is harder than the ferritic phase in all generations at both states; annealed and as-drawn. Hence, from Figure V-26, one can deduce that γ(200) can be a more realistic choice than γ(111) since, comparing to α(110), the γ(200) is the hardest plane during all deformation stages especially during plastic regime (III). It is mainly for this reason that γ(200) and α(110) reflection were chosen for the following analysis.

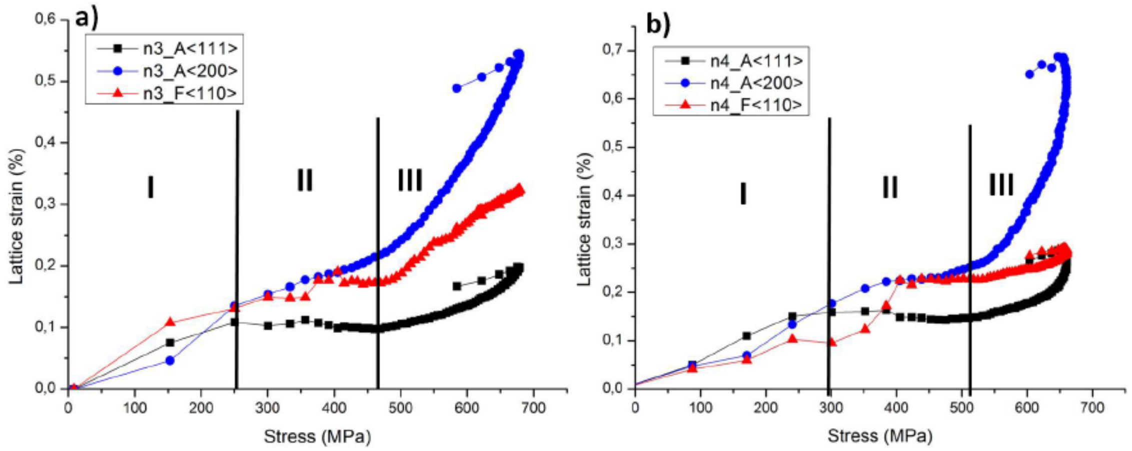

Figure V-26: evolution of lattice strain as function of macroscopic true stress for composite n3 a) and n4 b). A (austenite); F (ferrite).

Figure V-27 shows the evolution of the lattice strain of γ(200) and α(110) in the loading direction as a function of the applied stress. Three regimes can be differentiated by the slope change of one of the phases. Generally speaking, the austenite curve is always above that of the ferrite for all composites.

Figure V-28 illustrates the evolution of the lattice strain for γ(200) and α(110) reflections as a function of the macroscopic strain. As expected, it shows that the lattice strain in austenite is larger than in ferrite for all composites n2, n3, n4 and n5. Indeed, after a linear increase with macroscopic strain, the lattice strain of α(110) seems to rapidly saturate during straining where as the lattice strain of γ(200) keeps increasing monotonously.

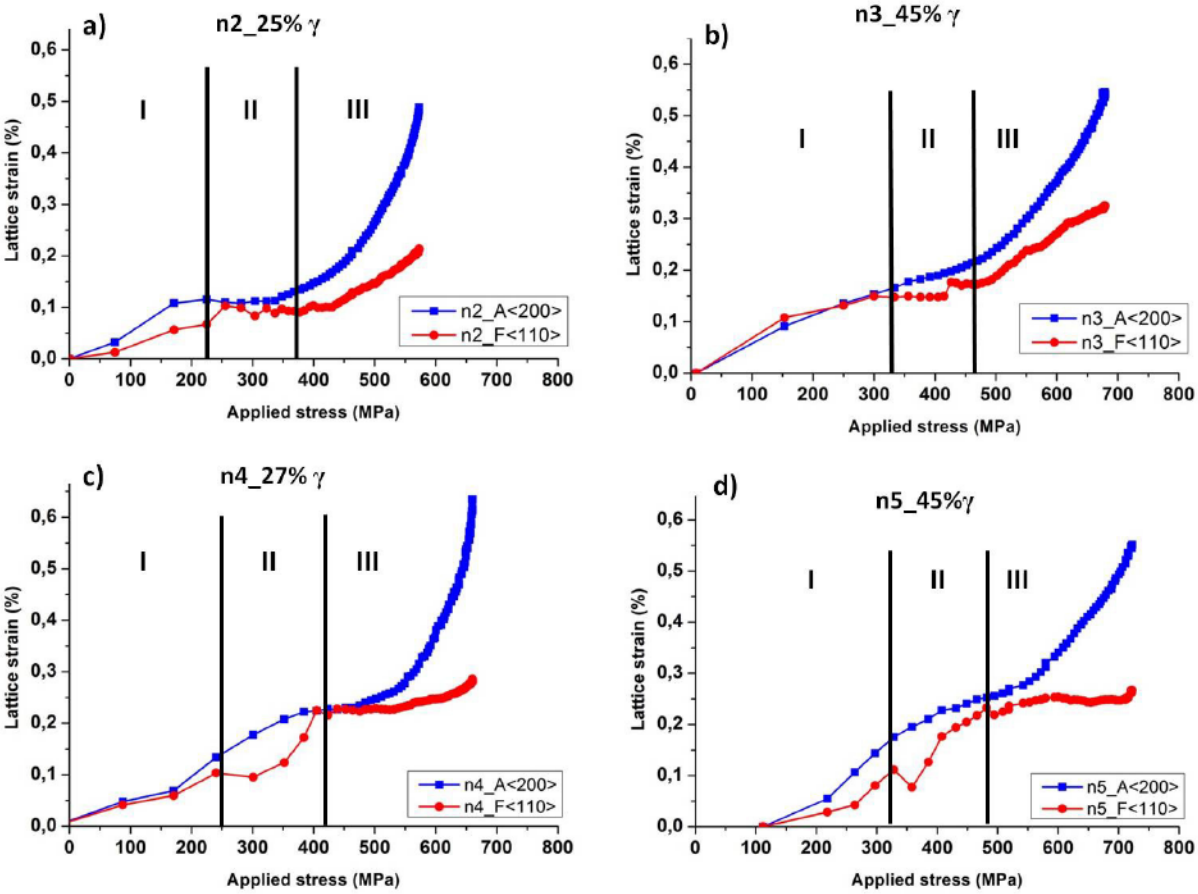

Figure V-27: Evolution of the lattice strain in the loading direction as a function of the applied stress for γ(200) and α(110) reflections for composites a)n2;b) n3; c)n4; d)n5 annealed at 850°C for 1hour

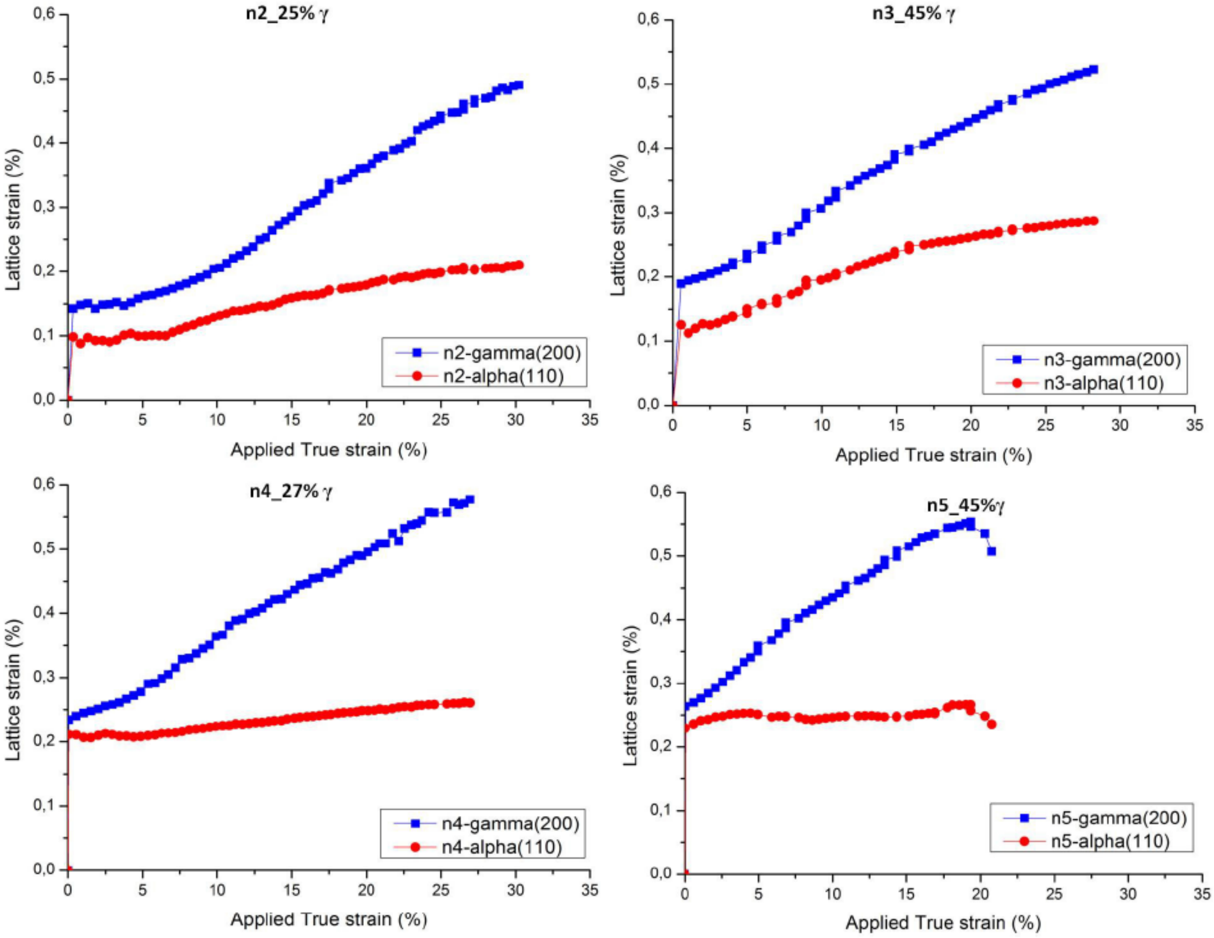

Figure V-28:Evolution of the lattice strain in the loading direction as a function of the macroscopic strain for γ(200) and α(110) reflections for composites n2, n3, n4 and n5 annealed at 850°C for 1hour

V.II.3 Discussion

In Figure V-27, three regimes can by identified by their change in slope. After an almost linear increase (stage I) in both phases, the rate of increase of lattice strain in α is lower compared to that of γ phase. This means that the austenite (the hard phase), carries an increasing load as compared to ferrite (soft phase) at this stage (II). For γ-phase, this trend continues in stage III where the rate of increase of the lattice strain increases more strongly compared to α-phase.

The results of Figure V-27 and Figure V-28 confirm our primary conclusion discussed in the first section of this chapter which is to say that the austenite is always the hardest phase in all composites.

However, in order to assess the load sharing between both phases, average phase stresses rather than average lattice strains are required. Thus, it is first necessary to estimate the different elastic moduli; E_{hkl} and υ_{hkl} for both phase to properly convert the measured lattice strains into stress levels. These moduli can be either: i) calculated using single crystal elastic constants using a self consistent method introduced primarily by [Kröner 1958]. The resultant moduli of this method are considered as the analytical values since no texture effect is accounted in this approach; ii) estimated directly from the evolution of the longitudinal lattice strain with the macroscopic stress (for the Young modulus) and the ratio of the longitudinal and transverse lattice strain (for the Poisson ratio). To measure these moduli, samples of n3, n4 and n5 in as-drawn state were used since better linearity is assumed in this state because of high yield strength. Figure V-29 shows the evolution of the macroscopic applied stress as a function of lattice strain of γ(200) and α(110) reflections of composites n3, n4 and n5 in as-drawn state. Thanks to these results, the different moduli were estimated. Table V-7 demonstrates a very a good agreement between the measured and analytical elastic moduli. The values of the latter are taken from [Daymond et al. 2002], [Oliver et al. 2004] and [Daymond et al.2000].

Table V-7: Meausred and calculated elastic constants E_{hkl} and υ_{hkl} for the BCC and FCC phases for each composite

	γ(200)		**α(110)**	
	$E_{hkl}\ (GPa)$	υ_{hkl}	$E_{hkl}\ (MPa)$	υ_{hkl}
n3	174.1	0.40	250.0	0.15
n4	173.3	0.36	224.6	0.17
n5	174.7	0.36	227.2	0.16
Calculated Kröner (self-consistent)	176.2	0.32	225.5	0.25

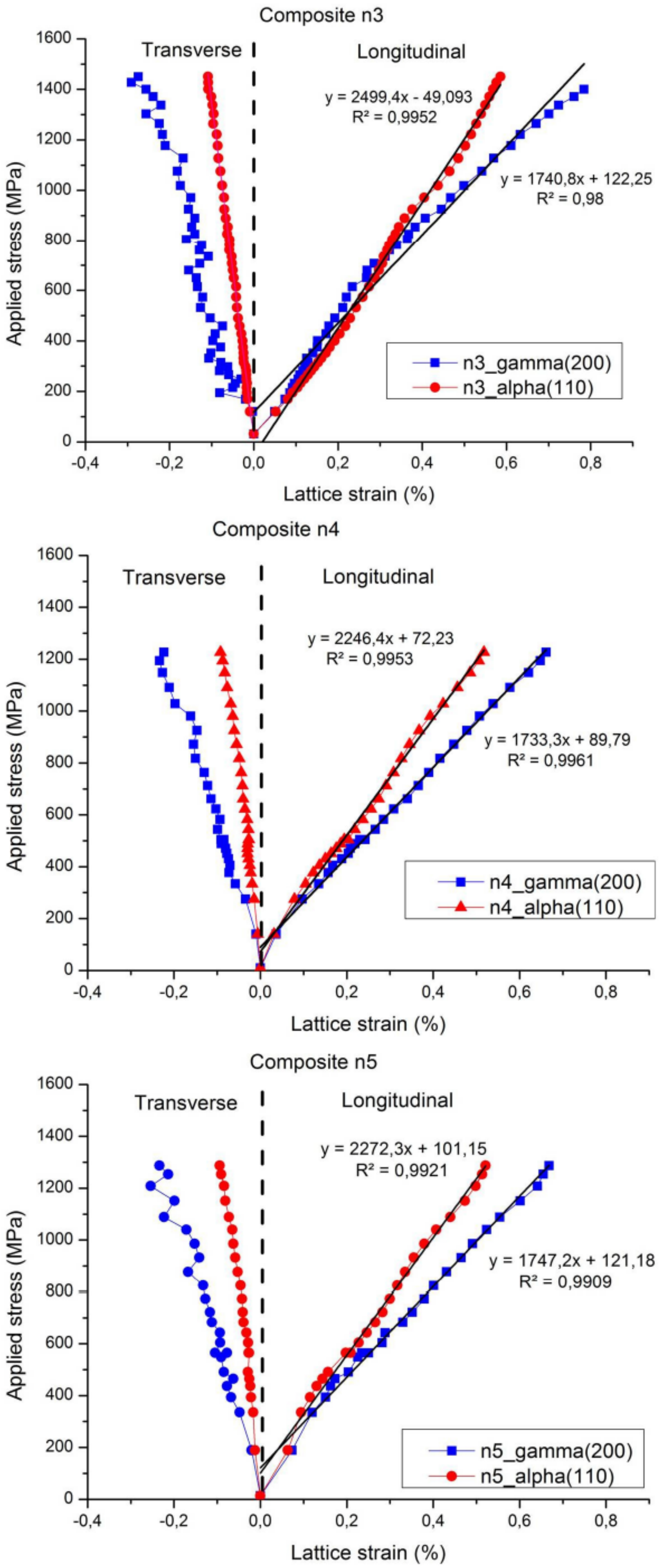

Figure V-29: Applied stress-Lattice strain for composites n3,n4 and n5 in as-drawn state

As shown in Figure V-25, the FCC phase (austenite) shows a more anistropic behavior. The degree to which the *hkl* lattices of the FCC are sensitive to the intergranular strains varies from one plane family to another [Daymond et al. 2002]. Indeed, as different grain subsets begin to deform plastically, differently-oriented subsets will accumulate elastic strains at different rate which leads to the build-up of intergranular stresses. This, in turn, gives rise to a non-linearity in the measured strains of certain planes as a function of applied stress, which is necessary to take into account to properly convert a measured elastic strain to equivalent stress by Hooke's law. However, in the present work, we assume that the chosen γ(200) reflection is less influenced by the intergranular stress and the linearity is ensured. Thus, the mean stresses in both α and γ phases can be calculated via Hooke's law. Using the measured E_{hkl} and ν_{hkl} in Table V-7, the stress of each phase can be calculated using the measured lattice strain. Thanks to the axisymetric geometry of our samples, one can consider that $\varepsilon_{22} = \varepsilon_{33}$ whereas ε_{11} represents the strain along the tensile axis. Thus, the average stress for a given phase (*ph*) can be written according to Hooke's law as following:

$$\sigma_{11}^{ph} = \frac{E^{hkl}}{(1+\nu^{hkl})(1-2\nu^{hkl})}\{(1-2\nu^{hkl})\varepsilon_{11}^{hkl} + 2\nu^{hkl}\varepsilon_{22}^{hkl})\} \qquad \text{Eq.V-12}$$

The following simplified equation is also used when transverse strain is not available.

$$\sigma_{11}^{ph} = E^{hkl}\varepsilon_{11}^{hkl} \qquad \text{Eq. V-13}$$

[Jacques et al. 2005] showed that, in duplex alloys, small difference is found between stresses issued from Eq.V-12 and Eq. V-13.

The calculated curves using Eq. V-13 are given in Figure V-30 which shows the stresses level of γ(200) and α(110) compared with the macroscopic response of each composite n2, n3, n4 and n5 after heat treatment using the annealing conditions cited in chapter III. Interesting features can be observed in Figure V-30:

- The calculated stress of γ(200) in n2 composite shows two different slopes in the plastic regime. A drastic change in the slope occurs after 10% of applied true strain. The same trend is observed in γ(200) of composite n3. The change in slope is significantly less pronounced in composites n4 and n5.
- The macroscopic curves show a quite good agreement with the average stress calculated by ROM σ_{ROM}^{c}:

$$\sigma_{ROM}^{c} = V^{\gamma}\sigma_{200} + V^{\alpha}\sigma_{110} \qquad \text{Eq. V-14}$$

However, for composites n2 and n3 where γ(200) show 2 slopes, the macroscopic response does not match well with the σ_{ROM}^{c}.

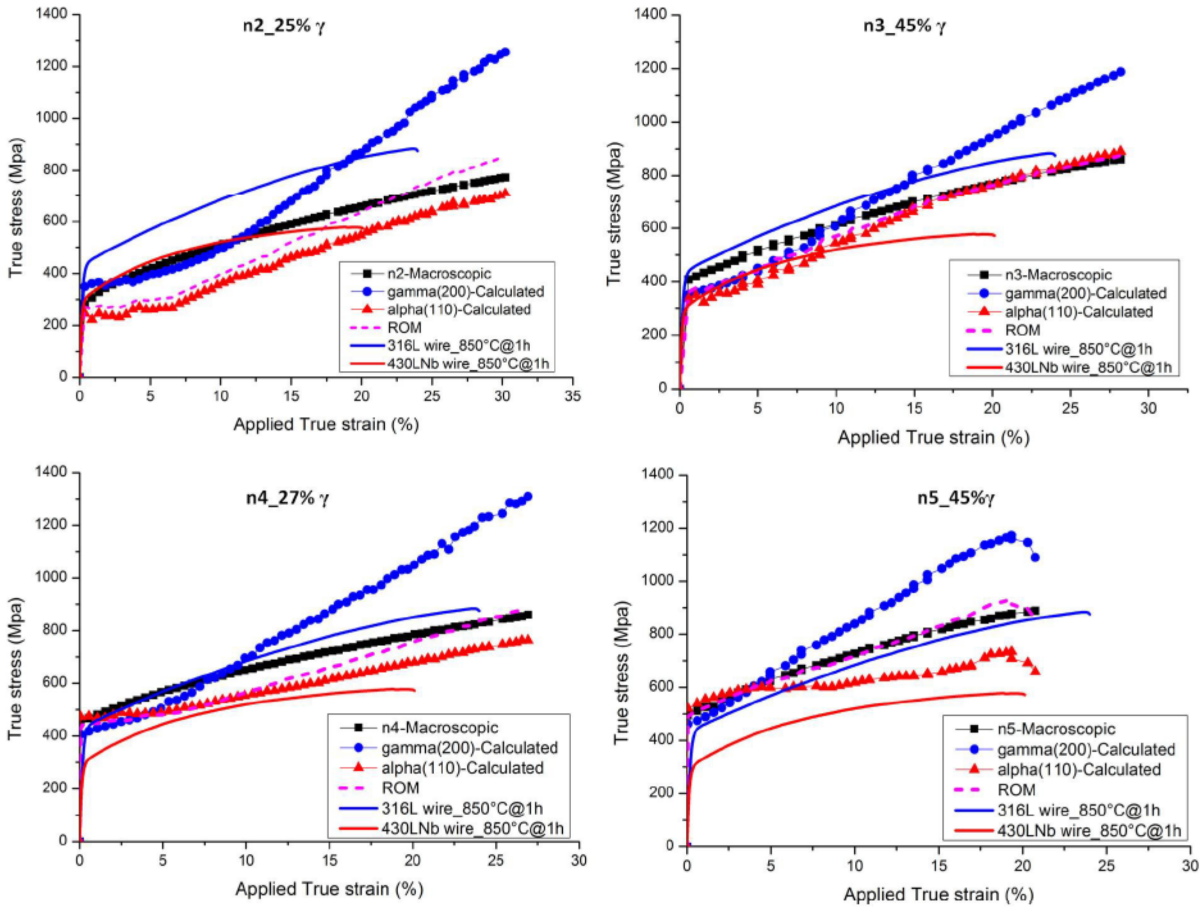

Figure V-30:True stress-Applied True strain issued from Synchrotron X-ray diffraction for composites n2,n3,n4 and n5 in as-annealed state

One possible explanation of the drastic change in the slope of γ(200) in composites n2 and n3 could be the contribution of a third phase in the strengthening process. As discussed in the sub-section V.I.3, no martensitic transformation occurred during the tensile test. However, both composites contain already a martensitic phase inherited from the previous steps. Therefore, this martensite may partly explain the change in slope in n2 and n3 composite knowing that the estimated martensite in these two composites is 1.6% and 5.1%, respectively.

On the opposite side, as described above, the change in slope is less pronounced in composites n4 and n5 while the estimated volume fractions of the martensite is significantly higher; 5.6% and 6% respectively. Moreover, very good agreement between the average stress calculated using Eq. V-14 and experiment is obtained. This may be explained by the change in chemical composition that occurred during annealing process within n1 cells which led to complete perturbation in the entire n2 cells inside composite n5. In fact, it is well known that the lattice parameter for a given phase depends on the chemical composition [Jimenez-Melero 2011], [N.H van Dijk 2005].

Despite the fact that γ phase has a strong anisotropy and γ(200) is influenced by the intergranular strains according to [Daymond et al. 2005], the results obtained give a good approximation and are consistent with the macroscopic characterization (tensile test and microhardness) presented in the previous section of this chapter. Indeed, Figure V-31 and Figure V-32 summarize the calculated stress evolution for γ(200) and α(110) of all composites as a function of the macroscopic true strain. The systematic increase of the calculated stresses for γ(200) and α(110) as a function of the composite n is also consistent with our discussion on the influence of the grain size within the phases.

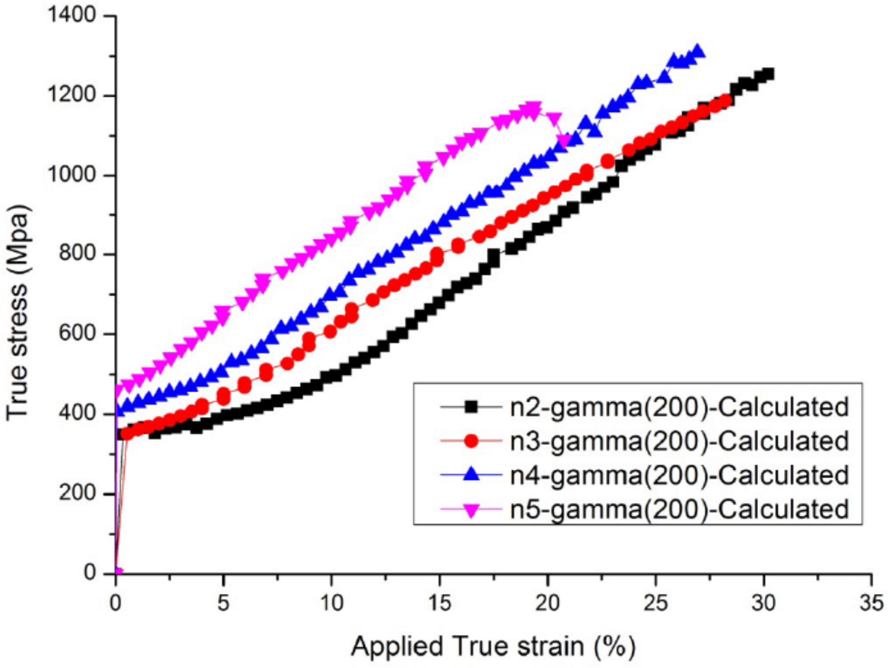

Figure V-31: Calculated stress *vs* Applied True strain of γ(200) reflection for each composite n2,n3,n4 and n5

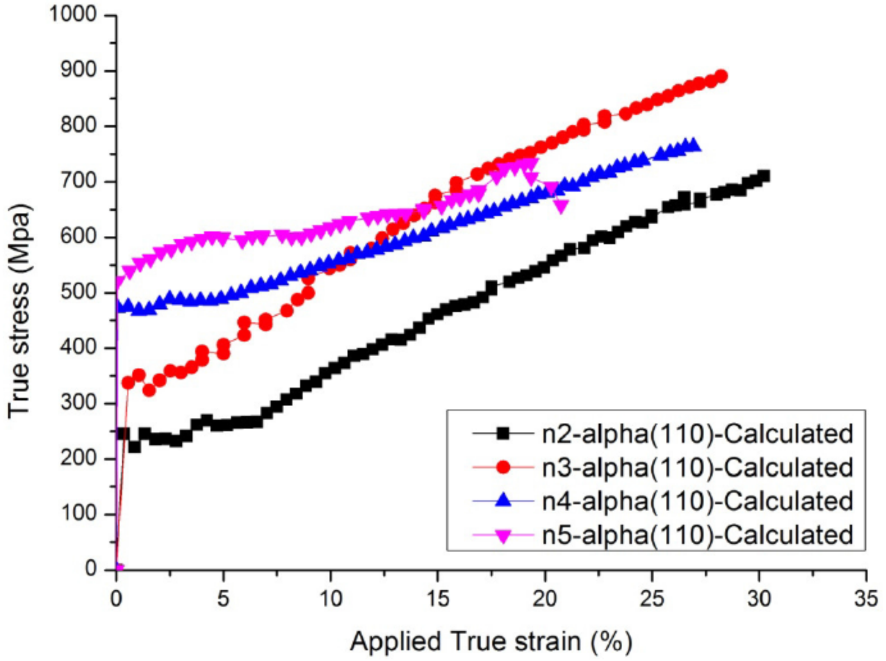

Figure V-32: Calculated stress *vs* Applied True strain of α(110) reflection for each composite n2, n3, n4 and n5

V.II.4 Summary

The following points summarize the experimental results presented in this section:

- Lattice strains of both phases BCC and FCC were successfully measured by synchrotron X-ray diffraction for composites of the 2nd architecture in as-drawn and as-annealed state.

- Strain partitioning in α and γ phases during tensile deformation was qualitatively described. It is found that γ phase is the hardest phase and carries more load than the ferrite.

- Stress partitioning was calculated via the measured lattice strains, γ(200) and α(110), using Hooke's law.

- The macroscopic flow stress of the composites n2, n3, is found to be almost between the estimated flow stress of γ(200) and α(110). Regarding n4 and n5 composites, their experimental flow stresses show good agreement with ROM calculated from stress of γ(200) and α(110).

- A systematic increase in the lattice strains of γ(200) and α(110) reflection in each composite n was found.

References

[Al-Fadhalah et al. 2008]
Al-Fadhalah, K. J. H., Li, C. M., Beaudoin, A. J., Korzekwa, D. A., & Robertson, I. M. (2008). Microplastic processes developed in pure Ag with mesoscale annealing twins. Acta Materialia, 56(19), 5764-5774.

[Brofman and Ansell 1978]
Brofman, P. J., & Ansell, G. S. (1978). On the effect of carbon on the stacking fault energy of austenitic stainless steels. Metallurgical and Materials Transactions A, 9(6), 879-880.

[Bouaziz et al. 2008]
Bouaziz O., S. Allain and C. Scott, Scr. Mater. 58 (2008) p.484.

[Calcagnotto et al. 2010]
Calcagnotto, M., Ponge, D., & Raabe, D. (2010). Effect of grain refinement to 1μm on strength and toughness of dual-phase steels. Materials Science and Engineering: A, 527(29), 7832-7840.

[Clausen et al. 1999]
Clausen, B. et al., Mater. Sci. Eng. A, vol. A259, p. 17, 1999.

[Daymond et al. 2002]
Daymond, M. R., & Priesmeyer, H. G. (2002). Elastoplastic deformation of ferritic steel and cementite studied by neutron diffraction and self-consistent modelling. Acta materialia, 50(6), 1613-1626.

[Daymond 2004]
Daymond, M. R. (2004). The determination of a continuum mechanics equivalent elastic strain from the analysis of multiple diffraction peaks. Journal of applied physics, 96(8), 4263-4272.

[Daymond et al. 2005]
Daymond, M. R., Hartig, C., & Mecking, H. (2005). Interphase and intergranular stress generation in composites exhibiting plasticity in both phases. Acta materialia, 53(9), 2805-2813.

[Daymond et al.2000]
Daymond, M. R., Tomé, C. N., & Bourke, M. A. M. (2000). Measured and predicted intergranular strains in textured austenitic steel. Acta materialia,48(2), 553-564.

[Embury 2010]
Embury, D., & Bouaziz, O. (2010). Steel-based composites: driving forces and classifications. Annual Review of Materials Research, 40, 213-241.

[Feaugas 1999]
Feaugas, X. (1999). On the origin of the tensile flow stress in the stainless steel AISI 316L at 300 K: back stress and effective stress. Acta materialia, 47(13), 3617-3632.

[Fischmeister and Karlsson 1977]
Fischmeister, H., & Karlsson, B. (1977). Plasticity of two-phase materials with a coarse microstructure. Z METALLKD.

[Friedel 1964]
Friedel, J., Dislocations, Addison-Wesley, Reading, Massachusetts, 1964.

[Gurland 1979]
Gurland, J. (1979). A structural approach to the yield strength of two-phase alloys with coarse microstructures. Materials Science and Engineering, 40(1), 59-71.

[Gutiérrez 2008]
Gutiérrez I. and M.A. Altuna, Acta Mater. 56 (2008) p.4682.

[Han et Dawson, 2005]
Han, T. S., & Dawson, P. R. (2005). Lattice strain partitioning in a two-phase alloy and its redistribution upon yielding. Materials Science and Engineering: A,405(1), 18-33.

[Harjo et al. 2001]
Harjo, S., Tomota, Y., Lukáš, P., Neov, D., Vrana, M., Mikula, P., & Ono, M. (2001). In situ neutron diffraction study of α–γ Fe–Cr–Ni alloys under tensile deformation. Acta materialia, 49(13), 2471-2479.

[Huang 2004]
Haung X., N. Hansen, Mater. Sci. Eng. A387–389 (2004) 186.

[Jacques et al. 2005]
Jacques, P. J., Furnemont, Q., Godet, S., Pardoen, T., Conlon, K. T., & Delannay, F. (2006). Micromechanical characterisation of TRIP-assisted multiphase steels by in situ neutron diffraction. Philosophical magazine, 86(16), 2371-2392.

[Jimenez-Melero 2011]
Jimenez-Melero, E., van Dijk, N. H., Zhao, L., Sietsma, J., Wright, J. P., & van der Zwaag, S. (2011). In situ synchrotron study on the interplay between martensite formation, texture evolution and load partitioning in low-alloyed TRIP steels. Materials Science and Engineering: A, 528(21), 6407-6416.

[Kocks 1975]
Kocks, U.F., M.F. A.S. Argon and M.F. Ashby, “Thermodynamics and Kinetics of Slip”, Progr. Mater. Sci., vol. 19, 1975.

[Kocks and Mecking 2003]
Kocks, U.F. and H. Mecking, Progr. Mater. Sci., vol. 48, p.171, 2003.

[Lloyd 1980]
Lloyd D.J., Met. Sci. 14 (1980) 193.

[Oliver et al. 2004]
Oliver E.C., M.R. Daymond and P.J. Withers, Acta Mater. 52 1937 (2004).

[Pickering and Dunlop 1985]
Pickering F.B., in: G.L. Dunlop (Ed.), Proceedings of the Stainless Steels 84, Chalmers University of Technology, Goteborg, September 3–4, 1984, The Institute of Metals, London, 1985, p. 12.

[Rhodes and Thompson 1977]
Rhodes C.G., A.W. Thompson, Metallurgical Transactions A 8 (1977) 1901.

[Riegger 1979]
Riegger S, Vö hringer O, Macherauch E. Metall 1979; 33:1139.

[Sinclair et al. 2006]
Sinclair, C. W., Poole, W. J., & Bréchet, Y. (2006). A model for the grain size dependent work hardening of copper. Scripta Materialia, 55(8), 739-742.

[Shadkam and Sinclair 2015]
Shadkam, A., & Sinclair, C. W. (2015). The coupled effect of grain size and solute on work hardening of Cu–Ni alloys. Philosophical Magazine Letters, 1-9.

[Spencer 2004]
Spencer K., THE WORK HARDENING OF AUSTENITIC STAINLESS STEEL, APPLIED TO THE FABRICATION OF HIGH-STRENGTH CONDUCTORS, (Doctoral desseration), 2004.

[Takeda et al 2008]
Takeda, K., Nakada, N., Tsuchiyama, T., & Takaki, S. (2008). Effect of interstitial elements on Hall-Petch coefficient of ferritic iron. ISIJ international,48(8), 1122-1125.

[Talonen 2007]
Talonen, J. (2007). Effect of strain-induced α'-martensite transformation on mechanical properties of metastable austenitic stainless steels.

[Tamura 1973]
Tamura, I. (1973). Strength and Ductility of Two-Phase Fe Alloys. Trans. Iron Steel Inst. Jap., 13(4), 283-292.

[Tamura 1982]
Tomota, Y., & TAMURA, I. (1982). Mechanical behavior of steels consisting of two ductile phases. Transactions of the Iron and Steel Institute of Japan, 22(9), 665-677.

[Tomota et al. 2004]
Tomota, Y., Tokuda, H., Adachi, Y., Wakita, M., Minakawa, N., Moriai, A., & Morii, Y. (2004). Tensile behavior of TRIP-aided multi-phase steels studied by in situ neutron diffraction. Acta Materialia, 52(20), 5737-5745.

[Underwood 1969]
Underwood, E. E. (1969). Stereology, or the quantitative evaluation of microstructures. Journal of microscopy, 89(2), 161-180.

[Van Dijk 2005]
Van Dijk, N. H., Butt, A. M., Zhao, L., Sietsma, J., Offerman, S. E., Wright, J. P., & Van der Zwaag, S. (2005). Thermal stability of retained austenite in TRIP steels studied by synchrotron X-ray diffraction during cooling. Acta Materialia,53(20), 5439-5447.

[Wanner and Dunand 2000]
Wanner, A., & Dunand, D. C. (2000). Synchrotron X-ray study of bulk lattice strains in externally loaded Cu-Mo composites. Metallurgical and Materials Transactions A, 31(11), 2949-2962.

[Yan 2012]
Yan, K. (2012). In-situ characterization by high-energy x-ray and neutron diffraction of micro-structural evolution of selected materials during thermo-mechanical processing.

VI Conclusion and perspectives

Chapter VI: Conclusion and perspectives

The use of DSS grades for structural applications is considered as one of the most significant advances impacting the construction sector. This is because of their high mechanical properties coupled with interesting functional properties such as corrosion resistance or even the low thermal conductivity compared to carbon steels. Due to their complex structure and interaction between the phases, DSS have a significant potential for unique properties. Thus, a better understanding will give the possibility to obtain breaking through properties on the one hand and on the other, it will provide the possibility to design tailor-made, architectured DSS for specific applications. In this work we propose a different approach from that used until now to understand the behavior of DSS. The strategy adopted in this work was the so-called *top-down* strategy in which at least two bulk metals with well known behavior and properties are mechanically alloyed by Severe Plastic Deformation (SPD). This proposed strategy is twofold: i) enhancing the properties by microstructure refinement down to sub-micron scale ii) elaborating a material model for understanding the DSS behavior obtained by the conventional metallurgical methods.
The main objective we have set at the beginning of this thesis was naturally to develop a process allowing the co-deformation to large strain of ferrite and austenite to obtain sub-micrometric composites of 316L and 430LNb.

Chapter III was devoted entirely to the implementation of a methodology of manufacturing for γ/α system. In this study, we discussed that the key for a successful drawing lies upon the lubrication quality which depends in turn on the ductility of the wire; the more the wire is hard the more the lubrication film separating die from wire is thin leading, by consequence, to a premature rupture during manufacturing due to the galling. Annealing step was therefore necessary to continue the drawing. At high annealing temperature (namely 1050°C for 10 minutes) a significant regression of the austenite phase has been observed. Having regards to these constraints, an optimization between annealing conditions and hardness of each phase in composite n1 has been performed. An optimum initial hardness value of 225HV±10HV was imposed for both phases beyond which the composite becomes difficult to draw down to 92% of section reduction without any intermediate annealing. The optimal annealing condition which fulfills the above mentioned constraints was found to be at 850°C for 1 hour. Using these optimal annealing conditions multi-scale micro-composites of γ/α have been obtained. Arriving to n5 composite the structure refinement reached its limits due to the quasi complete regression of the austenite phase issued from the finest n1 cells. This sketched out the limit of the process in microstructure refining for the couple 316L/430LNb.

In order to provide a better comprehension behind the phase regression and the limitation of the process, the microstructure of these composites has been evaluated (Chapter IV). In particular, the softening kinetics for both phases 316L and 430LNb inside the composite n4 was examined. The investigation was limited to the latter composite because of its well-preserved and fine architecture compared to the other ones. At temperatures 750°C, 850°C and 950°C, the finest phase (i.e. 316L and 430LNb issued from n1 cells) within the composite n4 was found to recrystallize faster than that of individual wires subjected exactly to the same section reduction. Such difference was attributed to the initial grain size. However, the other recent generations within the composite n4 yielded the same softening kinetics as the bulk wires. This suggests that softening behavior of a given phase differs from generation to another within the same composite. More importantly, this means that the annealing conditions that were found to be optimal for the composite as a whole are actually not adapted locally for the finest phase because of the important diffusion they induce relatively to the size of this phase.

Based on these findings, diffusion analysis was performed using EDS technique. A significant inter-diffusion of elements of substitution, in particular Ni, was observed. For n1 composite for instance the interdiffusion induced at high temperature (1050°C) led to a phase transformation $\gamma \rightarrow \alpha$ perceived through a significant interface migration. Within the area swept by the migrating interface, a martensitic layer was formed during rapid cooling. Thanks to Pickering Ms formula, the thickness of this layer was approximated to be around 1.3µm. By reducing the annealing temperature down to the optimal annealing conditions (850°C for 1hour) for composites n ($i \geq 2$) no interface migration has been noticed, however, the martensitic layer within the vicinity of 316L/430LNb interface is always preserved. Interesting features were noticed in EDS diffusion profile in particular: i) the martensitic layer is maintained even in as-drawn state ii) the thickness of this layer is constant for all composites.

The presence of this martensite layer before and after annealing has been confirmed by TEM observations on thin foil cut at the interface 316L/430LNb of n1 cells inside n4 composite. Arriving to n5 composite where the finest austenite and ferrite is about 2-4 µm, the size of the martensite becomes similar to that of 316L and 430LNb issued from n1 cells. It was found that before annealing the n5 composite preserves its architecture and the austenite of n1 cells keeps its nominal chemical composition. However, after annealing the architecture became disturbed and the austenite regressed significantly.

The good agreement between experience and diffusion simulation in n1 composite and n4 composites allowed us to use Dictra software with confidence to explain the microstructure obtained after annealing of n5 composite. In fact this regression was explained by the dilution of the austenite phase due to Ni diffusion. Simulation results showed that the nickel diffusion was controlled by the austenitic phase. This limitation is therefore governed by the effect of the couple diffusion and section reduction.

The mechanical behavior of these composites has been also investigated at each manufacturing step (Chapter V). Comparison has been made between the mechanical behavior of composites and that of individual wires which have been subjected to similar thermo-mechanical conditions. The Rule Of Mixture (ROM), using the individual wires predicted well the mechanical behavior of n1 composite (45% γ and 55% α) annealed at 1050°C. However, for composites n(i>1) annealed at the optimal temperature, a systematic increase in mechanical strength as a function of manufacturing step was noticed. Hall-Petch relation has been constructed for both 316L and 430LNb using individual wires in order to take into account the contribution of grains size of each component to the macroscopic strength of the composite n3 and n4. A significant difference between ROM and experience has been found. This may be attributed to the fact that HP relations, derived from bulk wires, are not representative for the composite's phases. In situ tensile tests using high energy X-ray synchrotron have been performed to provide a more in-depth explanation on this systematic increase. The results showed that no change occurred in austenite fraction during plastic deformation which means that no martensitic transformation took place. In addition, the stress partitioning of each phase has been determined by measuring the local elastic strains. The ferrite phase showed an isotropic behavior whereas the austenite was more anisotropic. However, the choice of the most representative crystallographic plan for both phases was based on the experimental analysis and the level of the intensity, leading to the selection of plans (200) and (110) for γ and α phases respectively. The results showed a good agreement between experimental flow stresses and ROM calculated from stresses of γ(200) and α(110) for composites n4 and n5. Regarding n2 and n3 composites, even though their experimental flow stresses were situated between those of γ(200) and α(110), they showed a slight difference with the calculated ROM. The local study demonstrated also that the strength of the phases in the composite were a function of manufacturing step which explains the above-mentioned observations. The most plausible explanation for such increase of the phases during manufacturing is the significant effect of the grain size. Moreover, the results showed also the reliability of our choice of the crystallographic plane for both phases.

Perspectives

- The question which is still raised is: *How to reach a finer scale microstructure for the architectured duplex stainless steel?* The following points could be considered for a possible extension for this work:

    1) Avoid interdiffusion during annealing: this strategy implies to choose (or design) different types of austenite and ferrite whose chemical compositions are in equilibrium at the recrystallization temperature (around 850°C). For this, two strategies can be considered:

        a. Designing a separate ferritic and austenitic wires and tubes whose chemical composition are similar to those of a commercial stabilized DSS obtained by the conventional metallurgical method.

        b. Modifying the chemical composition of the commercial austenite and ferrite in a way that their average chemical composition should be found in duplex region of Shaeffler diagram. Indeed, the average chemical composition of the assembly 316L/430LNb is found in region where austenite and ferrite coexist with martensite. In Figure VI-1, we positioned the Actual (Ac) grades (i.e. 316L and 430LNb) and their average in ShaEffler diagram; point $Ac_{average}(Cr_{eq} = 20{,}8; Ni_{eq} = 7{,}8)$. Thus, if we want to obtain an average chemical composition localized in duplex region only (A+F) with almost 50% of ferrite volume fraction, the optimal choice is the point New$(Cr_{eq} = 21{,}8; Ni_{eq} = 8{,}1)$. Hence, one can deduce from the later point the chemical composition of the new austenite and ferrite illustrated in Table VI-1.

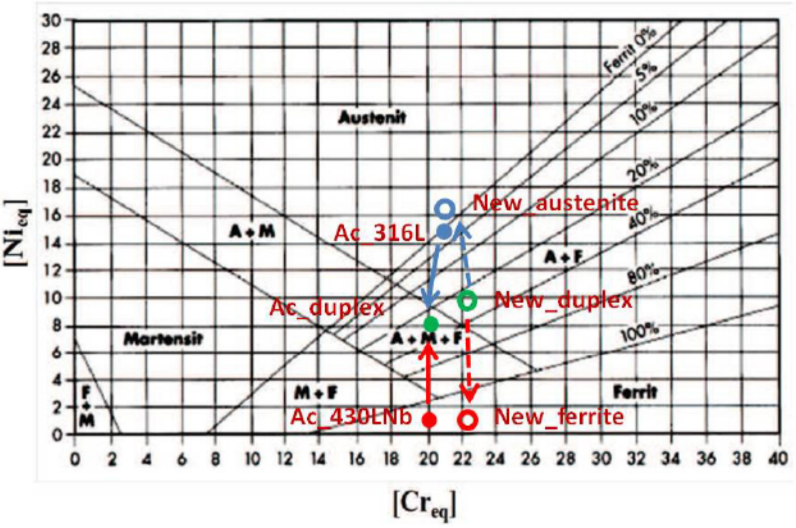

Figure VI-1: Localisation of the used and new grades on the Shaeffler diagram

Table VI-1: Chemical composition of the used and new austenite and ferrite stainless steel

W%	C	N	Cr	Ni	Mo	Mn	Nb
Ac_316L	0,02	0,03	16,7	11,09	2,03	0,795	0,03
New-austenite	0,02	0,05	16,7	11,09	2,03	0,795	0,03
Ac_430LNb	0,014	0,016	18,04	0,2	0,04	0,38	0,5
New_ferrite	0,014	0,016	20	0,2	0,04	0,38	0,5

2) Avoid annealing step: this strategy implies to modify (or change) the manufacturing technique. Indeed, in our technique the question arises about the possibility to draw composites with small phases because of increased hardness when the scale of the phases becomes sufficiently small. Thus, the criterion of the drawability should go beyond a simple criterion on hardness, or it will be the next limitation for creating small scale microstructures.

- In addition during this work, the use of in-situ high energy X-ray diffraction has been shown to be a powerful tool to evaluate the combined plastic behavior of two-phase steels. Our results provide data on the interaction between ferrite and austenite during co-deformation, in a simplified 1-D geometry. These results can be used to feed models for the elastoplastic behavior of these duplex materials.

- Obtaining very fine structures will not only give interesting mechanical properties but also new functional properties which need an in-depth investigation in a future work :

    1) Thermal conductivity: the thermal conductivity (or electrical resistivity) is directly related to the scale of the wstructure and the mean free path of electrons. In the case of very fine multi-filamentary structures of austenite (low conductivity) and ferrite (high conductivity), interesting thermal behavior could be obtained.

    2) Magnetic properties; Indeed, ferritic stainless steels are often used as soft magnetic materials to produce fast-response solenoid valves for fuel injection of car engine. In order to decrease the coercive field of the metal, one strategy is to increase the grain size, with serious drawbacks concerning brittleness. Another way is to produce a nano-crystalline structure as shown in Figure VI-2 that exhibits a very low coercive field.

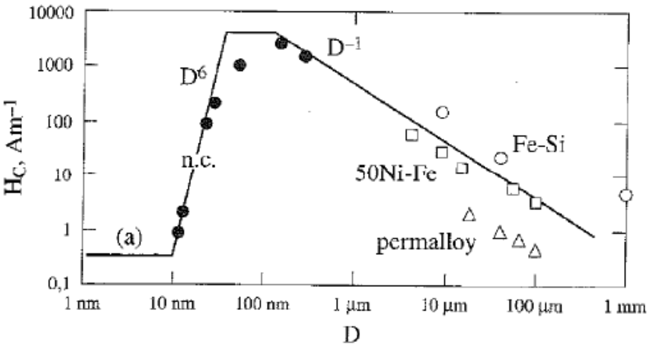

Figure VI-2:Coercitive field Hc as function of grain size D for different soft magnetic materials Amorphous (a), nanocristallized (n.c.) and cristallized (FeSi, 50FeNi and Permalloy) [Shafer et al. 1991]

- The micro-modeling using synchrotron results should be explored in-depth. Indeed, the estimation done to evaluate the average stress of each phases was made using a very approximate hypothesis. That is, the contribution of other grain families was neglected and the representativeness of the phase was only based on one hkl plane. Namely, the austenite phase whose behavior showed high anisotropy and the contribution of other hkl planes could not be neglected. This will give more insight about the elasto-plastic behavior of the composites and understanding their deformation mechanisms. Several techniques exist to estimate accurately the contribution of all grain families to the phase strain. However, one of the best methods is “the peak average” proposed by [Daymond 2004]. This technique was found to be the best choice for multiphase materials [Cai 2008]. In addition to its good accuracy, can be used even if the texture is not available.

Reference:

[Cai 2008]
Cai, S. (2008). Evolution of Interphase and Intergranular Strain in Zr-Nb Alloys During Deformation at Room Temperature.

[Daymond 2004]
Daymond, M. R. (2004). The determination of a continuum mechanics equivalent elastic strain from the analysis of multiple diffraction peaks. Journal of applied physics, 96(8), 4263-4272.

[Shafer et al. 1991]
Schafer R, A. Hubert, G. Herzter *J. Appl. Phys.* (1991) **69**, 5325

Résumé étendu

Introduction & contexte industriel

L'utilisation des aciers inoxydables duplex (DSS) pour des applications structurales est considérée comme présentant l'un des plus grands impacts potentiels sur le secteur de la construction. Ceci est grâce à ses propriétés mécaniques élevées couplées avec des propriétés fonctionnelles intéressantes telles que : i) le très bon compromis résistance/ductilité ii) la faible coefficient de conductivité thermique (<15W / mK) ; iii) le coût de fabrication réduit et stable grâce à sa faible teneur en Ni. Ainsi, ces propriétés rendent le DSS un matériau très concurrentiel non seulement par rapport aux aciers carbone mais aussi aux aciers inoxydables austénitiques. Tant au niveau scientifique qu'au niveau économique, cette nouvelle nuance des aciers inoxydables intéresse donc de plus en plus les industries métallurgiques ainsi que les institutions académiques. La société UGITECH, par exemple, est l'un des fabricants d'acier en France qui investit dans le développement de nouvelles nuances des aciers inoxydables duplex avec plusieurs brevets sur ces aciers dits *lean duplex*.

Il a été établi que les propriétés mécaniques élevées notamment le couple résistance/ductilité du DSS résultent d'une interaction complexe entre la phase ferritique et austénitique. Cette interaction conduit à un comportement mécanique qui ne peut être prédit à partir de celui des constituants seuls et par conséquent une déviation significative de la loi du mélange. De plus, il a été trouvé que la clef des propriétés uniques des aciers inoxydables duplex réside en effet sur sa microstructure. Néanmoins, le comportement mécanique résultant de cette interaction reste peu compris et contrôlé et fait encore un objet de large investigation dans la littérature. En effet, en fournissant une meilleure compréhension et une description complète du comportement mécanique du DSS, nous pouvons apporter un potentiel significatif à l'obtention des propriétés mécaniques hors du commun en particulier l'amélioration du couple résistance/ ductilité. En outre, une meilleure compréhension donnera également la possibilité de concevoir une nuance DSS sur mesure et architecturé pour des applications spécifiques. C'est dans ce cadre que la collaboration entre Ugitech et Centre d'Excellence des Matériaux Architecturé Multifonctionnels (CEMAM) a été développée pour lancer ce projet. Dans l'objectif d'étudier et d'appréhender le comportement mécanique de DSS, nous avons proposé une stratégie d'élaboration non-conventionnelle dite top-down consistant à fabriquer un DSS à partir d'acier ferritique et austénitique inoxydable à l'état bulk ayant un comportement mécanique bien défini et connu. Ceci nécessite une méthode d'élaboration spécifique permettant l'assemblage de matériaux massifs et la fabrication d'un DSS un micro-structuré. La Déformation Plastique Sévère (SPD) est l'une des techniques les plus utilisées et adaptées pour ce type d'application. L'avantage qu'offre cette stratégie, en utilisant la technique SPD, est qu'elle donne potentiellement plus de degrés de libertés en termes de paramètres à contrôler tels que : compositions chimiques des phases constitutives, distribution de phase, l'échelle, la fraction volumique, etc. De plus, cette approche peut permettre non seulement à comprendre le comportement DSS, en fabricant un matériau modèle avec des paramètres contrôlés, mais aussi développer de nouvelles propriétés via le raffinement de la microstructure.

Procédé d'élaboration

Le procédé de fabrication le plus adapté à notre application est le tréfilage et le r-empilement successif appelé *Accumulative Drawing and re-Bundling (ADB).* Ce procédé a été déjà utilisé pour de fabrication des fils supraconducteur Cu-Nb et Cu-Fe. Dans cette partie de la thèse, nous avons essayé de mettre en place une méthodologie de fabrication reproductive pour le système γ-α. Il est important de noter que c'est la première fois, à notre connaissance, que cette méthode est utilisée pour la fabrication de ce system.

• Matériaux

Les aciers 316L et 430LNb ont été choisis pour la phase austénitique et ferritique respectivement. Ce choix a été essentiellement basé sur leur degré de stabilité lors de différents traitements thermomécaniques. En effet, la nuance 316L montre une stabilité significative vis-à-vis à la transformation martensitique lors d'une déformation plastique grâce à son teneur en Ni élevé. Concernant l'acier ferritique 430LNb, cette nuance est stabilisée au niobium la rendant totalement ferritique jusqu'à la température de solidus lors des recuits de recristallisation. De plus, les deux nuances sont largement utilisées et disponibles dans le marché.

• Méthodologie

Le procédé tréfilage et ré-empilement successif se base sur les étapes suivantes:

0) Configuration du premier composite à partir de fils individuels et un tube. Ce composite constituera le motif élémentaire de la structure des composites suivants.
1) Tréfilage : opération dans laquelle le composite ré-empilé est réduit φ= 6 mm à φ = 1,5 mm de diamètre après 14 étapes
2) Recuit : ceci est l'une des étapes les plus importantes du procédé de fabrication. Elle permet d'adoucir le matériau et donner une ductilité suffisante afin de pouvoir continuer le procédé.
3) Ré-empilement du fil recuit dans un tube ferritique ou austénitique.

La répétition des étapes 1,2 et 3 donnera un composite multi-filamentaire. Figure III-16 schématise ces différentes étapes. Néanmoins, la réussite de ce procédé dépend des paramètres interdépendants tels que : lubrification, état de surface et traitement thermique ce qui rend le tréfilage un procédé complexe. L'ajustement de ces paramètres se réalise à travers des opérations intermédiaires suivantes :

- Revêtement : la couche de revêtement ajoutée joue un rôle d'un support pour le lubrifiant permettant d'assurer une bonne qualité de lubrification lors de tréfilage.
- Décapage : avant de traiter thermiquement les fils tréfilés, un nettoyage du résidu de lubrifiant est nécessaire.

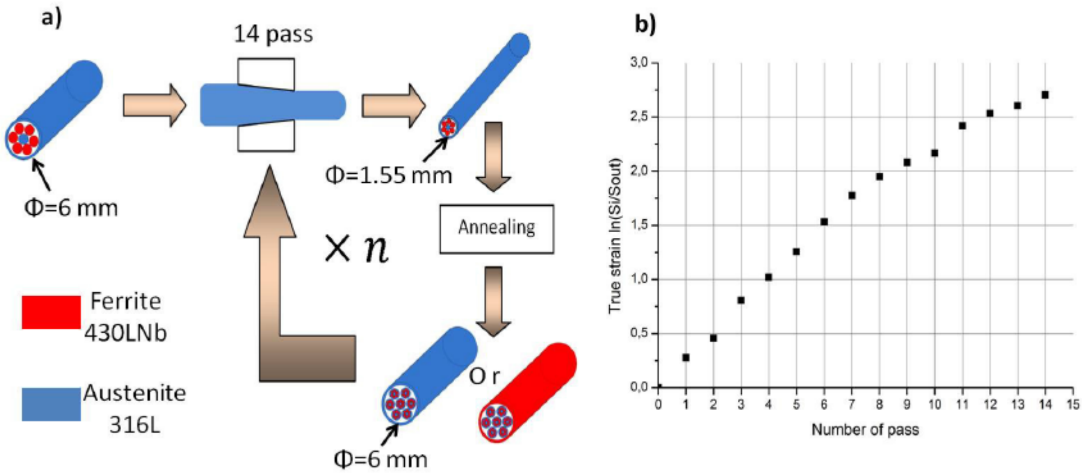

Figure 0-1 : a) Schematic illustration of the ADB process b) Evolution of the true deformation in function of the step number where S_i is the global input section and S_{out} is the global output section

A partir des fils et du tube bulks, nous avons obtenu le premier composite « n1 » dont la microstructure est donnée en Figure 0-2. Ce composite constitue le motif de base pour les composites de rang n>1. Afin de pouvoir fabriquer le deuxième composite « n2 », le composite n1 a été traité thermiquement à la température 1050°C pour une durée de 10 minutes.

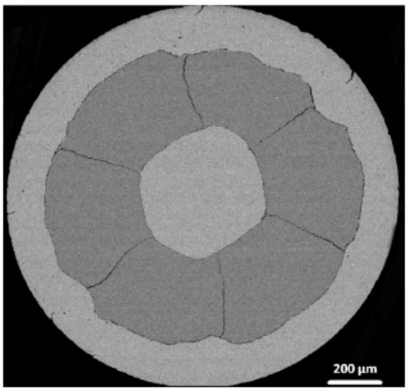

Figure 0-2:SEM image in BSE of the microstructure of n1 composite in the work-hardened state (Ferrite: dark grey, Austenite: clear grey)

Cependant, une régression significative de la phase austénitique en faveur de la phase ferritique a été constatée. Cette régression a été attribuée à la diffusion importante de Ni de l'austénite vers la ferrite (voir Figure III-21). Il a été donc important de limiter cette régression afin de préserver la phase austénitique du mieux possible jusqu'à l'échelle sub-micrométrique. Les paramètres de recuit devaient être donc modifiés. En effet, la température de recuit doit être baissée afin de minimiser la diffusion mais doit être suffisamment élevée pour assurer une bonne ductilité. Pour cela, plusieurs essais ont été réalisés afin de déterminer les conditions optimales en traçant la micro-dureté des deux phases en fonction de la température de recuit pour des temps de maintien de 30 minutes et 1h. Les conditions optimales trouvées pour les deux phases étaient **850°C@1h**.

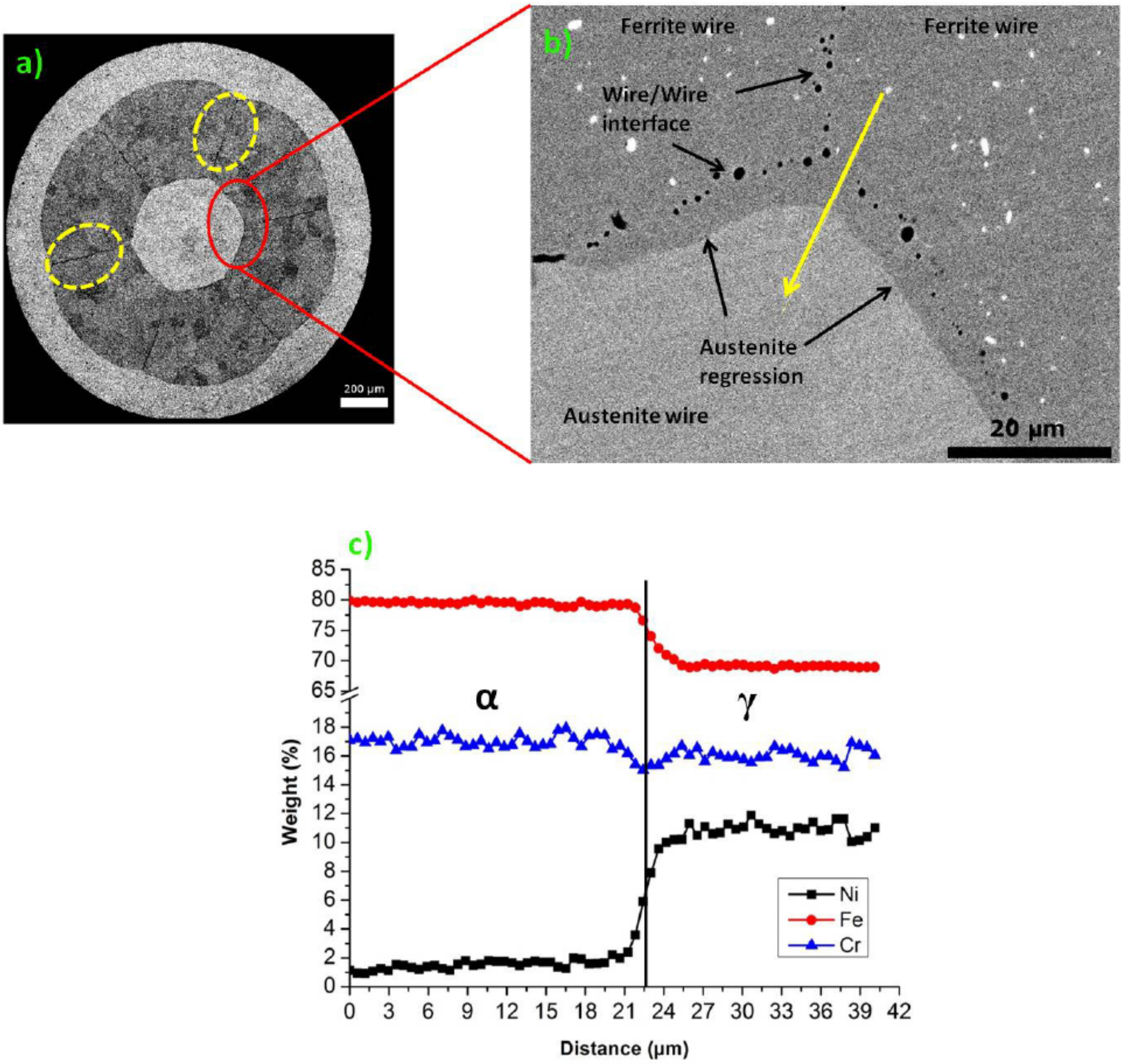

Figure 0-3:a) SEM image in BSE of the microstructure of n1 composite after annealing at 1050°C for 10 min holding time; the dashed circles indicates the unbounded interfaces; b) a magnification on the wires interface showing the austenite regression; the arrow indicates the direction in which the EDS analysis profile of c) was performed; c) EDS analysis showing the evolution of Fe, Cr, Ni weight percentage as a function of distance to the interface (marked by the vertical line).

- ## Microstructure résultante

Une fois les conditions optimales de recuit ont été choisies, des composites architecturés en acier inoxydable duplex multi-échelles ont été obtenus à partir du motif de base (composite n1) et présentés dans les figures suivantes:

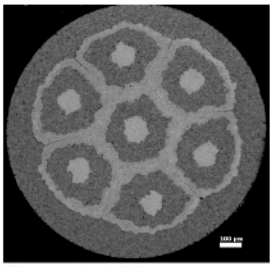

Figure 0-4:Microstructure of n2 composite after annealing (30%γ)

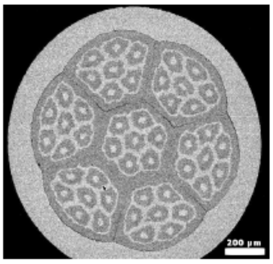

Figure 0-5:Microstructure of n3 composite after annealing (48%γ)

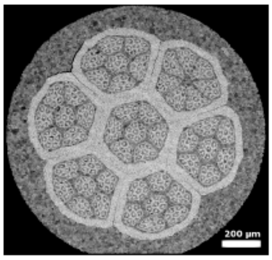

Figure 0-6:Microstructure of n4 composite after annealing (28%γ)

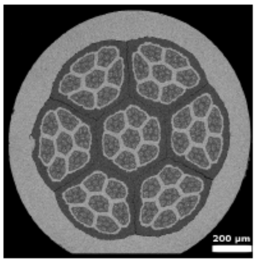

Figure 0-7: Microstructure of n5 composite after annealing (55%γ)

Nous nous somme également intéressés à l'évolution des phases après traitement thermique en particulier les phases constituant le motif de base (composite n1) au sein de chaque composite n>1. Ceci a été effectué grâce à la technique EBSD. Figure 0-8 et Figure 0-9 montrent les cartographies d'orientation des phases du motif de base au sein de composite n3 et n4, respectivement. La formation des petits grains dont l'orientation cristallographique est celle de la phase BCC ont été observés au niveau de l'interface 316L/430LNb. Dans certaines régions ces petits grains formés envahissent la phase austénitique. En arrivant au composite n5, Figure 0-10, nous avons remarqué qu'après traitement thermique à 850°C, la phase austénitique a significativement régressée donnant lieu à une forte perturbation de l'architecture. Ce constat trace la limite du raffinement de la microstructure pour obtenir des structures sub-micrométrique.

La question qu'on a posée par la suite était : *quel est le processus de régression ?* Plusieurs possibilités peuvent être à l'origine à cette régression complète de la phase austénitique : i) une transformation $\gamma \rightarrow \alpha$ lors du recuit par diffusion du Ni ; ii) transformation d'une partie de l'austénite en martensite thermique α' lors du refroidissement dans les zones appauvrie en Ni ; iii) les deux premières possibilités i.e. transformation $\gamma \rightarrow \alpha$ et $\gamma \rightarrow \alpha'$. Cette question a été traitée dans le chapitre IV du manuscrit.

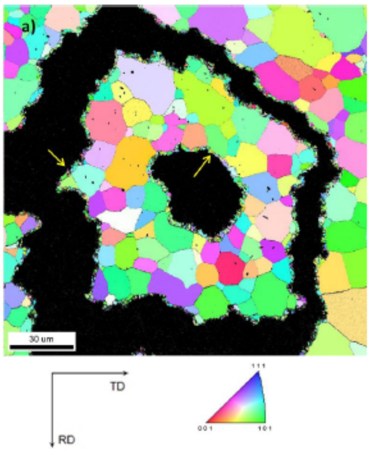

Figure 0-8: EBSD mapping (yellow arrows indicating the small grains) of n1 cell inside composite n3.

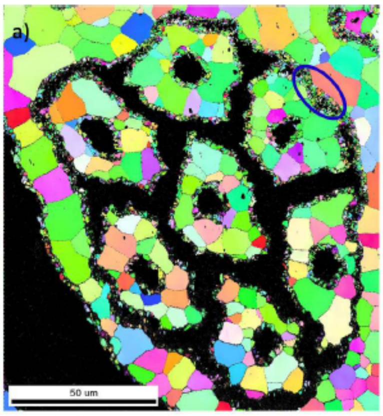

Figure 0-9:EBSD mapping (blue cercle indicating the small grains) of n1 cells inside composite n4.

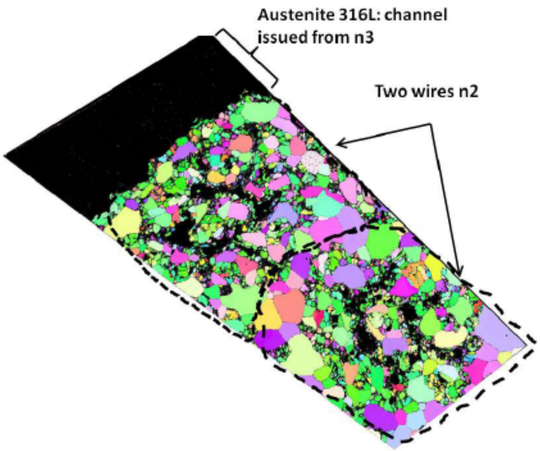

Figure 0-10:EBSD cartography after annealing of n2 cells inside n5 composite

Conclusion

- Le processus de la ADB a été implémenté avec succès pour le système d'aciers inoxydable austénitique/ferrite grâce auquel des micro- composites multi-échelles avec différentes architectures et des fractions de volume sont été obtenus.

- Le raffinement de la microstructure est limité lorsque l'une des phases commence à régresser de façon significative par l'inter-diffusion.

- La microstructure la plus fine est celle du composite n5 dans lequel des micro -domaines (1-3 µm) d'austénite et de ferrite sont obtenus.

Evolution microstructurale

Dans le quatrième chapitre de ce manuscrit, nous avons étudié le processus de régression de la phase austénitique. Cette étude a, tout d'abord, investigué la problématique de l'effet de la température de recuit choisie sur les phases la plus fine ainsi que la possibilité d'avoir une variabilité des conditions de recuit à chaque étape a été investiguée. Cette investigation a été menée par une analyse de la cinétique d'adoucissement des phases les plus fines dans le composite n4 comparée avec celle des fils austénitiques et ferritiques bulks ayant subis les mêmes conditions thermomécaniques. Ensuite une analyse approfondie des profils expérimentaux de diffusion au niveau de l'interface austénite/ferrite du motif de base dans chaque composite n. Cette analyse expérimentale a été rationalisée par une simulation numérique utilisant le logiciel DICTRA.

• Cinétique d'adoucissement

L'objectif de cette étude était de comparer la cinétique d'adoucissement des 316L austénitiques et 430LNb ferritiques dans les cellules fines du composite n4 avec celle des fils individuels de chaque type. Les fils bulks ainsi que le composite n4 ont été traités thermiquement, après une réduction de section d'environ 92%, dans un bain de sel aux températures 750°, 850°C et 950°C pour différentes durées qui varient de 5 sec à 1h.

➢ Fils bulks

L'effet de la température sur la recristallisation et la cinétique d'adoucissement des deux alliages 316L et 430LNb est résumé dans la Figure IV-20. Un des objectifs de cette étude a été également de trouver les conditions de recuit optimisées, pour les deux métaux 316L et 430LNb tréfilés à 92%, pour lesquels la ductilité soit suffisante pour poursuivre le processus et dont la diffusion soit réduite au minimum pour préserver la composition chimique de chaque phase. Les résultats montrent deux températures «extrêmes»; 750 ° C et 950 ° C. La première température (750°C) est très faible c'est-à-dire la dureté des deux phases, notamment 316L, reste élevée (au-dessus de la valeur de dureté acceptable pour le tréfilage imposée dans le chapitre III). En outre, aucun grain recristallisé n'a été révélé dans les deux alliages à l'exception des temps de vieillissement à long terme. La seconde température (950° C) montre une recristallisation instantanée dans 316L et 430LNb (près de 90% de la fraction de recristallisation est atteint après 5 secondes de recuit). Cependant, à une température intérmidère (850° C), la structure des deux alliages, en particulier 316L, recristallise et adoucit progressivement avec l'augmentation du temps de recuit. En effet, seulement après 1 heure de recuit, 316L est entièrement recristallisé et la valeur de dureté est légèrement inférieure à la dureté de tréfilage imposée, c'est-à-dire 225 HV.

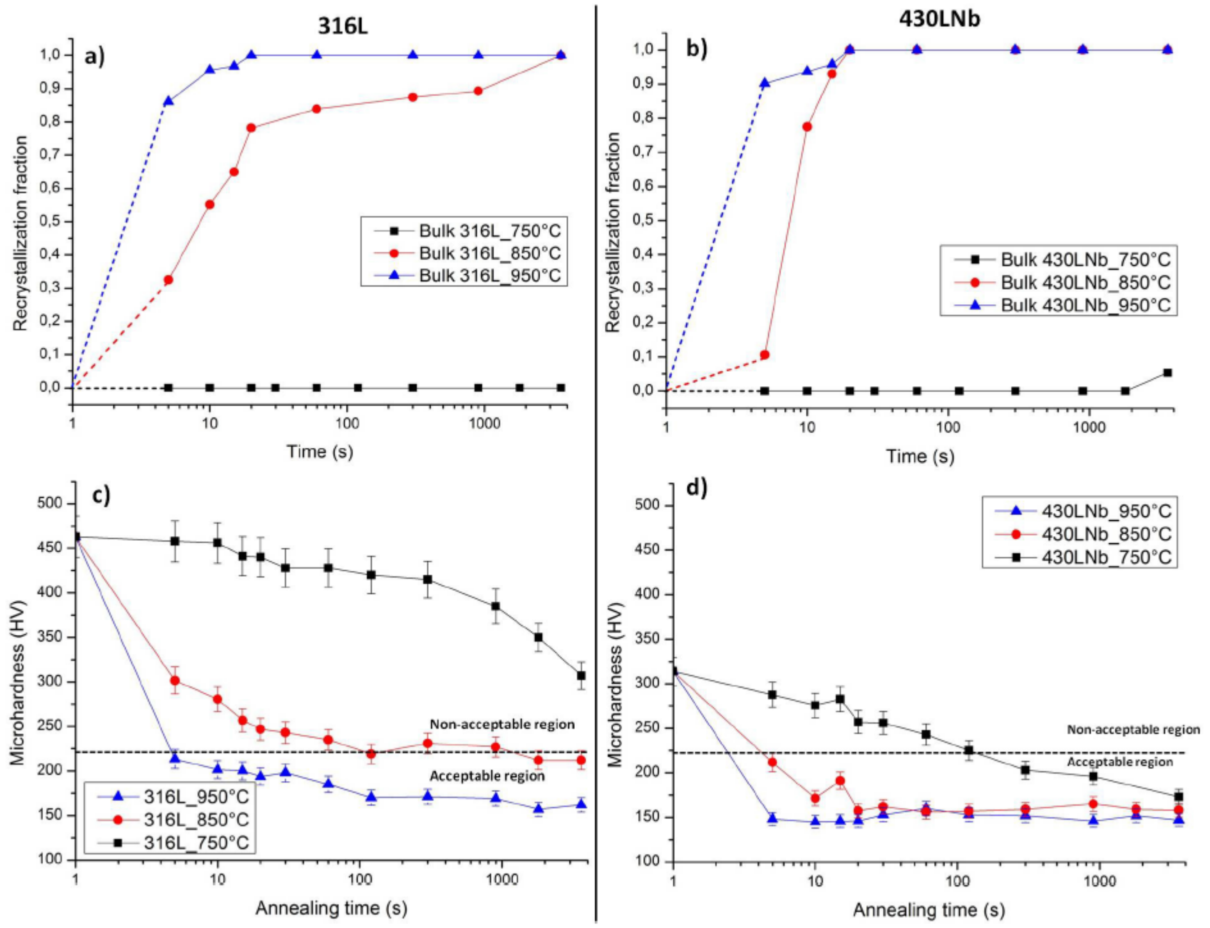

Figure 0-11: Summary of the temperature effect on the recrystallization and softening kinetics, respectively, of 316L; a) and c) and 430LNb; b) and d)

- **Fils bulks vs. Fils composites**

En ce qui concerne la première hypothèse, une étude de la cinétique d'adoucissement a été effectuée à l'aide du composite n4. La cinétique d'adoucissement des phases les plus fines au sein du composite n4 (par exemple 316 et 430LNb issus des cellules n1) a été comparée à celle des fils bulks individuels ayant été soumis à la même réduction de la section que celle des cellules 316 et 430LNb Figure 0-12. Le résultat a montré que les phases de cellules n1 à l'intérieur n4 composite recristallisent plus vite que celle des fils individuels pour des températures de 750° C à 850° C et 950° C. À 750° C, par exemple les phases des cellules n1 ont déjà été recristallisées après 1 heure, tandis que les fils individuels bulks n'ont guère recristallisés à peine. Cette différence de cinétique d'adoucissement a été attribuée à la taille initiale des grains.

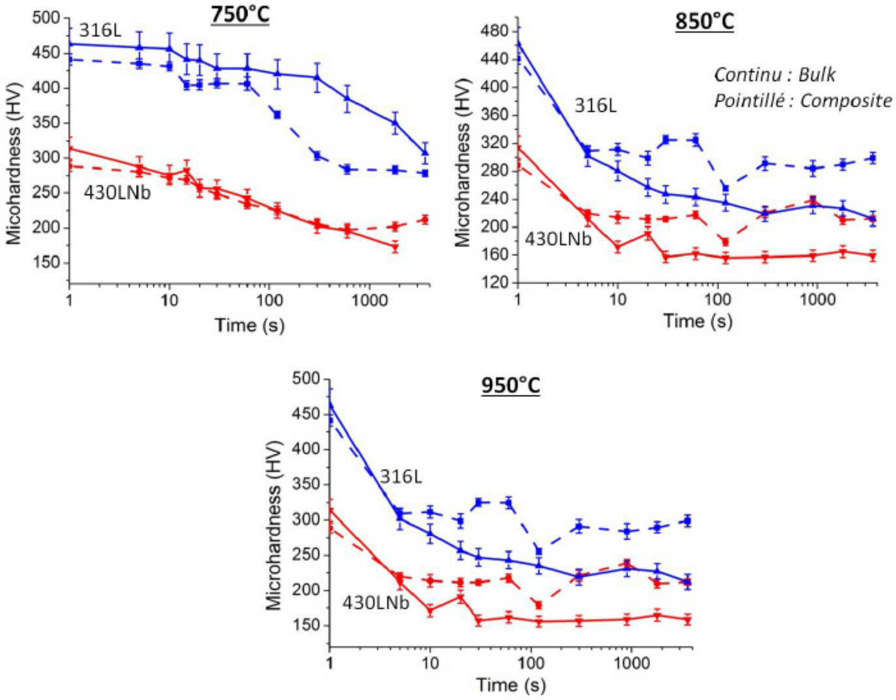

Figure 0-12: Hardness evolution as a function of annealing time and temperature of 316L and 430LNb in both cases bulk state and n4 composite a) 750°C, 850°C and 950°C

Ces résultats peuvent conduire à diminuer la température optimale. Cependant, les générations les plus récentes de ces deux phases, en particulier l'austénite a presque la même cinétique d'adoucissement que les fils bulks (voir Figure 0-13). Ceci suggère que le comportement d'adoucissement d'une phase donnée diffère d'une génération à une autre au sein du même composite. Cependant, la fraction volumique de l'austénite issue des cellules n1 ne représente que 1,9 %, tandis que la fraction volumique d'austénite issue de n3 est d'environ 24 %. Par conséquent, la contribution de la cinétique d'adoucissement des phases issues des cellules n1 à la cinétique d'adoucissement global du composite peut être négligeable devant celle des générations les plus récentes. Par conséquent, la variabilité des conditions optimales de recuit en fonction du composite n peut être négligeable.

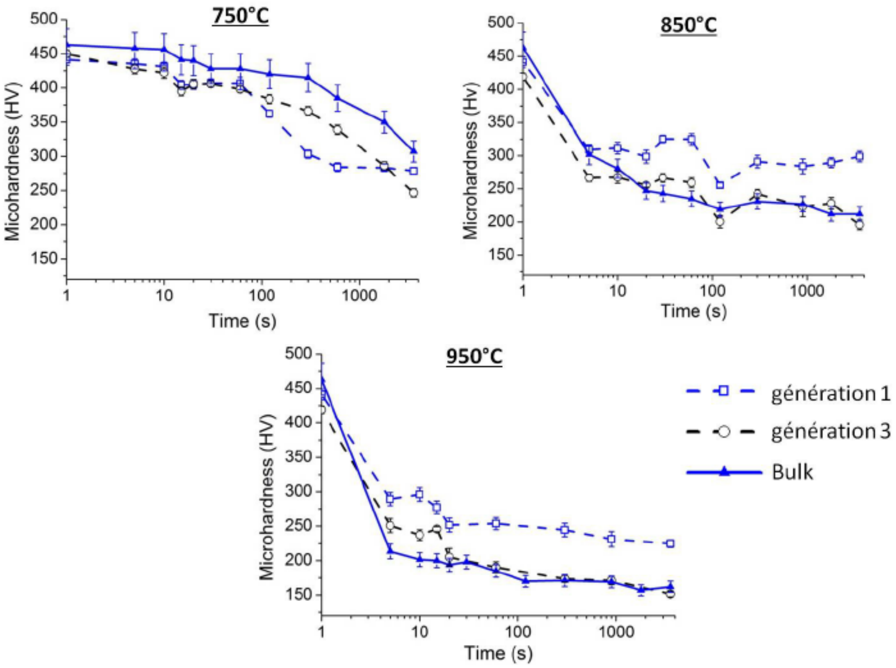

Figure 0-13: Softening kinetics comparison between individual 316L wires and different generation of the same phases inside n4 composite.

- ## Analyse de diffusion

➢ Résultats expérimentaux

La Figure IV-32 montre les mesures expérimentales de la concentration en Ni du couple de diffusion 316L / 430LNb dans le composite n1 et la cellule n1 à l'intérieur de composite ni (i=2,3 et 4) avant et après recuit à chaque étapes de fabrication. Cette analyse a été réalisée en utilisant la technique EDS. Une inter-diffusion importante des éléments de substitution a été observée dans le composite n1 recuit à 1050 ° C pendant 10 minutes. A cette température, une transformation $\gamma \rightarrow \alpha$ entraînant une migration d'interface significative a été observée. Dans la région d'interface suivant l'inter-diffusion, une couche martensitique a été formée au cours du refroidissement rapide d'une épaisseur d'environ 1,3µm. Cette formation a été confirmée grâce aux profils de composition basés sur le calcul de Ms via la formule empirique de Piekring. Cependant, pour les composites ($i \geq 2$) soumis aux conditions de recuit optimales (850° C pendant 1 heure), les caractéristiques suivantes ont été faites à partir des profils de diffusion EDS :

- La couche martensitique dans le voisinage de l'interface 316L / 430LNb est toujours préservée.
- L'épaisseur de cette couche est constante dans tous les composites.

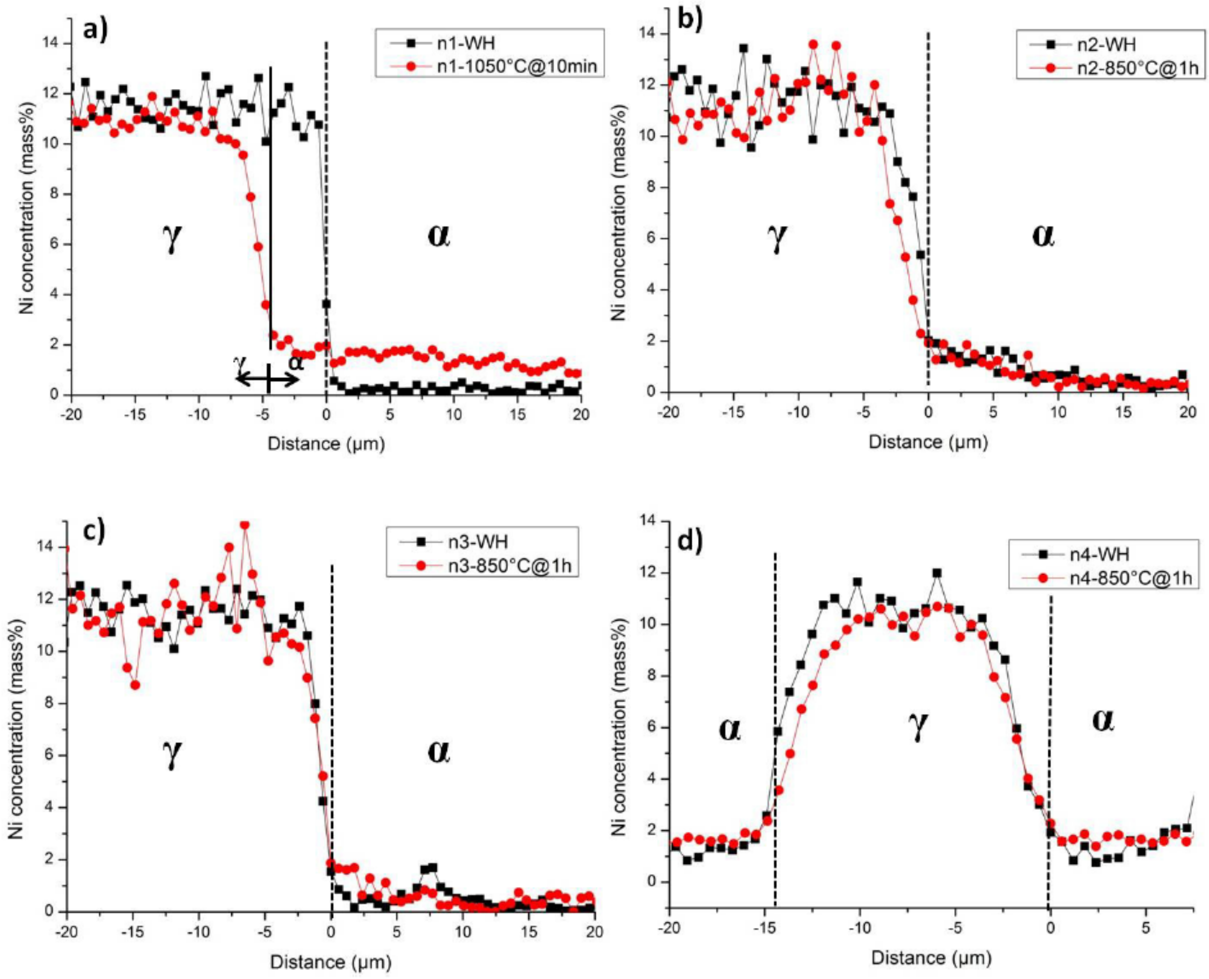

Figure 0-14:EDX profiles for Ni along 316L/430LNb interface at each step of manufacturing before and after annealing treatment: a) n1 composite b) n1 cell inside n2 c) n1 cell inside n3 d) n1 cell inside n4

Les observations MET ont confirmé la présence de la couche de martensite à l'interface 316L/430LNb des cellules n1 à l'intérieur du composite n4 avant et après recuit à 850° C et d'un temps de maintien de 1h. Ces observations ont révélé que l'épaisseur de cette couche de martensite est presque identique avant et après le traitement thermique.

➢ Simulation DICTRA

Le logiciel DICTRA a été utilisé dans cette étude afin de rationaliser la limite du procédé dans l'obtention d'un composite duplex architecturé de 316L/430LNb sub-micrométrique. En particulier, nous avons considéré la microstructure du composite n5 dans lequel les cellules n1 sont plus fines l'ordre de 4-5 µm. Avec cette taille, il a été difficile d'effectuer un profil d'analyse chimique par la technique EDS. C'est la principale raison pour laquelle DICTRA a été utilisé.

Les résultats expérimentaux des mesures EDS ont été reproduits avec succès par DICTRA pour les composites n1, n2, n3 et n4 (voir Figure 0-15). En s'approchant le mieux possible aux conditions expérimentales du recuit anisotherme, la migration d'interface observée dans le composite n1 a été reproduit. L'efficacité des simulations DICTRA dans la prédiction des profils de diffusions pour le couple 316L/430LNb nous a permis de prédire les profils de compositions chimiques de ce couple de diffusion de la cellule de base n1 au sein du composite n5. Ainsi, Cette prédiction a permis de mieux appréhender la microstructure résultante du composite n5 après traitement thermique. En effet, Les résultats de simulation ont montré une diffusion importante de Ni de la région austénitique (de 4 µm) à une ferrite (de 4 µm) de la cellule n1 à l'intérieur du n5 composite (Figure 0-16). Cette diffusion a été considérée comme étant à l'origine de la dilution de l'austénite. Les résultats de simulation montrent que la diffusion du nickel a été contrôlée par la phase austénitique. Cette limitation est donc régie par l'effet du couple diffusion et réduction de section par tréfilage.

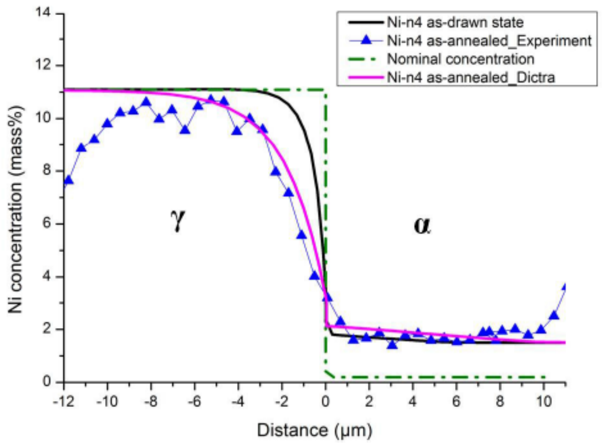

Figure 0-15:Nickel diffusion profiles in the vicinity of 316L/430LNb interface obtained from Dictra by introducing an experimental diffusion profiles as initial concentration with EDS meausurments

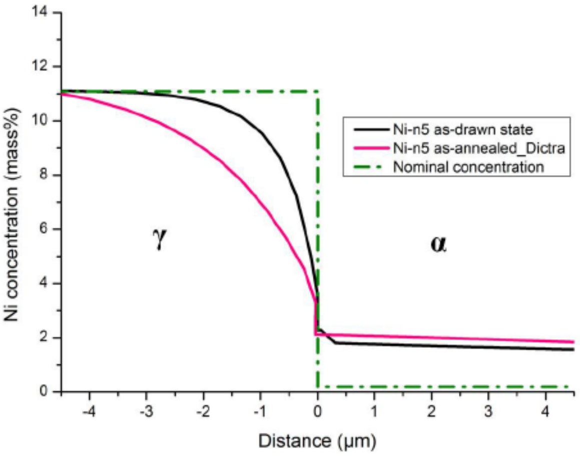

Figure 0-16:Nickel diffusion profile after annealing at 850°C predicted by Dictra

• Conclusion

- A l'état bulk, la température 850°C avec 1h de temps de maintien représentent les conditions optimales de recuit pour les deux phases austénitique et ferritique.
- d'adoucissement des phases les plus fines au sein de composite n4 est accélérée par rapport à celle des fils bulk.
- Au sein du même composite, la cinétique d'adoucissement, pour une phase donnée, diffère d'une génération à une autre.
- Grâce à une analyse de profils de diffusion, la limite de procédé a été tracée par une forte régression de la phase austénitique la plus fine due à la diffusion importante de Ni.
- Rationalisation de cette limite par une simulation DICTRA.

Propriétés mécaniques

Le comportement mécanique de ces composites a été investigué par des essais de traction uniaxiale à chaque étape d'élaboration à l'état recuit. Pour mieux comprendre la réponse mécanique de ces composites, deux approches ont été utilisées dans notre analyse : i) approche macroscopique qui consiste à une analyse comparative entre les courbes de tractions uniaxiale des composites avec celles des fils bulks soumis aux même conditions thermomécaniques ; ii) approche locale qui a pour objectif d'utiliser le comportement local de chacune des phases au sein du composite issu des essais de traction in-situ pour analyser le comportement macroscopique.

• Comportement macroscopique

Une comparaison a été réalisée entre le comportement mécanique des matériaux composites, et celui de fils individuels qui ont été soumis aux mêmes conditions thermomécaniques. La loi de mélange (ROM), en utilisant les fils individuels, a bien prédit le comportement mécanique du composite n1 (45% γ et 55% α) recuits à 1050° C Figure 0-17.

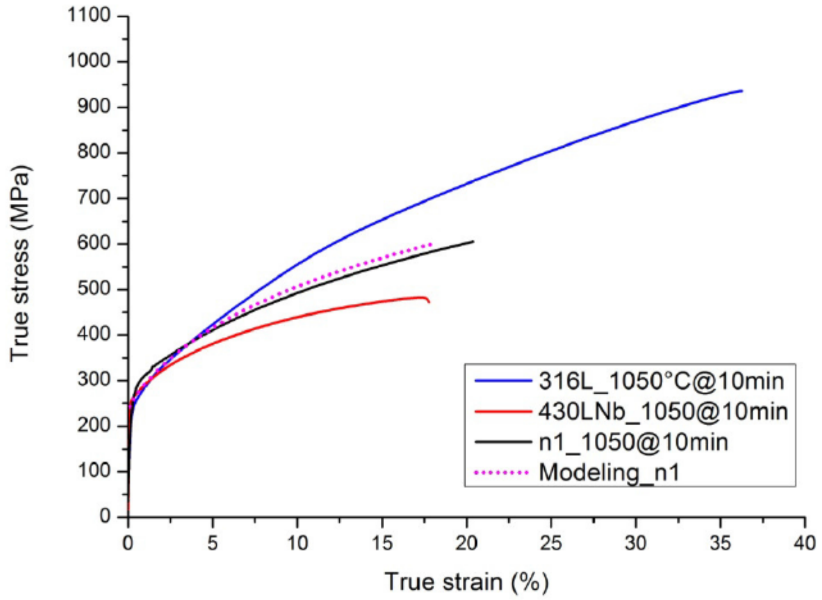

Figure 0-17: Mechanical response of composite n1 compared with bulk wires

Cependant, pour les composites n (i> 1) recuite à la température optimale, une augmentation systématique de la résistance mécanique en fonction de l'étape de fabrication a été remarqué (voir Figure 0-18 et Figure 0-19). L'influence de plusieurs facteurs comme la taille de grains, la composition chimique, la présence de la martensite...etc. a été discutée dans cette analyse. La taille de grains a été trouvée comme le facteur principal qui peut apporter une explication à cette augmentation systématique quelque soit la fraction volumique de chaque phase dans le composite. En effet, il a été constaté que dans le même composite, la taille des grains pour une phase donnée est plus faible dans les anciennes générations que celles dans les plus récentes. Pour une génération et une phase donnée, on peut remarquer une diminution systématique de la taille des grains pour des composites du rang supérieur (voir Figure V-13).

Afin de prendre en compte la contribution de la taille de grains de chaque composant au comportement macroscopique des composites, une relation Hall- Petch (HP) a été établie pour les deux phases 316L et 430LNb en utilisant des fils individuels. Une différence significative entre ROM et l'expérience a été trouvé. Cette différence a été attribuée au fait que la relation HP établie pour chacune des phases à l'état bulk n'est pas représentative pour celles du composite en question. Celui-ci est à son tour lié à la modification de la composition chimique. De plus la contribution de la martensite au comportement a été trouvé négligeable.

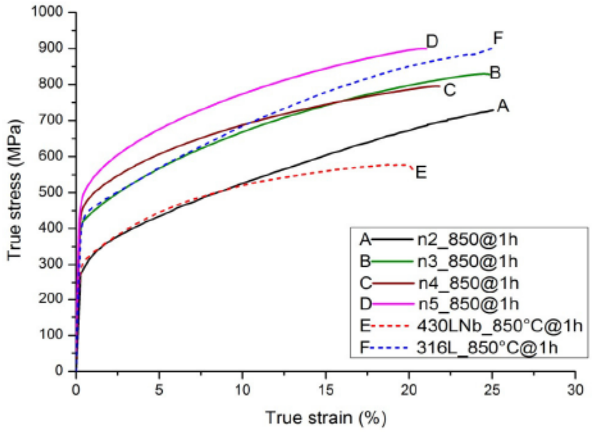

Figure 0-18:Mechanical response of composites n(i>1) compared with 316L and 430LNb wires after annealing at 850°C

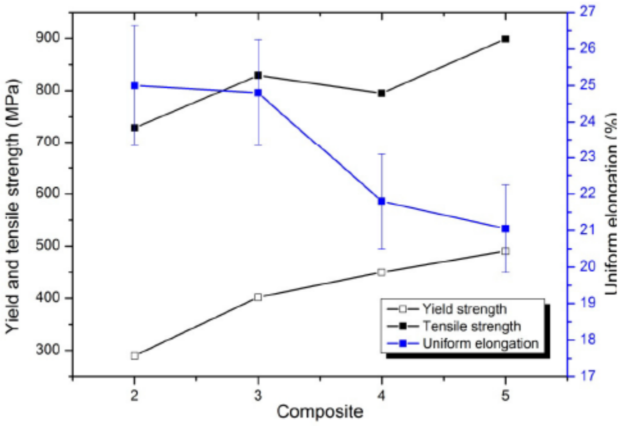

Figure 0-19:The evolution of the mechanical properties as a function of composite n

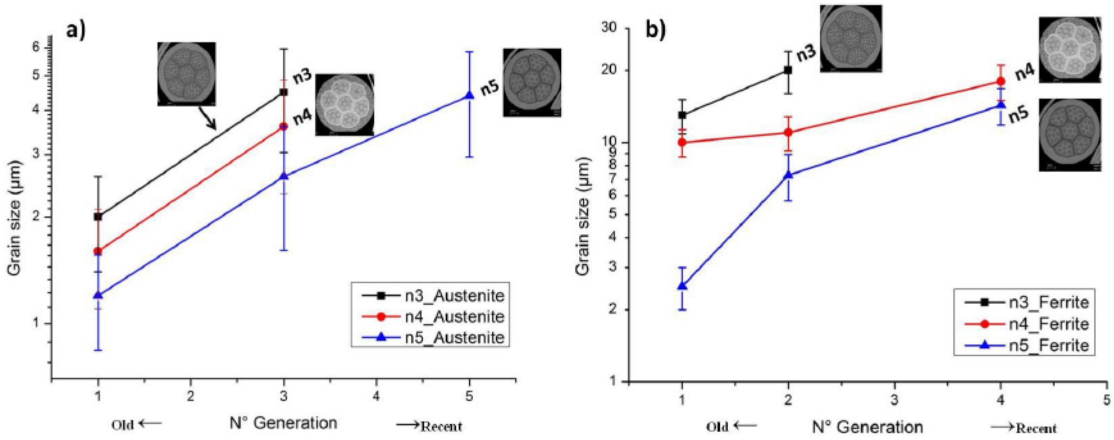

Figure 0-20: Grain size evolution of each component (generation) for composite n3, n4 and n5 after annealing at 850°C for 1 hour: a) austenite (316L) , b) ferrite (430LNb)

- ## Comportement mécanique local : essais in-situ par diffraction des rayons-X synchrotron à haute énergie

Des essais de traction in-situ uniaxiale assistés par diffraction des rayons-X synchrotron à haute énergie ont été effectués. Ces mesures avaient pour objectif de déterminer la répartition des contraintes entre les différentes phases au cours des essais de traction. Ceci nous permettra de mieux comprendre le comportement des composites et de fournir des éléments de réponse à l'augmentation systématique de la résistance mécanique en fonction de l'étape de fabrication.

Ces informations sont obtenues au moyen des diffractogrammes dans lesquels l'intensité diffractée est tracée en fonction de l'angle 2θ de Bragg. Le décalage en position observé d'un plan {hkl} spécifique résulte d'une variation de la déformation élastique moyenne d'un plan cristallographique {hkl} (<ε_{hkl}>). Cette dernière peut être calculée en utilisant l'expression suivante:

$$\varepsilon_{hkl} = \frac{d_{hkl} - d_{hkl}^0}{d_{hkl}^0}$$

Dans cette expréssion d_{hkl} et d_{hkl}^0 correspondent à la distance entre deux plans cristallographiques (ou distance inter-réticulaire) après et avant déformation respectivement.

Afin de simplifier notre analyse, un seul plan cristallographique a été choisi pour représenter la phase en question. Les plans (200) et (110) ont été choisis pour représenter les phases γ et α au sein du composite, respectivement.

La Figure V-27 montre l'évolution de la déformation du réseau de γ (200) et α (110) dans la direction de traction en fonction de la contrainte appliquée. Trois régimes peuvent être distingués par le changement de la pente d'une des phases. D'une manière générale, la courbe d'austénite est toujours supérieure à celle de ferrite pour tous les composites. Cela signifie que l'austénite encaisse plus de charge que la ferrite dans les trois régimes. La phase austénitique est alors la phase la plus dure dans ces composites et la ferritique est celle la plus molle. Ces résultats est en accord avec les mesures de dureté montrant que la phase austénitique est toujours la phase la plus dure au sein du composite quelque soit la génération.

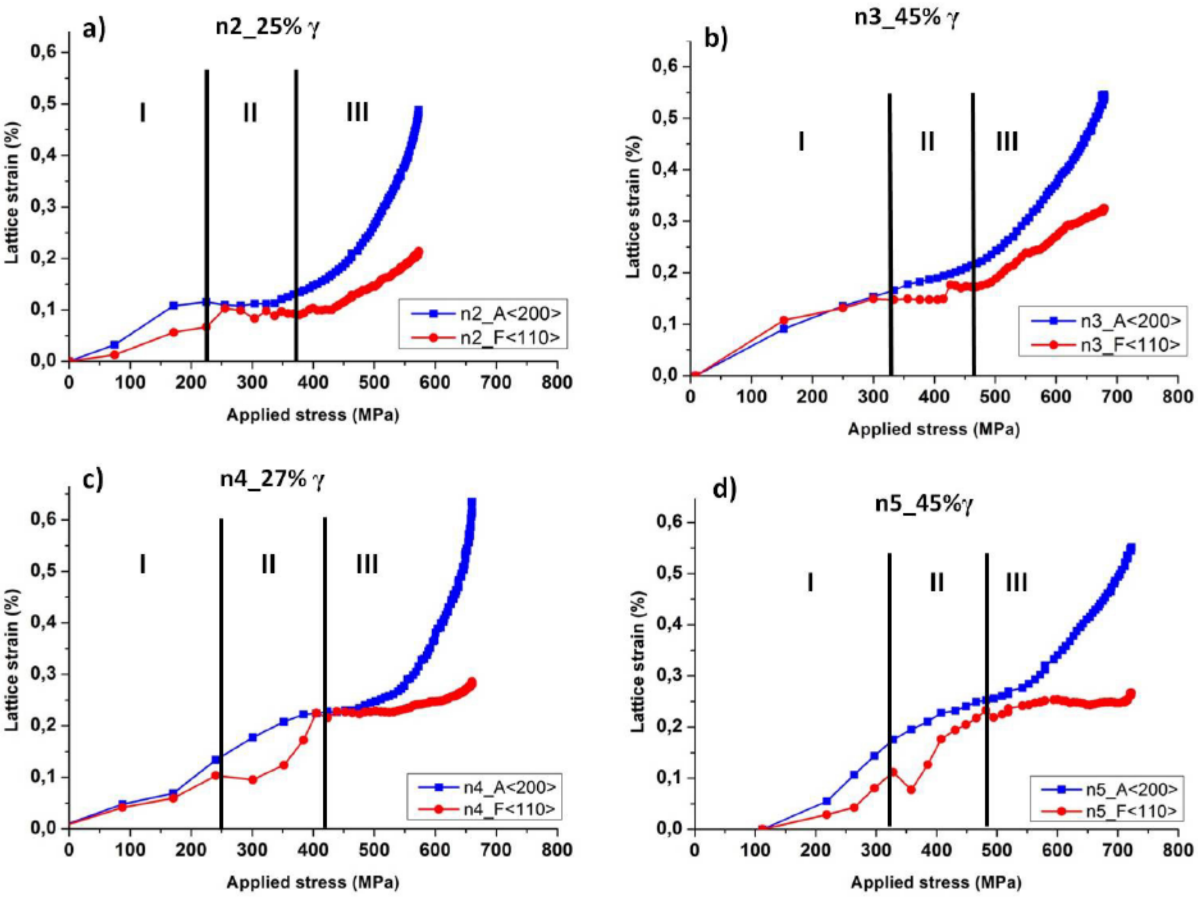

Figure 0-21: Evolution of the lattice strain in the loading direction as a function of the applied stress for γ(200) and α(110) reflections for composites a)n2;b) n3; c)n4; d)n5 annealed at 850°C for 1hour

La contrainte effective σ_{11}^{ph} d'une phase a été calculée à partir des déformations élastiques en supposant que l'influence des contraintes intergranulaires est négligeable et que la linéarité entre les déformations élastiques avec les contraints appliquées est assurée. Cette hypothèse nous a permis d'utiliser la loi d'Hook pour convertir les déformations élastiques d'un plan cristallographique hkl en contrainte.

Les Figure V-31 et Figure V-32 résument l'évolution de la contrainte calculée pour γ (200) et α (110) de tous les matériaux composites en fonction de la déformation vraie macroscopique. Une augmentation systématique des contraintes calculées pour γ (200) et α (110) en fonction du composite n a été trouvée. Ceci nous a permis de confirmer l'effet majeur de la taille des grains à l'intérieur des phases sur le comportement macroscopique du composite. Ce résultat est en accord avec notre discussion dans la section précédente.

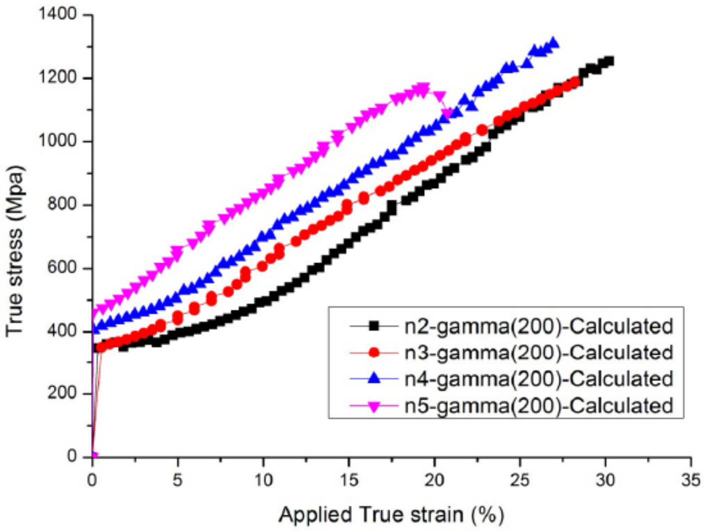

Figure 0-22: Calculated stress *vs* Applied True strain of γ(200) reflection for each composite n2,n3,n4 and n5

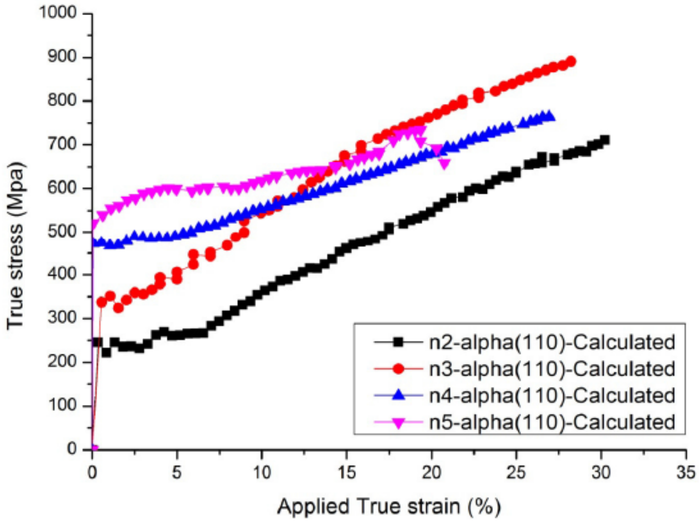

Figure 0-23: Calculated stress *vs* Applied True strain of α(110) reflection for each composite n2, n3, n4 and n5

• Conclusion

- Une augmentation systématique des propriétés mécaniques des composites à chaque étape n de fabrication a été observé
- Le comportement mécanique est significativement gouverné par l'influence de taille de grains.
- grâce aux essais de traction in-situ par diffraction des rayons-X synchrotron à haute énergie, nous avons pu déterminer le comportement élasto-plastique de chacune de phase.